UCLA
UCLA Electronic Theses and Dissertations

Title
Investigating Methods to Enhance T cell Antitumor Immunity and Reduce Graft-versus-Host Disease

Permalink
https://escholarship.org/uc/item/9tw9b83m

Author
Zeng, Samuel

Publication Date
2021

Peer reviewed|Thesis/dissertation

eScholarship.org Powered by the California Digital Library
University of California

University of California

Los Angeles

Investigating Methods to Enhance T cell Antitumor Immunity and Reduce Graft-versus-Host Disease

A dissertation submitted in partial satisfaction of the

Requirements for the degree Doctor of Philosophy

in Molecular Biology

by

Samuel Weijia Zeng

2021

Abstract of the Dissertation

Investigating Methods to Enhance T cell Antitumor Immunity and

Reduce Graft-versus-Host Disease

by

Samuel Weijia Zeng

Doctor of Philosophy in Molecular Biology

University of California, Los Angeles, 2021

Professor Lili Yang, Chair

In addition to defending against invasive microbes, T cells of the mammalian adaptive immune system also provide crucial protection against cancerous cells that spontaneously emerge from healthy host tissue. Cancer cells, in turn, co-opt many of the regulatory signaling pathways used by the body to prevent excessive T cell proliferation and activation. The tumor microenvironment (TMI) is frequently a highly immunosuppressive environment, and much research has been focused on identifying new targets that can enhance T cell antitumor immunity. Novel observations from my lab has found monoamine oxidase A (MAO-A) plays an important role in maintaining this immunosuppressive TMI. In Chapter 2, I observe that MAO-A functions as a "checkpoint" molecule that regulates $CD8^+$ T cell antitumor immunity through modulating metabolization of serotonin, a neurotransmitter previously unassociated with the immune response. In Chapter 3, I observe that MAO-A also indirectly affect T

cell antitumor immunity by promoting tumor associated macrophage polarization towards an immunosuppressive phenotype through signaling with oxidative stress. These two chapters provide exciting preclinical data and clinical correlation for repurposing clinical approved MAO-A inhibitors for cancer immunotherapy. Allogeneic hematopoietic stem cell transplantation is another approach to treating cancer, in particular hematological malignancies, and relies on donor T cell recognition of minor histocompatibility antigens to target residual cancer cells. However, its application is severely limited due to the risk of graft versus host disease (GvHD). Higher invariant natural killer T (iNKT) cell load following transplantation has been clinically associated with reduced GvHD without loss of the beneficial graft versus leukemia/lymphoma (GvL) effect. However, the accessibly of iNKT cells remains a major hurdle to their research and potential clinical application. In Chapter 4, I provide two protocols for generating large amounts of mouse and human iNKT cells *in vivo* through TCR engineering of hematopoietic stem cells (HSC-engineered iNKT) and a murine intermediary. In Chapter 5, a protocol to generate human HSC-engineered iNKT cells *in vitro* is introduced, and the resultant HSC-engineered iNKT are found capable of ameliorating xeno-GvHD without loss of GvL effect when added to the allograft, providing exciting preclinical data highlighting the possibly of using HSC-engineered iNKT cells as additives to the allograft to reduce GvHD risk and improve patient outcomes.

The dissertation of Samuel Weijia Zeng is approved.

Yvonne Chen

Arnold Chin

Gay Crooks

Markus Müschen

Lili Yang, Committee Chair

University of California, Los Angeles

2021

Table of Contents

Table of Figures

Acknowledgements

These past four years of my PhD training have been an incredible experience, and I have many people to thank for their support and encouragement to helping me reach this conclusion.

Thank you to my mentor Dr. Lili Yang for her constant patience and encouragement. She provided me both the freedom to pursue my scientific inquiries and the resources to bring about the answers. Dr. Yang was always there for me whenever I hit a rough patch in my research, a fount of both emotional support and intellectual insight. I could not have asked for a better thesis lab and mentor.

Thank you to my other thesis committee members: Dr. Gay Crooks, Dr. Arnold Chin, Dr. Yvonne Chen, and Dr. Markus Müschen, for their time and guidance during my PhD training.

Thank you to all members of the Yang Lab, past and present, for their support, encouragement, collaboration, and friendship during my PhD training: Dr. Yu-Chen (Ryan) Wang, Dr. Xi (Shirley) Wang, Dr. Xiaoya (Jessie) Ma, Dr. Zhe (Joanne) Li, Dr. Yu Jeong (YJ) Kim, Dr. Yanni Zhu, Dr. Stephano di Biase, Jie Huang, Jiaji (Victor) Yu, Yang (Alice) Zhou, Yan-Ruide (Charlie) Li, and Derek Lee. I am also grateful for my collaborators outside the Yang lab, include the Zeng lab at City of Hope. I would also like to express my thanks for the UCLA MBIDP administration, including Dr. Luisa Iruela-Arispe, Dr. Peter Bradley, Ashley Terhost, and Weiling Chen for their support during my training. Furthermore, a special thanks to the UCLA MSTP for providing me the opportunity to pursue a PhD in the first place: Dr. David Dawson, Dr. Carlos Portera-Cailliau, Dr. Leanne Jones as well as the wonderful Susie Esquivel and Josephine (Josie) O. Alviar.

Finally, my sincerest thanks to my family, whose love and support I could not have done without. To my parents Defu Zeng and Yanfei Chen, who are my greatest inspirations and sources of strength. To my wonderful wife Shanshan Tang, thank you for always being at my side. And to my dearest daughter Iris Zeng, I hope to be an inspiration for you.

Chapter 2 was originally published in Science Immunology. Xi Wang, Bo Li, Yu Jeong Kim, Hu-chen Wang, Zhe Li, Jiaji Yu, **Samuel Zeng**, Xiaoya Ma, In Young Choi, Stefano Di Biase, Drake J. Smith, Yang Zhou, Yan-Ruide Li, Feiyang Ma, Jie Huang, Nicole Clarke, Angela To, Laura Gong, Alex Pham, Heesung Moon, Matteo Pellegrini, Lili Yang. Targeting monoamine oxidase A for T cell-based cancer immunotherapy. Science Immunology 14 May 2021: Vol. 6, Issue 59, eabh2383 DOI: 10.1126/sciimmunol.abh238. The work is reprinted here with permission from the American Association for the Advancement of Science (AAAS). The work was supported by a Research Career Development Award from the STOP CANCER Foundation, a BSCRC-RHF Research Award from the Rose Hills Research Foundation, a JCCC/BSCRC Ablon Scholars Award from UCLA, and a Magnolia Council Senior Investigator Grant Award from the Tower Cancer Research Foundation. Z.L. was a postdoctoral fellow supported by the UCLA Tumour Immunology Training Grant (USHHS Ruth L. Kirschstein Institutional National Research Service Award # T32 CA 009120). J.Y. was a predoctoral fellow supported by the UCLA Broad Stem Cell Center (BSCRC) Predoctoral Fellowship. S.Z. was a predoctoral fellow supported by the UCLA Medical Scientist Training Program Grant (T32-GM008042). D.J.S. was a predoctoral fellow supported by the UCLA Tumor Immunology Training Grant (U.S. Department of Health and Human Services Ruth L. Kirschstein

Institutional National Research Service award no. T32 CA009056). Y-R.L. was a predoctoral fellow supported by the UCLA Whitcome Predoctoral Fellowship in Molecular Biology.

Chapter 3 was originally published in Nature Communications. Yu-Chen Wang, Xi Wang, Jiaji Yu, Feiyang Ma, Zhe Li, Yang Zhou, **Samuel Zeng**, Xiaoya Ma, Yan-Ruide Li, Adam Neal, Jie Huang, Angela To, Nicole Clarke, Sanaz Memarzadeh, Matteo Pellegrini & Lili Yan. Targeting monoamine oxidase A-regulated tumor-associated macrophage polarization for cancer immunotherapy. Nature Communications volume 12, Article number: 3530 (2021). The work is reprinted here with permission under a CC BY license (Creative Commons Attribution 4.0 International License). This work was supported by a Research Career Development Award from the STOP CANCER Foundation, a BSCRC-RHF Research Award from the Rose Hills Research Foundation, a JCCC/BSCRC Ablon Scholars Award from UCLA, and a Magnolia Council Senior Investigator Grant Award from the Tower Cancer Research Foundation. J.Y. was a predoctoral fellow supported by the UCLA Broad Stem Cell Research Center (BSCRC) Predoctoral Fellowship. Z.L. was a postdoctoral fellow supported by the UCLA Tumour Immunology Training Grant (USHHS Ruth L. Kirschstein Institutional National Research Service Award # T32 CA 009120). S.Z. was a predoctoral fellow supported by the UCLA Medical Scientist Training Program Grant (T32-GM008042). Y-R.L. was a predoctoral fellow supported by the UCLA Whitcome Predoctoral Fellowship in Molecular Biology.

Chapter 4 is unpublished work undergoing revision at Methods in Molecular Biology. Yang Zhou*, Yan-Ruide Li*, **Samuel Zeng**, and Lili Yang. Methods for Studying Mouse and Human Invariant Natural Killer T Cells. Methods in Molecular Biology: Humana Press (in press); 2021. This work was supported by a Director's New Innovator Award from the NIH (DP2 CA196335), a Partnering

Opportunity for Translational Research Projects Award from the California Institute for Regenerative Medicine (CIRM TRAN1-08533), a Stem Cell Research Award from the Concern Foundation, a Research Career Development Award from the STOP CANCER Foundation, and a BSCRC-RHF Research Award from the Rose Hills Research Foundation. Y.-R.L. was a predoctoral fellow supported by the UCLA Whitcome Predoctoral Fellowship in Molecular Biology. S.Z. was a predoctoral fellow supported by the UCLA Medical Scientist Training Program Grant (T32-GM008042).

Chapter 5 is unpublished work current undergoing submission at Nature Communications. It reflects the work performed by **Samuel Zeng***, Yan-Ruide Li*, Yang Zhou, Zhe Li, Jiaji Yu, Yu-Chen Wang, Josh Ku, Noah Cook, Adam Kramer, Jie Huang, and Lili Yang.

Vita

2011	I.I. Rabi Scholar; Columbia University; NY, NY
2014	Barry Goldwater Scholarship; Columbia University; NY, NY
2014	Bachelor of Arts in Biological Science, Magna Cum Laude and Biology Departmental Honors; Columbia University; NY, NY
2014	Phi Beta Kappa Honor Society; Columbia University; NY, NY
2015-Present	Medical Scientist Training Program; University of California, Los Angeles; Los Angeles, CA
2016	Lothar-Anne Rosenthal Fellowship; University of California, Los Angeles; Los Angeles, CA
2017-Present	Molecular Biology Interdepartmental Doctoral Program; University of California, Los Angeles; Los Angeles, CA

Publications

Tang S, Zhang M, **Zeng S**, Huang Y, Qin M, Nasri U, Santamaria P, Riggs A, Jin L, & Zeng D. **Reversal of autoimmunity by mixed chimerism enables reactivation of β cells and transdifferentiation of α cells in diabetic NOD mice**. PNAS December 8, 2020 117 (49) 31219-31230

Wang X, Li B, Kim Y, Wang H, Li Z, Yu J, **Zeng S**, Ma X, Choi I, Di Biase S, Smith D, Zhou Y, Li Y, Ma F, Huang J, Clarke N, To A, Gong L, Pham A, Moon H, Pellegrini M, & Yang L. **Targeting monoamine oxidase A for T cell-based cancer immunotherapy.** Science Immunology May 14, 2021: Vol. 6, Issue 59, eabh2383

Li Z, Lee D, **Zeng S**, & Yang L. **Invariant Natural Killer T Cell-Based Cancer Immunotherapy**. In: Successes and Challenges of NK Immunotherapy: Breaking Tolerance to Cancer Resistance. Academic Press: Elsevier. June 07, 2021.

Wang Y, Wang X, Yu J, Ma F, Li Z, Zhou Y, **Zeng S**, Ma X, Li Y, Neal A, Huang J, To A, Clarke N, Memarzadeh S, Pellegrini M & Yang L. **Targeting monoamine oxidase A-regulated tumor-associated macrophage polarization for cancer immunotherapy.** Nature Communications volume 12, Article number: 3530 (2021).

Zhou Y*, Li Y*, **Zeng S**, & Yang L. **Methods for Studying Mouse and Human Invariant Natural Killer T Cells.** Methods in Molecular Biology: Humana Press (2021, in press)

Zeng S*, Li Y*, Zhou Y, Li Z, Yu J, Wang Y, Ku J, Cook N, Kramer A, Huang J, & Yang L. **Development of off-the-shelf HSC-engineered iNKT cells for alleviating GvHD while preserving GvL in the treatment of blood cancers.** Nature Communications (In Submission)

Presentations

MBIDP Student Seminar Series. February 2019. UCLA Boyer Hall. **Zeng S**, Yang L. **iNKT cell therapy for the prevention of aGVHD while Augmenting GVL** (Talk)

UCLA-Caltech MSTP 2019 Annual Research Conference September 2019. UCLA DeNeve Auditorium. **Zeng S**, Lili Yang. **iNKT cell therapy for the prevention of aGVHD while Augmenting GVL** (Poster)

American Society of Hematology Annual Meeting. December 2019. Orange County Convention Center (OCCC), Orlando, FL. **Zeng S**, Song Q, Tang S, Wang X, Wang Y, Zeng D, Yang L. **Combination Therapy of Allogeneic HSCT and In Vivo Activated iNKT Cells Prevents Acute GvHD While Augmenting GvL Effect** (Poster).

Chapter 1: Introduction

Overview of T Lymphocytes

To defend itself against the plethora of pathogenic microbes, mammals have developed an intricate defensive system comprised of an innate and adaptive immune system[1]. The innate immune system provides broad spectrum protection and includes physical barriers (e.g. epithelial cell layers and mucosal linings), soluble proteins and bioactive small molecules (e.g. complement proteins and defensins), as well as first-responder immune cells that activate by recognizing pathogenic molecular patterns expressed on microbial surface (e.g. neutrophils and macrophages)[1]. Innate immune cells also activate the adaptive immune response. Whereas the innate immune system is broad spectrum, the adaptive immune system manifests exquisite specificity for its target antigens, largely through the antigen-specific receptors expressed on the surfaces of T- and B-lymphocytes[1]. T lymphocytes are named so for the somatically rearranged T cell receptor (TCR) expressed on their cell surface and provide an intricate armory of functions aimed at eliminating pathogen-infected and neoplastic cells[1].

Although T lymphocytes consist of several functionally and phenotypically heterogeneous subpopulations, the majority can be classified as either αβ or γδ according to their TCR rearrangement[2]. αβ T cells are by far the most abundant and the best-characterized circulating T cells. Most αβ T cells are also "conventional," meaning they recognize degraded proteins bound to major histocompatibility complex (peptide-MHC, pMHC) molecules found at the cell surface[3]. However, a rarer, but significant, fraction of αβ T cells do not recognize pMHC. These "unconventional" αβ T cells include: (i) mucosal-associated invariant T (MAIT) cells that display limited diversity and are involved in anti-bacterial immunity[4, 5]; (ii) invariant natural killer T (iNKT) cells; and (iii) germline-encoded mycolyl-reactive (GEM) T cells. iNKT and GEMT cells are dedicated to the recognition of glycolipids in the context of

CD1d and CD1b, respectively[6, 7]. Although there are other T cells believed to recognize lipid antigens in the context of CD1a and CD1c, these subsets have not been well characterized or named.

T Lymphocytes Development

The complete T cell repertoire that provides targeted protection against a vast array of microbial pathogens is comprised of a myriad of T cells that each express antigen receptors of a single specificity. T cell development begins when lymphoid progenitors derived from hematopoietic stem cells residing in the bone marrow migrate to the thymic subcapsular zone (Figure 1)[8]. There, they undergo rearrangement of the TCR variable (V), diversity (D), and joining (J) gene elements (Figure 2)[9]. Lymphoid-specific RAG1 and RAG2 proteins initiate this process by cleaving the DNA near the V, D, and J segments. The gene segments are rejoined by a collection of non-lymphoid-specific DNA repair enzymes including DNA-dependent protein kinase (DNA-PK), Ku, XRCC4, XLF, DNA ligase IV, and the Artemis nuclease[10]. XRCC4, XLF, and DNA-PK also recruit the enzyme terminal deoxynucleotidyl transferase (TdT), which adds deoxynucleotides into some of the VDJ junctions and provides additional junctional diversity to the recombined gene sequences[11]. Due to the apparently random process in assembling the V, D, and J gene elements, huge diversity of receptor sequences are formed, but non-functional TCRs are also a frequent byproduct.

Once a productive $V_\beta D_\beta J_\beta$ (TCR β) chains is assembled, developing T cells migrate to the thymic cortex and undergo TCR α chain rearrangement[8]. In the cortex, surface expression of the CD3, CD4 and CD8 proteins is induced. $CD4^+CD8^+$ (double positive) T cells are tested on whether their receptors have sufficient affinity for self major histocompatibility complex (MHC) molecules; this "positive" selection involves interaction between the developing lymphocyte and the specialized cortical epithelium[12,13].

Lymphocytes that fail this positive selection undergo apoptosis and are cleared by thymic cortical macrophages. Those with adequate affinity to recognize a self MHC Class I (MHC I) protein retain CD8 expression and extinguish CD4 expression; those that recognize a self MHC Class II (MHC II) proteins retain CD4 expression and extinguishes CD8 expression. This process is central to establishing CD4 with class II MHC restricted antigen recognition and CD8 with class I restricted antigen recognition[13].

CD4/CD8 single positive (SP) cells then migrate to the thymic medulla and are screened for potential autoreactivity. During this process, T cells are exposed to an extensive array of tissue-specific proteins expressed by a population of thymic medullary epithelial cells under the control of a gene called *AIRE* (autoimmune regulator)[12]. Those that recognize self-peptides are removed by apoptosis. T cells that survive the combination of positive and negative selection (<5% of all developing T cells) are released into circulation as naïve T cells.

The aforementioned αβTCR developmental process describes approximately 90–95% of circulating T cells; the other 5–10% use an alternate heterodimeric TCR composed of γ and δ chains. A portion of the γδ T cells is generated in the thymus via RAG1/RAG2-mediated rearrangement of V, D (for the δ chain only), and J elements, but a major fraction appears to be generated in an extrathymic compartment[14].

Major Histocompatibility Molecules

Conventional T cells recognize peptide fragments bound to an MHC molecule (humans MHC is designated human leukocyte antigen [HLA]) presented on the cell surface. MHC molecules bind protein

peptide fragments that either have been synthesized within the cell (class I MHC molecules) or that have been ingested by the cell and proteolytically processed (class II MHC molecules).

Class I MHC Molecules

All nucleated cells express MHC class I (MHC I) molecules and present protein fragments of cytosolic and nuclear origin onto their cell surface. Structurally, MHC I is a cell surface heterodimer comprised of a polymorphic transmembrane 44-kd α-chain (also designated the class I heavy chain) associated with the 12-kd non-polymorphic β_2-microglobulin (β_2m) protein[15]. Humans have three major HLA class I molecules, each encoded by a distinct gene and designated as HLA-A, -B, and -C. The three HLA-A, -B, and -C α-chain genes are located on chromosome 6, while the β_2-microglobulin gene is encoded on chromosome 15.

The composite structure formed from a MHC and antigenic peptide is necessary for TCR recognition; antigenic peptide alone generates no measurable TCR affinity, and MHC plus other peptides creates minimal affinity. This biological phenomenon of "MHC restriction," described by studies of Zinkernagel and Doherty[16], compels T cell to ignore free extracellular antigen, ignore unrecognized MHC-peptide complexes, and solely focus on the cells that present the particular MHC-antigenic peptide complex. Furthermore, because the α_3 domain of the class I heavy chain requires binding from the CD8 molecule for proper recognition, this restricts the recognition of antigenic peptides that are presented on MHC molecules to $CD8^+$ cytotoxic T cells (Figure 3)[9].

Generally, the antigenic peptides found bound to MHC I are generated within the cell presenting the MHC I complex, and consequently are described as "endogenous" antigens. However, recent studies

have shown that under certain circumstances, exogenous antigens (synthesized outside the antigen presenting cell) may be internalized by endocytosis and presented on MHC I. This form of "cross presentation"[17] is of particularly important in antiviral immunity[18].

A prominent characteristic of HLA molecules is their structural polymorphism; over 650 alleles at the HLA-A locus, over 1,000 alleles at the HLA-B locus, and over 350 alleles at the HLA-C locus have been recognize by the ImMunoGeneTics HLA Database (http://www.ebi.ac.uk/imgt/hal/atats.html). Three distinct HLA class I genes, each of which is highly polymorphic, means that all individuals who are heterozygous at these loci have 6 distinct peptide binding grooves. Having 6 peptide binding molecules greatly strengthens the immune system's ability to recognize antigenic peptides. Ironically however, this great diversity also presents great challenges for HLA matching in modern transplantation medicine.

Class II Major MHC Molecules

MHC Class II (MHC II) molecules also consist of two polypeptide chains. But in this case, both are MHC-encoded transmembrane proteins and are designated α and β[9]. Humans have three major class II proteins -- HLA-DR, HLA-DQ, and HLA-DP[15,] but this belies the true number of Class II molecules present; the HLA-DR locus encodes for a minimally polymorphic HLA-DR α chain and two polymorphic HLA-DR β chains, translating to 4 distinct HLA-DR proteins per heterozygous individual; both the α chains and the β chains of the HLA-DQ and HLA-DP proteins are polymorphic, such that 4 different HLA-DQ and 4 different HLA-DP proteins are possible based on pairing between the gene products of both the maternal and the paternal chromosome.

MHC II is constitutively expressed by professional antigen presenting cells, including B cells, dendritic cells, monocytes and macrophages[1]. Additionally, expression of MHC II can be induced on many additional cell types, including epithelial and endothelial cells, following IFN-γ stimulation[1]. Antigens presented on MHC II are derived via the "exogenous" pathway, which begins by endocytosis or phagocytosis of extracellular proteins. Exogenous antigens include antigenic proteins of extracellular pathogens such as most bacteria, parasites, and virus particles that have been released from infected cells as well as environmental proteins and glycoproteins such as pollens and venoms, and alloantigens[19]. The appropriate MHC II and antigenic peptide complex is necessary for TCR recognition. Additionally, because the β2 domain of MHC II requires CD4 binding, this limits MHC II activation to $CD4^+$ T cells, in a manner similar to MHC I and $CD8^+$ T cells (Figure 3)[9].

T Cell Activation and Functions

Normal activation of naïve T cells typically requires multiple signals (Figure 4)[9]. Engagement of specific peptide:MHC complex with the T-cell receptor (Signal 1) is essential for T cell activation, but Signal 1 alone actually induces T cell inactivation (anergy) and or apoptosis. Additional signaling that promote survival and expansion (Signal 2) is provide by the same APC, the best studied of which are the B7 molecules that bind to CD28 on T cells. Cytokines, released either by APCs or by activated T cells, constitute a Signal 3 that drive T-cell differentiation into different effector subtypes. Indeed, because unregulated T cell activation can lead to catastrophic consequences, there are several evolutionarily conserved negative regulators of T cell activation, "checkpoint" molecules that fine-tune the immune response and regulate hyperactivation. Cytotoxic T lymphocyte antigen 4 (CTLA4) and programmed cell death 1 (PD1) are among the most potent examples of T cell immune checkpoint molecules. CTLA4 is minimally expressed in quiescent T cells, upregulated following T cell activation,

and inhibits T cell activation and proliferation by interfering with CD28–B7 interaction[19, 20, 21, 22]. PD1 is also upregulated in T cells following TCR stimulation and binds the B7 homologues PDL1 (also known as B7-H1) and PDL2 (also known as B7-DC), which are present constitutively on APCs and inducible in non-hematopoietic tissues in response to pro-inflammatory cytokines[23, 24, 25]. PD1 restrains immune responses primarily through inhibitory intracellular signaling in effector T cells and regulatory T cells[26].

The vast majority of T cells in circulation in the blood and secondary lymphoid organs are either $CD4^+CD8^-$ ($CD4^+$, 60–70%) or $CD4^-CD8^+$ ($CD8^+$, 30–40%). $CD4^+$ T cells are also designated as "helper" T cells because of their major role in modulating the immune system, ranging from activating other immune cells (e.g. cells of the innate immune system, B cells, and $CD8^+$ cytotoxic T cells) and non-immune cells to suppressing the immune response altogether[27]. Upon activation in response to an antigen-MHC Class II complex, naïve $CD4^+$ T cells initially produce IL-2 and are designated Th0. Then depending on the nature of the cytokines present at the site of activation, Th0 polarize towards one of several extremes: Th1, Th2, and Th17 (although more Th subtypes have been identified in recent studies[27]). In general, Th1 cells support cell mediated immune responses, including in response to intracellular pathogens and is associated with organ-specific autoimmunity[28]. The characteristic cytokines of Th1 response are IL-2 and IFN-γ. Th2 cells support humoral (B cell activation and antibody maturation) and allergic responses[27]. The characteristic cytokines of Th2 response are IL-4, IL-5, IL-9, IL-13[27]. Although Th1 and Th2 cells often participate together in immune responses, prolonged activation frequently polarizes the immune response to become dominantly Th1-like or Th2-like. Th17 cells are induced early in the adaptive response to extracellular bacteria[27]. They have also been associated with the destructive inflammatory responses of many autoimmune diseases.

Regulatory $CD4^+$ helper T (Treg) cells are another important subtype with the unique function of suppressing the immune responses. Tregs fall into two categories: the first group develops its regulatory function in the thymus and is therefore termed natural Tregs (nTregs)[29]. The second group is thought to differentiate in the periphery from naïve $CD4^+$ T cells in response to specific antigen and is therefore called induced Tregs (iTregs)[30]. Treg cells are typically identified by their surface expression of CD4 and CD25 and by nuclear expression of the forkhead box P3 transcription factor (Foxp3)[31]. A major portion of Treg cells suppress the activation of other cell types in large part due to their secretion of TGFβ and IL-10[29].

$CD8^+$ T cells are also called cytotoxic or cytolytic lymphocytes because their primary means of action is the direct cytolysis of target cells mediated by perforin release and Fas. However, $CD8^+$ T cells can also secrete cytokines such as tumor necrosis factor (TNF) and interferon-γ (IFN-γ) that play important roles in antimicrobial defense. Furthermore, pathogen-specific $CD8^+$ T cells express chemokines that attract inflammatory cells to sites of infection. $CD8^+$ T cells respond to pathogen-derived peptides complexed with MHC I molecules presented on the cell surface and protect against microbes that introduce antigens into the cytosol of infected cells[32].

Role of T Cells in Cancer Immunosurveillance

In addition to protecting the body from pathogenic microbes, T cells also play a major role in the control of cancerous cells. Cancerous cells, in turn, have developed strategies of evading T cells and other immune cells.

Immune editing hypothesis

Cancerous cells arise when mutations in the DNA disrupt regulated growth and lead to uncontrolled cellular division. Studies with mice have shown that tumors derived through mutagenesis in immunocompetent mice tumors are much less immunogenic compared to those arising in immunodeficient mice[33, 34]. This indicates the immune system affect tumor growth by applying selective pressure on developing tumors. To evade immune detection and continue to grow, tumors undergo "immunoediting"[35, 36, 37], which occurs in three phases within the context of the immune system: elimination**,** equilibrium, and escape.

Elimination describes the initial encounter and killing of nascent transformed cells by the immune system. Because T cells are an important contributor to eliminating newly transformed cells, genes that compromise T cell development and or effector functions such as IFN-γ, perforin, and Fas/FasL are all associated with tumorigenesis[35, 37, 38, 39, 40, 41]. In addition to T cells, certain innate immune cells also mediate immunosurveillance, including NK cells, which have been shown to kill tumors through NKG2D recognition[42, 43]. It should be noted, however, that despite the strong evidence for the elimination phase, the process itself has not been directly observed since the nascent tumors that are subject to elimination are expected to exist only transiently and are thus difficulty to study. And although the immunosurveillance hypothesis is commonly described in three phases, malignancies may not follow the defined paths, nor their development always readily fall into one of these phases. Nevertheless, that a tumor must evolve to exist in the presence of an active immune system is a well-established concept and central to understanding tumor immunity.

During **"**Equilibrium," tumor cells that survived the elimination phase are kept in equilibrium by the immune system, such that the immune system fails to completely eliminate these cells but prevents

tumors from growing. This equilibrium phase is thought to represent the longest of the three phases of tumor development and can persist for years[44, 45].

"Escape" is when equilibrium is broken, and the tumor cells grow even in the presence of an immune system. The tumor co-opts the many mechanisms in place that regulate the immune response, originally intended to prevent autoimmunity and damage to self-tissues that may occur through overzealous responses to pathogens, and employs them to evade both adaptive and innate immune defenses [46, 47].

Mechanisms of T cell antitumor immunity

$CD8^+$ T cells are the primary effectors in antitumor immune responses because of their capability to recognize and kill cancer cells. Like nearly all nucleated cells in the body, most tumor cells express MHC I molecules on their surface. The altered proteins and peptide antigens presented as a result of becoming cancerous opens cancer cells to be attacked by $CD8^+$ T cells. As such, tumors commonly alter their expression of MHC I to evade immunity[48].

Whereas the role of $CD8^+$ T cells in antitumor immunity is relatively straight forward, $CD4^+$ T cells have many more diverse roles that may either be antitumor or pro-tumor. $CD4^+$ T cells recognize MHC II, the expression of which is largely restricted to professional APCS and not usually present on cancer cells themselves. Thus, $CD4^+$ T cells do not generally mediate their effects through direct recognition of cancer[49]. Nevertheless, similar to $CD8^+$ T cells, $CD4^+$ T cells infiltrate cancers and affect prognosis[50]. The different subtypes of $CD4^+$ effector T cells apparently affect the antitumor response in different ways. Th1 subtypes cells secrete large amounts of IFN-γ, inhibit angiongensis, and helps recruit APC and NK cells and prime $CD8^+$ T cells to promote antitumor immunity[51]. Th2 subtypes, through

secretion of IL-4 or IL-13, can induce an influx of eosinophils and macrophages into the tumor that promote antitumor cytotoxic activity [52, 53, 54]. However, production of IL-10, another Th2 cytokine, has also been reported to be immunosuppressive and promote tumor evasion[55, 56, 57]. T_H17 subtypes have also been described in multiple tumor models, but their roles in cancer are poorly understood. Under certain circumstances, T_H17 cells may contribute to a protumorigenic inflammation; in other scenarios, T_H17 T cells can effectively drive antitumor responses[58, 59]. Finally, Tregs are enriched in many tumors, and high Treg/$CD8^+$ T cell ratios portend a poor prognosis[60, 61]. This suggests Tregs may contribute to tumor growth through suppression of tumor infiltrating lymphocytes.

Mechanisms of tumor escape

Given the prominent role of T cells in antitumor immunity, tumors have evolved many mechanisms to diminish T cell antitumor activity. These include: 1) diminishing T-cell recruitment to tumors site through decreasing chemokine expression (e.g. CXCL9 and CXCL10) and altering the vascular endothelium; 2) downregulating MHC expression to reduce T cell recognition; 3) creating a highly immunosuppressive tumor microenvironment (TMI)[62, 63]. Immunosuppressive TMI, in particularly, can be driven by the tumor stroma itself, for instance through increased expression of inhibitory molecules like CTLA-4 and PD-L1 on tumors, or through recruiting immunosuppressive immune cells, such as tumor-associated macrophages (TAMs) and Tregs.

In Chapter 2 of this dissertation, I examine the roles of monoamine oxidase A (MAO-A) on T cell antitumor immunity, and the potential of targeting intratumoral monoamine oxidase A (MAO-A) activity for immunotherapy. MAO-A is an outer mitochondrial membrane-bound enzyme best known for its function in the brain, where it is involved in the degradation of a variety of monoamine

neurotransmitters. There is limited literature on the role it plays in the immune response. In Chapter 2, I provide novel evidence suggesting MAO-A is an important "checkpoint" molecule to T cell antitumor immunity by regulating the availability of serotonin, a neurotransmitter previously unassociated with the immune response. In Chapter 3, I provide further evidence that MAO-A can also indirectly modulate T cell antitumor immunity by promoting immunosuppressive TAM polarization in the TMI. TAMs residing in mature TMI are typically highly immunosuppressive and promote tumor growth, malignancy, and metastasis[64, 65]. However, plasticity remains one of the key features of TAMs, enabling TAMs to change their phenotype under appropriate stimulation. Targeting intratumoral MAO-A activity induces TAM reprogramming and suppresses tumor growth. Both chapters therefore provide compelling preclinical data suggesting potential benefits to repurposing MAO inhibitors for immunotherapy.

Allogeneic Hematopoietic Stem Cell Transplantation (Allo-HCT)

Modern transplantation medicine provides another avenue through which to treat hematological malignancies. The two major forms of hematopoietic transplantation are 1) autologous transplantation, in which recipients receive ablation of their immune system (such as via chemotherapy or irradiation) and are then reconstituted with their own bone marrow that had been preserved beforehand and 2) allogeneic transplantation (allo-HCT), in which recipients receive ablation of their immune system followed by reconstitution with another person's bone marrow. Allo-HCT is a potentially curative procedure for a variety of malignant and non-malignant conditions. Of the more than 47,000 bone marrow transplantations were performed worldwide in 2018, 19,000 (41%) of them were allogeneic and nearly all for the treatment of acute and chronic leukemias and myelodysplastic and myeloproliferative syndromes[66]. Allo-HCT is associated with lower rates of malignant relapse owing to an immune-

mediated graft versus leukemia/lymphoma (GvL) effect; however, graft versus host disease (GvHD) remains a serious concern.

Graft versus Leukemia/Lymphoma (GvL) and Graft versus Host Disease (GvHD)

Unaltered allograft given in allo-HCT contains a mixture of mature donor immune cells (e.g. T, B, natural killer, and myeloid cells) and $CD34^+$ hematopoietic stem cells. T cells are identified as the major mediators of both the beneficial GvL effect and the detrimental GvHD. Removal of T cells from the allograft can reduce the incidence and severity of GvHD but provides little clinical benefits due to the increased risk of graft rejection, infections, and relapse[67]. The mechanism through which donor T cells execute their alloreactivity is, in essence, no different from their normal function of attacking cells with intracellular pathogen. Thymic selection (as discussed previously) removes T cells that recognize "self" peptides presented on "self" HLA molecules. The residual T-cell repertoire, due to the diversity of TCRs, can theoretically recognize any combination besides self-peptide presented on self-HLA molecule. In the context of allo-HCT, the main mechanism of alloreactivity is the presentation of nonself peptides on self HLA molecules (Figure 5)[68]. This is because most allo-HCT performed involve donors and recipients who are fully HLA matched (or very closely matched), such that the HLA alleles of the donor and recipient are identical. However, other genes besides HLA are not matched, and many are polymorphic or contain single nucleotide polymorphisms. Thus the "same" proteins between individuals often contain small amino acid differences. These polymorphic peptides, when presented on HLA molecules, are capable of inducing an immune response between HLA identical individuals and are called minor histocompatibility antigens (MiHAs). MiHA presented on hematopoietic cells of recipient origin can induce donor T cell elimination of residual malignant hematopoietic cells, providing the beneficial GvL response. However, if donor T-cell targets MiHA that are expressed on non-

hematopoietic tissues, detrimental GvHD occurs. GvHD remains the leading cause of patient mortality following allo-HCT and remains a major obstacle to the greater application of allo-HCT as treatment.

In the context of HLA identical allo-HCT, alloreactive donor T cells are largely naïve cells[69]. Thus they normally require the presence of activated DC in an inflammatory environment for maximal activation in response to MiHA presented on recipient cells[70]. GvHD target tissues such as the gut, skin, liver, and lung often contain large numbers of activated recipient APC that may present a variety of MiHA expressed in these tissues and contribute to GvHD. Likewise donor allograft contains large numbers of APCs. It has been suggested that donor and host APCs contribute greatly to GvHD development but less so towards GvL effect[71, 72, 73], making them potential targets for reducing GvHD while sustaining GvL effect.

Invariant Natural Killer T Cells for GvHD prevention

Extensive research focused on identifying other cellular components of the graft that could modulate donor T cells and reduce the risk and severity of GvHD without diminishing GVL have identified invariant natural killer T cells (iNKT cells) as potentially fulfilling this unique niche.

Biology of iNKT cells

NKT cells are a unique subset of αβ T lymphocytes characterized by their expression of both a αβ T-cell receptor (TCR) and NK surface markers. This small population of T cells (~0.1-1% in mouse blood and ~0.01-1% in human blood) arise from the same lymphoid precursor pool as conventional T cells and mature in the thymus [74, 75]. However, unlike conventional T cells that recognize peptide antigens, NKT cells respond to lipid antigens presented by the non-polymorphic major histocompatibility complex

(MHC) class I-like molecule CD1d. During an immune response, NKT cells are some of the first cells to be activated and can rapidly produce copious amounts of cytokines and chemokines, thereby functioning as a "bridge" linking the innate and adaptive immune responses [76].

Two major categories of NKT cells have been identified based on their TCR expression. Type I, or invariant NKT (iNKT) cells, express a restricted TCR recombinant comprising a semi-invariant TCR α chain (Vα14-Jα18 in the mouse, Vα24-Jα18 in humans) paired to a limited repertoire of Vβ chains (Vβ 2, 7 or 8.2 in mice and Vβ 11 in humans) and are the most prevalent type of NKT cells [75, 76]. iNKT cells can be further divided based on their CD4 and CD8 expressions. Human have $CD4^+CD8^-$ ($CD4^+$), $CD4^-$ $CD8^+$ ($CD8^+$) and $CD4^-CD8^-$ (DN) iNKT populations, whereas mice only have $CD4^+$ and DN populations [75]. For both mice and humans, iNKT cells are also functionally defined by their ability to recognize the prototypic antigen α-galactosylceramide (α-GalCer) presented on CD1d [77, 78]. α-GalCer is a strong activator of iNKT cells and has been widely used to study iNKT cell biology. Type II NKT cells, in contrast, express more diverse TCRs and are therefore also called variant NKT cells [79, 80, 81]. Notably, Type II NKT cells do not respond to α-GalCer.

Activation of iNKT cells

There are three main mechanisms to activating iNKT cells: 1) via TCR/CD1d/lipid stimulation 2) via cytokine stimulation and 3) via activating NK receptor stimulation[82, 83, 84, 85]. iNKT cells can be directly activated in a TCR-dependent manner and without the need for costimulation or cytokine receptor engagement through exposure to potent glycolipid antigens (e.g., α-GalCer) presented by CD1d[76]. However, in a more physiological context, iNKT cells are stimulated by microbial or self-lipid antigens that are weakly immunogenic and thus requires a second activation signal from pro-inflammatory

cytokines [86]. Sometimes, cytokines alone (e.g., IL-12, IL-18, IL-23, and IL-25) are sufficient to activate iNKT cells even in the absence of TCR engagement. Several studies have found that iNKT cells release IFN-γ when stimulated by IL-12 during viral infections[87, 88]. The heighted capacity of iNKT cells to respond to cytokines is due to their elevated expression of functional receptors at baseline. Because iNKT cells also express activating and inhibitory NK receptors (NKR) and killer cell immunoglobulin-like receptors (KIR), they can become activated when the summation of stimulatory signals overcomes the inhibitory signals. Activating NKRs recognize a variety of MHC-like molecules and cellular targets frequently referred to as "stress proteins." For example, DNAM-1 recognizes the poliovirus receptor and Nectin-2; the NKG2D receptor recognizes MHC class I-like molecules (MIC) A and B and unique long-binding proteins (ULBPs). Inhibitory NKRs and KIRs, in contrast, often bind to HLA molecules[85].

Effector functions of iNKT cells

In contrast to conventional T cells that emerge from the thymus "naïve," recently emigrated iNKT cells are able to perform their effector functions immediately without priming[75, 89, 90]. Activated NKT cells are known to secrete copious amounts of cytokines, including T helper (Th)1-like (IFN-γ), Th2-like (IL-4, IL-13), Th17-like (IL-17, IL-22), and regulatory (IL-10) cytokines[75, 91]. The mechanisms of cell activation, the location, and the iNKT cell subsets all affect what cytokines are produced. For example, the activation of iNKT cells with the potent agonist α-GalCer leads to the production of both Th1- and Th2-like cytokines, whereas activation involving both recognition of the endogenous ligand/CD1d complexes and cytokine costimulation leads to the polarized production of Th1-like IFN-γ, but not Th2-like cytokines[86, 92]. Additionally, both human $CD8^+$ and DN iNKT cells have been found to predominately express Th1 cytokines whereas human $CD4^+$ iNKT cells predominately express Th2 cytokines, although this distinction is less apparent with mouse iNKT cells[93, 94]. Interestingly, subsets

expressing different cytokines, transcription factors, and surface markers appear to be acquired during thymic development rather than as a result of peripheral experience[75, 95].

In addition to cytokines, iNKT cells also produce cytolytic proteins such as perforin and granzyme B, and surface molecules involved in cytotoxicity such as Fas Ligand (FasL) and tumor necrosis factor α (TNFα)-related apoptosis-inducing ligand (TRAIL)[96, 97]. Owing to their ability to produce an array of effector molecules, iNKT cells can profoundly influence many other cell types, including dendritic cells (DCs), macrophages, neutrophils, NK cells, and T and B cells and orchestrate immune responses during infection, autoimmune disease, allergy and cancer[75]. Because they affect many different immunological processes, iNKT cells have great clinical potentials, most notably their ability to reduce GvHD without loss of GvL in allo-HCT and their capability to enhance antitumor immunity[75, 76, 98, 99].

Role of iNKT cells in suppressing GvHD in allo-HCT

Preclinical studies have demonstrated iNKT cells can simultaneously prevent GvHD while retaining GvL effect following allo-HCT. Selective depletion of host conventional T cells through fractionated total lymphoid irradiation (TLI) and anti-thymocyte globulin (ATG), and thereby selectively enriching host iNKT cells, prior to allo-HCT, attenuated GvHD through host iNKT cell elevation of IL-4 secretion and polarization of donor T cells toward a Th2 cytokine pattern. This, in turn, inhibited donor T cell early expansion and infiltration of GvHD target organs[100]. Administration of synthetic iNKT TCR ligand α-GalCer on the day of transplantation was also found to significantly reduced mortality and morbidity from GvHD[101, 102, 103, 104]. Likewise, the addition of donor or third-party $CD4^+$ iNKT cells to the allograft was found to prevent GvHD by inhibiting T- cell proliferation, promoting Th2-biased cytokine response, and expanding donor MDSCs [105, 106]. Notably, enrichment of the iNKT cells, whether host,

donor or third party, did not abrogate donor T cell GvL [100, 105, 106]. In all these studies, it was found that iNKT cells promoted donor T cell polarization toward a Th2 cytokine pattern, expanded donor Treg populations, and significantly reduced production of IFN-γ and tumor necrosis factor (TNF)-alpha [100, 104, 106, 107]. Myeloid-derived suppressor cells (MDSCs) or $CD8^+$ dendritic cells (DC) were also found to play important roles in the interplay between iNKT cells and Tregs [106, 108].

The protective role of human iNKT cells against GvHD has also been highlighted by several clinical studies. Non-myeloablative conditioning with TLI/ATG prior to allo-HCT was associated with a higher iNKT/T cell ratio, increased IL-4 production, decreased incidence of GvHD, and retained GvL effect[109, 110]. Patients with acute GvHD were found to have reduced numbers of total iNKT cells[111], whereas enhanced iNKT cell reconstitution following allo-HCT positively correlated with reduction in GvHD without loss of GvL effect[112]. Separately, low $CD4^-$ iNKT cell numbers in donor graft was associated with clinically significant GvHD in patients receiving HLA-identical allo-HCT[113]. Thus, increasing the iNKT cell numbers of allograft that contain few iNKT cells may provide an attractive strategy for suppressing GvHD while preventing leukemia relapse.

However, as previously mentioned, iNKT are but a tiny fraction of total lymphocytes (~0.1-1% in mouse blood and ~0.01-1% in human blood), making their accessibility a significant to their research and application. In Chapter 4 of this dissertation, I provide detailed protocols for generating large quantities of both human and mouse iNKT cells through TCR-engineering of hematopoietic stem cells and *in vivo* reconstitution. The resultant engineered iNKT cells are capable of mediating antitumor activity and can potentially address the lack of iNKT cells for research. However, the protocols' reliance on *in vivo* intermediary severely limit their clinical translation. Thus, in Chapter 5, I describe

the most recent effort in my lab to generate large quantities of engineered human iNKT cells *in vitro*. Furthermore, addition of these third-party, engineered human iNKT cells to the allograft of a PBMC humanized mouse model was able to significant ameliorate the development and severity of xeno-GvHD. Importantly, my results indicate that the GvL effect was retained in two leukemia models. Mechanistically, third party engineered HSC-iNKT cells were capable of quickly eliminating GvHD-inducing donor $CD14^+$ myeloid population, in part through CD1d recognition. These findings providing important preclinical data suggesting the potential for third-party engineered HSC-iNKT cells to be used as additives to allografts for the prevention of GvHD while preserving GvL effect.

Figures

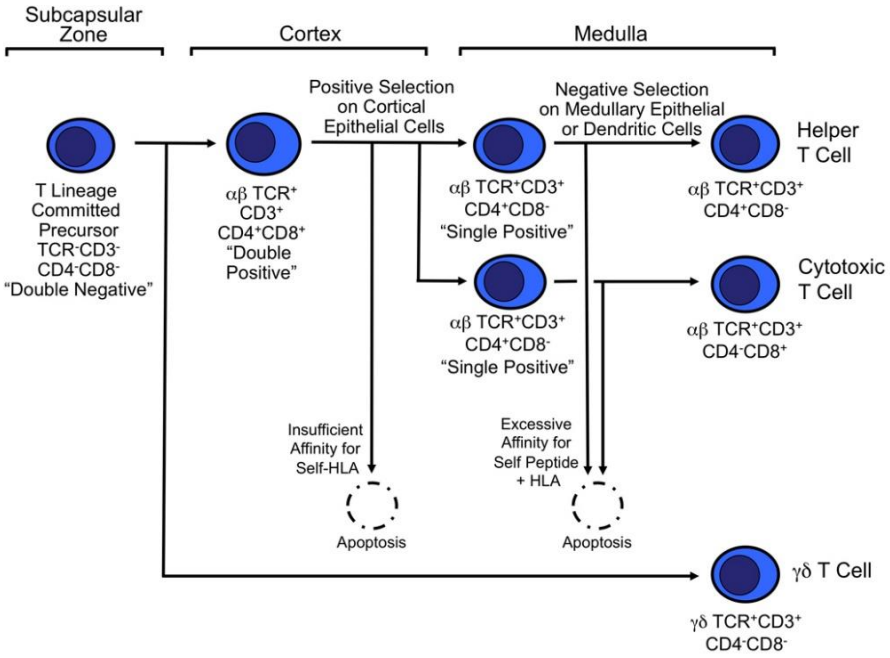

Figure 1: Differentiation and Maturation of T Cells in the Thymus[8]

Hematopoietic stem cells which do not express CD3, CD4 or CD8 but which are committed to T cell differentiation move from the bone marrow to the thymic subcapsular zone. There they begin rearrangement of the TCR genes. Once a productive TCR β chain has been produced, they move the thymic cortex where TCR α chain rearrangement occurs and surface expression of the CD3, CD4 and CD8 proteins is induced. These CD4+CD8+ (double positive) cells are positively selected on cortical epithelial cells for their ability to recognize self Class I or Class II MHC proteins. If the developing T cell has adequate affinity to recognize a self Class I protein, then it retains expression of CD8 and extinguishes expression of CD4. If the cell recognizes a self Class II protein, then it retains expression of CD4 and extinguishes expression of CD8. Selected CD4/CD8 single positive (SP) cells then move to the thymic medulla where they are negatively selected on medullary epithelial cells to remove cells with excessive affinity for self-antigens presented in HLA molecules. Cells emerge from positive selection SP for CD4 or CD8 expression and then are exported to the periphery. Cells that fail positive or negative selection are removed by apoptosis. A small fraction of cells differentiate from to rearrange their TCR γ and δ chains, rather than their TCR α and β chains.

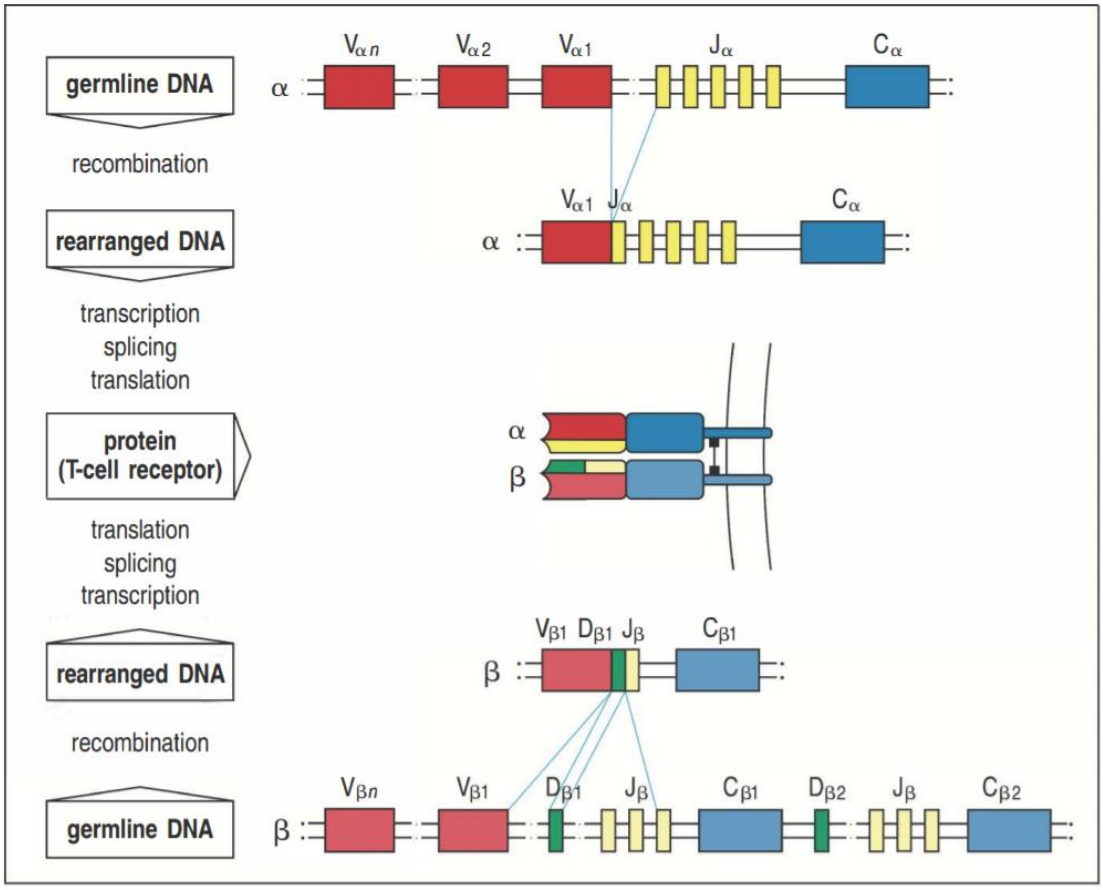

Figure 2: T-cell receptor α- and β-chain gene rearrangement and expression[9]

The TCRα- and β-chain genes are composed of discrete segments that are joined by somatic recombination during development of the T cell. Functional α- and β-chain genes are generated in the same way that complete immunoglobulin genes are created. For the α chain (upper part of figure), a V_α gene segment rearranges to a J_α gene segment to create a functional V-region exon. Transcription and splicing of the VJ_α exon to C_α generates the mRNA that is translated to yield the T-cell receptor α-chain protein. For the β chain (lower part of figure), like the immunoglobulin heavy chain, the variable domain is encoded in three gene segments, V_β, D_β, and J_β. Rearrangement of these gene segments generates a functional VDJ_β V-region exon that is transcribed and spliced to join to C_β; the resulting mRNA is translated to yield the T-cell receptor β chain. The α and β chains pair soon after their biosynthesis to yield the α:β T-cell receptor heterodimer. Not all J gene segments are shown, and the leader sequences preceding each V gene segment are omitted for simplicity.

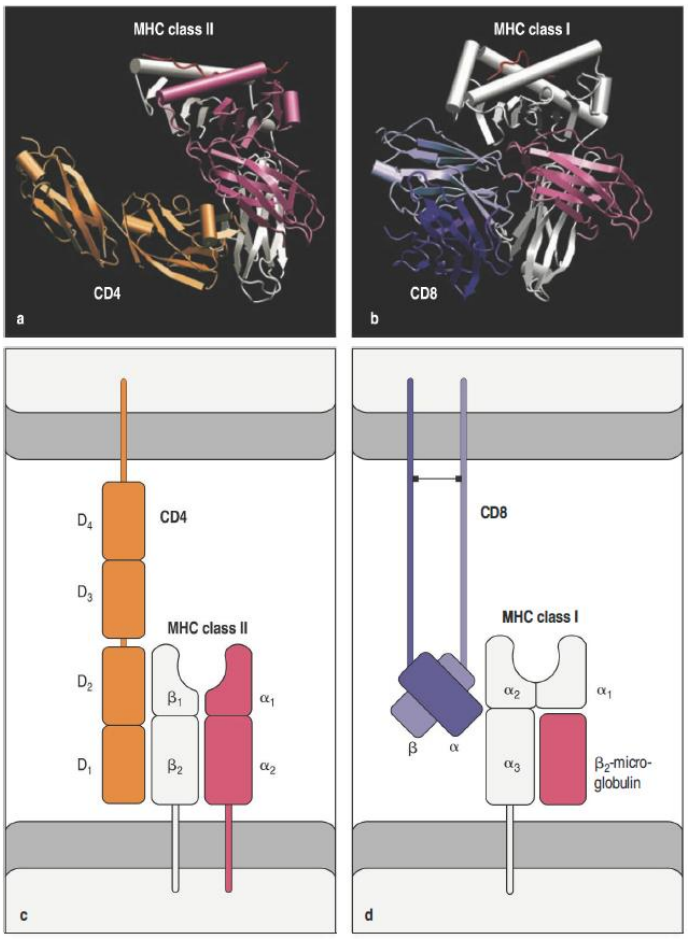

Figure 3: The binding sites for CD4 and CD8 on MHC class II and class I molecules lie in the Ig-like domains[9]

The binding sites for CD4 and CD8 on the MHC class II and class I molecules, respectively, lie in the Ig-like domains nearest to the membrane and distant from the peptide-binding cleft. The binding of CD4 to an MHC class II molecule is shown as a structure graphic in panel a and schematically in panel c. The α chain of the MHC class II molecule is shown in pink, and the β chain in white, while CD4 is in gold. Only the D_1 and D_2 domains of the CD4 molecule are shown in panel a. The binding site for CD4 lies at the base of the β_2 domain of an MHC class II molecule, in the hydrophobic crevice between the β_2 and α_2 domains. The binding of CD8 to an MHC class I molecule is shown in panel b and schematically in panel d. The class I heavy chain and β_2-microglobulin are shown in white and pink, respectively, and the two chains of the CD8 dimer are shown in light and dark purple. The structure is actually of the binding of the CD8α homodimer, but the CD8α:β heterodimer is believed to bind in a similar way. The binding site for CD8 on the MHC class I molecule lies in a similar position to that of CD4 in the MHC class II molecule, but CD8 binding also involves the base of the α1 and α2 domains, and thus the binding of CD8 to MHC class I is not completely equivalent to the binding of CD4 to MHC class II.

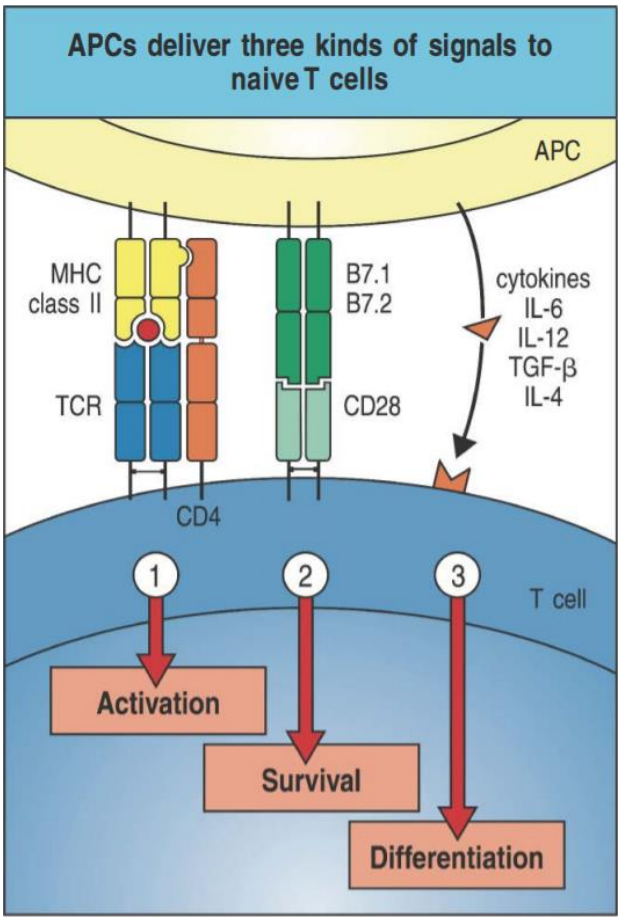

Figure 4: Three kinds of signals are involved in activation of naive T cells by antigen-presenting cells [9]

Binding of the foreign-peptide:self-MHC complex by the T-cell receptor and, in this example, a CD4 co-receptor, transmits a signal (arrow 1) to the T cell that antigen has been encountered. Effective activation of naive T cells requires a second signal (arrow 2), the co-stimulatory signal, to be delivered by the same antigen presenting cell (APC). In this example, CD28 on the T cell encountering B7 molecules on the antigen-presenting cell delivers signal 2, whose net effect is the increased survival and proliferation of the T cell that has received signal 1. ICOS and various members of the TNF receptor family may also provide co-stimulatory signals. For CD4 T cells in particular, different pathways of differentiation produce subsets of effector T cells that carry out different effector responses, depending on the nature of a third signal (arrow 3) delivered by the antigen-presenting cell. Cytokines are commonly, but not exclusively, involved in directing this differentiation.

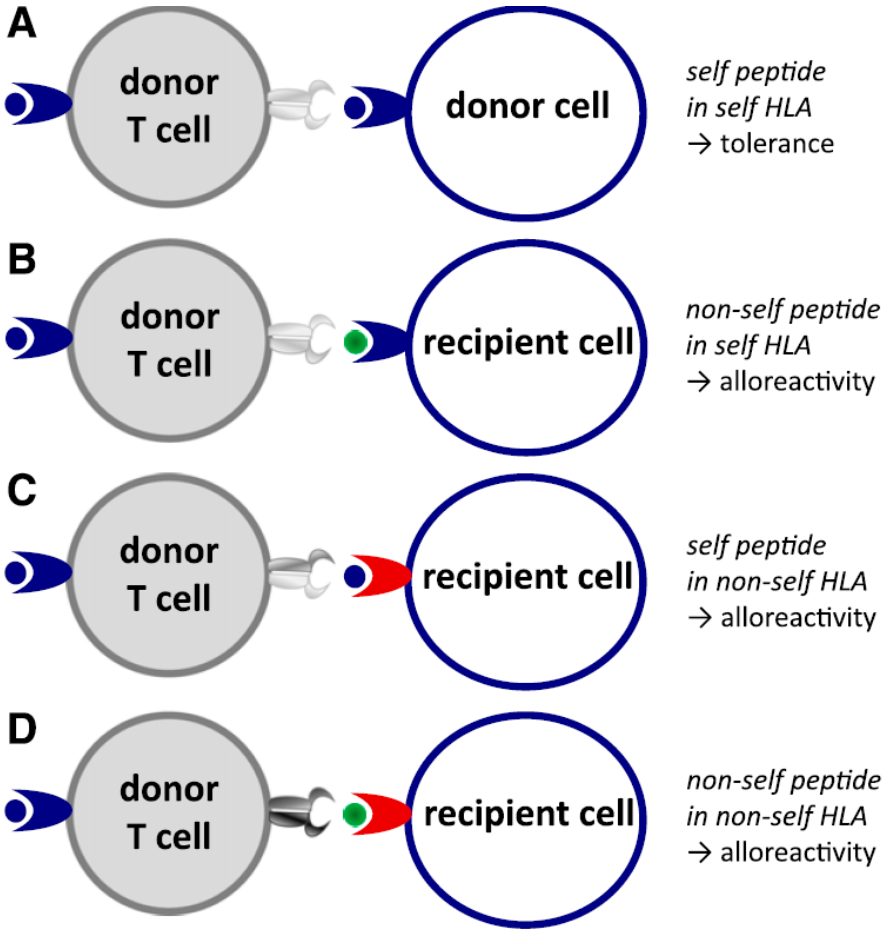

Figure 5: Peptide/HLA complexes as targets of T cell–mediated alloimmune reactivity[68]

(A) Self peptides expressed in self HLA molecules induce tolerance. (B) Polymorphic nonself peptides recognized in the context of self HLA molecules can induce alloreactivity; these polymorphic nonself peptides are called minor histocompatibility antigens (MiHA). (C) Monomorphic (self) peptides presented in the context of nonself HLA molecules provoke alloreactivity. (D) Polymorphic nonself peptides in the context of nonself HLA molecules can also provoke alloreactivity.

References

1. Chaplin DD. Overview of the immune response. *The Journal of allergy and clinical immunology* **125**, S3-23 (2010).

2. Attaf M, Legut M, Cole DK, Sewell AK. The T cell antigen receptor: the Swiss army knife of the immune system. *Clinical and experimental immunology* **181**, 1-18 (2015).

3. Zinkernagel RM, Doherty PC. Restriction of in vitro T cell-mediated cytotoxicity in lymphocytic choriomeningitis within a syngeneic or semiallogeneic system. *Nature* **248**, 701-702 (1974).

4. Treiner E, *et al.* Selection of evolutionarily conserved mucosal-associated invariant T cells by MR1. *Nature* **422**, 164-169 (2003).

5. Le Bourhis L, *et al.* Antimicrobial activity of mucosal-associated invariant T cells. *Nature immunology* **11**, 701-708 (2010).

6. Beckman EM, Porcelli SA, Morita CT, Behar SM, Furlong ST, Brenner MB. Recognition of a lipid antigen by CD1-restricted alpha beta+ T cells. *Nature* **372**, 691-694 (1994).

7. Van Rhijn I, *et al.* A conserved human T cell population targets mycobacterial antigens presented by CD1b. *Nature immunology* **14**, 706-713 (2013).

8. Huston DP. The biology of the immune system. *Jama* **278**, 1804-1814 (1997).

9. Murphy KM, Janeway CA, Travers P, Mowat A, Weaver CT. *Janeway's immunobiology*. Garland Science (2012).

10. Gellert M. V(D)J recombination: RAG proteins, repair factors, and regulation. *Annual review of biochemistry* **71**, 101-132 (2002).

11. Nguyen HH, *et al.* Heterosubtypic immunity to influenza A virus infection requires a properly diversified antibody repertoire. *Journal of virology* **81**, 9331-9338 (2007).

12. Nitta T, Murata S, Ueno T, Tanaka K, Takahama Y. Thymic microenvironments for T-cell repertoire formation. *Advances in immunology* **99**, 59-94 (2008).

13. von Boehmer H, Kisielow P, Kishi H, Scott B, Borgulya P, Teh HS. The expression of CD4 and CD8 accessory molecules on mature T cells is not random but correlates with the specificity of the alpha beta receptor for antigen. *Immunological reviews* **109**, 143-151 (1989).

14. Ishikawa H, *et al.* Curriculum vitae of intestinal intraepithelial T cells: their developmental and behavioral characteristics. *Immunological reviews* **215**, 154-165 (2007).

15. Bjorkman PJ. MHC restriction in three dimensions: a view of T cell receptor/ligand interactions. *Cell* **89**, 167-170 (1997).

16. Zinkernagel RM, Doherty PC. The discovery of MHC restriction. *Immunology today* **18**, 14-17 (1997).

17. Melief CJ. Mini-review: Regulation of cytotoxic T lymphocyte responses by dendritic cells: peaceful coexistence of cross-priming and direct priming? *European journal of immunology* **33**, 2645-2654 (2003).

18. Sigal LJ, Crotty S, Andino R, Rock KL. Cytotoxic T-cell immunity to virus-infected non-haematopoietic cells requires presentation of exogenous antigen. *Nature* **398**, 77-80 (1999).

19. Linsley PS, Brady W, Urnes M, Grosmaire LS, Damle NK, Ledbetter JA. CTLA-4 is a second receptor for the B cell activation antigen B7. *The Journal of experimental medicine* **174**, 561-569 (1991).

20. Walunas TL, *et al.* CTLA-4 can function as a negative regulator of T cell activation. *Immunity* **1**, 405-413 (1994).

21. Krummel MF, Allison JP. CD28 and CTLA-4 have opposing effects on the response of T cells to stimulation. *The Journal of experimental medicine* **182**, 459-465 (1995).

22. Krummel MF, Allison JP. CTLA-4 engagement inhibits IL-2 accumulation and cell cycle progression upon activation of resting T cells. *The Journal of experimental medicine* **183**, 2533-2540 (1996).

23. Latchman Y, *et al.* PD-L2 is a second ligand for PD-1 and inhibits T cell activation. *Nature immunology* **2**, 261-268 (2001).

24. Francisco LM, Sage PT, Sharpe AH. The PD-1 pathway in tolerance and autoimmunity. *Immunological reviews* **236**, 219-242 (2010).

25. Freeman GJ, *et al.* Engagement of the PD-1 immunoinhibitory receptor by a novel B7 family member leads to negative regulation of lymphocyte activation. *The Journal of experimental medicine* **192**, 1027-1034 (2000).

26. Keir ME, Butte MJ, Freeman GJ, Sharpe AH. PD-1 and its ligands in tolerance and immunity. *Annual review of immunology* **26**, 677-704 (2008).

27. Luckheeram RV, Zhou R, Verma AD, Xia B. CD4(+)T cells: differentiation and functions. *Clinical & developmental immunology* **2012**, 925135 (2012).

28. Del Prete G. Human Th1 and Th2 lymphocytes: their role in the pathophysiology of atopy. *Allergy* **47**, 450-455 (1992).

29. Sakaguchi S, *et al.* Foxp3+ CD25+ CD4+ natural regulatory T cells in dominant self-tolerance and autoimmune disease. *Immunological reviews* **212**, 8-27 (2006).

30. Curotto de Lafaille MA, Lafaille JJ. Natural and adaptive foxp3+ regulatory T cells: more of the same or a division of labor? *Immunity* **30**, 626-635 (2009).

31. Huehn J, Polansky JK, Hamann A. Epigenetic control of FOXP3 expression: the key to a stable regulatory T-cell lineage? *Nature reviews Immunology* **9**, 83-89 (2009).

32. Wong P, Pamer EG. CD8 T Cell Responses to Infectious Pathogens. *Annual review of immunology* **21**, 29-70 (2003).

33. Shankaran V, *et al.* IFNgamma and lymphocytes prevent primary tumour development and shape tumour immunogenicity. *Nature* **410**, 1107-1111 (2001).

34. Svane IM, Engel AM, Thomsen AR, Werdelin O. The susceptibility to cytotoxic T lymphocyte mediated lysis of chemically induced sarcomas from immunodeficient and normal mice. *Scandinavian journal of immunology* **45**, 28-35 (1997).

35. Dunn GP, Old LJ, Schreiber RD. The Three Es of Cancer Immunoediting. *Annual review of immunology* **22**, 329-360 (2004).

36. Schreiber RD, Old LJ, Smyth MJ. Cancer Immunoediting: Integrating Immunity's Roles in Cancer Suppression and Promotion. *Science* **331**, 1565-1570 (2011).

37. Mittal D, Gubin MM, Schreiber RD, Smyth MJ. New insights into cancer immunoediting and its three component phases--elimination, equilibrium and escape. *Current opinion in immunology* **27**, 16-25 (2014).

38. Street SE, Cretney E, Smyth MJ. Perforin and interferon-gamma activities independently control tumor initiation, growth, and metastasis. *Blood* **97**, 192-197 (2001).

39. Dighe AS, Richards E, Old LJ, Schreiber RD. Enhanced in vivo growth and resistance to rejection of tumor cells expressing dominant negative IFN gamma receptors. *Immunity* **1**, 447-456 (1994).

40. Kaplan DH, *et al.* Demonstration of an interferon gamma-dependent tumor surveillance system in immunocompetent mice. *Proceedings of the National Academy of Sciences of the United States of America* **95**, 7556-7561 (1998).

41. van den Broek ME, *et al.* Decreased tumor surveillance in perforin-deficient mice. *The Journal of experimental medicine* **184**, 1781-1790 (1996).

42. Woo S-R, Corrales L, Gajewski TF. Innate Immune Recognition of Cancer. *Annual review of immunology* **33**, 445-474 (2015).

43. Marcus A, *et al.* Recognition of tumors by the innate immune system and natural killer cells. *Advances in immunology* **122**, 91-128 (2014).

44. Loeb LA, Loeb KR, Anderson JP. Multiple mutations and cancer. *Proceedings of the National Academy of Sciences* **100**, 776-781 (2003).

45. Faries MB, Steen S, Ye X, Sim M, Morton DL. Late recurrence in melanoma: clinical implications of lost dormancy. *Journal of the American College of Surgeons* **217**, 27-34; discussion 34-26 (2013).

46. Beatty GL, Gladney WL. Immune Escape Mechanisms as a Guide for Cancer Immunotherapy. *Clinical Cancer Research* **21**, 687-692 (2015).

47. Vinay DS, *et al.* Immune evasion in cancer: Mechanistic basis and therapeutic strategies. *Seminars in Cancer Biology* **35**, S185-S198 (2015).

48. Garrido F, Aptsiauri N, Doorduijn EM, Garcia Lora AM, van Hall T. The urgent need to recover MHC class I in cancers for effective immunotherapy. *Current opinion in immunology* **39**, 44-51 (2016).

49. Haabeth OA, *et al.* How Do CD4(+) T Cells Detect and Eliminate Tumor Cells That Either Lack or Express MHC Class II Molecules? *Frontiers in immunology* **5**, 174 (2014).

50. Kim H-J, Cantor H. CD4 T-cell Subsets and Tumor Immunity: The Helpful and the Not-so-Helpful. *Cancer Immunology Research* **2**, 91-98 (2014).

51. Nishimura T, *et al.* Distinct role of antigen-specific T helper type 1 (Th1) and Th2 cells in tumor eradication in vivo. *The Journal of experimental medicine* **190**, 617-627 (1999).

52. Modesti A, *et al.* Ultrastructural evidence of the mechanisms responsible for interleukin-4-activated rejection of a spontaneous murine adenocarcinoma. *International journal of cancer* **53**, 988-993 (1993).

53. Tepper RI, Coffman RL, Leder P. An eosinophil-dependent mechanism for the antitumor effect of interleukin-4. *Science* **257**, 548-551 (1992).

54. Pericle F, *et al.* An efficient Th2-type memory follows CD8+ lymphocyte-driven and eosinophil-mediated rejection of a spontaneous mouse mammary adenocarcinoma engineered to release IL-4. *Journal of immunology* **153**, 5659-5673 (1994).

55. Matsuda M, *et al.* Interleukin 10 pretreatment protects target cells from tumor- and allo-specific cytotoxic T cells and downregulates HLA class I expression. *The Journal of experimental medicine* **180**, 2371-2376 (1994).

56. Hagenbaugh A, *et al.* Altered immune responses in interleukin 10 transgenic mice. *The Journal of experimental medicine* **185**, 2101-2110 (1997).

57. Sharma S, *et al.* T cell-derived IL-10 promotes lung cancer growth by suppressing both T cell and APC function. *Journal of immunology* **163**, 5020-5028 (1999).

58. Martin-Orozco N, *et al.* T Helper 17 Cells Promote Cytotoxic T Cell Activation in Tumor Immunity. *Immunity* **31**, 787-798 (2009).

59. Muranski P, *et al.* Tumor-specific Th17-polarized cells eradicate large established melanoma. *Blood* **112**, 362-373 (2008).

60. Quezada SA, Peggs KS, Curran MA, Allison JP. CTLA4 blockade and GM-CSF combination immunotherapy alters the intratumor balance of effector and regulatory T cells. *The Journal of clinical investigation* **116**, 1935-1945 (2006).

61. Selby MJ, *et al.* Anti-CTLA-4 antibodies of IgG2a isotype enhance antitumor activity through reduction of intratumoral regulatory T cells. *Cancer Immunol Res* **1**, 32-42 (2013).

62. Slaney CY, Kershaw MH, Darcy PK. Trafficking of T Cells into Tumors. *Cancer Research* **74**, 7168-7174 (2014).

63. Gajewski TF, Schreiber H, Fu Y-X. Innate and adaptive immune cells in the tumor microenvironment. *Nature immunology* **14**, 1014-1022 (2013).

64. Biswas SK. Metabolic Reprogramming of Immune Cells in Cancer Progression. *Immunity* **43**, 435-449 (2015).

65. DeNardo DG, *et al.* CD4(+) T cells regulate pulmonary metastasis of mammary carcinomas by enhancing protumor properties of macrophages. *Cancer cell* **16**, 91-102 (2009).

66. Passweg JR, *et al.* The EBMT activity survey on hematopoietic-cell transplantation and cellular therapy 2018: CAR-T's come into focus. *Bone Marrow Transplantation* **55**, 1604-1613 (2020).

67. Apperley JF, *et al.* Bone marrow transplantation for patients with chronic myeloid leukaemia: T-cell depletion with Campath-1 reduces the incidence of graft-versus-host disease but may increase the risk of leukaemic relapse. *Bone Marrow Transplant* **1**, 53-66 (1986).

68. Falkenburg JHF, Jedema I. Graft versus tumor effects and why people relapse. *Hematology* **2017**, 693-698 (2017).

69. Bleakley M, *et al.* Leukemia-associated minor histocompatibility antigen discovery using T-cell clones isolated by in vitro stimulation of naive CD8+ T cells. *Blood* **115**, 4923-4933 (2010).

70. Ferrara JL, Levine JE, Reddy P, Holler E. Graft-versus-host disease. *Lancet* **373**, 1550-1561 (2009).

71. Chakraverty R, Sykes M. The role of antigen-presenting cells in triggering graft-versus-host disease and graft-versus-leukemia. *Blood* **110**, 9-17 (2007).

72. Jardine L, *et al.* Donor monocyte-derived macrophages promote human acute graft-versus-host disease. *The Journal of clinical investigation* **130**, 4574-4586 (2020).

73. Anderson BE, McNiff JM, Jain D, Blazar BR, Shlomchik WD, Shlomchik MJ. Distinct roles for donor- and host-derived antigen-presenting cells and costimulatory molecules in murine chronic graft-versus-host disease: requirements depend on target organ. *Blood* **105**, 2227-2234 (2005).

74. Godfrey DI, Stankovic S, Baxter AG. Raising the NKT cell family. *Nature immunology* **11**, 197-206 (2010).

75. Brennan PJ, Brigl M, Brenner MB. Invariant natural killer T cells: an innate activation scheme linked to diverse effector functions. *Nature Reviews Immunology* **13**, 101-117 (2013).

76. Bendelac A, Savage PB, Teyton L. The biology of NKT cells. *Annu Rev Immunol* **25**, 297-336 (2007).

77. Kawano T, *et al.* CD1d-restricted and TCR-mediated activation of Vα14 NKT cells by glycosylceramides. *Science* **278**, 1626-1629 (1997).

78. Brossay L, *et al.* CD1d-mediated recognition of an α-galactosylceramide by natural killer T cells is highly conserved through mammalian evolution. *The Journal of experimental medicine* **188**, 1521-1528 (1998).

79. Dasgupta S, Kumar V. Type II NKT cells: a distinct CD1d-restricted immune regulatory NKT cell subset. *Immunogenetics* **68**, 665-676 (2016).

80. Marrero I, Ware R, Kumar V. Type II NKT cells in inflammation, autoimmunity, microbial immunity, and cancer. *Frontiers in immunology* **6**, 316 (2015).

81. Dhodapkar MV, Kumar V. Type II NKT cells and their emerging role in health and disease. *The Journal of Immunology* **198**, 1015-1021 (2017).

82. Kumar A, Suryadevara N, Hill TM, Bezbradica JS, Van Kaer L, Joyce S. Natural killer T cells: an ecological evolutionary developmental biology perspective. *Frontiers in immunology* **8**, 1858 (2017).

83. Bedard M, Salio M, Cerundolo V. Harnessing the power of invariant natural killer T cells in cancer immunotherapy. *Frontiers in immunology* **8**, 1829 (2017).

84. Reilly EC, Wands JR, Brossay L. Cytokine dependent and independent iNKT cell activation. *Cytokine* **51**, 227-231 (2010).

85. Krijgsman D, Hokland M, Kuppen PJ. The role of natural killer T cells in cancer—a phenotypical and functional approach. *Frontiers in immunology* **9**, 367 (2018).

86. Brigl M, Bry L, Kent SC, Gumperz JE, Brenner MB. Mechanism of CD1d-restricted natural killer T cell activation during microbial infection. *Nature immunology* **4**, 1230-1237 (2003).

87. Wesley JD, Tessmer MS, Chaukos D, Brossay L. NK cell–like behavior of Vα14i NK T cells during MCMV infection. *PLoS Pathog* **4**, e1000106 (2008).

88. Tyznik AJ, Tupin E, Nagarajan NA, Her MJ, Benedict CA, Kronenberg M. Cutting edge: the mechanism of invariant NKT cell responses to viral danger signals. *The Journal of Immunology* **181**, 4452-4456 (2008).

89. Rossjohn J, Pellicci DG, Patel O, Gapin L, Godfrey DI. Recognition of CD1d-restricted antigens by natural killer T cells. *Nature reviews Immunology* **12**, 845-857 (2012).

90. Wolf BJ, Choi JE, Exley MA. Novel approaches to exploiting invariant NKT cells in cancer immunotherapy. *Frontiers in immunology* **9**, 384 (2018).

91. Stetson DB, *et al.* Constitutive cytokine mRNAs mark natural killer (NK) and NK T cells poised for rapid effector function. *The Journal of experimental medicine* **198**, 1069-1076 (2003).

92. Nagarajan NA, Kronenberg M. Invariant NKT cells amplify the innate immune response to lipopolysaccharide. *The Journal of Immunology* **178**, 2706-2713 (2007).

93. Gumperz JE, Miyake S, Yamamura T, Brenner MB. Functionally distinct subsets of CD1d-restricted natural killer T cells revealed by CD1d tetramer staining. *The Journal of experimental medicine* **195**, 625-636 (2002).

94. Lee PT, Benlagha K, Teyton L, Bendelac A. Distinct functional lineages of human V(alpha)24 natural killer T cells. *The Journal of experimental medicine* **195**, 637-641 (2002).

95. Watarai H, *et al.* Development and Function of Invariant Natural Killer T Cells Producing TH 2-and TH 17-Cytokines. *PLoS Biol* **10**, e1001255 (2012).

96. Kawano T, *et al.* Natural killer-like nonspecific tumor cell lysis mediated by specific ligand-activated Vα14 NKT cells. *Proceedings of the National Academy of Sciences* **95**, 5690-5693 (1998).

97. Wingender G, Krebs P, Beutler B, Kronenberg M. Antigen-specific cytotoxicity by invariant NKT cells in vivo is CD95/CD178-dependent and is correlated with antigenic potency. *The Journal of Immunology* **185**, 2721-2729 (2010).

98. Terabe M, Berzofsky JA. The immunoregulatory role of type I and type II NKT cells in cancer and other diseases. *Cancer Immunology, Immunotherapy* **63**, 199-213 (2014).

99. Nair S, Dhodapkar MV. Natural killer T cells in cancer immunotherapy. *Frontiers in immunology* **8**, 1178 (2017).

100. Lan F, Zeng D, Higuchi M, Higgins JP, Strober S. Host conditioning with total lymphoid irradiation and antithymocyte globulin prevents graft-versus-host disease: the role of CD1-reactive natural killer T cells. *Biology of blood and marrow transplantation : journal of the American Society for Blood and Marrow Transplantation* **9**, 355-363 (2003).

101. Morecki S, *et al.* Effect of KRN7000 on induced graft-vs-host disease. *Experimental hematology* **32**, 630-637 (2004).

102. Hashimoto D, *et al.* Stimulation of host NKT cells by synthetic glycolipid regulates acute graft-versus-host disease by inducing Th2 polarization of donor T cells. *Journal of immunology* **174**, 551-556 (2005).

103. Duramad O, Laysang A, Li J, Ishii Y, Namikawa R. Pharmacologic expansion of donor-derived, naturally occurring CD4+ Foxp3+ regulatory T cells reduces acute graft-versus-host disease lethality without abrogating the graft-versus-leukemia effect in murine models. *Biology of Blood and Marrow Transplantation* **17**, 1154-1168 (2011).

104. Hirai T, *et al.* A novel approach inducing transplant tolerance by activated invariant natural killer T cells with costimulatory blockade. *American Journal of Transplantation* **14**, 554-567 (2014).

105. Schneidawind D, *et al.* CD4+ invariant natural killer T cells protect from murine GVHD lethality through expansion of donor CD4+CD25+FoxP3+ regulatory T cells. *Blood* **124**, 3320-3328 (2014).

106. Schneidawind D, *et al.* Third-party CD4+ invariant natural killer T cells protect from murine GVHD lethality. *Blood* **125**, 3491-3500 (2015).

107. Leveson-Gower DB, *et al.* Low doses of natural killer T cells provide protection from acute graft-versus-host disease via an IL-4–dependent mechanism. *Blood, The Journal of the American Society of Hematology* **117**, 3220-3229 (2011).

108. Weber M, *et al.* Host-derived CD8+ dendritic cells protect against acute graft-versus-host disease after experimental allogeneic bone marrow transplantation. *Biology of Blood and Marrow Transplantation* **20**, 1696-1704 (2014).

109. Lowsky R, *et al.* Protective conditioning for acute graft-versus-host disease. *New England Journal of Medicine* **353**, 1321-1331 (2005).

110. Kohrt HE, *et al.* TLI and ATG conditioning with low risk of graft-versus-host disease retains antitumor reactions after allogeneic hematopoietic cell transplantation from related and unrelated donors. *Blood* **114**, 1099-1109 (2009).

111. Haraguchi K, *et al.* Recovery of V α 24+ NKT cells after hematopoietic stem cell transplantation. *Bone marrow transplantation* **34**, 595-602 (2004).

112. Rubio M-T, *et al.* Early posttransplantation donor-derived invariant natural killer T-cell recovery predicts the occurrence of acute graft-versus-host disease and overall survival. *Blood* **120**, 2144-2154 (2012).

113. Chaidos A, *et al.* Graft invariant natural killer T-cell dose predicts risk of acute graft-versus-host disease in allogeneic hematopoietic stem cell transplantation. *Blood* **119**, 5030-5036 (2012).

Chapter 2: Targeting monoamine oxidase A for T cell-based cancer immunotherapy

IMMUNOTHERAPY

Targeting monoamine oxidase A for T cell–based cancer immunotherapy

Copyright © 2021 The Authors, some rights reserved; exclusive licensee American Association for the Advancement of Science. No claim to original U.S. Government Works

Xi Wang[1], Bo Li[1], Yu Jeong Kim[1], Yu-Chen Wang[1], Zhe Li[1], Jiaji Yu[1], Samuel Zeng[1], Xiaoya Ma[1], In Young Choi[1], Stefano Di Biase[1], Drake J. Smith[1], Yang Zhou[1], Yan-Ruide Li[1], Feiyang Ma[2], Jie Huang[1], Nicole Clarke[1], Angela To[1], Laura Gong[1], Alexander T. Pham[1], Heesung Moon[1], Matteo Pellegrini[2,3], Lili Yang[1,4,5,6]*

Monoamine oxidase A (MAO-A) is an enzyme best known for its function in the brain, where it breaks down neurotransmitters and thereby influences mood and behavior. Small-molecule MAO inhibitors (MAOIs) have been developed and are clinically used for treating depression and other neurological disorders. However, the involvement of MAO-A in antitumor immunity has not been reported. Here, we observed induction of the *Maoa* gene in tumor-infiltrating immune cells. *Maoa* knockout mice exhibited enhanced antitumor T cell immunity and suppressed tumor growth. MAOI treatment significantly suppressed tumor growth in preclinical mouse syngeneic and human xenograft tumor models in a T cell–dependent manner. Combining MAOI and anti–PD-1 treatments generated synergistic tumor suppression effects. Clinical data correlation studies associated intratumoral *MAOA* expression with T cell dysfunction and decreased patient survival in a broad range of cancers. We further demonstrated that MAO-A restrains antitumor T cell immunity through controlling intratumoral T cell autocrine serotonin signaling. Together, these data identify MAO-A as an immune checkpoint and support repurposing MAOI antidepressants for cancer immunotherapy.

INTRODUCTION

CD8 cytotoxic T cells are potent immune cells capable of recognizing and eradicating malignant cells; these immune cells are therefore attractive therapeutic targets for treating cancer (*1*–*3*). However, the antitumor responses of CD8 T cells can be severely restrained by negative-regulator (immune checkpoint) pathways that are particularly prevalent in the tumor immunosuppressive environment (*4*). To release this suppression and harness the antitumor potential of CD8 T cells, several immune checkpoint blockade (ICB) therapies have been developed over the past decade (*5*, *6*). Blockade of the cytotoxic T lymphocyte–associated protein 4 (CTLA-4) and programmed cell death protein 1 (PD-1)/programmed cell death 1 ligand 1 (PD-L1) inhibitory pathways have achieved remarkable clinical responses and revolutionized the treatment of many cancers; so far, the U.S. Food and Drug Administration (FDA) has approved these two ICB therapies for treating more than 10 different malignancies (*5*, *6*). Despite these impressive successes, only a fraction of patients with cancer respond to CTLA-4 and PD-1/PD-L1 blockade therapies, and most responders suffer tumor recurrence due to the development of tumor immune evasion (*7*). These limitations of existing ICB therapies are thought to be largely caused by the presence of multiple immune checkpoint pathways, as well as the different roles of individual immune checkpoint pathways in regulating specific cancer types and disease stages (*7*). Thus, the identification of new immune checkpoints and the development of new combination treatments are a major focus of current cancer immunotherapy studies.

Monoamine oxidase A (MAO-A) is an enzyme that catalyzes the degradation of biogenic and dietary monoamines (*8*, *9*). MAO-A is located on the outer membrane of mitochondria and, in humans, is encoded by the X-linked *MAOA* gene. MAO-A is best known for its function in the brain, where it regulates the homeostasis of key monoamine neuronal transmitters including serotonin, dopamine, epinephrine, and norepinephrine and thereby influences human mood and behavior (*8*, *9*). Complete MAO-A deficiency in humans caused by a mutation of the *MAOA* gene leads to an excess of monoamine neuronal transmitters in the brain and results in Brunner syndrome, which is characterized by problematic impulsive behaviors and mood swings (*10*). Genetic association studies also identified several *MAOA* gene variants linked to altered MAO-A enzyme expression levels: Low-activity forms of the *MAOA* gene are associated with aggression and hyperactivity disorders, whereas high-activity forms are associated with depression disorders (*11*, *12*). Because of its link with aggressive and even violent behavior in men, a low-activity variant of the *MAOA* gene, *MAOA-L*, has previously received broad publicity and is popularly referred to as the "warrior gene" (*13*). On the other hand, small-molecule MAO inhibitors (MAOIs) have been developed and are clinically used for treating depression symptoms (*14*). However, MAO-A's functions outside of the brain are largely unexplored. In particular, the involvement of MAO-A in antitumor immunity is unknown. Here, we investigated the role of MAO-A in regulating CD8 T cell antitumor immunity and evaluated the possibility of repurposing MAOIs for cancer immunotherapy using knockout (KO) and transgenic mice, preclinical mouse syngeneic and human xenograft tumor models, and clinical data correlation studies.

[1]Department of Microbiology, Immunology and Molecular Genetics, University of California, Los Angeles, CA 90095, USA. [2]Department of Molecular, Cell and Developmental Biology, University of California, Los Angeles, CA 90095, USA. [3]Institute for Genomics and Proteomics, University of California, Los Angeles, CA 90095, USA. [4]Molecular Biology Institute, University of California, Los Angeles, CA 90095, USA. [5]Eli and Edythe Broad Center of Regenerative Medicine and Stem Cell Research, University of California, Los Angeles, CA 90095, USA. [6]Jonsson Comprehensive Cancer Center, the David Geffen School of Medicine, University of California, Los Angeles, CA 90095, USA.
*Corresponding author. Email: liliyang@ucla.edu

RESULTS

MAO-A deficiency enhances CD8 T cell antitumor immunity

To search for new drug targets regulating antitumor immunity, we grew B16–ovalbumin (OVA) melanoma solid tumors in C57BL/6J mice, isolated tumor-infiltrating immune cells (TIIs), and evaluated TII gene expression profiles using quantitative reverse transcription polymerase chain reaction (RT-PCR). Immune cells isolated from the spleen of tumor-bearing and tumor-free mice were included as controls. In addition to the classical immune regulatory genes, we detected significant changes in the expression of a group of genes typically classified as neuronal regulatory genes. In particular, we detected the induction of a *Maoa* gene in TIIs (Fig. 1A), suggesting that, along with its known function in the brain as a regulator of neuronal activity (*8*), it might also function in the tumor as a regulator of antitumor reactivity. We were especially interested to study whether MAO-A might regulate CD8 cytotoxic T cells, which play a critical role in immune response against cancer.

To test this, we began by studying MAO-A–deficient mice that carry a hypomorphic *Maoa* mutant (*15*). Although a degree of *Maoa* expression leakage in the brain was previously reported in these mice (*15*), analysis of their immune system showed a nearly complete ablation of *Maoa* mRNA and protein expression in the major immune organs including thymus and spleen (fig. S1, A and B). Since we focused on studying immune cells, here, we refer to these mice as *Maoa*-KO mice. *Maoa*-KO mice showed normal T cell development in the thymus and contained normal numbers of T cells in the periphery, compared with the wild-type control mice (*Maoa*-WT mice) (fig. S1, C to H). Before tumor challenge, these T cells displayed a typical naïve phenotype ($CD25^{lo}CD69^{lo}CD44^{lo}CD62L^{hi}$; fig. S1I). When challenged with tumors, compared with *Maoa*-WT mice, *Maoa*-KO mice exhibited significantly suppressed tumor growth in two syngeneic mouse tumor models, the MC38 colon cancer model and the B16-OVA melanoma model (Fig. 1, B to D). Flow cytometry analysis detected similar levels of tumor-infiltrating CD8 T cells in *Maoa*-KO and *Maoa*-WT mice (fig. S2A). However, in *Maoa*-KO mice, these tumor-infiltrating T cells displayed an enhanced effector phenotype: They produced higher levels of effector cytokines and cytotoxic molecules [i.e., interferon-γ (IFN-γ) and

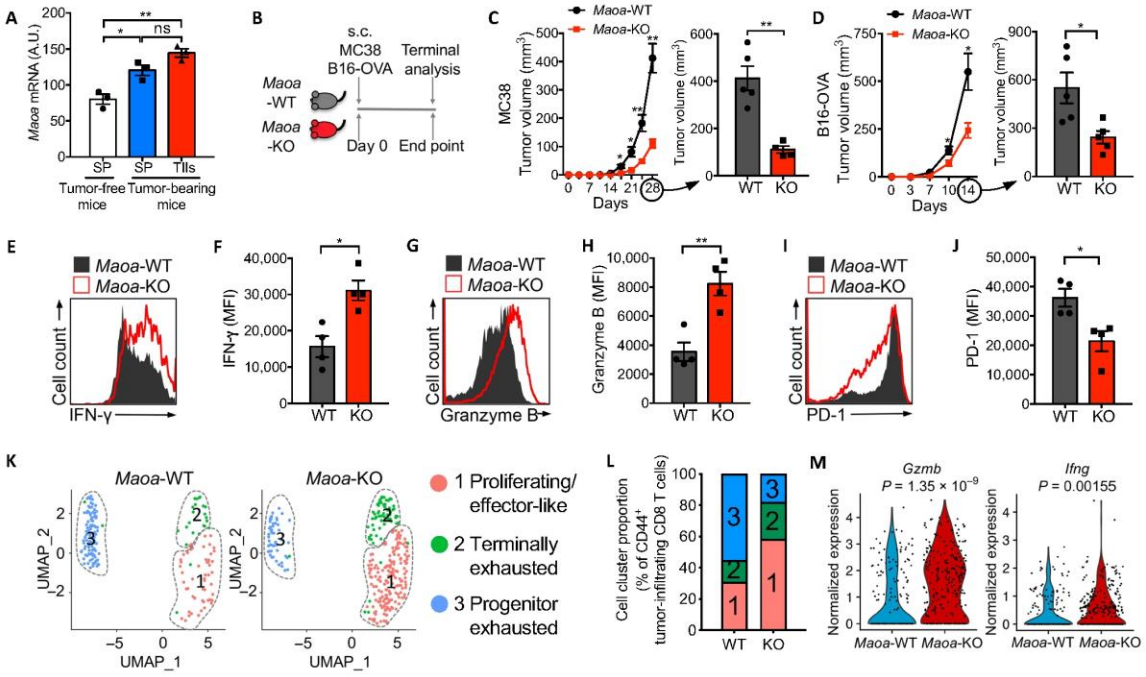

Fig. 1. MAO-A–deficient mice show suppressed tumor growth and enhanced CD8 T cell antitumor immunity. (**A**) qPCR analyses of *Maoa* mRNA expression in TIIs isolated from day 14 B16-OVA melanoma tumors grown in wild-type B6 mice ($n = 3$). Spleen (SP) cells collected from the tumor-bearing and tumor-free B6 mice were included as controls. A.U., artificial unit. (**B** to **D**) Syngeneic tumor growth in *Maoa*-WT and *Maoa*-KO mice. s.c., subcutaneous. (B) Experimental design. (C) MC38 colon cancer tumor growth ($n = 4$ and 5). (D) B16-OVA melanoma tumor growth ($n = 5$). (**E** to **J**) Flow cytometry analysis of tumor-infiltrating CD8 T cells isolated from day 14 B16-OVA tumors grown in *Maoa*-WT and *Maoa*-KO mice ($n = 4$). FACS plots and quantifications are presented, showing the measurements of intracellular IFN-γ (E and F) and Granzyme B (G and H) production, as well as cell surface PD-1 expression (I and J). MFI, mean fluorescence intensity. (**K** to **M**) scRNA-seq analysis of antigen-experienced ($CD44^+$) tumor-infiltrating CD8 T cells isolated from day 14 B16-OVA tumors grown in *Maoa*-WT and *Maoa*-KO mice (10 tumors were combined for each group). (K) UMAP plots showing the formation of three major cell clusters. Each dot represents a single cell and is colored according to its cell cluster assignment. Gene signature profiling analysis identified cluster 1 cells to be proliferating/effector-like CD8 T cells, cluster 2 cells to be terminally exhausted CD8 T cells, and cluster 3 cells to be progenitor exhausted CD8 T cells. (L) Bar graphs showing the cell cluster proportions. (M) Violin plots showing the expression distribution of *Gzmb* and *Ifng* genes. Each dot represents an individual cell. Representative of one (K to M), two (A), and three (B to J) experiments. Data are presented as the means ± SEM. ns, not significant; $^*P < 0.05$ and $^{**}P < 0.01$ by one-way ANOVA (A) or by Student's *t* test (C, D, F, H, and J). *P* values of violin plots (M) were determined by Wilcoxon rank sum test.

Granzyme B; Fig. 1, E to H], and they expressed lower levels of T cell exhaustion markers (i.e., PD-1; Fig. 1, I and J).

To further investigate how MAO-A deficiency may affect the tumor-infiltrating CD8 T cell compartment, we isolated TIIs from tumor-bearing *Maoa*-WT and *Maoa*-KO mice and performed a single-cell RNA sequencing (scRNA-seq) study. Uniform Manifold Approximation and Projection (UMAP) analysis of antigen-experienced ($CD44^+$) tumor-infiltrating CD8 T cells revealed the formation of three major cell clusters (Fig. 1K); signature gene profiling study (fig. S2, B and C) and gene set enrichment analysis (GSEA; fig. S2, D to F) identified cluster 1 cells as proliferating/effector-like CD8 T cells, cluster 2 cells as terminally exhausted CD8 T cells, and cluster 3 cells as progenitor-exhausted CD8 T cells (*16*). Compared with their wild-type counterparts, *Maoa*-KO tumor-infiltrating CD8 T cells were enriched for proliferating/effector-like (cluster 1) cells while decreased for exhausted (clusters 2 and 3), especially the progenitor-exhausted (cluster 3) cells (Fig. 1, K and L). Single-gene expression analysis also showed an overall enhanced expression of genes associated with cytotoxic T cell effector function (i.e., *Gzmb* and *Ifng*; Fig. 1M) and genes associated with mitochondrial function that is a notable factor in T cell effector function (i.e., mitochondrial electron transport chain genes; fig. S3) (*17*), in tumor-infiltrating CD8 T cells isolated from *Maoa*-KO mice. Collectively, these scRNA-seq results suggest a possible role of MAO-A in regulating the generation/maintenance of active effector-like antitumor CD8 T cells. Together, these in vivo studies using MAO-A–deficient mice indicate that MAO-A is involved in regulating antitumor immunity, especially in regulating CD8 T cell antitumor effector functions.

MAO-A directly regulates CD8 T cell antitumor immunity

In our *Maoa*-KO mice tumor challenge study, MAO-A deficiency affected both immune and nonimmune cells. To determine whether MAO-A directly or indirectly regulates immune cells, we performed a pair of two-way bone marrow (BM) transfer experiments: In one experiment, we confined MAO-A deficiency comparison to immune cells by reconstituting CD45.1 wild-type recipient mice with BM cells from either CD45.2 *Maoa*-WT or *Maoa*-KO donor mice, followed by B16-OVA tumor challenge; in another experiment, we confined MAO-A deficiency comparison to nonimmune cells by reconstituting either CD45.2 *Maoa*-WT or *Maoa*-KO recipient mice with BM cells from CD45.1 wild-type donor mice, followed by B16-OVA tumor challenge (Fig. 2A). Successful reconstitution of immune cells, particularly T cells, was confirmed in both experiments (fig. S4, A to D). Suppressed tumor growth was observed only when MAO-A deficiency was confined to the immune cells, indicating that MAO-A affects tumor growth via directly regulating immune cell antitumor reactivity (Fig. 2, B and C).

To further study whether MAO-A directly regulates the antitumor reactivity of CD8 T cells, we bred *Maoa*-KO mice with *OT1* transgenic (*OT1*-Tg) mice and generated *OT1*-Tg/*Maoa*-KO mice producing OVA-specific CD8 T cells deficient in MAO-A (fig. S5A). We isolated OT1 T cells from either the *OT1*-Tg or *OT1*-Tg/*Maoa*-KO mice (denoted as OT1-WT or OT1-KO T cells, respectively) and separately transferred these cells into CD45.1 wild-type mice bearing preestablished B16-OVA tumors (Fig. 2D and fig. S5B). In this experiment, MAO-A deficiency comparison was confined solely to tumor-specific OT1 T cells. Both OT1-WT and OT1-KO T cells actively infiltrated tumors and showed an antigen-experienced phenotype ($CD44^{hi}CD62L^{lo}$; Fig. 2E and fig. S5, C and D). However, OT1-KO T cells were more effective in controlling tumor growth, corresponding with their enhanced effector function and reduced exhaustion phenotype (Fig. 2F and fig. S5, E to J). Collectively, these in vivo studies demonstrate that MAO-A works as an autonomous factor directly regulating CD8 T cell antitumor immunity.

MAO-A restrains the CD8 T cell response to antigen stimulation

Analysis of *Maoa* mRNA expression in tumor-infiltrating CD8 T cells showed an induction of the *Maoa* gene in these T cells compared with naïve CD8 T cells (Fig. 3A). Further analysis of tumor-infiltrating CD8 T cell subsets revealed that *Maoa* gene expression levels were positively correlated with the exhaustion and dysfunction status of these T cells: Compared with $PD\text{-}1^{lo}$ cells, $PD\text{-}1^{hi}$ "exhausted" T cells expressed higher levels of *Maoa* mRNA, and the $PD\text{-}1^{hi}$ cells coexpressing T cell immunoglobulin mucin 3 (Tim-3) and lymphocyte activation gene 3 protein (LAG-3), which were considered "most exhausted", expressed the highest levels of *Maoa* mRNA (Fig. 3A) (*18*, *19*). These in vivo data suggest that *Maoa* may be induced by tumor antigen recognition and then act as a negative-feedback regulator inhibiting CD8 T cell antitumor reactivity.

To test this hypothesis, we isolated CD8 T cells from *Maoa*-WT or *Maoa*-KO mice and then stimulated these T cells in vitro with anti-CD3, mimicking tumor antigen stimulation. We observed an induction of *Maoa* mRNA expression in *Maoa*-WT CD8 T cells, in agreement with previous reports; minimal *Maoa* mRNA expression was detected in *Maoa*-KO CD8 T cells, confirming their *Maoa* deficiency phenotype (Fig. 3B) (*20*). The induction of MAO-A protein expression in *Maoa*-WT CD8 T cells was also confirmed by Western blot analysis; the MAO-A isoenzyme, MAO-B, was not detected in CD8 T cells (fig. S6A). Compared with their *Maoa*-WT counterparts, *Maoa*-KO CD8 T cells showed an enhancement in almost all aspects of T cell activation, including cell proliferation (Fig. 3C), surface activation marker up-regulation (i.e., CD25; Fig. 3, D and E), effector cytokine production [i.e., interleukin-2 (IL-2) and IFN-γ; Fig. 3, F and G], and cytotoxic molecule production (i.e., Granzyme B; Fig. 3, H and I). Study of *Maoa*-KO OVA-specific OT1 T cells gave similar results, suggesting a general role of MAO-A in regulating CD8 T cells of diverse antigen specificities (fig. S7, A to D); study of *Maoa*-KO CD8 T cells stimulated with both anti-CD3 and anti-CD28 also yielded similar results, suggesting a general role of MAO-A in regulating CD8 T cell responses in the presence or absence of costimulation (fig. S6, B to I). To verify whether MAO-A deficiency directly contributed to the hyperresponsiveness of the *Maoa*-KO CD8 T cells, we performed a rescue experiment. We constructed a MIG [murine stem cell virus–internal ribosomal entry site–green fluorescent protein (MSCV-IRES-GFP)]-*Maoa* retroviral vector, used this vector to transduce *Maoa*-KO CD8 T cells, and achieved overexpression of MAO-A in these T cells (Fig. 3, J to L). MAO-A overexpression significantly reduced the hyperactivation of *Maoa*-KO CD8 T cells and their expression of multiple effector genes (i.e., *Il2*, *Ifng*, and *Gzmb*; Fig. 3, M to O). Together, these results indicate that MAO-A acts as a negative-feedback regulator restraining the CD8 T cell response to antigen stimulation.

MAO-A regulates CD8 T cell autocrine serotonin signaling

Next, we sought to investigate the molecular mechanisms mediating MAO-A restraint of CD8 T cell response to antigen stimulation. MAO-A is well known for its function in the brain where it breaks down neuron-produced serotonin, thereby regulating neuronal activity

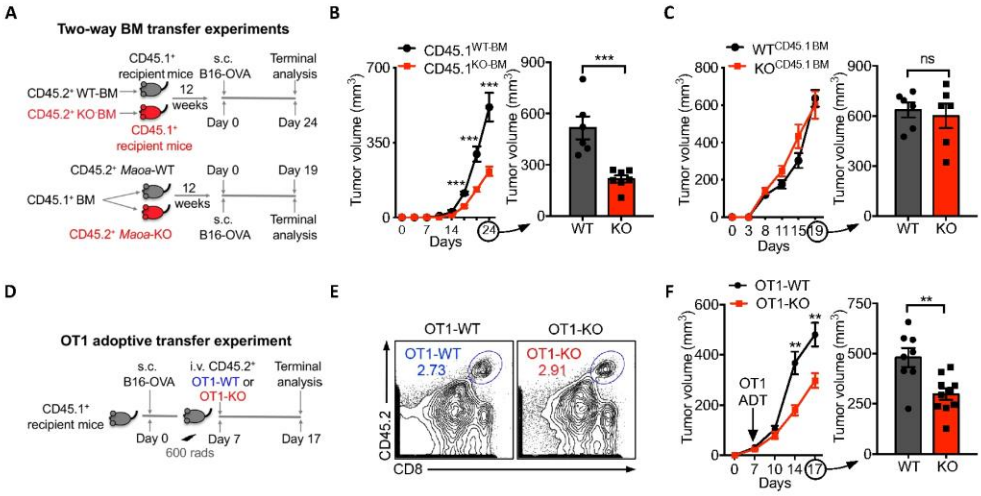

Fig. 2. MAO-A directly regulates CD8 T cell antitumor immunity. (**A** to **C**) Two-way BM transfer experiments. (A) Experimental design. (B) B16-OVA tumor growth in CD45.1 wild-type recipient mice reconstituted with BM cells from CD45.2 *Maoa*-WT or *Maoa*-KO donor mice (denoted as $CD45.1^{WT\text{-}BM}$ or $CD45.1^{KO\text{-}BM}$ mice, respectively) ($n = 6$ and 7). (C) B16-OVA tumor growth in CD45.2 *Maoa*-WT or *Maoa*-KO recipient mice reconstituted with BM cells from CD45.1 wild-type donor mice (denoted as $WT^{CD45.1\ BM}$ or $KO^{CD45.1\ BM}$ mice, respectively) ($n = 6$). (**D** to **F**) OT1 T cell adoptive transfer experiment ($n = 8$ to 10). i.v., intravenous. (D) Experimental design. OT1, OVA-specific transgenic CD8 T cell; OT1-WT, wild-type OT1 T cell; OT1-KO, MAO-A–deficient OT1 T cell. (E) FACS plots showing the detection of intratumoral OT1-WT and OT1-KO T cells (gated as $CD45.2^+CD8^+$ cells) in day 17 B16-OVA tumors. (F) Tumor growth. Representative of two experiments. ADT, adoptive transfer. Data are presented as the means ± SEM. $^{**}P < 0.01$ and $^{***}P < 0.001$ by Student's *t* test.

(*8*, *9*). CD8 T cells have been reported to synthesis serotonin, and serotonin has been implicated as an accessory signal to enhance T cell activation by signaling through T cell surface serotonin receptors [5-hydroxytryptamine receptors (5-HTRs)] (*20*–*22*). We therefore postulated that MAO-A might regulate CD8 T cell activity through modulating T cell autocrine serotonin production and signaling (Fig. 4A).

To test this hypothesis, we cultured *Maoa*-WT and *Maoa*-KO CD8 T cells in vitro, stimulated them with anti-CD3 to mimic antigen stimulation, and then analyzed their autocrine serotonin signaling pathway. After antigen stimulation, *Maoa*-WT CD8 T cells up-regulated the expression of the *Tph1* gene, which encodes the rate-limiting enzyme controlling serotonin synthesis, and also the expression of the *Maoa* gene, which would induce serotonin degradation, indicating the presence of an antigen stimulation–induced serotonin synthesis/degradation loop in CD8 T cells (Fig. 4, A to C). Considering the function of MAO-A, we speculated that MAO-A deficiency would not interfere with the serotonin synthesis arm but would impede the serotonin degradation arm, leading to enhanced secretion of serotonin by CD8 T cells. Compared with their wild-type counterparts, *Maoa*-KO CD8 T cells expressed comparable levels of *Tph1* but secreted much higher levels of serotonin after antigen stimulation (Fig. 4, B and D). Pharmacological inhibition of MAO-A in *Maoa*-WT CD8 T cells using an established MAOI, phenelzine, recapitulated the serotonin overproduction phenotype of *Maoa*-KO CD8 T cells (Fig. 4E). Correspondingly, phenelzine treatment of *Maoa*-WT CD8 T cells recapitulated the hyperactivation phenotype of *Maoa*-KO CD8 T cells, shown by increased production of the effector cytokines IL-2 and IFN-γ (Fig. 4, F and G). Supplementing serotonin to *Maoa*-WT CD8 T cells resulted in T cell hyperactivation and elevated production of IL-2 and IFN-γ (Fig. 4, H and I), whereas blocking T cell surface 5-HTRs using the antagonist asenapine eliminated the cytokine production difference between *Maoa*-WT and *Maoa*-KO CD8 T cells (Fig. 4, J and K). Serotonin has been reported to enhance T cell activation by signaling through the mitogen-activated protein kinase (MAPK) pathway that cross-talks with the T cell receptor (TCR) signaling pathways (*21*). We compared the signaling pathways in *Maoa*-WT and *Maoa*-KO CD8 T cells after antigen stimulation and found that *Maoa*-KO T cells showed an enhancement of MAPK signaling [i.e., extracellular signal–regulated kinase (ERK) phosphorylation; Fig. 4L and fig. S8, B and C] and TCR downstream signaling [i.e., nuclear translocation of nuclear factor of activated T cells (NFAT), nuclear factor κB (NF-κB), and c-Jun transcription factors; Fig. 4M and fig. S8, D to I]; this enhancement was largely abrogated by blocking 5-HTRs (Fig. 4, L and M, and fig. S8, B to I). There are multiple 5-HTR family members; in mice, there are 13 5-HTR family members (*21*). Analyses of the expression of all 13 5-HTR genes in CD8 T cells before and after anti-CD3 stimulation revealed that these cells predominantly expressed 2 of the 13 5-HTR genes: *Htr2b* and *Htr7*; there was a further up-regulation of *Htr7* after anti-CD3 stimulation (fig. S8J). These data suggest that serotonin signaling in mouse CD8 T cells may mainly be mediated through Htr2b and Htr7; in particular, Htr7 may mediate the activation-related signaling events. Collectively, these in vitro data suggest that MAO-A regulates CD8 T cell activation through modulating T cell autocrine serotonin production and signaling (Fig. 4A and fig. S8A).

To validate this working model in vivo, we directly measured intratumoral serotonin in *Maoa*-KO and *Maoa*-WT mice, as well as in wild-type mice treated or untreated with phenelzine. Consistent with the in vitro results, increased levels of serotonin were detected specifically in tumors collected from the *Maoa*-KO mice (Fig. 4N)

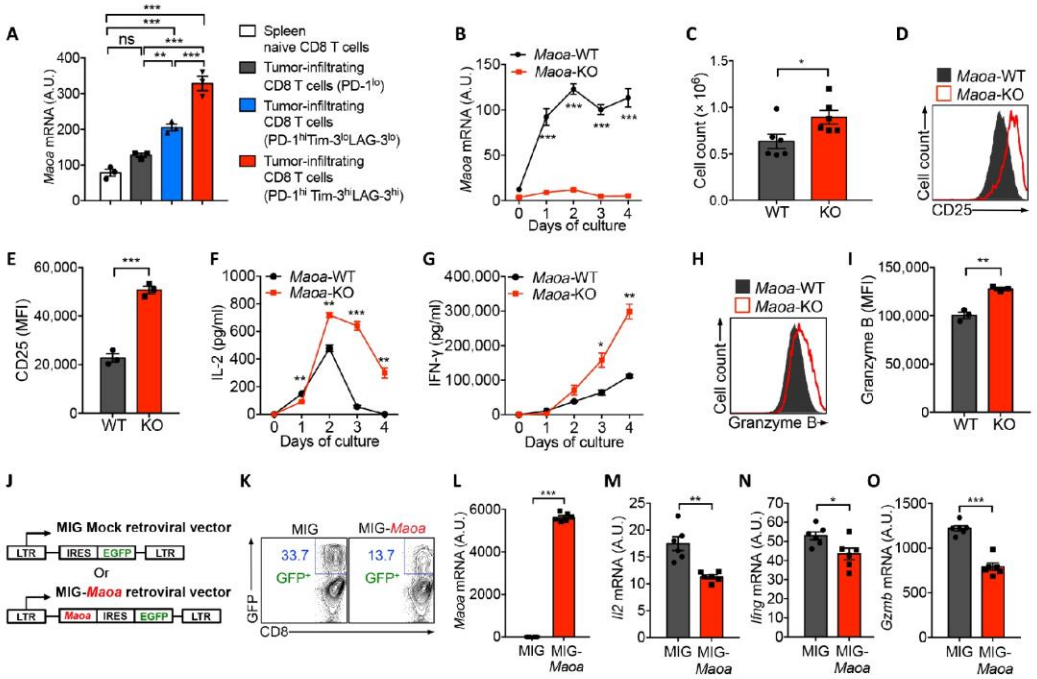

Fig. 3. MAO-A acts as a negative-feedback regulator to restrain CD8 T cell activation. (**A**) qPCR analyses of *Maoa* mRNA expression in tumor-infiltrating CD8 T cell subsets isolated from day 14 B16-OVA tumors grown in wild-type B6 mice ($n = 3$). Naïve CD8 T cells (gated as TCRβ$^+$CD8$^+$CD44^{lo}CD62L^{hi} cells) sorted from the spleen of tumor-free B6 mice were included as controls. (**B** to **I**) Activation of *Maoa*-WT and *Maoa*-KO CD8 T cells ($n = 3$ to 6). CD8 T cells were purified from *Maoa*-WT and *Maoa*-KO mice and stimulated in vitro with anti-CD3. The analyses of *Maoa* mRNA expression (B), cell proliferation (C), activation marker expression [i.e., CD25 (D and E)], effector cytokine production [i.e., IL-2 (F) and IFN-γ (G)], and cytotoxic molecule production [i.e., Granzyme B (H and I)] are shown, either over a 4-day time course (B, F, and G) or at day 3 after anti-CD3 stimulation (C to E, H, and I). (**J** to **O**) Activation of *Maoa*-KO CD8 T cells with MAO-A overexpression ($n = 6$). LTR, long terminal repeats; EGFP, enhanced green fluorescent protein. CD8 T cells were isolated from *Maoa*-KO mice, stimulated in vitro with anti-CD3 and transduced with a MIG-*Maoa* retrovector or a MIG mock retrovector (J). The analyses of retroviral transduction efficiency (K), *Maoa* mRNA expression (L), effector cytokine mRNA expression [i.e., *Il2* (M) and *Ifng* (N)], and cytotoxicity molecule mRNA expression [i.e., *Gzmb* (O)] at day 4 after stimulation are presented. Representative of two (A and J to O) and three (B to I) experiments. Data are presented as the means ± SEM. *$P < 0.05$, **$P < 0.01$, and ***$P < 0.001$ by one-way ANOVA (A) or by Student's *t* test (B, C, E to G, I, and L to O).

and phenelzine-treated *Maoa*-WT mice (Fig. 4O). Depletion of CD8 T cells in *Maoa*-WT mice largely abolished the phenelzine treatment–induced accumulation of serotonin in the tumor, indicating that tumor-infiltrating CD8 T cells are major producers of serotonin in the tumor and that this is negatively regulated by MAO-A (Fig. 4O and fig. S8L). There were no significant changes in serotonin levels in serum under any conditions (fig. S8, K and M), suggesting that MAO-A regulation of serotonin in the tumor is largely a local effect, resembling MAO-A regulation of serotonin in the brain (*8*, *9*).

Together, these in vitro and in vivo data support a working model that MAO-A negatively regulates CD8 T cell antitumor immunity, at least partly, through modulating CD8 T cell autocrine serotonin signaling in the tumor.

MAO-A blockade for cancer immunotherapy

The identification of MAO-A as a new immune checkpoint negatively regulating CD8 T cell antitumor immunity marks it as a promising drug target for developing new forms of ICB therapy. Because of MAO-A's well-characterized function in the brain, small-molecule MAOIs have been developed and clinically used for treating depression symptoms, making it a highly feasible and attractive approach to repurpose these established MAOI antidepressants for cancer immunotherapy (*23*). Some MAOIs cross-inhibit the MAO-A isoenzyme MAO-B; however, only MAO-A effectively degrades serotonin, and all MAOIs exhibit their antidepressant function mainly through inhibiting MAO-A enzyme activity, thereby regulating serotonin signaling in the brain (*14*, *23*). When tested in vitro, multiple MAOIs efficiently induced CD8 T cell hyperactivation (i.e., up-regulated expression of CD25, Granzyme B, IL-2, and IFN-γ; Fig. 5A and fig. S9, A to F). When tested in vivo in a B16-OVA melanoma prevention model, these MAOIs markedly suppressed tumor growth (Fig. 5, B and C). The MAOIs that we tested were phenelzine, clorgyline, and moclobemide, covering the major categories of established MAOIs classified on the basis of whether they are nonselective or selective for MAO-A and whether their effect is reversible (fig. S9A) (*23*). Among these MAOIs, phenelzine (trade name: Nardil) is clinically available in the United States (*23*). In the following studies, we chose phenelzine as a representative to further evaluate the cancer therapy potential of MAOI drugs.

First, we studied the efficacy of phenelzine in treating preestablished B16-OVA melanoma solid tumors and found that phenelzine treatment effectively suppressed tumor progression (Fig. 5, D and E).

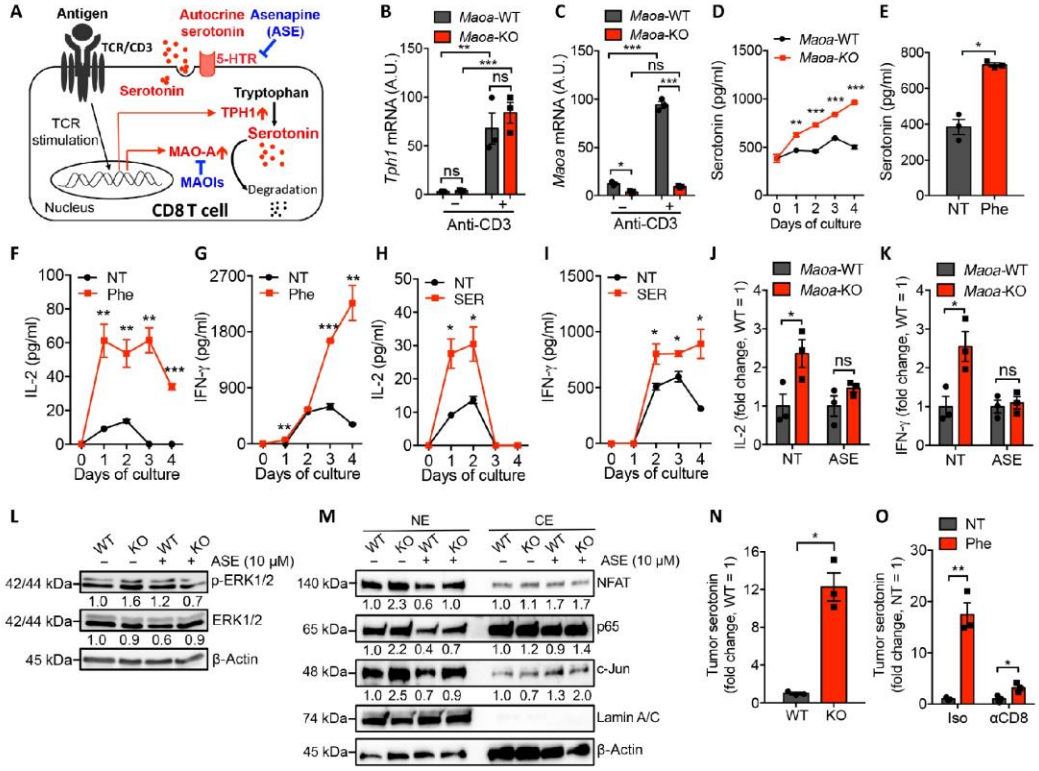

Fig. 4. MAO-A regulates CD8 T cell autocrine serotonin signaling. (**A**) Schematics showing the antigen stimulation-induced serotonin synthesis/degradation loop in a CD8 T cell. Possible pharmacological interventions are indicated. ASE, asenapine (an antagonist blocking a majority of 5-HTRs). (**B** and **C**) qPCR analyses of *Tph1* (B) and *Maoa* (C) mRNA expression in *Maoa*-WT and *Maoa*-KO CD8 T cells, at 24 hours after anti-CD3 stimulation ($n = 3$). (**D** and **E**) CD8 T cell serotonin production in vitro ($n = 3$). (D) Serotonin levels in *Maoa*-WT and *Maoa*-KO CD8 T cell cultures over a 4-day time course after anti-CD3 stimulation. (E) Serotonin levels in *Maoa*-WT CD8 T cell cultures at 24 hours after anti-CD3 stimulation, with or without phenelzine treatment [Phe or no treatment (NT)]. Serotonin levels were measured by ELISA. (**F** to **K**) CD8 T cell effector cytokine production in vitro ($n = 3$). (F and G) IL-2 and IFN-γ levels in *Maoa*-WT CD8 T cell cultures over a 4-day time course after anti-CD3 stimulation, with or without phenelzine (Phe) treatment (Phe or NT). (H and I) IL-2 and IFN-γ levels in *Maoa*-WT CD8 T cell cultures over a 4-day time course after anti-CD3 stimulation, with or without serotonin (SER) treatment (SER or NT). (J and K) IL-2 and IFN-γ levels in *Maoa*-WT and *Maoa*-KO CD8 T cell cultures at day 2 after anti-CD3 stimulation, with or without asenapine treatment (ASE or NT). Cytokine levels were measured by ELISA. (**L** and **M**) CD8 T cell 5-HTR and TCR signaling cross-talk in vitro. *Maoa*-WT and *Maoa*-KO CD8 T cells were stimulated with anti-CD3 for 2 days in the presence or absence of asenapine. Cells were then rested on ice for 2 hours and restimulated with anti-CD3 for 20 min, followed by total protein extraction (L) or nuclear protein extraction and cytoplasmic protein extraction (NE and CE; M) and Western blot analysis of key signaling molecules involved in 5-HTR (L) and TCR (M) signaling pathways. (**N** and **O**) CD8 T cell serotonin production in vivo in a B16-OVA melanoma model ($n = 3$). On day 14 after tumor challenge, tumors were collected from experimental mice for serotonin measurement using HPLC. (N) Intratumoral serotonin levels in *Maoa*-WT and *Maoa*-KO mice (denoted as WT and KO, respectively). (O) Intratumoral serotonin levels in *Maoa*-WT mice, with or without phenelzine treatment (Phe or NT) and with or without antibody-induced depletion of CD8 T cells (αCD8 or Iso). Representative of two (L to O) and three (B to K) experiments. Data are presented as the means ± SEM. $^*P < 0.05$, $^{**}P < 0.01$, and $^{***}P < 0.001$, by two-way ANOVA (B and C) or by Student's *t* test (D to K, N, and O).

This MAOI-induced tumor suppression effect was mediated by CD8 T cells, because no tumor suppression was observed when we depleted CD8 T cells in tumor-bearing B6 wild-type mice (fig. S10, A and B). Correspondingly, analysis of total tumor-infiltrating CD8 T cells under phenelzine treatment showed a hyperactivation phenotype of these T cells, evidenced by their enhanced production of effector molecules (i.e., IFN-γ and Granzyme B; Fig. 5, F to I) and reduced expression of exhaustion markers (i.e., PD-1; Fig. 5, J and K); analysis of tumor antigen-specific CD8 T cells (i.e., OVA^+ T cells) showed the similar results (fig. S10, I to P). To further study the impact of phenelzine treatment on antitumor T cell exhaustion, we tracked the PD-1–positive subpopulation of tumor-infiltrating CD8 T cells over time; we detected a significant decrease of the PD-1–positive subpopulation in phenelzine-treated mice (fig. S10, C and D). Functional analysis showed an enhanced production of effector molecules (i.e., IFN-γ and Granzyme B) in PD-1–positive subpopulations under phenelzine treatment (fig. S10, E to H). Therefore, MAO-A blockade could alleviate T cell exhaustion and improve the overall effector function of tumor-infiltrating CD8 T cells.

Next, we studied the potential of phenelzine treatment for combination therapy, particularly combining with other ICB therapies such as the PD-1/PD-L1 blockade therapy (Fig. 5L) (*6*). In the MC38 colon cancer model, which is sensitive to immunotherapy, phenelzine treatment completely suppressed tumor growth as effectively as the

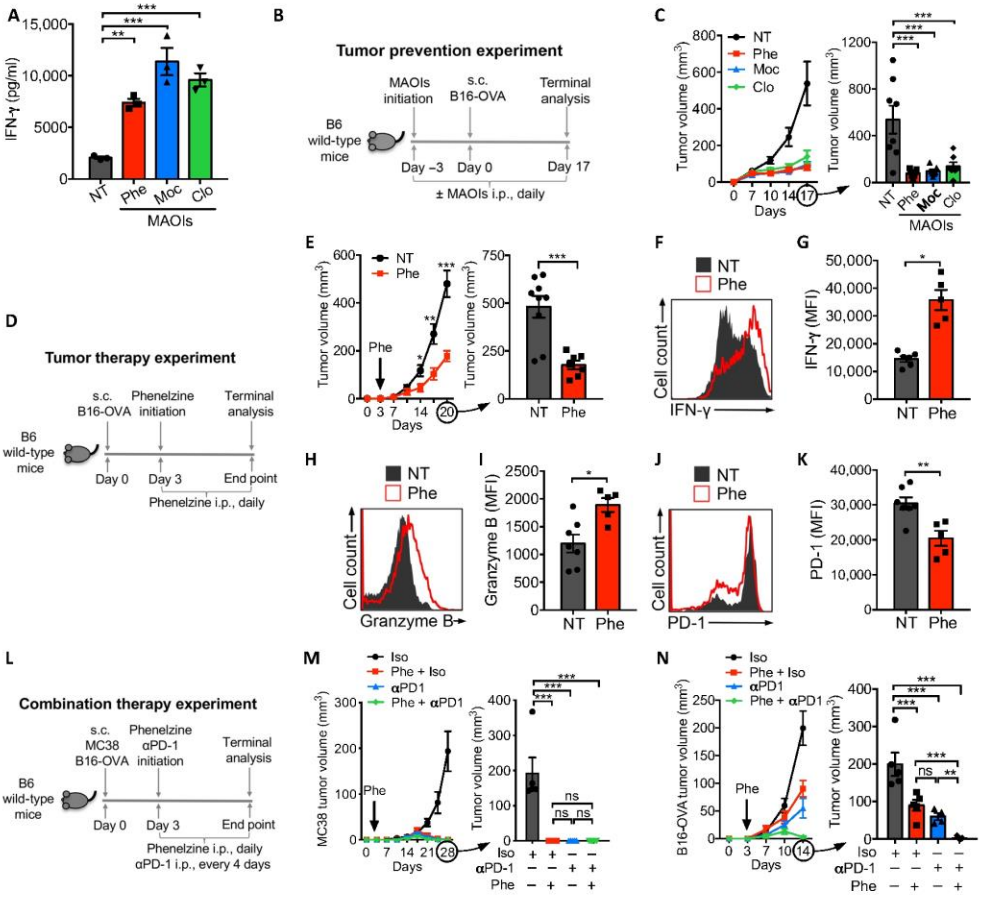

Fig. 5. MAO-A blockade for cancer immunotherapy: Syngeneic mouse tumor model studies. (**A**) Effect of MAOI treatment on CD8 T cell activation in vitro. CD8 T cells were purified from B6 wild-type mice and stimulated with anti-CD3 for 3 days in the absence (NT) or presence of MAOIs (Phe; Moc, moclobemide; Clo, clorgyline). ELISA analyses of IFN-γ production are presented ($n = 3$). (**B** and **C**) Cancer therapy potential of MAOI treatment in a B16-OVA melanoma model. i.p., intraperitoneal. (B) Experimental design. B6 wild-type mice were untreated (NT) or treated with MAOIs (Phe, Moc, and Clo). (C) Tumor growth ($n = 6$ to 8). (**D** to **K**) Cancer therapy potential of phenelzine treatment in a B16-OVA melanoma model. (D) Experimental design. (E) Tumor growth in B6 wild-type mice with or without phenelzine treatment (Phe or NT; $n = 7$ to 9). (F to K) Analysis of tumor-infiltrating CD8 T cells in B6 wild-type mice with or without phenelzine treatment. On day 20 after tumor inoculation, tumors were collected, followed by TIl isolation and FACS analysis. The analyses of tumor-infiltrating CD8 T cells (pregated as $CD45.2^+TCR\beta^+CD8^+$ cells) for their intracellular production of effector cytokines [i.e., IFN-γ (F and G)] and cytotoxic molecules [i.e., Granzyme B (H and I)], and their surface expression of exhaustion markers [i.e., PD-1 (J and K)] are presented. (**L** to **N**) Cancer therapy potential of MAOI treatment in combination with anti–PD-1 treatment in a MC38 colon cancer model and a B16-OVA melanoma model. (L) Experimental design. B6 wild-type mice were inoculated with tumor cells, with or without phenelzine treatment and with or without anti–PD-1 treatment (Iso, Phe + Iso, αPD-1, or Phe + αPD-1). (M) MC38 tumor growth ($n = 5$). (N) B16-OVA tumor growth ($n = 4$ and 5). Representative of two (B, C, and L to N) and three (A, and D to K) experiments. Data are presented as the means ± SEM. $^*P < 0.05$, $^{**}P < 0.01$, and $^{***}P < 0.001$ by one-way ANOVA (A, C, M, and N) or by Student's t test (E to K).

anti–PD-1 treatment (Fig. 5M). In the B16-OVA melanoma model, which is less sensitive to immunotherapy, phenelzine treatment significantly suppressed tumor growth at a level comparable with the anti–PD-1 treatment; the combination of phenelzine and anti–PD-1 treatments yielded superior efficacy and totally suppressed tumor growth (Fig. 5N). These tumor suppression effects of phenelzine were likely mediated by its immune regulatory function, because phenelzine treatment did not affect the tumor cells themselves and did not suppress the growth of MC38 and B16-OVA tumors in immunodeficient NOD scid gamma (NSG) mice (fig. S11, A to D). Collectively, these syngeneic mouse tumor model studies provided proof-of-principle evidence for the cancer immunotherapy potential of MAOIs.

To explore the translational potential of MAO-A blockade therapy, we studied human CD8 T cells and confirmed that they also up-regulated *MAOA* gene expression after antigen stimulation, resembling their mouse counterparts (Fig. 6A). To directly evaluate whether MAOI treatment could enhance human CD8 T cell antitumor efficacy in vivo, we used a human T cell adoptive transfer and human tumor xenograft NSG mouse model (*24*). NY-ESO-1, a well-recognized tumor antigen common in many human cancers,

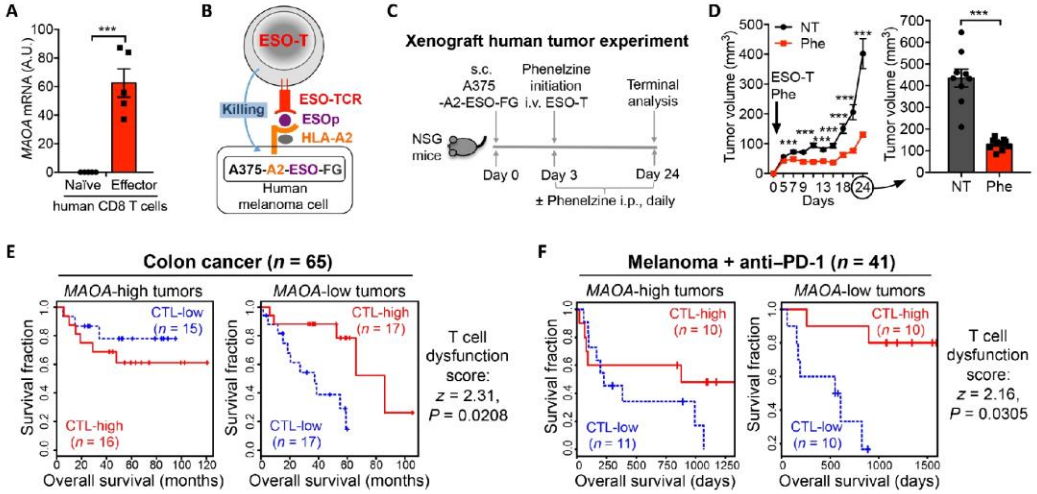

Fig. 6. MAO-A blockade for cancer immunotherapy: Human T cell and clinical data correlation studies. (**A** to **D**) Translational potential of MAOI treatment for improving human CD8 T cell antitumor reactivity. (A) qPCR analyses of *MAOA* mRNA expression in naïve and anti-CD3/anti-CD28 stimulated human CD8 T cells of random healthy donors ($n = 5$). (B) Schematics showing a human tumor–T cell pair designated for the study of human CD8 T cell antitumor reactivity. A375-A2-ESO-FG, a human A375 melanoma cell line engineered to express an NY-ESO-1 tumor antigen, its matching MHC molecule (HLA-A2), and a dual reporter comprising a firefly luciferase and an enhanced green fluorescence protein (FG). ESO-T, human peripheral blood CD8 T cells engineered to express an NY-ESO-1 antigen-specific TCR (ESO-TCR; clone 3A1). ESOp, NY-ESO-1 peptide. (C) Experimental design to study the cancer therapy potential of MAOI treatment in a human T cell adoptive transfer and human melanoma xenograft NSG mouse model. (D) Tumor growth from (C) ($n = 9$ and 10). (**E** and **F**) Clinical data correlation studies. A TIDE computational method was used to study the association between the tumor-infiltrating CD8 T cell (also known as cytotoxic T lymphocyte, CTL) level and overall patient survival in relation to the intratumoral *MAOA* gene expression level. For each patient cohort, tumor samples were divided into *MAOA*-high (samples with *MAOA* expression one standard derivation above the average; shown in left survival plot) and *MAOA*-low (remaining samples; shown in right survival plot) groups, followed by analyzing the association between the CTL levels and survival outcomes in each group. The CTL level was estimated as the average expression level of *CD8A*, *CD8B*, *GZMA*, *GZMB*, and *PRF1*. Each survival plot presented tumors in two subgroups: CTL-high group (red) had above-average CTL values among all samples, whereas CTL-low group (blue) had below-average CTL values. A T cell dysfunction score (z score) was calculated for each patient cohort, correlating the *MAOA* expression level with the beneficial effect of CTL infiltration on patient survival. A positive z score indicates that the expression of *MAOA* is negatively correlated with the beneficial effect of tumor-infiltrating CTL on patient survival. The P value indicates the comparison between the *MAOA*-low and *MAOA*-high groups and was calculated by two-sided Wald test in a Cox-PH regression. (E) TIDE analysis of a colon cancer patient cohort (GSE29621; $n = 65$). $z = 2.31$; $P = 0.0208$. (F) TIDE analysis of a melanoma patient cohort receiving anti–PD-1 treatment (ENA PRJEB23709; $n = 41$). $z = 2.16$, $P = 0.0305$. Representative of two experiments. Data are presented as the means ± SEM. ***$P < 0.001$ by Student's t test (A and D).

was chosen as the model tumor antigen (*24*). An A375 human melanoma cell line was engineered to coexpress NY-ESO-1 and its matching major histocompatibility complex (MHC) molecule, human leukocyte antigen serotype A2 (HLA-A2), to serve as the human tumor target; the cell line was also engineered to express a dual reporter comprising a firefly luciferase and an enhanced green fluorescence protein (denoted as A375-A2-ESO-FG) (*25*). A Retro/ESO-TCR retroviral vector was constructed to encode an NY-ESO-1–specific TCR (clone 3A1; denoted as ESO-TCR) and was used to transduce healthy donor peripheral blood CD8 T cells; the resulting T cells (denoted as ESO-T cells) expressed ESO-TCRs and specifically targeted A375-A2-ESO-FG tumor cells, thereby modeling the tumor-specific human CD8 T cells (Fig. 6B and fig. S12, A to D). A375-A2-ESO-FG cells were subcutaneously injected into NSG mice to establish solid tumors, followed by intravenous injection of ESO-T cells with or without phenelzine treatment (Fig. 6C). MAOI treatment effectively suppressed tumor growth; this therapeutic effect was mediated by tumor-specific ESO-T cells because no tumor suppression was observed in NSG mice that did not receive adoptive transfer of ESO-T cells (Fig. 6D and fig. S12, E and F). Collectively, this human xenograft tumor model study supports the translational potential of MAO-A blockade for cancer immunotherapy.

Last, we conducted clinical data correlation studies to investigate whether *MAOA* gene expression is correlated with CD8 T cell [also known as cytotoxic T lymphocyte (CTL)] antitumor activities and clinical outcomes in patients with cancer. A Tumor Immune Dysfunction and Exclusion (TIDE) computational method was used, which models the induction of CD8 T cell dysfunction in tumors by analyzing the interactions of three variants: (i) the intratumoral expression of a selected gene, (ii) the intratumoral level of CD8 T cells, and (iii) patient survival (*26*). *MAOA* expression level was negatively correlated with the beneficial effect of tumor-infiltrating CD8 T cell on patient survival in multiple cancer patient cohorts spanning colon cancer (Fig. 6E) (*27*), lung cancer (fig. S13A) (*28*), cervical cancer (fig. S13B) (*29*), and pancreatic cancer (fig. S13C) (*30*). Moreover, analysis of a melanoma patient cohort receiving anti–PD-1 treatment showed that high levels of intratumoral *MAOA* expression largely abrogated the patient survival benefit offered by tumor-infiltrating CD8 T cells, suggesting that combining MAO-A blockade therapy with PD-1/PD-L1 blockade therapy may provide synergistic therapeutic benefits through further activating tumor-infiltrating CD8 T cells (Fig. 6F) (*31*). These whole-tumor lysate transcriptome data analyses could not localize the *MAOA* expression to a specific cell type (i.e., CD8 T cells); future studies of quality transcriptome data

generated from single cells or sorted tumor-infiltrating CD8 T cells are needed to produce such information. Nonetheless, the present clinical data correlation studies identified MAO-A as a possible negative regulator of CD8 T cell antitumor function in a broad range of patients with cancer, including those receiving existing ICB therapies, suggesting MAO-A as a potential drug target for developing new forms of ICB therapy and combination therapy. Together, these preclinical animal studies and clinical data correlation studies suggest that MAO-A is a promising new drug target of T cell–based cancer immunotherapy and that repurposing of established MAOI antidepressants is a promising path to develop MAO-A blockade immunotherapy.

DISCUSSION

On the basis of our findings, we propose an "intratumoral MAO-A–serotonin axis" model to elucidate the role of MAO-A in regulating CD8 T cell antitumor immunity (fig. S14). Analogous to the well-characterized MAO-A–serotonin axis in the brain, where MAO-A controls the availability of serotonin in a neuron-neuron synapse, thereby regulating neuronal activity, the "MAO-A–serotonin axis" in a tumor controls the availability of serotonin in a tumor cell–T cell immune synapse, thereby regulating antitumor T cell reactivity (fig. S14). The resemblance is notable, considering that both the nervous system and the immune system are evolved to defend a living organism by sensing and reacting to environmental danger, externally and internally, including tissue traumas, infections, and malignancies (*32*). Despite their distinct anatomic structures, the nervous system has a fixed organization, whereas the immune system comprises mobile and disperse cells; from an evolutionary point of view, it makes sense that some critical molecular regulatory pathways are preserved for both defense systems. Neurons and immune cells share a broad collection of signal transducers, surface receptors, and secretory molecules (*32*). In particular, many neurotransmitters and neuropeptides traditionally considered specific for neurons are expressed in immune cells, although their functions in the immune system are, to a large extent, still unknown (*33*). Studying this group of molecules and their regulatory circuits in tumor immunology thus may provide new opportunities for generating knowledge and identifying new drug targets for developing next-generation cancer immunotherapies; our current finding of this MAO-A–serotonin axis regulation of CD8 T cell antitumor immunity can be such an example.

Our study showed that *Maoa* expression was induced by antigen-TCR stimulation in CD8 T cells and, in turn, restrained T cell activation (Fig. 3). This negative-feedback loop qualifies MAO-A as an immune checkpoint and adds it to the expanding immune checkpoint family comprising PD-1/PD-L1, CTLA-4, Tim-3, LAG-3, T cell immunoreceptor with Ig and ITIM domains (TIGIT), V-domain Ig suppressor of T cell activation (VISTA), and others (*4*). However, MAO-A is unique in this group because it is already a well-established drug target due to its known function in the brain (*23*). Small-molecule MAOIs have been developed to block MAO-A activity, thereby regulating serotonin signaling in the brain, and were the first drugs approved for treating depression (*23*). In our study, we tested multiple clinically approved MAOIs (phenelzine, moclobemide, and clorgyline) and demonstrated their T cell–enhancing and tumor suppression effects in preclinical animal models, pointing to the possibility of repurposing these drugs for cancer immunotherapy (Fig. 5 and fig. S9). Developing new cancer drugs is extremely costly and time consuming; drug repurposing offers an economic and speedy pathway to additional cancer therapies, because approved drugs have known safety profiles and modes of actions and thus can enter the clinic quickly (*34*). MAOIs were introduced in the 1950s and were used extensively over the subsequent two decades, but since then, their use has dwindled because of reported side effects and the introduction of other classes of antidepressant agents (*23*). However, these MAOI side effects were vastly overstated and should be revisited (*23*). For instance, a claimed major side effect of MAOIs is their risk of triggering tyramine-induced hypertensive crisis when patients eat tyramine-rich foods such as aged cheese (hence, "the cheese effects"); this concern led to cumbersome food restrictions that are now considered largely unnecessary (*23*). A transdermal delivery system for selegiline (Emsam) has also been developed that can largely avoid potential food restrictions (*23*). Therefore, interest in MAOIs as a major class of antidepressants is reviving (*23*), and repurposing MAOIs for cancer immunotherapy can be an attractive new application of these potent drugs.

Depression and anxiety are common in patients with cancer: Prevalent rates of major depression among patients with cancer are four times higher than the general population, and up to a quarter of patients with cancer have clinically significant depression and anxiety symptoms (*35*). Repurposing MAOIs for cancer immunotherapy thus may provide patients with cancer with dual antidepressant and antitumor benefits. A large majority of antidepressants, including MAOIs, selective serotonin reuptake inhibitors (SSRIs), serotonin modulators and stimulators (SMSs), serotonin antagonists and reuptake inhibitors (SARIs), and serotonin-norepinephrine reuptake inhibitors (SNRIs), all work through regulating serotonin signaling in the brain via inhibiting the various key molecules that control serotonin degradation, reuptake, and detection (*36*). Our study revealed the existence of a MAO-A–serotonin axis in tumors that regulates CD8 T cell antitumor immunity (fig. S14). It is plausible to postulate that the other key serotonin regulatory molecules that function in the brain may also function in the tumor regulating T cell antitumor immunity (*36*). A recent nationwide cohort study in Israel reported that adherence to antidepressant medications is associated with reduced premature mortality in patients with cancer (*35*). Another clinical study reported lymphocyte subset changes associated with antidepressant treatments in patients with a major depression disorder (*37*). Studying patients with cancer for possible correlations between antidepressant treatments, antitumor immune responses, and clinical outcomes therefore might yield valuable knowledge informing the immune regulatory function of antidepressants and instructing the potential repurposing of select antidepressant drugs for cancer immunotherapy.

In our study, we found that *Maoa* gene was highly expressed in tumor-infiltrating CD8 T cells, with the most "exhausted" cells (PD-1^{hi}Tim-3^{hi}LAG-3^{hi}) expressing the highest levels of *Maoa*, suggesting that these cells may benefit the most from the MAOI treatment (*18*, *19*). We also found that MAO-A regulated CD8 T cell antitumor immunity, at least partly, through modulating the serotonin-MAPK pathway, which is nonredundant to other major immune checkpoint regulatory pathways, suggesting that MAOI treatment can be a valuable component for combination therapy (*4*). MAOI treatment synergized with anti–PD-1 treatment in suppressing syngeneic mouse tumor growth, and *MAOA* expression levels dictated patient survival in patients with melanoma receiving anti–PD-1 therapy (Figs. 5 and 6). Patients undergoing cancer treatment,

including traditional chemo/radio therapies and the new immunotherapies such as ICB therapies, often report incurred or exacerbated depression symptoms; these central nervous system (CNS) side effects are considered to be associated with treatment-induced immune reaction and inflammation (*38*–*40*). Adding MAOIs with antidepressant function to a combination cancer therapy thus may both improve antitumor efficacy and alleviate CNS side effects. Some earlier studies reported that MAOIs can directly suppress the growth of androgen-sensitive and castration-resistant prostate cancer cells, presumably through regulating cancer cell autophagy and apoptosis, suggesting additional mechanisms that MAOIs may deploy to target certain cancers (*41*, *42*).

In summary, here, we identified MAO-A as an immune checkpoint and demonstrated the potential of repurposing established MAOI antidepressants for cancer immunotherapy. The notion that *MAOA*, "the warrior gene," not only acts in the brain to regulate the aggressiveness of human behavior but also acts in a tumor to control the aggressiveness of antitumor immunity is interesting. Future clinical studies are encouraged to investigate the clinical correlations between MAOI treatment and clinical outcomes in patients with cancer and to explore the possibility of repurposing MAOIs for combination cancer immunotherapy. Meanwhile, the immune regulatory function of MAO-A certainly goes beyond regulating CD8 T cells. We have detected MAO-A expression in other immune cells (e.g., dendritic cells, macrophages, and regulatory T cells); and in *Maoa*-KO mice, we have observed the hyperresponsiveness of multiple immune cells in various mouse tumor models. It is also likely that MAO-A regulates immune reactions to multiple diseases beyond cancer, such as infections and autoimmune diseases. Studying the roles of MAO-A in regulating various immune cells under different health and disease conditions will be interesting topics for future research.

MATERIALS AND METHODS

Study design

To search for new drug targets regulating antitumor immunity, we isolated TIIs from B16-OVA melanoma tumors and evaluated TII gene expression profiles; we detected a significant change in *Maoa* gene expression. To study MAO-A as an autologous factor regulating antitumor CD8 T cell immunity, we conducted a series of in vivo tumor experiments involving multiple syngeneic mouse tumor models (i.e., B16-OVA melanoma and MC38 colon cancer models), *Maoa*-KO mice, as well as BM and T cell adoptive transfer approaches. Tumor growth was monitored, and the tumor-infiltrating CD8 T cells were analyzed using flow cytometry and scRNA-seq. To investigate the MAO-A regulation of CD8 T cell activation through modulating T cell autocrine serotonin, we stimulated *Maoa*-KO and *Maoa*-WT CD8 T cells in vitro and compared their T cell activation, TCR signaling, and serotonin secretion and signaling using flow cytometry, enzyme-linked immunosorbent assay (ELISA), qPCR, and Western blot; serotonin modulation was also validated in vivo in the B16-OVA melanoma model using high-performance liquid chromatography (HPLC). To evaluate the potential of repurposing MAOI antidepressants for cancer immunotherapy, we studied the T cell regulatory and antitumor effects of MAOI treatment in vitro in T cell culture and in vivo in B16-OVA and MC38 tumor models alone or in combination with anti–PD-1 treatment. To explore the translational potential of MAO-A blockade therapy, we examined the *MAOA* gene expression in primary human CD8 T cells and studied the therapeutic effects of MAOI treatment in a human T cell adoptive transfer and human melanoma xenograft NSG mouse model. Last, we conducted clinical data correlation studies and investigated the correlation of intratumoral *MAOA* gene expression with CD8 T cell antitumor activities and clinical outcomes in multiple cancer patient cohorts spanning melanoma, colon cancer, lung cancer, cervical cancer, and pancreatic cancer.

Mice

C57BL/6J (B6), B6.SJL-*Ptprc*^{a}*Pepc*^{b}/BoyJ (CD45.1), 129S-*Maoa*^{tm1Shih}/J (*Maoa*-KO) (*15*), C57BL/6-Tg (TcraTcrb)1100Mjb/J (*OT1*-Tg), and NOD.Cg-*Prkdc*^{scid} *Il2rg*^{tm1Wjl}/SzJ (Nod scid gamma or NSG) mice were purchased from the Jackson Laboratory (JAX; Bar Harbor). The *OT1*-Tg mice deficient of *Maoa* (*OT1*-Tg/*Maoa*-KO) were generated at the University of California, Los Angeles (UCLA) through breeding *OT1*-Tg mice with *Maoa*-KO mice. All animals were maintained in the animal facilities at UCLA. Eight- to 12-week-old females were used for all experiments unless otherwise indicated. All animal experiments were approved by the Institutional Animal Care and Use Committee of UCLA.

Cell lines

The B16-OVA mouse melanoma cell line and the PG13 retroviral packaging cell line were provided by P. Wang (University of Southern California, CA, USA) (*43*). The MC38 mouse colon adenocarcinoma cell line was provided by M. Bosenberg (Yale University, CT, USA) (*44*). The human embryonic kidney 293T and Phoenix-ECO retroviral packaging cell lines were purchased from the American Type Culture Collection (ATCC). The A375-A2-ESO-FG human melanoma cell line was previously reported (*24*, *25*). The Phoenix-ECO-MIG, Phoenix-ECO-MIG-*Maoa*, and PG13-ESO-TCR stable virus producing cell lines were generated in this study.

Viral vectors

The MIG retroviral vector was reported previously (*45*). MIG-*Maoa* and Retro/ESO-TCR retroviral vectors were generated in this study.

Media and reagents

Adherent cell culture medium (denoted as D10 medium) was made of Dulbecco's modified Eagle's medium (DMEM; catalog no. 10013, Corning) supplemented with 10% fetal bovine serum (FBS; catalog no. F2442, Sigma-Aldrich) and 1% penicillin-streptomycin-glutamine (catalog no. 10378016, Gibco). T cell culture medium (denoted as C10 medium) was made of RPMI 1640 (catalog no. 10040, Corning) supplemented with 10% FBS (catalog no. F2442, Sigma-Aldrich), 1% penicillin-streptomycin-glutamine (catalog no. 10378016, Gibco), 0.2% Normocin (catalog no. ant-nr-2, InvivoGen), 1% Minimal Essential Medium (MEM) Non-essential Amino Acid Solution (catalog no. 11140050, Gibco), 1% HEPES (catalog no. 15630080, Gibco), 1% sodium pyruvate (catalog no. 11360070, Gibco), and 0.05 mM β-mercaptoethanol (catalog no. M3148, Sigma-Aldrich).

Cell culture reagents—including purified no azide/low endotoxin (NA/LE) anti-mouse CD3ε (catalog no. 553057, clone 145-2C11), purified NA/LE anti-mouse CD28 (catalog no. 553294, clone 37.51), anti-human CD3 (catalog no. 56685, clone OKT3), and anti-human CD28 (catalog no. 555725, clone CD28.2)—were purchased form BD Biosciences. Recombinant human IL-2 (catalog no. 200-02) was purchased from PeproTech.

In vivo depletion antibodies, including anti-mouse CD8α (catalog no. BE0061, clone RMP2.43) and its isotype control [rat immunoglobulin G2b (IgG2b), catalog no. BE0090], were purchased from BioXCell. In vivo PD-1–blocking antibody (catalog no. BE0146, clone RMP1-14) and its isotype control (rat IgG2a, catalog no. BE0089) were purchased from BioXCell.

MAOIs—including phenelzine (catalog no. P6777), moclobemide (catalog no. M3071), and clorgyline (catalog no. M3778)—were purchased from Sigma-Aldrich. Serotonin (catalog no. H9532) and serotonin receptor (5-HTR) antagonist asenapine (catalog no. A7861) were also purchased from Sigma-Aldrich.

Syngeneic mouse tumor models

B16-OVA melanoma cells (1×10^6 per animal) or MC38 colon cancer cells (3×10^5 per animal) were subcutaneously injected into experimental mice to form solid tumors. In some experiments, mice received intraperitoneal injection of MAOIs [i.e., phenelzine (30 mg/kg per day), moclobemide (50 mg/kg per day), or clorgyline (50 mg/kg per day)] to block MAO-A activity. In some experiments, mice received intraperitoneal injection of anti-mouse CD8α antibodies (200 μg per animal, twice per week) to deplete CD8 T cells; mice that received intraperitoneal injection of isotype antibodies were included as controls. In some experiments, mice received intraperitoneal injection of anti-mouse PD-1 antibodies (300 μg per animal, twice per week) to block PD-1; mice that received intraperitoneal injection of isotype antibodies were included as controls.

During an experiment, tumor growth was monitored twice per week by measuring tumor size using a Fisherbrand Traceable digital caliper (Thermo Fisher Scientific); tumor volumes were calculated by formula $1/2 \times L \times W^2$. At the end of an experiment, TIIs were isolated for analysis using qPCR, flow cytometry, and/or scRNA-seq. In some experiments, sera were also collected for serotonin measurement.

Two-way BM transfer B16-OVA tumor model

BM cells were collected from femurs and tibias of donor mice and were transferred into the recipient mice through retro-orbital (r.o.) injection. Recipient mice were preconditioned with whole-body irradiation (1200 gray). For BM transfer experiments confining MAO-A deficiency comparison to immune cells, *Maoa*-WT or *Maoa*-KO BM cells were transferred into CD45.1 recipient mice (8 to 10×10^6 cells per recipient mouse). For BM transfer experiments confining MAO-A deficiency comparison to nonimmune cells, WT CD45.1 BM cells were transferred into *Maoa*-WT or *Maoa*-KO recipient mice (8 to 10×10^6 cells per recipient mouse). After BM transfer, recipient mice were maintained on antibiotic water (Amoxil; 0.25 mg/ml) for 4 weeks. Periodic bleedings were performed to monitor immune cell reconstitution using flow cytometry. At 8 to 12 weeks after BM transfer, recipient mice were fully immune-reconstituted and were used for tumor challenge experiments. B16-OVA mouse melanoma cells were subcutaneously injected into experimental mice to form solid tumors (1×10^6 cells per animal). Tumor growth was monitored twice per week by measuring tumor size using a Fisherbrand Traceable digital caliper; tumor volumes were calculated by formula $1/2 \times L \times W^2$.

Adoptive OT1 T cell transfer B16-OVA tumor model

Spleen and lymph node cells were harvested from the *OT1*-Tg or *OT1*-Tg/*Maoa*-KO mice and were subjected to magnetic-activated cell sorting (MACS) using the Mouse CD8 T Cell Isolation Kit (catalog no. 120117044, Miltenyi Biotec) following the manufacturer's instructions. The purified OT1 T cells (identified as $CD8^+TCR\ V\beta5^+$ cells) were adoptively transferred to tumor-bearing CD45.1 wild-type mice (1×10^5 cells per recipient mouse). CD45.1 mice were subcutaneously inoculated with B16-OVA tumor cells 1 week in advance (1×10^6 cells per animal). Before OT1 T cell adoptive transfer, recipient mice were preconditioned with whole-body irradiation (600 gray). During an experiment, tumor growth was monitored twice per week by measuring tumor size using a Fisherbrand Traceable digital caliper; tumor volumes were calculated by formula $1/2 \times L \times W^2$. Mice were terminated at the indicated time points, and TIIs were isolated for flow cytometry analysis of surface marker expression and intracellular effector molecule production.

Xenograft human tumor model

The A375-A2-ESO-FG human melanoma cells (10×10^6 cells per animal) were subcutaneously injected into NSG mice to form solid tumors. In some experiments, mice received phenelzine treatment through intraperitoneal injection (30 mg/kg per day). In some experiments, mice received adoptive transfer of ESO-T cells through retro-orbital injection (4×10^6 cells per recipient mouse). Before ESO-T cell adoptive transfer, recipient mice were preconditioned with total body irradiation (100 gray). During an experiment, tumor growth was monitored twice per week by measuring tumor size using a Fisherbrand Traceable digital caliper; tumor volumes were calculated by formula $1/2 \times L \times W^2$.

TII isolation and analysis

Solid tumors were harvested from experimental mice and mechanically disrupted through 70-μm nylon mesh strainers to release single cells (catalog no. 07-201-431, Corning). Single cells were washed once with C10 medium, resuspended in 50% Percoll (catalog no. P4937, Sigma-Aldrich), and centrifuged at 800*g* at 25°C for 30 min with brake off. Cell pellets enriched with TIIs were then collected and resuspended in C10 medium for further analysis.

In the experiments studying the *Maoa* gene expression in TIIs, day 14 B16-OVA tumors were harvested from B6 wild-type mice to prepare TII suspensions. TII suspensions were then sorted using a FACSAria II flow cytometer (BD Biosciences) to purify immune cells (gated as $DAPI^-CD45.2^+$ cells), which were then subjected to qPCR analysis of *Maoa* mRNA expression.

In the experiments studying the *Maoa* gene expression in tumor-infiltrating CD8 T cell subsets, day 14 B16-OVA tumors were harvested from B6 wild-type mice to prepare TII suspensions. Tumor-infiltrating CD8 T cells (pregated as $CD45.2^+TCR\beta^+CD8^+$ cells) were sorted into three subsets (gated as $PD\text{-}1^{lo}$, $PD\text{-}1^{hi}Tim\text{-}3^{lo}LAG\text{-}3^{lo}$, and $PD\text{-}1^{hi}Tim\text{-}3^{hi}LAG\text{-}3^{hi}$ cells) using a FACSAria II flow cytometer and then were subjected to qPCR analysis of *Maoa* mRNA expression.

In the experiments studying gene expression profiling of TIIs, day 14 B16-OVA tumors were harvested from *Maoa*-WT and *Maoa*-KO mice to prepare TII suspensions. TII suspensions were then sorted using a FACSAria II flow cytometer to purify immune cells (gated as $DAPI^-CD45.2^+$ cells), which were then subjected to scRNA-seq analysis.

In other experiments, TII suspensions prepared under indicated experimental conditions were directly analyzed by flow cytometry to study surface marker expression and intracellular effector molecule production of CD8 T cells (pregated as $CD45.2^+TCR\beta^+CD8^+$ cells).

In vitro mouse CD8 T cell culture

Spleen and lymph node cells were harvested from *Maoa*-KO or *Maoa*-WT (B6 wild-type) mice and subjected to MACS using the Mouse CD8 T Cell Isolation Kit (catalog no. 120117044, Miltenyi Biotec) following the manufacturer's instructions. Purified mouse CD8 T cells were cultured in vitro in C10 medium, in a 24-well plate at 0.5×10^6 cells/ml medium per well, in the presence of plate-bound anti-mouse CD3ε (5 μg/ml) for up to 4 days. At indicated time points, cells were collected for flow cytometry analysis of surface marker expression and intracellular effector molecule production and for qPCR analysis of mRNA expression; cell culture supernatants were collected for ELISA analysis of effector cytokine production.

In experiments studying serotonin signaling, cells were cultured in C10 medium made of serotonin-depleted FBS that was pretreated overnight with charcoal-dextran (1 g per 50 ml of FBS; catalog no. C6241, Sigma-Aldrich). L-Ascorbic acid (100 μM; catalog no. A4403, Sigma-Aldrich) was added to C10 medium to stabilize T cell–produced or –supplemented serotonin. In some experiments, cells were treated with MAOIs to block MAO-A activity; MAOIs studied were phenelzine (10 μM), moclobemide (200 μM), or clorgyline (20 μM). In some experiments, cells were supplemented with exogenous serotonin (10 μM) to stimulate serotonin signaling. In some experiments, cells were treated with serotonin receptor antagonist asenapine (10 μM) to block serotonin receptor signaling.

In vitro human CD8 T cell culture

Healthy donor human peripheral blood mononuclear cells (PBMCs) were purchased from the UCLA Center for AIDS Research (CFAR) Virology Core Laboratory. PBMCs were cultured in C10 medium in the presence of plate-bound anti-human CD3 (1 μg/ml) and soluble anti-human CD28 (1 μg/ml). After 5 days, activated CD8 T cells were sorted out on the basis of surface markers ($CD45^+TCR\alpha\beta^+CD8^+$) using a FACSAria II flow cytometer (BD Biosciences). Naïve CD8 T cells were sorted from the same donors based on surface markers ($CD45^+TCR\alpha\beta^+CD8^+CD62L^{hi}CD45RO^{low}$) and were included as controls. The purified naïve and effector human CD8 T cells were then analyzed for *MAOA* mRNA expression using qPCR.

In vitro OT1 T cell culture

Spleen and lymph node cells were harvested from the *OT1*-Tg or *OT1*-Tg/*Maoa*-KO mice and then subjected to MACS sorting using the Mouse CD8 T Cell Isolation Kit (catalog no. 120117044, Miltenyi Biotec) following the manufacturer's instructions. The purified OT1 T cells (identified as $CD8^+TCR\ V\beta5^+$ cells) were cultured in C10 medium, in a 24-well plate at 0.5×10^6 cells per ml medium per well, in the presence of plate-bound anti-mouse CD3ε (5 μg/ml) for up to 4 days. At the indicated time points, cells were collected for flow cytometry analysis of surface marker expression; cell culture supernatants were collected for ELISA analysis of effector cytokine production.

MIG-Maoa retroviral vector and mouse CD8 T cell transduction

The MIG-*Maoa* retroviral vector was constructed by inserting a codon-optimized *Maoa* complementary DNA (cDNA) [synthesized by Integrated DNA Technologies (IDT)] into the parental MIG retroviral vector (*45*). The vesicular stomatitis virus glycoprotein (VSVG)–pseudotyped MIG and MIG-*Maoa* retroviruses were produced using 293T virus–packaging cells following a standard calcium precipitation method (*46*, *47*) and then were used to transduce Phoenix-ECO cells to generate stable cell lines producing ECO-pseudotyped MIG or MIG-*Maoa* retroviruses (denoted as Phoenix-ECO-MIG and Phoenix-ECO-MIG-*Maoa* cell lines, respectively). For virus production, Phoenix-ECO-MIG and Phoenix-ECO-MIG-*Maoa* cells were seeded at a density of 0.8×10^6 cells/ml in D10 medium and cultured in a 15-cm dish (30 ml per dish) for 2 days; virus supernatants were then harvested and freshly used for spin infection.

MACS-purified CD8 T cells isolated from the *Maoa*-KO mice were cultured in vitro and stimulated with plate-bound anti-mouse CD3ε (5 μg/ml) for 4 days. On days 2 and 3, cells were spin-infected with ECO-pseudotyped MIG or MIG-*Maoa* retroviral supernatants supplemented with polybrene (10 μg/ml; catalog no. TR-1003-G, Millipore) at 1321*g* at 30°C for 90 min. On day 4, cells were collected for flow cytometry analysis of transduction efficiency and for qPCR analysis of effector gene expression.

Retro/ESO-TCR retroviral vector and human CD8 T cell transduction

The Retro/ESO-TCR vector was constructed by inserting into the parental pMSGV vector a synthetic gene encoding an HLA-A2–restricted, NY-ESO-1 tumor antigen-specific human CD8 TCR (clone 3A1) (*24*). VSVG-pseudotyped Retro/ESO-TCR retroviruses were generated by transfecting 293T cells following a standard calcium precipitation protocol and an ultracentrifugation concentration protocol (*48*); the viruses were then used to transduce PG13 cells to generate a stable retroviral packaging cell line producing gibbon ape leukemia virus (GaLV) glycoprotein-pseudotyped Retro/ESO-TCR retroviruses (denoted as PG13-ESO-TCR cell line). For virus production, the PG13-ESO-TCR cells were seeded at a density of 0.8×10^6 cells/ml in D10 medium and cultured in a 15-cm dish (30 ml per dish) for 2 days; virus supernatants were then harvested and stored at −80°C for future use.

Healthy donor PBMCs were stimulated with plate-bound anti-human CD3 (1 μg/ml) and soluble anti-human CD28 (1 μg/ml) in the presence of recombinant human IL-2 (300 U/ml). On day 2, cells were spin-infected with frozen-thawed Retro/ESO-TCR retroviral supernatants supplemented with polybrene (10 μg/ml) at 660*g* at 30°C for 90 min after an established protocol (*25*). Transduced human CD8 T cells (denoted as ESO-T cells) were expanded for another 7 to 10 days and then cryopreserved for future use. Mock-transduced human CD8 T cells (denoted as Mock-T cells) were generated as controls.

In vitro A375-A2-ESO-FG human melanoma cell-killing assay

The A375-A2-ESO-FG human melanoma cells (5 to 10×10^3 cells per well) were cocultured with either ESO-T cells or Mock-T cells at indicated ratios in C10 medium in a Corning 96-well clear bottom black plate (catalog no. 3603, Corning). At 24 hours, live tumor cells were quantified by adding D-luciferin (150 μg/ml; part no. 119222, Caliper Life Science) to cell cultures and reading out luciferase activities using an Infinite M1000 microplate reader (Tecan) according to the manufacturer's instructions.

Flow cytometry (FACS)

Flow cytometry, also known as fluorescence-activated cell sorting (FACS), was used to analyze surface marker and intracellular effector molecule expression of T cells. Fluorochrome-conjugated monoclonal antibodies specific for mouse CD45.2 (clone 104), TCRβ

(clone H57-597), CD4 (clone RM4-5), CD8 (clone 53-6.7), CD69 (clone H1.2F3), CD25 (clone PC61), CD44 (clone IM7), CD62L (clone MEL-14), and IFN-γ (clone XMG1.2) were purchased from BioLegend. Monoclonal antibodies specific for mouse tumor necrosis factor–α (TNF-α; clone JES6-5H4) and Fc block (anti-mouse CD16/32) (clone 2.4G2) were purchased from BD Biosciences. Monoclonal antibodies specific for mouse PD-1 (clone RMP1-30) was purchased from Thermo Fisher Scientific. Fluorochrome-conjugated monoclonal antibodies specific for human CD45 (clone H130), TCRαβ (clone I26), CD4 (clone OKT4), CD8 (clone SK1), CD45RO (clone UCHL1), CD62L (clone DREG-56), and human Fc receptor–blocking solution (TruStain FcX, catalog no. 422302) were purchased from BioLegend. Fixable Viability Dye eFluor 506 (catalog no. 65-0866) was purchased from Thermo Fisher Scientific. OVA dextramer (catalog no. JD2163) was purchased from Immudex.

To study T cell surface marker expression, cells were stained with Fixable Viability Dye first, followed by Fc blocking and surface marker staining, according to a standard procedure as described previously (*47*). To study T cell intracellular cytokine production, CD8 T cells or primary TIIs were stimulated with phorbol-12-myristate-13-acetate (PMA) (50 ng/ml; catalog no. 80055-400, VWR) and ionomycin (500 ng/ml; catalog no. 80056-892, VWR) in the presence of GolgiStop (4 μl per 6-ml culture; catalog no. 554724, BD Biosciences) for 4 hours. At the end of the culture, cells were collected, and intracellular cytokine (i.e., IFN-γ and TNF-α) staining was performed using the Fixation/Permeabilization Solution Kit (catalog no. 554714, BD Biosciences) and following the manufacturer's instructions. To study T cell intracellular cytotoxicity molecule production, CD8 T cells or primary TIIs were collected and then directly subjected to intracellular Granzyme B staining using the Fixation/Permeabilization Solution Kit (BD Biosciences). These cells were costained with surface markers to identify CD8 T cells (gated as $TCR\beta^+CD8^+$ cells in vitro or $CD45.2^+TCR\beta^+CD8^+$ cells in vivo) or OT1 cells (gated as $CD45.2^+CD8^+$ cells in vivo). Stained cells were analyzed by using a MACSQuant Analyzer 10 flow cytometer (Miltenyi Biotec). A FlowJo software (Tree Star) was used to analyze the data.

Enzyme-linked immunosorbent assay (ELISA)

To study T cell cytokine production, MACS-purified mouse CD8 T cells were cultured in C10 medium under indicated experimental conditions for up to 4 days. At indicated time points, cell culture supernatants were collected for cytokine ELISA analysis following a standard protocol from the BD Biosciences. The coating and biotinylated antibodies for the detection of mouse IFN-γ (coating antibody, catalog no. 554424; biotinylated detection antibody, catalog no. 554426) and IL-2 (coating antibody, catalog no. 551216; biotinylated detection antibody, catalog no. 554410) were purchased from BD Biosciences. The streptavidin–horseradish peroxidase (HRP) conjugate (catalog no. 18410051) was purchased from Invitrogen. Mouse IFN-γ (catalog no. 575309) and IL-2 (catalog no. 575409) standards were purchased from BioLegend. The 3,3′,5,5′-tetramethylbenzidine (TMB; catalog no. 51200048) substrate was purchased from Kirkegaard & Perry Laboratories (KPL). The absorbance at 450 nm was measured using an Infinite M1000 microplate reader (Tecan).

To study T cell serotonin production, MACS-purified mouse CD8 T cells were cultured in C10 medium made of serotonin-depleted FBS and supplemented with L-ascorbic acid, in the presence of plate-bound anti-mouse CD3ε (5 μg/ml) for up to 4 days. At indicated time points, cell culture supernatants were collected for serotonin ELISA analysis using a commercial kit following the manufacturer's instructions (SEU39-K01, Eagle Biosciences). The absorbance at 450 nm was measured using an Infinite M1000 microplate reader (Tecan).

Western blots

CD8 T cells purified from *Maoa*-WT and *Maoa*-KO mice were cultured in vitro in a 24-well plate at 0.5×10^6 cells per well for 2 days, in the presence of plate-bound anti-mouse CD3ε (5 μg/ml), with or without asenapine treatment (10 μM). Cells were then rested on ice for 2 hours and restimulated with plate-bound anti-mouse CD3ε (5 μg/ml) for 20 min. Total protein was extracted using a lysis buffer containing 20 mM HEPES (pH 7.6), 150 mM NaCl, 1 mM EDTA, 1% TritonX-100, and protease/phosphatase inhibitor cocktail (catalog no. 5872S, Cell Signaling Technology). Nuclear protein was extracted using the Nuclear Protein Extraction Kit (catalog no. P178833, Thermo Fisher Scientific). Protein concentration was measured using the Bicinchoninic Acid (BCA) Assay Kit (catalog nos. 23228 and 1859078, Thermo Fisher Scientific). Equal amounts of protein were resolved on a 10% SDS–polyacrylamide gel electrophoresis gel and then transferred to a polyvinylidene difluoride (PVDF) membrane by electrophoresis. MAO-A antibody was purchased from Abcam (catalog no. ab126751, clone EPR7101). The following antibodies were purchased from the Cell Signaling Technology and used to blot for the proteins of interest: anti-mouse NF-κB p65 (catalog no. 8242P, clone D14E12), anti-mouse c-Jun (catalog no. 9165S, clone 60A8), anti-mouse NFAT (catalog no. 4389S), anti-mouse ERK1/2 (catalog no. 9107S, clone 3A7), anti-mouse p-ERK1/2 (catalog no. 4370S, clone D13.14.4E), secondary anti-mouse (catalog no. 7076P2), and secondary anti-rabbit (catalog no. 7074P2). β-Actin (catalog no. sc-69879, clone AC-15, Santa Cruz Biotechnology) was used as an internal control for total protein extracts, whereas Lamin A/C (catalog no. 39287, clone 3A6-4C11, Active Motif) was used as an internal control for nuclear protein extracts. Signals were visualized with autoradiography using an enhanced chemiluminesence (ECL) system (catalog no. RPN2232, Thermo Fisher Scientific). The data were analyzed using an Image Lab software (Bio-Rad).

High-performance liquid chromatography (HPLC)

HPLC was used to measure intratumoral and serum serotonin levels as previously described (*49*, *50*). Briefly, tumors and sera were collected from experimental mice at indicated time points and were snap-frozen using liquid nitrogen. Frozen samples were thawed and homogenized using methanol and acetonitrile by vortexing. Homogenized samples were centrifuged, and supernatants were collected to new tubes and evaporated under a stream of argon. Dried sample pellets were then reconstituted in HPLC running buffer and were ready for analysis. Serotonin concentration was quantified using a C18 column by reverse-phase HPLC (System Gold 166P detector, Beckman Coulter). For tumor samples, both intracellular and interstitial serotonin were analyzed.

mRNA quantitative RT-PCR (mRNA qPCR)

Total RNA was isolated using TRIzol reagent (catalog no. 15596018, Invitrogen, Thermo Fisher Scientific) according to the manufacturer's instructions. cDNA was prepared using the SuperScript III First-Strand Synthesis SuperMix Kit (catalog no. 18080400, Invitrogen,

Thermo Fisher Scientific). Gene expression was measured using the KAPA SYBR FAST qPCR Kit (catalog no. KM4117, Kapa Biosystems) and the 7500 Real-time PCR System (Applied Biosystems) according to the manufacturer's instructions. *Ube2d2* was used as an internal control for mouse immune cells, and *ACTIN* was used as an internal control for human immune cells. The relative expression of the mRNA of interest was calculated using the $2^{\Delta\Delta CT}$ method. Primer sequences are available in table S1.

Single-cell RNA sequencing (scRNA-seq)

scRNA-seq was used to analyze the gene expression profiling of TIIs. Day 14 B16-OVA tumors were harvested from *Maoa*-WT and *Maoa*-KO mice to prepare TII suspensions (10 tumors were combined for each group). TII suspensions were then sorted using a FACSAria II flow cytometer to purify immune cells (gated as $DAPI^{-}CD45.2^{+}$ cells). Sorted TIIs were immediately delivered to the Technology Center for Genomics & Bioinformatics (TCGB) facility at UCLA for library construction and sequencing. Briefly, purified TIIs were quantified using a Cell Countess II automated cell counter (Invitrogen/Thermo Fisher Scientific). A total of 10,000 TIIs from each experimental group were loaded on the Chromium platform (10x Genomics), and libraries were constructed using the Chromium Single Cell 3′ Library & Gel Bead Kit v2 (catalog no. PN-120237, 10x Genomics) according to the manufacturer's instructions. Libraries were sequenced on an Illumina NovaSeq using the NovaSeq 6000 S2 Reagent Kit (100 cycles; 20012862, Illumina). Data analysis was performed using a Cell Ranger Software Suite (10x Genomics). Binary base call (BCL) files were extracted from the sequencer and used as inputs for the Cell Ranger pipeline to generate the digital expression matrix for each sample. Then, cellranger aggr command was used to aggregate the two samples into one digital expression matrix. The matrix was analyzed using Seurat, an R package designed for scRNA-seq. Specifically, cells were first filtered to have at least 300 unique molecular identifiers (UMIs), at least 100 genes, and at most 50% mitochondrial gene expression; only one cell did not pass the filter. The filtered matrix was normalized using the Seurat function NormalizeData. Variable genes were found using the Seurat function FindVariableGenes. The matrix was scaled to regress out the sequencing depth for each cell. Variable genes that had been previously identified were used in principal components analysis (PCA) to reduce the dimensions of the data. After this, 13 principal components (PCs) were used in Uniform Manifold Approximation and Projection (UMAP) to further reduce the dimensions to two. The same 13 PCs were also used to group the cells into different clusters by the Seurat function FindClusters. Next, marker genes were found for each cluster and used to define the cell types. Subsequently, three clusters of antigen-experienced tumor-infiltrating CD8 T cells (identified by coexpression of *Cd8a*, *Cd3d*, and *Cd44* marker genes) were extracted and compared between the *Maoa*-WT and *Maoa*-KO samples.

For GSEA, signal-to-noise ratio was used to rank the genes in correlation with indicated gene signatures. For each cluster, the average expression of each gene in this cluster and in all other clusters was calculated. Fold changes were calculated by comparing the average expressions. The genes were then ranked by fold changes from high to low. To compare our data to preannotated datasets, we used the CD8 T cell subtype marker genes published by Miller *et al.* (*16*). GSEA was performed on these marker genes against the ranked genes in our dataset.

Tumor Immune Dysfunction and Exclusion (TIDE) computational method

TIDE analysis was performed as previously described (*26*, *51*) (http://tide.dfci.harvard.edu/query/). Briefly, this method was used to study the association between the tumor-infiltrating CD8 T cell [also known as cytotoxic T lymphocyte (CTL)] level and overall patient survival in relation to the intratumoral *MAOA* gene expression level. For each patient cohort, tumor samples were divided into *MAOA*-high (samples with *MAOA* expression one standard derivation above the average) and *MAOA*-low (remaining samples) groups, followed by analyzing the association between the CTL levels and survival outcomes in each group. The CTL level was estimated as the average expression level of *CD8A*, *CD8B*, *GZMA*, *GZMB*, and *PRF1*. Each survival plot presented tumors in two subgroups: "CTL-high" group had above-average CTL values among all samples, whereas "CTL-low" group had below-average CTL values. A T cell dysfunction score (*z* score) was calculated for each patient cohort, correlating the *MAOA* expression level with the beneficial effect of CTL infiltration on patient survival. A positive *z* score indicates that the expression of *MAOA* is negatively correlated with the beneficial effect of tumor-infiltrating CTL on patient survival. The *P* value indicates the comparison between the *MAOA*-low and *MAOA*-high groups and was calculated by two-sided Wald test in a Cox proportional hazards (Cox-PH) regression.

Statistics

A GraphPad Prism 7 software (GraphPad Software) was used for the graphic representation and statistical analysis of the data. Pairwise comparisons were made using a two-tailed Student's *t* test. Multiple comparisons were performed using an ordinary one-way analysis of variance (ANOVA) followed by Tukey's multiple comparisons test or a two-way repeated measures ANOVA followed by Sidak multiple comparisons test. Data are presented as the means ± SEM, unless otherwise indicated. A *P* value of less than 0.05 was considered significant. ns, not significant; $*P < 0.05$, $**P < 0.01$, and $***P < 0.001$. The *P* values of violin plots were determined by Wilcoxon rank sum test. The *P* values of comparison between survival plots were calculated by testing the association between TIDE prediction scores and overall survival with the two-sided Wald test in a Cox-PH regression.

SUPPLEMENTARY MATERIALS

immunology.sciencemag.org/cgi/content/full/6/59/eabh2383/DC1

Fig. S1. Characterization of *Maoa*-KO mice (related to Fig. 1).

Fig. S2. MAO-A–deficient mice show suppressed tumor growth and enhanced CD8 T cell antitumor immunity (related to Fig. 1, E to M).

Fig. S3. MAO-A–deficient tumor-infiltrating CD8 T cells show enhanced mitochondrial electron transport chain gene expression (related to Fig. 1, K to M).

Fig. S4. MAO-A directly regulates antitumor immunity (related to Fig. 2, A to C).

Fig. S5. MAO-A directly regulates CD8 T cell antitumor immunity (related to Fig. 2, D to F).

Fig. S6. MAO-A acts as a negative-feedback regulator to restrain CD8 T cell activation (related to Fig. 3).

Fig. S7. MAO-A acts as a negative-feedback regulator to restrain CD8 T cell activation: Studying antigen-specific T cells (related to Fig. 3).

Fig. S8. MAO-A regulates CD8 T cell autocrine serotonin signaling (related to Fig. 4).

Fig. S9. MAOI treatment induces CD8 T cell hyperactivation in vitro (related to Fig. 5A).

Fig. S10. MAO-A blockade for cancer immunotherapy: Syngeneic mouse tumor model studies (related to Fig. 5).

Fig. S11. MAO-A blockade for cancer immunotherapy: Immunodeficient NSG mouse tumor model studies (related to Fig. 5).

Fig. S12. MAO-A blockade for cancer immunotherapy: Human T cell studies (related to Fig. 6, A to D).

Fig. S13. Clinical data correlation studies identify MAO-A as a negative regulator of T cell antitumor function in patients with cancer (related to Fig. 6, E and F).

Fig. S14. The intratumoral MAO-A–serotonin axis model.
Table S1. Primer sequences for qPCR.
Table S2. Raw data file (Excel spreadsheet).
Reproducibility checklist

View/request a protocol for this paper from *Bio-protocol*.

REFERENCES AND NOTES

1. J. Couzin-Frankel, Breakthrough of the year 2013. Cancer immunotherapy. *Science* **342**, 1432–1433 (2013).
2. S. A. Rosenberg, N. P. Restifo, Adoptive cell transfer as personalized immunotherapy for human cancer. *Science* **348**, 62–68 (2015).
3. W. A. Lim, C. H. June, The principles of engineering immune cells to treat cancer. *Cell* **168**, 724–740 (2017).
4. S. H. Baumeister, G. J. Freeman, G. Dranoff, A. H. Sharpe, Coinhibitory pathways in immunotherapy for cancer. *Annu. Rev. Immunol.* **34**, 539–573 (2016).
5. D. B. Page, M. A. Postow, M. K. Callahan, J. P. Allison, J. D. Wolchok, Immune modulation in cancer with antibodies. *Annu. Rev. Med.* **65**, 185–202 (2014).
6. A. Ribas, Releasing the brakes on cancer immunotherapy. *N. Engl. J. Med.* **373**, 1490–1492 (2015).
7. M. Dougan, G. Dranoff, S. K. Dougan, Cancer immunotherapy: Beyond checkpoint blockade. *Annu. Rev. Cancer Biol.* **3**, 55–75 (2019).
8. J. C. Shih, K. Chen, M. J. Ridd, Monoamine oxidase: From genes to behavior. *Annu. Rev. Neurosci.* **22**, 197–217 (1999).
9. J. E. Pintar, X. O. Breakefield, Monoamine oxidase (MAO) activity as a determinant in human neurophysiology. *Behav. Genet.* **12**, 53–68 (1982).
10. H. G. Brunner, M. Nelen, X. O. Breakefield, H. H. Ropers, B. A. van Oost, Abnormal behavior associated with a point mutation in the structural gene for monoamine oxidase A. *Science* **262**, 578–580 (1993).
11. J. H. Meyer, N. Ginovart, A. Boovariwala, S. Sagrati, D. Hussey, A. Garcia, T. Young, N. Praschak-Rieder, A. A. Wilson, S. Houle, Elevated monoamine oxidase a levels in the brain: an explanation for the monoamine imbalance of major depression. *Arch. Gen. Psychiatry* **63**, 1209–1216 (2006).
12. J. Tiihonen, M. R. Rautiainen, H. M. Ollila, E. Repo-Tiihonen, M. Virkkunen, A. Palotie, O. Pietiläinen, K. Kristiansson, M. Joukamaa, H. Lauerma, J. Saarela, S. Tyni, H. Vartiainen, J. Paananen, D. Goldman, T. Paunio, Genetic background of extreme violent behavior. *Mol. Psychiatry* **20**, 786–792 (2015).
13. A. Gibbons, American Association of Physical Anthropologists meeting. Tracking the evolutionary history of a "warrior" gene. *Science* **304**, 818 (2004).
14. M. Bortolato, K. Chen, J. C. Shih, Monoamine oxidase inactivation: From pathophysiology to therapeutics. *Adv. Drug Deliv. Rev.* **60**, 1527–1533 (2008).
15. M. Bortolato, K. Chen, S. C. Godar, G. Chen, W. Wu, I. Rebrin, M. R. Farrell, A. L. Scott, C. L. Wellman, J. C. Shih, Social deficits and perseverative behaviors, but not overt aggression, in MAO-A hypomorphic mice. *Neuropsychopharmacology* **36**, 2674–2688 (2011).
16. B. C. Miller, D. R. Sen, R. Al Abosy, K. Bi, Y. V. Virkud, M. W. LaFleur, K. B. Yates, A. Lako, K. Felt, G. S. Naik, M. Manos, E. Gjini, J. R. Kuchroo, J. J. Ishizuka, J. L. Collier, G. K. Griffin, S. Maleri, D. E. Comstock, S. A. Weiss, F. D. Brown, A. Panda, M. D. Zimmer, R. T. Manguso, F. S. Hodi, S. J. Rodig, A. H. Sharpe, W. N. Haining, Subsets of exhausted $CD8^+$ T cells differentially mediate tumor control and respond to checkpoint blockade. *Nat. Immunol.* **20**, 326–336 (2019).
17. F. Malinarich, K. Duan, R. A. Hamid, A. Bijin, W. X. Lin, M. Poidinger, A. M. Fairhurst, J. E. Connolly, High mitochondrial respiration and glycolytic capacity represent a metabolic phenotype of human tolerogenic dendritic cells. *J. Immunol.* **194**, 5174–5186 (2015).
18. L. T. Nguyen, P. S. Ohashi, Clinical blockade of PD1 and LAG3–potential mechanisms of action. *Nat. Rev. Immunol.* **15**, 45–56 (2015).
19. E. J. Wherry, M. Kurachi, Molecular and cellular insights into T cell exhaustion. *Nat. Rev. Immunol.* **15**, 486–499 (2015).
20. Y. Chen, M. Leon-Ponte, S. C. Pingle, P. J. O'Connell, G. P. Ahern, T lymphocytes possess the machinery for 5-HT synthesis, storage, degradation and release. *Acta Physiol (Oxf.)* **213**, 860–867 (2015).
21. M. León-Ponte, G. P. Ahern, P. J. O'Connell, Serotonin provides an accessory signal to enhance T-cell activation by signaling through the 5-HT_7 receptor. *Blood* **109**, 3139–3146 (2007).
22. P. J. O'Connell, X. Wang, M. Leon-Ponte, C. Griffiths, S. C. Pingle, G. P. Ahern, A novel form of immune signaling revealed by transmission of the inflammatory mediator serotonin between dendritic cells and T cells. *Blood* **107**, 1010–1017 (2006).
23. M. Wimbiscus, O. Kostenko, D. Malone, MAO inhibitors: Risks, benefits, and lore. *Cleve. Clin. J. Med.* **77**, 859–882 (2010).
24. M. T. Bethune, X. H. Li, J. Yu, J. McLaughlin, D. Cheng, C. Mathis, B. H. Moreno, K. Woods, A. J. Knights, A. Garcia-Diaz, S. Wong, S. Hu-Lieskovan, C. Puig-Saus, J. Cebon, A. Ribas, L. Yang, O. N. Witte, D. Baltimore, Isolation and characterization of NY-ESO-1-specific T cell receptors restricted on various MHC molecules. *Proc. Natl. Acad. Sci. U.S.A.* **115**, E10702–E10711 (2018).
25. Y. Zhu, D. J. Smith, Y. Zhou, Y.-R. Li, J. Yu, D. Lee, Y.-C. Wang, S. D. Biase, X. Wang, C. Hardoy, J. Ku, T. Tsao, L. J. Lin, A. T. Pham, H. Moon, J. M. Laughlin, D. Cheng, R. P. Hollis, B. Campo-Fernandez, F. Urbinati, L. Wei, L. Pang, V. Rezek, B. Berent-Maoz, M. H. Macabali, D. Gjertson, X. Wang, Z. Galic, S. G. Kitchen, D. S. An, S. Hu-Lieskovan, P. J. Kaplan-Lefko, S. N. De Oliveira, C. S. Seet, S. M. Larson, S. J. Forman, J. R. Heath, J. A. Zack, G. M. Crooks, C. G. Radu, A. Ribas, D. B. Kohn, O. N. Witte, L. Yang, Development of hematopoietic stem cell-engineered invariant natural killer T cell therapy for cancer. *Cell Stem Cell* **25**, 542–557 (2019).
26. P. Jiang, S. Gu, D. Pan, J. Fu, A. Sahu, X. Hu, Z. Li, N. Traugh, X. Bu, B. Li, J. Liu, G. J. Freeman, M. A. Brown, K. W. Wucherpfennig, X. S. Liu, Signatures of T cell dysfunction and exclusion predict cancer immunotherapy response. *Nat. Med.* **24**, 1550–1558 (2018).
27. D.-T. Chen, J. M. Hernandez, D. Shibata, S. M. McCarthy, L. A. Humphries, W. Clark, A. Elahi, M. Gruidl, D. Coppola, T. Yeatman, Complementary strand microRNAs mediate acquisition of metastatic potential in colonic adenocarcinoma. *J. Gastrointest. Surg.* **16**, 905–912 (2012).
28. S. Rousseaux, A. Debernardi, B. Jacquiau, A.-L. Vitte, A. Vesin, H. Nagy-Mignotte, D. Moro-Sibilot, P.-Y. Brichon, S. Lantuejoul, P. Hainaut, J. Laffaire, A. de Reyniès, D. G. Beer, J.-F. Timsit, C. Brambilla, E. Brambilla, S. Khochbin, Ectopic activation of germline and placental genes identifies aggressive metastasis-prone lung cancers. *Sci. Transl. Med.* **5**, 186ra66 (2013).
29. Cancer Genome Atlas Research Network, J. N. Weinstein, E. A. Collisson, G. B. Mills, K. R. M. Shaw, B. A. Ozenberger, K. Ellrott, I. Shmulevich, C. Sander, J. M. Stuart, The Cancer Genome Atlas Pan-Cancer analysis project. *Nat. Genet.* **45**, 1113–1120 (2013).
30. J. K. Stratford, D. J. Bentrem, J. M. Anderson, C. Fan, K. A. Volmar, J. S. Marron, E. D. Routh, L. S. Caskey, J. C. Samuel, C. J. der, L. B. Thorne, B. F. Calvo, H. J. Kim, M. S. Talamonti, C. A. Iacobuzio-Donahue, M. A. Hollingsworth, C. M. Perou, J. J. Yeh, A six-gene signature predicts survival of patients with localized pancreatic ductal adenocarcinoma. *PLOS Med.* **7**, e1000307 (2010).
31. T. N. Gide, C. Quek, A. M. Menzies, A. T. Tasker, P. Shang, J. Holst, J. Madore, S. Y. Lim, R. Velickovic, M. Wongchenko, Y. Yan, S. Lo, M. S. Carlino, A. Guminski, R. P. M. Saw, A. Pang, H. M. McGuire, U. Palendira, J. F. Thompson, H. Rizos, I. P. da Silva, M. Batten, R. A. Scolyer, G. V. Long, J. S. Wilmott, Distinct immune cell populations define response to anti-PD-1 monotherapy and anti-PD-1/Anti-CTLA-4 combined therapy. *Cancer Cell* **35**, 238–255 (2019).
32. S. Talbot, S. L. Foster, C. J. Woolf, Neuroimmunity: Physiology and pathology. *Annu. Rev. Immunol.* **34**, 421–447 (2016).
33. M. Levite, *Nerve-Driven Immunity. Neurotransmitters and Neuropeptides in the Immune System* (Springer, 2012).
34. C. H. Schein, Repurposing approved drugs on the pathway to novel therapies. *Med. Res. Rev.* **40**, 586–605 (2019).
35. G. Shoval, R. D. Balicer, B. Feldman, M. Hoshen, G. Eger, A. Weizman, G. Zalsman, B. Stubbs, P. Golubchik, B. Gordon, A. Krivoy, Adherence to antidepressant medications is associated with reduced premature mortality in patients with cancer: A nationwide cohort study. *Depress. Anxiety* **36**, 921–929 (2019).
36. P. M. Pilowsky, *Serotonin: The Mediator That Spans Evolution* (Elsevier, 2019).
37. M. E. Hernandez, D. Martinez-Fong, M. Perez-Tapia, I. Estrada-Garcia, S. Estrada-Parra, L. Pavón, Evaluation of the effect of selective serotonin-reuptake inhibitors on lymphocyte subsets in patients with a major depressive disorder. *Eur. Neuropsychopharmacol.* **20**, 88–95 (2010).
38. G. J. McGinnis, J. Raber, CNS side effects of immune checkpoint inhibitors: Preclinical models, genetics and multimodality therapy. *Immunotherapy* **9**, 929–941 (2017).
39. A. H. Miller, C. L. Raison, The role of inflammation in depression: From evolutionary imperative to modern treatment target. *Nat. Rev. Immunol.* **16**, 22–34 (2016).
40. D. M. Pardoll, The blockade of immune checkpoints in cancer immunotherapy. *Nat. Rev. Cancer* **12**, 252–264 (2012).
41. Y. C. Lin, Y. T. Chang, M. Campbell, T. P. Lin, C. C. Pan, H. C. Lee, J. C. Shih, P. C. Chang, MAOA-a novel decision maker of apoptosis and autophagy in hormone refractory neuroendocrine prostate cancer cells. *Sci. Rep.* **7**, 46338 (2017).
42. S. Gaur, M. E. Gross, C. P. Liao, B. Qian, J. C. Shih, Effect of Monoamine oxidase A (MAOA) inhibitors on androgen-sensitive and castration-resistant prostate cancer cells. *Prostate* **79**, 667–677 (2019).
43. Y. Liu, L. Xiao, K. I. Joo, B. Hu, J. Fang, P. Wang, In situ modulation of dendritic cells by injectable thermosensitive hydrogels for cancer vaccines in mice. *Biomacromolecules* **15**, 3836–3845 (2014).
44. B. Homet Moreno, J. M. Zaretsky, A. Garcia-Diaz, J. Tsoi, G. Parisi, L. Robert, K. Meeth, A. Ndoye, M. Bosenberg, A. T. Weeraratna, T. G. Graeber, B. Comin-Anduix, S. Hu-Lieskovan, A. Ribas, Response to programmed cell death-1 blockade in a murine melanoma syngeneic model requires costimulation, CD4, and CD8 T cells. *Cancer Immunol. Res.* **4**, 845–857 (2016).

45. S. Di Biase, X. Ma, X. Wang, J. Yu, Y.-C. Wang, D. J. Smith, Y. Zhou, Z. Li, Y. J. Kim, N. Clarke, A. To, L. Yang, Creatine uptake regulates CD8 T cell antitumor immunity. *J. Exp. Med.* **216**, 2869–2882 (2019).
46. D. J. Smith, S. Liu, S. Ji, B. Li, J. McLaughlin, D. Cheng, O. N. Witte, L. Yang, Genetic engineering of hematopoietic stem cells to generate invariant natural killer T cells. *Proc. Natl. Acad. Sci. U.S.A.* **112**, 1523–1528 (2015).
47. B. Li, X. Wang, I. Y. Choi, Y.-C. Wang, S. Liu, A. T. Pham, H. Moon, D. J. Smith, D. S. Rao, M. P. Boldin, L. Yang, miR-146a modulates autoreactive Th17 cell differentiation and regulates organ-specific autoimmunity. *J. Clin. Invest.* **127**, 3702–3716 (2017).
48. D. J. Smith, L. J. Lin, H. Moon, A. T. Pham, X. Wang, S. Liu, S. Ji, V. Rezek, S. Shimizu, M. Ruiz, J. Lam, D. M. Janzen, S. Memarzadeh, D. B. Kohn, J. A. Zack, S. G. Kitchen, D. S. An, L. Yang, Propagating humanized BLT mice for the study of human immunology and immunotherapy. *Stem Cells Dev.* **25**, 1863–1873 (2016).
49. J. Thomas, R. Khanam, D. Vohora, A validated HPLC-UV method and optimization of sample preparation technique for norepinephrine and serotonin in mouse brain. *Pharm. Biol.* **53**, 1539–1544 (2015).
50. T. M. Alshammari, A. A. Al-Hassan, T. B. Hadda, M. Aljofan, Comparison of different serum sample extraction methods and their suitability for mass spectrometry analysis. *Saudi Pharm J.* **23**, 689–697 (2015).
51. M. B. Dong, G. Wang, R. D. Chow, L. Ye, L. Zhu, X. Dai, J. J. Park, H. R. Kim, Y. Errami, C. D. Guzman, X. Zhou, K. Y. Chen, P. A. Renauer, Y. Du, J. Shen, S. Z. Lam, J. J. Zhou, D. R. Lannin, R. S. Herbst, S. Chen, Systematic immunotherapy target discovery using genome-scale in vivo CRISPR screens in CD8 T cells. *Cell* **178**, 1189–1204 (2019).

Acknowledgments: We thank the UCLA animal facility for providing animal support, the UCLA/CFAR Virology Core Laboratory for providing human PBMCs, the UCLA TCGB facility for assisting with scRNA-seq, the laboratory of M. Bosenberg (Yale University, CT, USA) for providing the MC38 cell line, the laboratory of P. Wang (University of Southern California, CA, USA) for providing the B16-OVA and PG13 cell lines, J. Mac from the laboratory of P. Wang for assisting with HPLC, and Life Science Editors for editing the manuscript. **Funding:** This work was supported by a Research Career Development Award from the STOP CANCER Foundation (to L.Y.), a BSCRC-RHF Research Award from the Rose Hills Research Foundation (to L.Y.), a JCCC/BSCRC Ablon Scholars Award from UCLA (to L.Y.), and a Magnolia Council Senior Investigator Grant Award from the Tower Cancer Research Foundation (to L.Y.). Z.L. was a postdoctoral fellow supported by the UCLA Tumor Immunology Training Grant (USHHS Ruth L. Kirschstein Institutional National Research Service award no. T32 CA009120). J.Y. was a predoctoral fellow supported by the UCLA Broad Stem Cell Research Center (BSCRC) Predoctoral Fellowship. S.Z was a predoctoral fellow supported by the UCLA Medical Scientist Training Program Grant (T32-GM008042). D.J.S was a predoctoral fellow supported by the UCLA Tumor Immunology Training Grant (U.S. Department of Health and Human Services Ruth L. Kirschstein Institutional National Research Service award no. T32 CA009056). Y-R.L. was a predoctoral fellow supported by the UCLA Whitcome Predoctoral Fellowship in Molecular Biology. **Author contributions:** X.W. and L.Y. designed the study, analyzed the data, and wrote the manuscript. X.W. performed all experiments, with the assistance from B.L. (Fig. 2C and fig. S4); Y.J.K. (Fig. 4, N and O, and fig. S8, K and M); Y.-C.W. (Fig. 1, E to H, and fig. S1B); Z.L. (Fig. 5, B and C, and figs. S1A; S11, C and D; and S12, E and F); J.Y. (Fig. 6, C and D, and fig. S12, A to D); S.Z. (Figs. 3, F and G, and 4, F to K); X.M., Y.Z., and Y.-R.L. (Fig. 1, E to H); I.Y.C., S.D.B., and D.J.S. (Fig. 2, D to F); M.P. and F.M. (Fig. 1, K to M, and figs. S2, B to F; and S3); and J.H., N.C., A.T., L.G., A.T.P., and H.M. (fig. S5A). L.Y. supervised the entire study. **Competing interests:** X.W. and L.Y. are inventors on patents related to this study filed by UCLA. The authors declare that they have no other competing interests. **Data and materials availability:** All sequencing datasets are deposited in the Genome Expression Omnibus (GEO) under accession number GSE153615. All other data supporting the findings of this study are available within the paper or in the Supplementary Materials. New viral constructs and cell lines generated in this study are available upon signing a material transfer agreement with UCLA.

Submitted 24 February 2021
Accepted 15 April 2021
Published 14 May 2021
10.1126/sciimmunol.abh2383

Citation: X. Wang, B. Li, Y. J. Kim, Y.-C. Wang, Z. Li, J. Yu, S. Zeng, X. Ma, I. Y. Choi, S. Di Biase, D. J. Smith, Y. Zhou, Y.-R. Li, F. Ma, J. Huang, N. Clarke, A. To, L. Gong, A. T. Pham, H. Moon, M. Pellegrini, L. Yang, Targeting monoamine oxidase A for T cell–based cancer immunotherapy. *Sci. Immunol.* **6**, eabh2383 (2021).

Chapter 3: Targeting monoamine oxidase A-regulated tumor-associated macrophage polarization for cancer immunotherapy

nature COMMUNICATIONS

ARTICLE

https://doi.org/10.1038/s41467-021-23164-2 OPEN

Targeting monoamine oxidase A-regulated tumor-associated macrophage polarization for cancer immunotherapy

Yu-Chen Wang[1], Xi Wang[1], Jiaji Yu[1], Feiyang Ma[2], Zhe Li[1], Yang Zhou[1], Samuel Zeng[1], Xiaoya Ma[1], Yan-Ruide Li[1], Adam Neal[3,4], Jie Huang[1], Angela To[1], Nicole Clarke[1], Sanaz Memarzadeh[3,4,5,6,7], Matteo Pellegrini[2] & Lili Yang[1,3,6,7]✉

Targeting tumor-associated macrophages (TAMs) is a promising strategy to modify the immunosuppressive tumor microenvironment and improve cancer immunotherapy. Monoamine oxidase A (MAO-A) is an enzyme best known for its function in the brain; small molecule MAO inhibitors (MAOIs) are clinically used for treating neurological disorders. Here we observe MAO-A induction in mouse and human TAMs. MAO-A-deficient mice exhibit decreased TAM immunosuppressive functions corresponding with enhanced anti-tumor immunity. MAOI treatment induces TAM reprogramming and suppresses tumor growth in preclinical mouse syngeneic and human xenograft tumor models. Combining MAOI and anti-PD-1 treatments results in synergistic tumor suppression. Clinical data correlation studies associate high intratumoral *MAOA* expression with poor patient survival in a broad range of cancers. We further demonstrate that MAO-A promotes TAM immunosuppressive polarization via upregulating oxidative stress. Together, these data identify MAO-A as a critical regulator of TAMs and support repurposing MAOIs for TAM reprogramming to improve cancer immunotherapy.

[1] Department of Microbiology, Immunology and Molecular Genetics, University of California, Los Angeles, CA, USA. [2] Department of Molecular, Cell and Developmental Biology, and Institute for Genomics and Proteomics, University of California, Los Angeles, CA, USA. [3] Eli and Edythe Broad Center of Regeneration Medicine and Stem Cell Research, University of California, Los Angeles, CA, USA. [4] Department of Obstetrics and Gynecology, David Geffen School of Medicine, University of California Los Angeles, Los Angeles, CA, USA. [5] The VA Greater Los Angeles Healthcare System, Los Angeles, CA, USA. [6] Jonsson Comprehensive Cancer Center, the David Geffen School of Medicine, University of California, Los Angeles, CA, USA. [7] Molecular Biology Institute, University of California, Los Angeles, CA, USA. ✉email: liliyang@ucla.edu

Over the past decade, cancer immunotherapy has achieved significant breakthroughs. In particular, immune checkpoint blockade (ICB) therapy has yielded remarkable clinical responses and revolutionised the treatment of many cancers[1]. So far, the FDA has approved cytotoxic T-lymphocyte antigen 4 (CTLA-4) and programmed cell death protein 1/ligand 1 (PD-1/PD-L1) blockade therapies for treating more than ten different malignancies[2]; however, only a small fraction of cancer patients respond to these therapies[3,4]. Most ICB therapies work through enhancing antitumor $CD8^+$ T-cell responses, which can be greatly limited by the immunosuppressive tumor microenvironment (TME)[5]. Tumor-associated macrophages (TAMs), a key component of the immunosuppressive TME, dampen T-cell antitumor reactivity in the majority of solid tumors[6–9]. Growing evidence suggests that TAMs are responsible for inhibiting antitumor T-cell reactivity and limiting the ICB therapy efficacy, making TAMs potential targets for reversing the immunosuppressive TME and improving cancer immunotherapy[10–12].

In general, TAMs are considered to mature from bone marrow-derived circulating monocytes; these monocytes are recruited to the tumor sites, exposed to chemokines and growth factors in the TME, and subsequently differentiate into TAMs[13,14]. There is also increasing evidence for tissue-resident macrophage-originated TAMs[15]. Depending on the surrounding immune environment, macrophages can be polarized towards an immunostimulatory phenotype by pro-inflammatory stimuli (e.g., IFN-γ) or towards an immunosuppressive phenotype by anti-inflammatory stimuli (e.g., IL-4 and IL-13)[16]. Although a binary polarization system is commonly used in macrophage studies, in most large-scale transcriptome analyses, TAMs showed a continuum of phenotypes expressing both immunostimulatory and immunosuppressive markers in addition to the extreme ends of polarization[16,17]. These mixed phenotypes and polarization states suggest the complexity of the TME and the residential TAM functionality. As a tumor develops, the enrichment of IL-4 and IL-13 produced by tumor cells and $CD4^+$ T cells in the TME results in the polarization of TAMs towards an immunosuppressive phenotype, that promotes tumor growth, malignancy, and metastasis[16,18]. In established solid tumors, TAMs predominately exhibit an immunosuppressive phenotype, evidenced by their production of anti-inflammatory cytokines and arginase-1 (Arg1), as well as their expression of mannose receptor (CD206) and scavenger receptors[19,20]. Through metabolising L-arginine via Arg1, TAMs can directly suppress cytotoxic $CD8^+$ T-cell responses[21,22]. Mannose receptor (CD206) expressed by TAMs can impair cytotoxicity of $CD8^+$ T cells by suppressing CD45 phosphatase activity[23]. In addition, TAMs can inhibit T-cell activities through immune checkpoint engagement by expressing the ligands of the inhibitory receptors PD-1 and CTLA-4. For example, PD-L1 and PD-L2 expressed on TAMs interact with PD-1 of T cells to directly inhibit TCR signalling, cytotoxic function, and proliferation of $CD8^+$ T cells[19]. These characteristics of TAMs make them potential targets for reversing the immunosuppressive TME to augment antitumor immunity.

Although the predominant phenotype of TAMs in established solid tumors is immunosuppressive, polarization is not fixed. Plasticity, one of the key features of TAMs, enables TAMs to change their phenotype in solid tumors and thereby providing a therapeutic window[24,25]. Repolarizing/reprogramming TAMs from an immunosuppressive and tumor-promoting phenotype towards an immunostimulatory and tumoricidal phenotype has thus become an attractive strategy in immunotherapy[18]. Preclinical and clinical studies are ongoing, evaluating TAM-repolarizing reagents (e.g., CD40 agonists, HDAC inhibitors, PI3Kγ inhibitors, creatine, etc.) for improving ICB therapy; certain efficacies have been reported[11,19,26]. Therefore, the search for new molecules regulating TAM polarization and the development of new combination treatments targeting TAM reprogramming is an active direction of current cancer immunotherapy studies.

Monoamine oxidase A (MAO-A) is an outer mitochondrial membrane-bound enzyme encoded by the X-linked *MAOA* gene. MAO-A is best known for its function in the brain, where it is involved in the degradation of a variety of monoamine neurotransmitters, including serotonin, dopamine, epinephrine, and norepinephrine. Through regulating the availability of serotonin, MAO-A modulates neuronal activities thereby influencing mood and behaviour in humans[27,28]. Through regulating the availability of dopamine and the abundance of dopamine breakdown by-product hydrogen peroxide (H_2O_2; hence oxidative stress), MAO-A is involved in multiple neurodegenerative diseases, including Parkinson's disease (PD)[29,30]. FDA-approved small-molecule MAO inhibitors (MAOIs) are currently available for the treatment of neurological disorders, including depression and PD[30–32]. However, the functions of MAO-A outside of the brain are largely unknown.

In this study, we investigate the role of MAO-A in regulating TAM polarization and evaluate the possibility of repurposing MAOIs for reprogramming TAMs and improving cancer immunotherapy. We demonstrate that MAO-A promotes TAM immunosuppressive polarization and subsequent inhibition of antitumor immunity in mice via upregulating oxidative stress. MAOI treatment induces TAM reprogramming and suppresses tumor progression in preclinical mouse syngeneic and human xenograft tumor models. Combining MAOI and anti-PD-1 treatments result in synergistic tumor suppression. Clinical data correlation studies associate high intratumoral MAO-A expression with poor patient survival in a broad range of cancers. Together, these data identify MAO-A as a critical regulator of TAMs and support repurposing MAOIs for TAM reprogramming to improve cancer immunotherapy.

Results

MAO-A-deficient mice show reduced tumor growth associated with altered TAM polarization. In a search for new molecules regulating TAM reprogramming, we inoculated C57BL/6J mice with syngeneic B16-OVA melanoma tumors, isolated TAMs and assessed TAM gene expression profiles. Monocytes isolated from tumor-free and tumor-bearing mice were included as controls. In addition to changes in classical genes involved in regulating macrophage immune responses, we observed the induction of a *Maoa* gene in TAMs (Fig. 1a), suggesting that MAO-A may be involved in modulating TAM activities.

To study the role of MAO-A in antitumor immunity in vivo, we used MAO-A-deficient mice that carry a hypomorphic MAO-A mutant[33]. Although a degree of *Maoa* expression leakage in the brain had been previously reported in these mice[33], analysis of their immune system showed nearly complete ablation of MAO-A expression in major lymphoid organs, including the spleen and bone marrow (BM) (Supplementary Fig. 1a). Since we focused on immune cells in this study, we denote these mice as *Maoa* knockout (KO) mice. When challenged with B16-OVA melanoma cells (Fig. 1b), tumor growth in *Maoa* KO mice was significantly suppressed compared to that in *Maoa* wild-type (WT) mice (Fig. 1c, d). Although similar levels of TAMs (gated as $CD45.2^+CD11b^+Ly6G^-Ly6C^{-/low}F4/80^+$ cells) were detected in *Maoa* WT and *Maoa* KO mice (Supplementary Fig. 1b, c), compared to their WT counterparts, TAMs isolated from *Maoa* KO mice exhibited a less immunosuppressive phenotype, indicated by their decreased expression of immunosuppressive markers (i.e., CD206; Fig. 1e), and their increased expression of immunostimulatory molecules (i.e., CD69, CD86 and MHC class

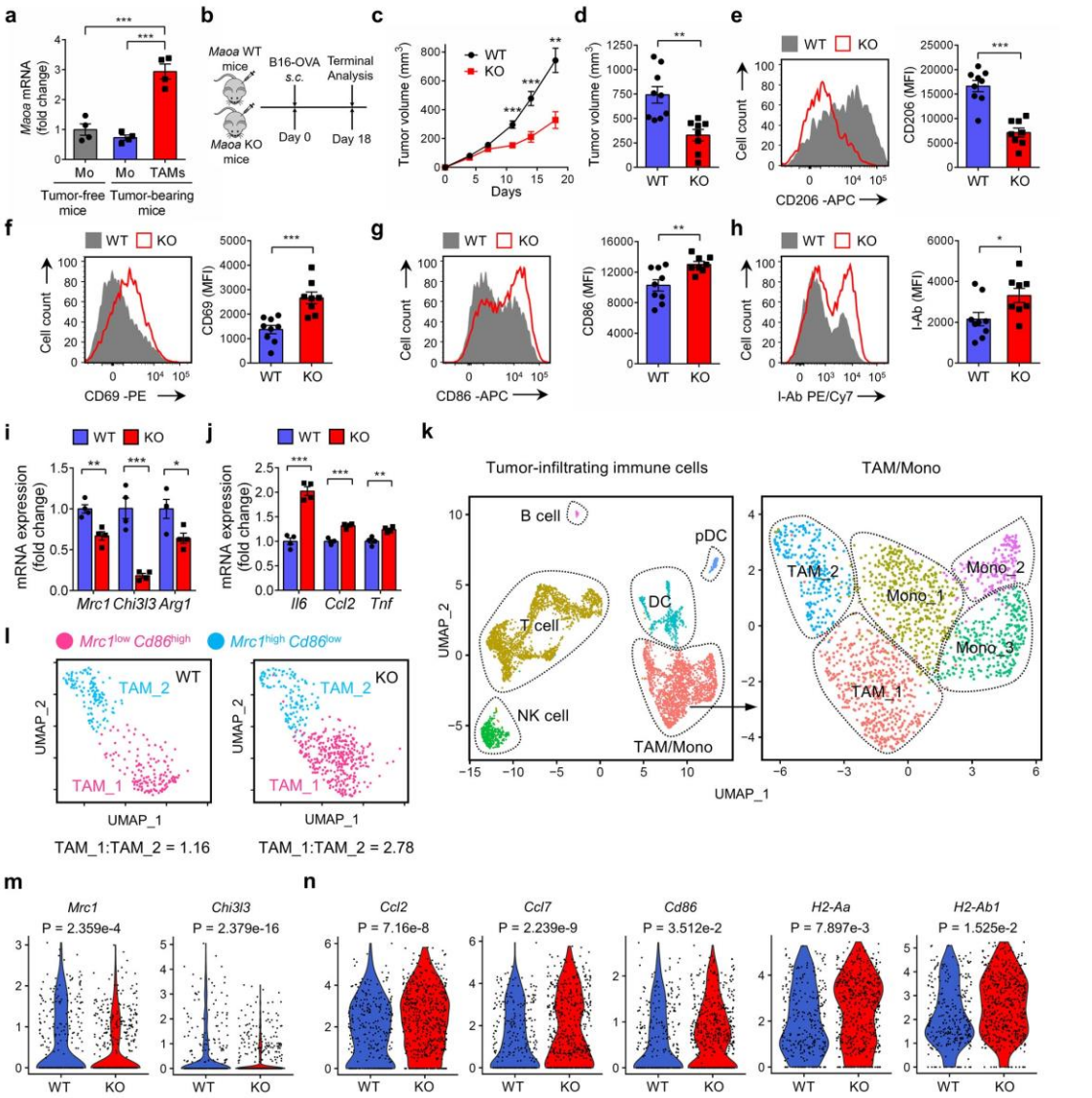

Fig. 1 MAO-A-deficient mice show reduced tumor growth associated with altered TAM polarization. a QPCR analyses of *Maoa* mRNA expression in TAMs isolated from wild-type mice-bearing B16-OVA tumors. Monocytes (Mo) were isolated from peripheral blood of tumor-free and tumor-bearing mice (***$p < 0.001$). $N = 4$. **b**–**j** Studying B16-OVA tumor growth in *Maoa* WT and *Maoa* KO mice. **b** Experimental design. **c** Tumor growth (**$p = 0.0038$, ***$p <$ 0.001). **d** Tumor volume at day 18 (**$p = 0.0038$). **e**–**h** FACS analyses of CD206 (**e**) (***$p < 0.001$), CD69 (**f**) (***$p < 0.001$), CD86 (**g**) (**$p = 0.0064$) and I-Ab (**h**) (*$p = 0.0275$) expression on TAMs at day 18. WT, $n = 9$; KO, $n = 8$. MFI mean fluorescence intensity. **i**, **j** QPCR analyses of immunosuppressive (*Mrc1*, **$p = 0.0041$; *Chi3l3*, ***$p < 0.001$ and *Arg1*, *$p = 0.0339$; **i**) and immunostimulatory (*Il6*, ***$p < 0.001$; *Ccl2*, ***$p < 0.001$ and *Tnf*, **$p = 0.0036$; **j**) signature genes mRNA expression in TAMs ($n = 4$). **k**–**n** scRNAseq analyses of tumor-infiltrating immune cells (TIIs) from *Maoa* WT and *Maoa* KO mice at day 14 post B16-OVA tumors challenge. **k** Uniform Manifold Approximation and Projection (UMAP) of single TIIs showing the formation of six cell clusters (TAM/Mono, T cell, NK cell, B cell, DC and pDC) from total CD45.2$^+$ TIIs and five cell clusters (TAM_1, TAM_2, Mono_1, Mono_2 and Mono_3) from the TAM/Mono subpopulation. Each dot represents one single cell and is coloured according to cell types. Mono monocyte, NK natural killer cell, DC dendritic cell, pDC plasmacytoid dendritic cell. **l** UMAP of the TAM subpopulation, showing the formation of two clusters (TAM_1: *Mrc1*^{low}*Cd86*^{high}; and TAM_2: *Mrc1*^{high}*Cd86*^{low}). Each dot represents one single cell and is coloured according to cell clusters. Ratios of TAM_1:TAM_2 are presented. **m**, **n** Violin plots of immunosuppressive (*Mrc1* and *Chi3l3*; **m**) and immunostimulatory (*Ccl2*, *Ccl7*, *Cd86*, *H2-Aa*, and *H2-Ab1*; **n**) signature genes expression in single TAMs. Each dot represents an individual cell. Representative of 1 (**k**–**n**), 3 (**a**), and 5 (**b**–**j**) experiments. Analysed by one-way ANOVA (**a**) or by Student's *t* test (**c**–**j**). *p* values of violin plots are determined by Wilcoxon rank-sum test (**m**, **n**). Statistics are all two-sided. Source data are provided as a Source Data file.

II I-Ab; Fig. 1f–h). Further analysis showed that TAMs from *Maoa* KO mice expressed reduced levels of immunosuppression-associated genes (i.e., *Mrc1*, *Chi3l3* and *Arg1*; Fig. 1i) and increased levels of pro-inflammatory cytokine genes (i.e., *Il6*, *Tnfα* and *Ccl2*; Fig. 1j). Corresponding to the altered TAM polarization in *Maoa* KO mice, tumor-infiltrating $CD8^+$ T cells in these mice showed enhanced activation (i.e., increased production of Granzyme B; Supplementary Fig. 1d). Single-cell RNA sequencing (scRNAseq) analysis was performed on tumor-infiltrating immune cells (TIIs) isolated from *Maoa* WT and *Maoa* KO mice. Uniform Manifold Approximation and Projection (UMAP) of total TIIs showed the formation of 6 cell clusters (TAM/Mono, T cell, NK cell, B cell, DC and pDC; Fig. 1k and Supplementary Fig. 1e); cell cluster distributions were similar comparing *Maoa* WT and KO TIIs (Supplementary Fig. 1f, g). Further UMAP analysis of the TAM/Mono subpopulation showed the formation of five cell clusters (TAM_1, TAM_2, Mono_1, Mono_2 and Mono_3; Fig. 1k and Supplementary Fig. 1h). Compared to that in *Maoa* WT mice, the TAM subpopulation in *Maoa* KO mice comprised an increased ratio of TAM_1 ($Mrc1^{low}Cd86^{high}$) to TAM_2 ($Mrc1^{high}Cd86^{low}$) cells, corresponding to a reduced immunosuppressive phenotype of TAMs in *Maoa* KO mice (Fig. 1l and Supplementary Fig. 1i); the monocyte subpopulation in *Maoa* WT and KO mice comprised a similar composition of Mono_1 ($Ly6c2^{med}$), Mono_2 ($Ly6c2^{lo}$), and Mono_3 ($Ly6c2^{hi}$) cells (Supplementary Fig. 1j, k). Gene expression profile analysis confirmed a reduction of TAMs expressing immunosuppressive genes (i.e., *Mrc1* and *Chi3l3*; Fig. 1m) and an enrichment of TAMs expressing immunostimulatory genes (i.e., *Ccl2*, *Ccl7*, *Cd86*, *H2-Aa*, and *H2-Ab1*; Fig. 1n) in *Maoa* KO mice. These data strongly indicate that MAO-A is involved in regulating TAM polarization thereby modulating antitumor immunity.

MAO-A directly regulates TAM polarization and influences TAM-associated T-cell antitumor reactivity. In our *Maoa* KO mice tumor challenge study, MAO-A deficiency impacted both immune and non-immune cells (Fig. 1b). To determine whether MAO-A directly regulates immune cells, we conducted a BM transfer experiment wherein BM cells harvested from *Maoa* WT or KO mice were adoptively transferred into BoyJ (CD45.1) WT-recipient mice followed by B16-OVA tumor challenge (Fig. 2a). In this experiment, MAO-A deficiency comparison was confined to immune cells. MAO-A deficiency in immune cells resulted in suppressed tumor growth (Fig. 2b, c), altered TAM polarization (i.e., downregulation of immunosuppressive markers such as CD206, Fig. 2d; and upregulation of immunostimulatory markers such as CD69, CD86 and MHC class II I-Ab; Fig. 2e, f and Supplementary Fig. 2a), and enhanced tumor-infiltrating $CD8^+$ T-cell activation (i.e., increased production of cytotoxic molecules such as Granzyme B; Supplementary Fig. 2b), indicating that MAO-A directly regulates immune cell antitumor activity, in particular TAM polarization and T-cell antitumor reactivity.

To further study whether MAO-A acts as a macrophage autonomous factor directly regulating TAM polarization and thereby influencing antitumor immunity, we performed a macrophage adoptive transfer tumor experiment. BM cells were harvested from *Maoa* WT and KO mice then cultured into bone marrow-derived macrophages (BMDMs). These *Maoa* WT or KO BMDMs were then mixed with B16-OVA melanoma cells and subcutaneously (s.c.) injected into BoyJ WT-recipient mice to establish solid tumors (Fig. 2g). In this study, MAO-A-deficiency comparison was confined to TAMs. Suppressed tumor growth (Fig. 2h, i), downregulated expression of TAM immunosuppressive markers (i.e., CD206; Fig. 2j), upregulated expression of TAM immunostimulatory markers (i.e., CD69 and CD86; Fig. 2k, l) and enhanced tumor-infiltrating $CD8^+$ T-cell reactivity (i.e., increased production of Granzyme B; Fig. 2m) were observed in mice receiving *Maoa* KO BMDMs. Collectively, these in vivo studies demonstrate that MAO-A acts as an autonomous factor directly regulating TAM polarization, and thereby influencing T-cell antitumor reactivity and impacting tumor growth.

MAO-A promotes macrophage immunosuppressive polarization. To study MAO-A regulation of macrophage polarization, we cultured *Maoa* WT and KO BMDMs in vitro and polarized these macrophages towards an immunosuppressive phenotype by adding anti-inflammatory stimuli (i.e., IL-4 and IL-13; Fig. 3a). We observed a sharp induction of *Maoa* mRNA expression in *Maoa* WT BMDMs during M-CSF-induced macrophage differentiation; *Maoa* expression was then plateaued in matured BMDMs and maintained over IL-4/IL-13-induced immunosuppressive polarization (Fig. 3b, c). MAO-A expression was undetectable in *Maoa* KO BMDMs, confirming their *Maoa*-deficiency genotype (Fig. 3b, d). Compared to their wild-type counterpart, *Maoa* KO macrophages displayed a less immunosuppressive phenotype under IL-4/IL-13 stimulation, evidenced in their reduced expression of immunosuppressive markers (i.e., CD206; Fig. 3e) and signature genes (i.e., *Chi3l3* and *Arg1*; Fig. 3f, g and Supplementary Fig. 3a). When tested in a macrophage/T-cell co-culture assay (Fig. 3h), in agreement with their less immunosuppressive phenotype, IL-4/IL-13-polarized *Maoa* KO macrophages exhibited impaired suppression of wild-type $CD8^+$ T cells under anti-CD3/CD28 stimulation, shown as their attenuated inhibition of $CD8^+$ T-cell proliferation (Fig. 3i) and activation marker expression (i.e., upregulation of CD25 and CD44, and downregulation of CD62L; Fig. 3j, k and Supplementary Fig. 3b).

To verify whether MAO-A deficiency directly contributed to the alleviated immunosuppressive polarization of *Maoa* KO macrophages, we performed a rescue experiment. We constructed a MIG-*Maoa* retroviral vector, used this vector to transduce *Maoa* KO BMDMs, and achieved overexpression of MAO-A in these macrophages (Fig. 3l–n and Supplementary Fig. 3c). MAO-A overexpression significantly exacerbated the immunosuppressive phenotype of IL-4/IL-13-stimulated *Maoa* KO BMDMs (i.e., upregulation of immunosuppressive signature genes such as *Chi3l3* and *Arg1*; Fig. 3o, p). Taken together, these results indicate that MAO-A acts as an autonomous factor promoting macrophage immunosuppressive polarization under anti-inflammatory stimuli.

MAO-A promotes macrophage immunosuppressive polarization via ROS upregulation. Next, we sought to investigate the molecular mechanisms regulating MAO-A promotion of macrophage immunosuppressive polarization. It has been reported that intracellular reactive oxygen species (ROS; hence, oxidative stress) elicit macrophage immunosuppressive features[34–36]. MAO-A catalyzes the oxidative deamination of monoamines, thereby generating hydrogen peroxide (H_2O_2) as a by-product that can increase intracellular ROS levels. We, therefore, speculated that MAO-A might promote TAM immunosuppressive polarization in TME via upregulating ROS levels in TAMs (Fig. 4a).

To test this hypothesis, we directly measured ROS levels in TAMs isolated from *Maoa* WT and KO mice-bearing B16-OVA tumors and detected significantly lower levels of ROS in *Maoa* KO TAMs (Fig. 4b, c). Measurement of ROS levels in in vitro-cultured *Maoa* WT and KO BMDMs also showed reduced levels of ROS in *Maoa* KO BMDMs, with or without IL-4/IL-13 stimulation, in agreement with the in vivo TAM results (Fig. 4d). Supplementing H_2O_2 to IL-4/IL-13-stimulated *Maoa* WT and KO BMDMs elevated their intracellular ROS to similar

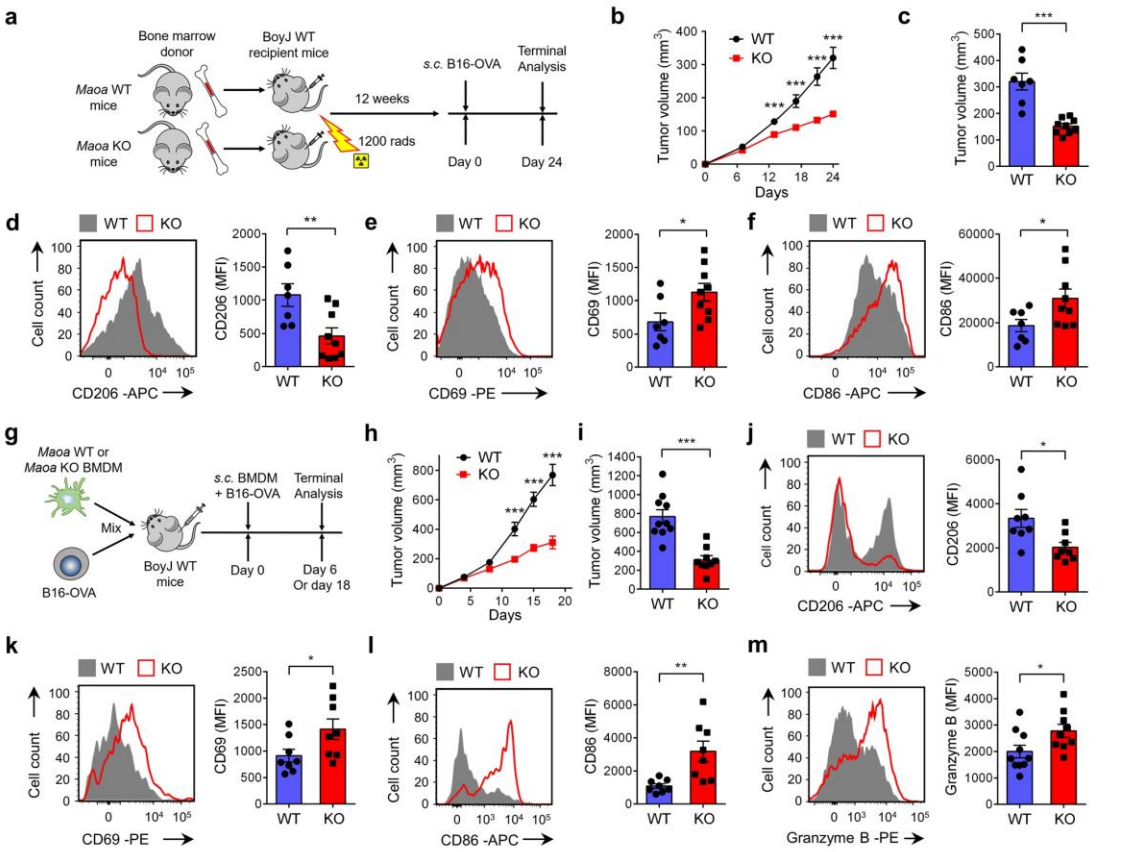

Fig. 2 MAO-A directly regulates TAM polarization and influences TAM-associated antitumor T-cell reactivity. a–f Studying B16-OVA tumor growth and TAM phenotype in BoyJ (CD45.1) wild-type mice reconstituted with bone marrow cells isolated from either *Maoa* WT or *Maoa* KO donor mice (denoted as WT or KO experimental mice, respectively). **a** Experimental design. **b** Tumor growth (***$p < 0.001$). **c** Tumor volume at day 24 (***$p < 0.001$). **d–f** FACS analyses of CD206 (**d**) (**$p = 0.0087$), CD69 (**e**) (*$p = 0.0349$) and CD86 (*$p = 0.0429$). **f** Expression on TAMs at day 24. WT, $n = 7$; KO, $n = 9$. **g–m** Studying B16-OVA tumor growth and antitumor T-cell reactivity in a tumor-TAM co-inoculation in vivo experiment. BoyJ wild-type mice received s.c. inoculation of B16-OVA tumor cells mixed with either *Maoa* WT or *Maoa* KO BMDMs (denoted as WT or KO experimental mice, respectively). BMDM bone marrow-derived macrophage. **g** Experimental design. **h** Tumor growth ($n = 9$–10) (***$p < 0.001$). **i** Tumor volume at day 18 (***$p < 0.001$). WT, $n = 10$; KO, $n = 9$. **j, l** FACS analyses of CD206 (**j**) (*$p = 0.0139$), CD69 (**k**) (*$p = 0.0443$) and CD86 (**l**) (**$p = 0.0047$) expression on CD45.2$^+$ TAMs at day 6 ($n = 8$). **m** FACS analyses of intracellular Granzyme B production in tumor-infiltrating CD45.1$^+$CD8$^+$ T cells at day 18 (*$p = 0.0371$) (WT, $n = 10$; KO, $n = 9$). Representative of three experiments. Analysed by Student's *t* test. Statistics are all two-sided. Source data are provided as a Source Data file.

levels (Supplementary Fig. 4a, b) and eliminated their differences in expression of immunosuppressive markers (i.e., CD206; Fig. 4e) and signature genes (i.e., *Chi3l3* and *Arg1*; Fig. 4f, g).

On the other hand, supplementation of tyramine, a substrate of MAO-A, increased ROS levels and upregulated the expression of immunosuppressive genes (i.e., *Chi3l3* and *Arg1*) in *Maoa* WT BMDMs but not in *Maoa* KO BMDMs (Fig. 4h–j). Taken together, these data indicate that MAO-A regulates macrophage immunosuppressive polarization via modulating macrophage intracellular ROS levels.

The JAK-Stat6 signalling pathway plays a key role in mediating IL-4/IL-13-induced immunosuppressive polarization of TAMs in TME[37,38]. After IL-4/IL-13 stimulation, JAK is phosphorylated and subsequently phosphorylates Stat6; phosphorylated Stat6 dimerises and migrates to the nucleus, where it binds to the promoters of IL-4 and IL-13 responsive genes including those involved in macrophage immunosuppressive functions[39]. ROS has been reported to promote JAK and Stat6 phosphorylation in a variety of cell types[40,41]. Since we observed decreased ROS levels in *Maoa* KO macrophages compared to those in *Maoa* WT macrophages (Fig. 4b, c), we postulated that MAO-A may impact macrophage polarization through upregulating ROS levels and thereby sensitising the JAK-Stat6 signalling pathway. Indeed, direct analysis of TAMs isolated from B16-OVA tumor-bearing *Maoa* WT and *Maoa* KO mice confirmed that compared to wild-type TAMs, MAO-A-deficient TAMs showed reduced Stat6 activation (i.e., reduced Stat6 phosphorylation; Fig. 4k, l). Further analysis of IL-4/IL-13-induced JAK-Stat6 signalling pathway in *Maoa* KO BMDMs compared to that in *Maoa* WT BMDMs showed significantly reduced JAK-Stat6 signalling (i.e., reduced JAK1, JAK2, JAK3 and Stat6 phosphorylation; Fig. 4m). Supplementing H_2O_2 to IL-4/IL-13-stimulated *Maoa* WT and KO BMDMs increased their JAK-Stat6 signalling to similar levels (i.e., comparable JAK1, JAK2, JAK3 and Stat6 phosphorylation;

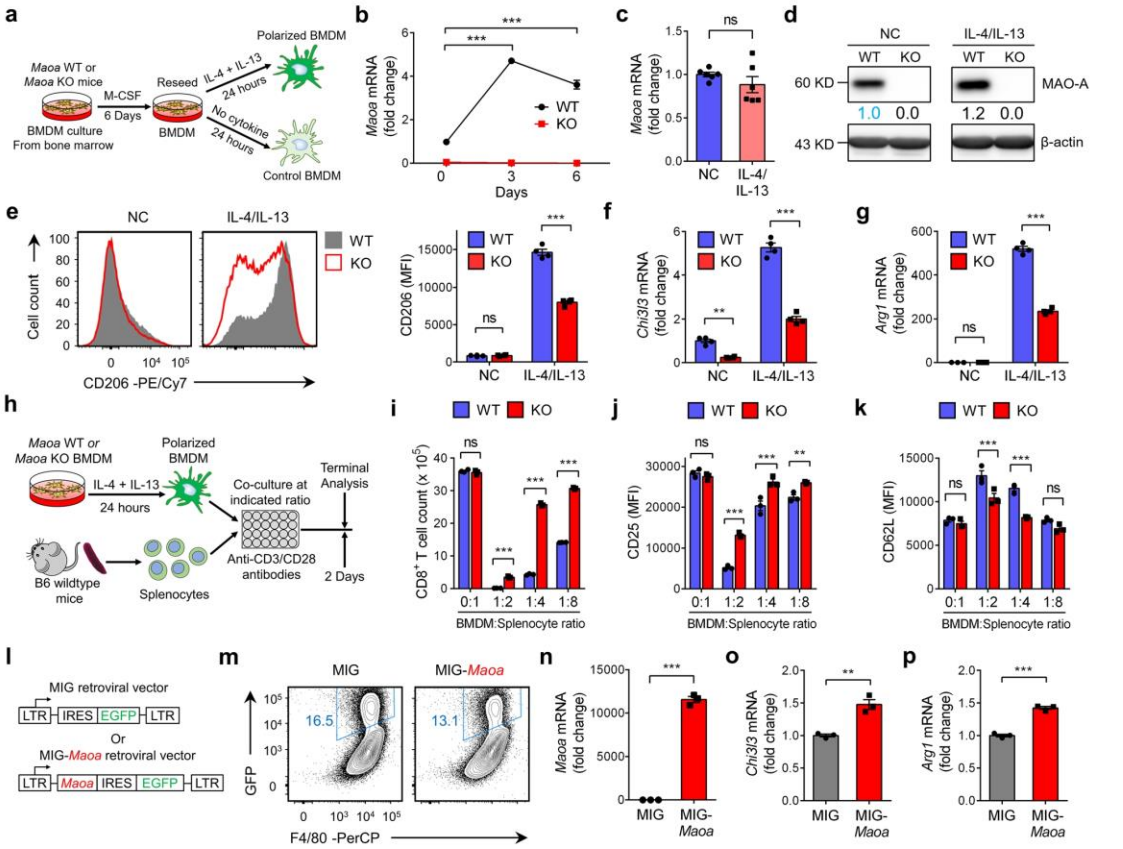

Fig. 3 MAO-A promotes macrophage immunosuppressive polarization. a–g Studying the in vitro differentiation and IL-4/IL-13-induced polarization of *Maoa* WT (WT) and *Maoa* KO (KO) BMDMs. **a** Experimental design. **b**, **c** QPCR analyses of *Maoa* mRNA expression over the 6-day BMDM differentiation culture (**b**) (***$p < 0.001$) and IL-4/IL-13-induced polarization (**c**) ($n = 6$). **d** Western blot analyses of MAO-A protein expression in the indicated BMDMs. Source data are provided as a Source Data file. **e** FACS analyses of CD206 expression on the indicated BMDMs (***$p < 0.001$) ($n = 4$). **f**, **g** QPCR analyses of *Chi3l3* (**f**) (NC, **$p = 0.0023$; IL-4/IL-13, ***$p < 0.001$) and *Arg1* (**g**) (***$p < 0.001$) mRNA expression in the indicated BMDMs ($n = 4$). NC no cytokine control BMDMs, IL-4/IL-13 IL-4 and IL-13-polarized BMDMs, ns not significant. **h–k** Studying the T-cell suppression function of *Maoa* WT (WT) and *Maoa* KO (KO) IL-4/IL-13-polarized BMDMs in an in vitro macrophage/T-cell co-culture assay ($n = 3$). **h** Experimental design. **i** FACS quantification of $CD8^+$ T cells (identified as $TCR\beta^+CD4^-CD8^+$ cells) (***$p < 0.001$). **j**, **k** FACS analyses of CD25 (**j**) (1:2, ***$p < 0.001$; 1:4, ***$p < 0.001$; 1:8, **$p = 0.0038$) and CD62L (**k**) (***$p < 0.001$) expression on $CD8^+$ T cells. **l–p** Studying the IL-4/IL-13-induced polarization of *Maoa* KO BMDMs with MAO-A overexpression ($n = 3$). In vitro-cultured *Maoa* KO BMDMs were transduced with either a MIG-*Maoa* retrovector or a MIG mock retrovector, polarized with IL-4/IL-13, followed by FACS sorting of GFP^+ *Maoa* KO BMDMs for further analyses. **l** Schematics of the MIG and MIG-*Maoa* retrovectors. **m** FACS analyses of prior-to-sorting *Maoa* KO BMDMS, showing retrovector transduction efficiency (measured as $\%GFP^+$ cells). **n–p** QPCR analyses of sorted GFP^+ *Maoa* KO BMDMs, showing the mRNA expression of *Maoa* (**n**) (***$p < 0.001$), *Chi3l3* (**o**) (**$p = 0.0038$), and *Arg1* (**p**) (***$p < 0.001$). Representative of three (**h–k**, **l–p**) and four (**a–g**) experiments. ns not significant. Analysed by one-way ANOVA (**b**), two-way ANOVA (**e–g, i–k**) or by Student's *t* test (**c**, **n–p**). Statistics are all two-sided. Source data are provided as a Source Data file.

Fig. 4m), corresponding to their comparable high levels of ROS (Supplementary Fig. 4a, b). These data indicate that MAO-A promotes macrophage immunosuppressive polarization via ROS-sensitised JAK-Stat6 pathway activation.

Collectively, these in vivo and in vitro data support a working model that MAO-A promotes TAM immunosuppressive polarization in TME, at least partly through upregulating TAM intracellular ROS levels and thereby enhancing the IL-4/IL-13-induced JAK-Stat6 signalling pathway.

MAO-A blockade for cancer immunotherapy—syngeneic mouse tumor model studies. The identification of MAO-A as a key regulator of TAM immunosuppressive polarization makes MAO-A a promising drug target for cancer immunotherapy. Because of the known functions of MAO-A in the brain, small-molecule MAOIs have been developed and clinically utilised for treating various neurological disorders, making it a highly feasible and attractive approach to repurpose these established MAOI drugs for cancer immunotherapy[31,42]. In an in vitro WT BMDM IL-4/IL-13-induced polarization culture (Fig. 5a), addition of multiple MAOIs efficiently reduced ROS levels in BMDMs (Fig. 5b) and suppressed their immunosuppressive polarization, evidenced by their decreased expression of immunosuppressive markers (i.e., CD206; Fig. 5c) and immunosuppressive genes (i.e., *Chi3l3* and *Arg1*; Fig. 5d, e). Notably, the MAOIs that we tested

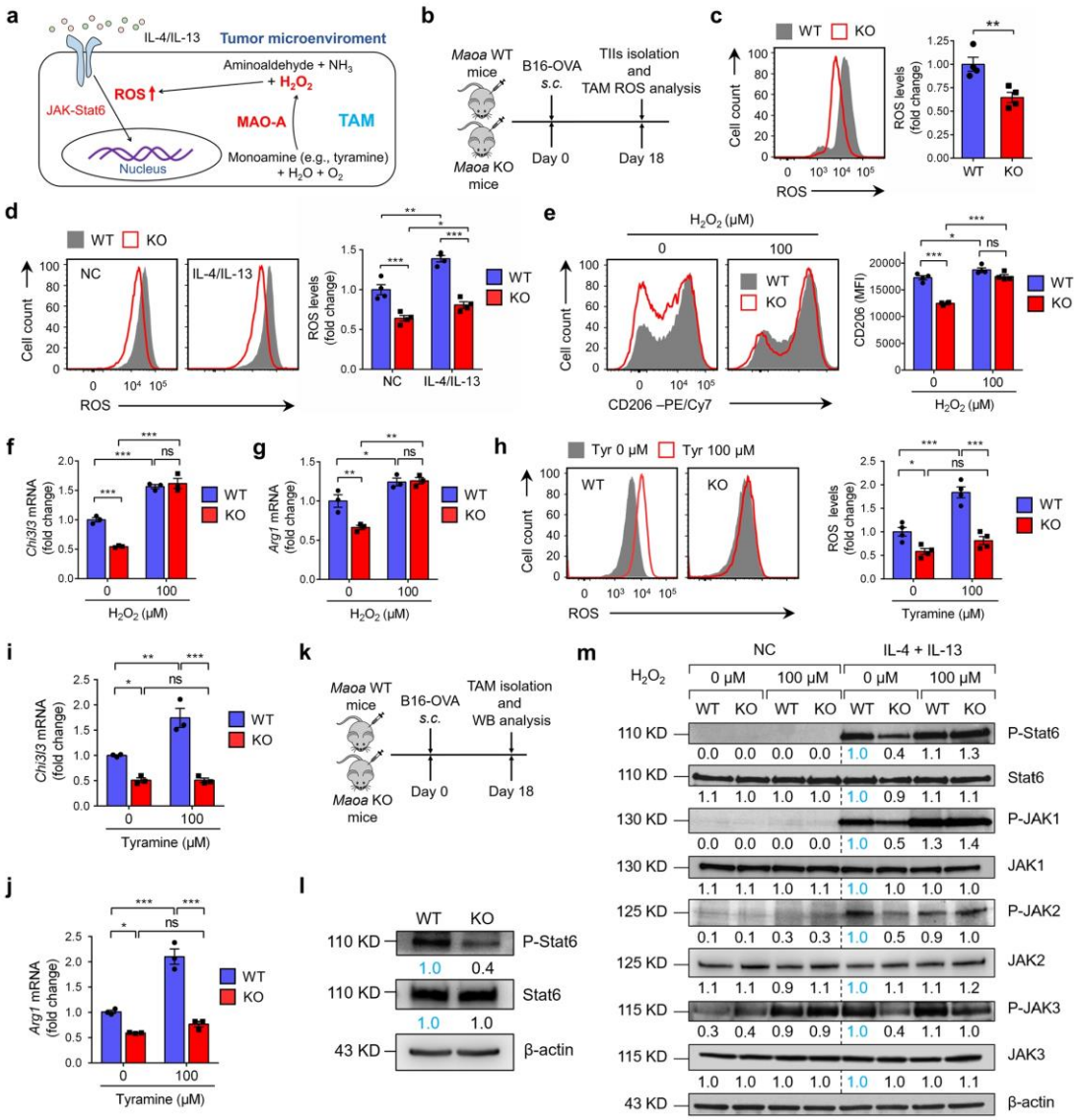

Fig. 4 MAO-A promotes macrophage immunosuppressive polarization via ROS upregulation. a Schematics showing MAO-A breaks down monoamines and generates hydrogen peroxide (H_2O_2) as a by-product, thereby increasing reactive oxygen species (ROS) levels in a TAM. **b**, **c** Studying the in vivo ROS levels in TAMs isolated from *Maoa* WT and *Maoa* KO mice-bearing B16-OVA tumors ($n = 4$). **b** Experimental design. **c** FACS analyses of ROS levels in TAMs at day 18. TAMs were gated as the CD45.2$^+$CD11b$^+$Ly6G$^-$Ly6C$^{-/low}$F4/80$^+$ cells of total TIIs ($^{**}p = 0.0088$). **d** FACS analyses of ROS levels in in vitro-cultured *Maoa* WT and *Maoa* KO BMDMs, without or without IL-4/IL-13 polarization ($n = 4$). NC no cytokine, IL-4/IL-13 IL-4/IL-13-polarized. $^*p < 0.05$, $^{**}p < 0.01$ and $^{***}p < 0.001$. **e**–**g** Study of IL-4/IL-13-polarized *Maoa* WT and *Maoa* KO BMDMs, with or without H_2O_2 treatment ($n = 3$). **e** FACS analyses of CD206 expression. **f**, **g** QPCR analyses of *Chi3l3* (**f**) and *Arg1* (**g**) mRNA expression. $^*p < 0.05$, $^{**}p < 0.01$ and $^{***}p < 0.001$. **h**–**j** Study of IL-4/IL-13-polarized *Maoa* WT and *Maoa* KO BMDMs, with or without tyramine supplement ($n = 3$). **h** FACS analyses of ROS levels. **i**, **j** QPCR analyses of *Chi3l3* (**i**) and *Arg1* (**j**) mRNA expression. $^*p < 0.05$, $^{**}p < 0.01$ and $^{***}p < 0.001$. **k**, **l** Study of TAMs isolated from *Maoa* WT and *Maoa* KO mice-bearing B16-OVA tumors at day 18 (combined from five mice per group). **k** Experimental design. **l** Western blot analyses of TAMs. TAMs were FACS sorted as the DAPI$^-$CD45.2$^+$CD11b$^+$Ly6G$^-$Ly6C$^{-/low}$F4/80$^+$ cells from total TIIs. Source data are provided as a Source Data file. **m** Western blot analyses of JAK-Stat6 signalling in *Maoa* WT and *Maoa* KO BMDMs, with or without IL-4/IL-13 polarization and H_2O_2 treatment. BMDMs were treated with H_2O_2 for 30 min prior to IL-4/IL-13 stimulation for another 30 min. Representative of three experiments. Analysed by two-way ANOVA (**d**–**j**) or by Student's *t* test (**c**). Statistics are all two-sided. Source data are provided as a Source Data file.

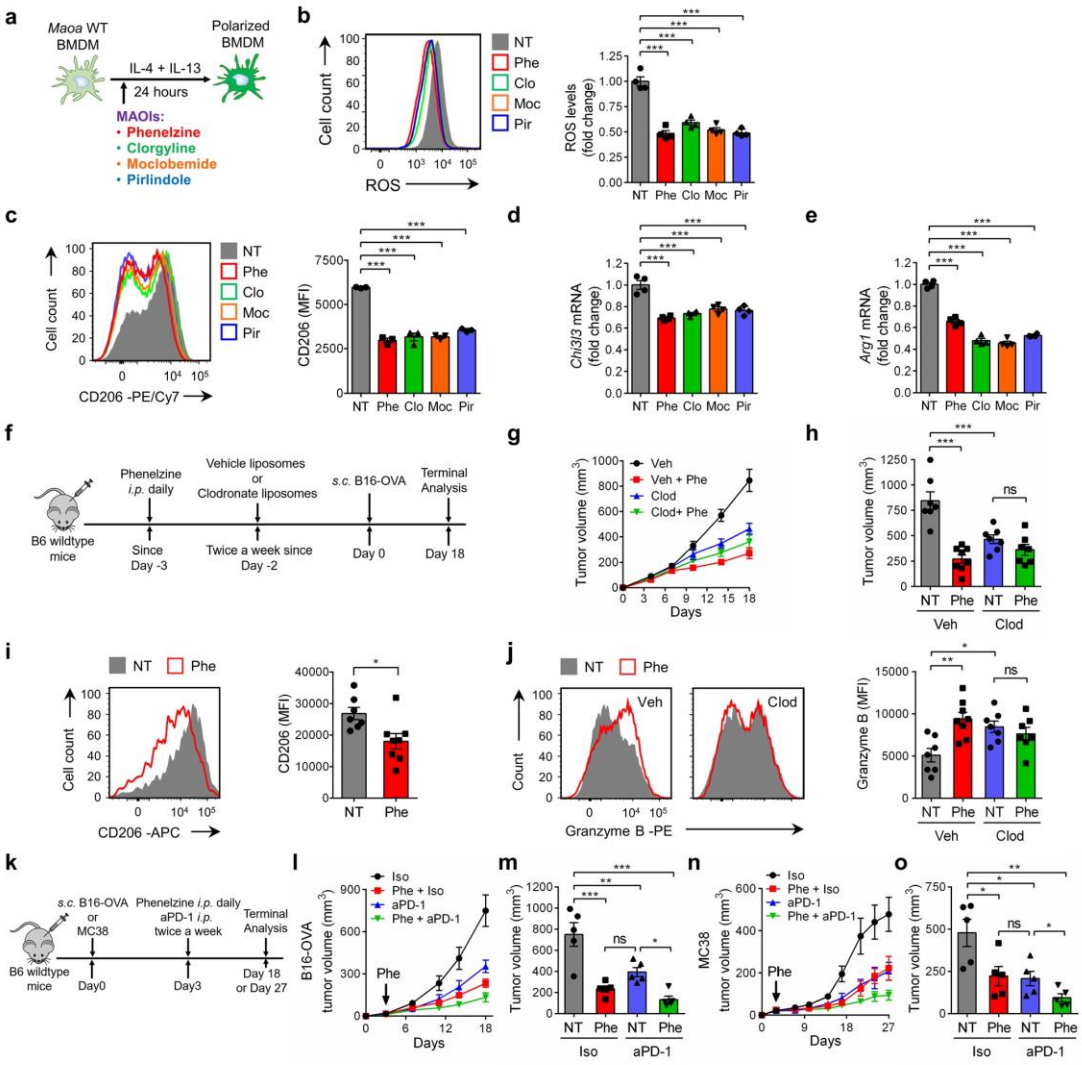

Fig. 5 MAO-A blockade for cancer immunotherapy—syngeneic mouse tumor model studies. a–e Studying the effect of MAOI treatment on IL-4/IL-13-induced BMDM polarization in vitro ($n = 4$). **a** Experimental design. Wild-type BMDMs were stimulated with IL-4/IL-13 with or without MAOI treatment. MAOIs (monoamine oxidase inhibitors) studied were phenelzine (Phe; 20 μM), clorgyline (Clo; 20 μM), moclobemide (Moc; 200 μM), and pirlindole (Pir; 20 μM). NT no MAOI treatment. **b** FACS analyses of ROS levels in BMDMs. **c** FACS analyses of CD206 expression on BMDMs. **d**, **e** QPCR analyses of *Chi3l3* (**d**) and *Arg1* (**e**) mRNA expression in BMDMs. ***$p < 0.001$. **f–j** Studying the TAM-related cancer immunotherapy potential of MAOI treatment in a B16-OVA melanoma syngeneic mouse tumor model. **f** Experimental design. B6 wild-type mice were treated with clodronate liposomes (Clod) to serve as TAM-depleted experimental mice or treated with vehicle liposomes (Veh) to serve as TAM-intact control mice. Phe phenelzine treatment, NT no phenelzine treatment. **g** Tumor growth. **h** Tumor volume at day 18 (***$p < 0.001$). **i** FACS analyses of CD206 expression on TAMs of TAM-intact experimental mice (*$p = 0.0164$). **j** FACS analyses of intracellular Granzyme B production in tumor-infiltrating $CD8^+$ T cells of all experimental mice (NT, *$p = 0.0257$; Veh, **$p = 0.0025$). Veh NT, $n = 7$; Veh Phe, $n = 8$; Clod NT, $n = 7$; Clod Phe, $n = 7$. **k–o** Studying the cancer therapy potential of MAOI treatment in combination with anti-PD-1 treatment in the B16-OVA melanoma and MC38 colon cancer syngeneic mouse tumor models ($n = 5$). **k** Experimental design. Tumor-bearing mice were treated with anti-PD-1 antibody (aPD-1) or isotype control (Iso), together with or without phenelzine (Phe) treatment. NT no Phe treatment. **l** B16-OVA tumor growth. **m** B16-OVA tumor volume at day 18. **n** MC38 tumor growth. **o** MC38 tumor volume at day 27. *$p < 0.05$, **$p < 0.01$ and ***$p < 0.001$. Representative of three experiments. Analysed by one-way ANOVA (**b–e**, **h**, **j**, **m**, **o**) or by Student's *t* test (**i**). Statistics are all two-sided. Source data are provided as a Source Data file.

include phenelzine, clorgyline, moclobemide, and pirlindole, covering the major categories of established MAOIs classified on the basis of whether they are non-selective or selective for MAO-A, and whether their effect is reversible (Fig. 5a)[31,43]. Among these MAOIs, phenelzine (trade name: Nardil) is clinically available in the United States[42]. In the following studies, we chose phenelzine as a representative to study the possibility of repurposing MAOIs for cancer immunotherapy, using two syngeneic

mouse tumor models: a B16-OVA melanoma model and a MC38 colon cancer model[44]. Of note, phenelzine is a non-selective irreversible MAOI that inhibits both MAO-A and its isoenzyme MAO-B[31]; however, because mouse macrophages predominantly express MAO-A over MAO-B, phenelzine treatment mainly regulates TAM reprogramming via inhibiting MAO-A in these tumor models (Supplementary Fig. 5a).

First, we studied the therapeutic potential of phenelzine in a B16-OVA tumor prevention model (Fig. 5f). Phenelzine treatment effectively suppressed B16-OVA tumor growth in B6 wild-type mice (Fig. 5g, h). No tumor growth difference was observed when we depleted TAMs in experimental mice via a clodronate liposome treatment, indicating that phenelzine suppressed tumor growth via modulating TAMs (Fig. 5g, h and Supplementary Fig. 5b). Correspondingly, TAMs isolated from phenelzine-treated mice displayed a less immunosuppressive phenotype, evidenced by their decreased expression of immunosuppressive markers (i.e., CD206; Fig. 5i) and signature genes (i.e., *Chi3l3* and *Arg1*; Supplementary Fig. 5c) while increased expression of immunostimulatory markers (i.e., CD69, CD86 and I-Ab; Supplementary Fig. 5d–f), that was correlated with an enhanced antitumor reactivity of tumor-infiltrating $CD8^+$ T cells (i.e., increased production of Granzyme B; Fig. 5j) in these mice. Further studies showed that phenelzine treatment also effectively suppressed the progression of pre-established solid tumors in both B16-OVA and MC38 models (Supplementary Fig. 5g–k). Notably, similar to that for the B16-OVA tumor model, direct challenge of *Maoa* WT and KO mice with MC38 tumor cells also resulted in a significantly suppressed tumor growth in *Maoa* KO mice, confirming a general impact of MAO-A-deficiency on tumor growth for multiple tumor models (Fig. 1b–d and Supplementary Fig. 5l–n).

Next, we evaluated the potential of phenelzine for combination therapy, in particular combining with other ICB therapies, such as PD-1/PD-L1 blockade therapy (Fig. 5k). Although most ICB therapies target $CD8^+$ T cells, these cells are in fact closely regulated by TAMs in the TME, making targeting TAMs another potential avenue for immunotherapy[9,26]. In both B16-OVA and MC38 tumor models, phenelzine treatment significantly suppressed the progression of pre-established solid tumors at a level comparable to the anti-PD-1 treatment; importantly, the combination of phenelzine and anti-PD-1 treatments yielded synergistic tumor suppression efficacy (Fig. 5l–o). These tumor suppression effects of phenelzine were due to immunomodulation but not direct tumor inhibition, because phenelzine treatment did not suppress the growth of B16-OVA and MC38 tumors in immunodeficient NSG mice (Supplementary Fig. 5o–s).

Collectively, these syngeneic mouse tumor model studies provided proof-of-principle evidence for the cancer immunotherapy potential of MAOIs via targeting TAM reprogramming and thereby enhancing antitumor T-cell responses.

MAO-A blockade for cancer immunotherapy—human TAM and clinical data correlation studies. To explore the translational potential of MAO-A blockade therapy, we first studied MAO-A regulation of human macrophage polarization. Using a Tumor Immune Dysfunction and Exclusion (TIDE) computational method[45], we analysed the gene expression signatures of in vitro-cultured immunostimulatory M1-like and immunosuppressive M2-like human monocyte-derived macrophages (MDMs) (GSE35449)[46]. Interestingly, among all immune checkpoint, immunostimulatory, and immunosuppressive genes examined, *MAOA* ranked as the top gene with the most dramatically elevated expression in M2-like MDMs (i.e., 7.28 M2/M1 log-fold change; Fig. 6a), suggesting a possible role of MAO-A in promoting human macrophage immunosuppressive polarization. Time-course analysis of MDM culture confirmed an upregulation of MAO-A gene and protein expression during macrophage differentiation that was further upregulated post-IL-4/IL-13-induced immunosuppressive polarization (Fig. 6b–d). Blockade of MAO-A using phenelzine significantly inhibited IL-4/IL-13-induced immunosuppressive polarization of MDMs, evidenced by their decreased expression of immunosuppressive markers (i.e., CD206 and CD273; Fig. 6e and Supplementary Fig. 6a) and signature genes (i.e., *ALOX15* and *CD200R1*; Fig. 6f, g). Collectively, these in vitro data suggest that MAO-A is highly expressed in human macrophages especially during their immunosuppressive polarization, and that MAO-A blockade has the potential to reprogramme human macrophage polarization.

To directly evaluate whether MAOIs could reprogramme human TAM polarization in vivo, we established a human tumor/TAM xenograft NSG mouse model. A375 human melanoma cells were mixed with monocytes sorted from healthy donor peripheral blood mononuclear cells (PBMCs), and s.c. injected into NSG mice to form solid tumors, with or without phenelzine treatment after inoculation (Fig. 6h). Phenelzine treatment effectively suppressed immunosuppressive polarization of human TAMs (gated as $hCD45^+hCD11b^+hCD14^+$; Supplementary Fig. 6b), supported by their decreased expression of immunosuppressive markers (i.e., CD206 and CD273; Fig. 6i, j).

Next, we studied whether MAOI-induced human TAM reprogramming could impact human T-cell antitumor reactivity, using a 3D human tumor/TAM/T-cell organoid culture (Fig. 6k). NY-ESO-1, a well-recognised tumor antigen commonly expressed in a large variety of human cancers[47], was chosen as the model tumor antigen. An A375 human melanoma cell line was engineered to co-express NY-ESO-1 as well as its matching MHC molecule, HLA-A2, to serve as the human tumor target (denoted as A375-A2-ESO; Supplementary Fig. 6c, d). NY-ESO-1-specific human $CD8^+$ T cells were generated by transducing healthy donor peripheral blood $CD8^+$ T cells with a Retro/ESO-TCR retroviral vector encoding a NY-ESO-1-specific TCR (clone 3A1; denoted as ESO-TCR); the resulting T cells, denoted as ESO-T cells, expressed ESO-TCRs and specifically targeted A375-A2-ESO tumor cells, thereby modelling the tumor-specific human $CD8^+$ T cells (Supplementary Fig. 6e, f). Human MDMs were cultured from healthy donor PBMCs, followed by IL-4/IL-13 stimulation to induce immunosuppressive polarization in the presence or absence of phenelzine treatment (Fig. 6k). The A375-A2-ESO human melanoma cells, ESO-T cells, and IL-4/IL-13-polarized MDMs were mixed at a 2:2:1 ratio and placed in a 3D tumor organoid culture mimicking TME (Fig. 6k). IL-4/IL-13-polarized MDMs effectively suppressed ESO-T-cell-mediated killing of A375-A2-ESO tumor cells; this immunosuppressive effect was largely alleviated by phenelzine treatment during MDM polarization (Fig. 6l). Accordingly, ESO-T cells co-cultured with phenelzine-treated MDMs, compared to those co-cultured with non-phenelzine-treated MDMs, showed an enhancement in T-cell activation (i.e., increased cell number, increased CD25 expression, and decreased CD62L expression; Fig. 6m and Supplementary Fig. 6g). Collectively, these data suggest that MAOI-induced human TAM reprogramming has the potential to improve antitumor T-cell responses.

To study *MAOA* gene expression in primary human TAMs, we collected fresh ovarian cancer tumor samples from patients, isolated TAMs (sorted as $DAPI^-hCD45^+hCD11b^+hTCR\alpha\beta^-hCD14^+$ cells; Supplementary Fig. 6h), and assessed their *MAOA* gene expression. Primary human monocytes isolated from healthy donor PBMCs (sorted as $DAPI^-hCD45^+hCD11b^+hTCR\alpha\beta^-hCD14^+$ cells; Sup-

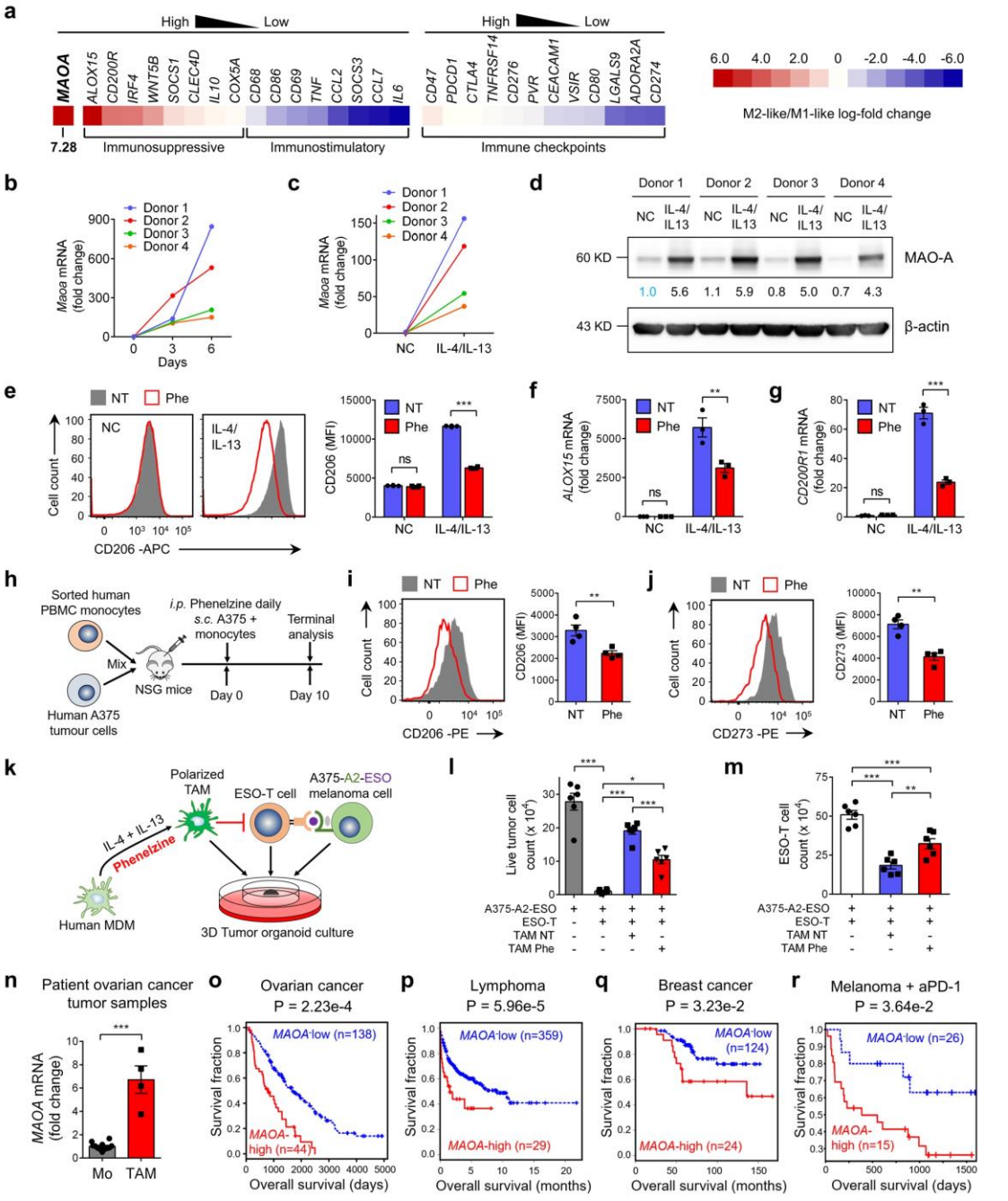

plementary Fig. 6i) were included as controls. Like mouse TAMs, human TAMs expressed high levels of *MAOA* gene, confirming MAO-A as a valid drug target in human TAMs (Figs. 1a and 6n).

Lastly, we conducted clinical data correlation studies to investigate whether intratumoral *MAOA* gene expression is correlated with clinical outcomes in cancer patients, using the TIDE computational method[45]. Intratumoral *MAOA* expression level was negatively correlated with patient survival in multiple cancer patient cohorts spanning ovarian cancer (Fig. 6o)[48], lymphoma (Fig. 6p)[49], and breast cancer (Fig. 6q)[50]. Moreover, analysis of a melanoma patient cohort receiving anti-PD-1 treatment showed that high levels of intratumoral *MAOA* expression largely abrogated the survival benefit offered by the PD-1 treatment, suggesting that combining MAO-A blockade

Fig. 6 MAO-A blockade for cancer immunotherapy—human TAM and clinical data correlation studies. a Heatmap showing the mRNA expression fold change of the indicated genes in human M2-like/M1-like macrophages. **b**–**d** Studying the MAO-A expression in in vitro-cultured human monocyte-derived macrophages (MDMs) ($n = 4$). **b**, **c** QPCR analyses of *MAOA* mRNA expression in MDMs over the 6-day differentiation culture (**b**) and post the IL-4/IL-13-induced polarization (**c**). **d** Western blot analyses of MAO-A protein expression in IL-4/IL-13-polarized MDMs. **e**–**g** Studying the IL-4/IL-13-induced polarization of human MDMs ($n = 3$). **e** FACS analyses of CD206 expression (***$p < 0.001$). **f**, **g** QPCR analyses of *ALOX15* (**f**) (**$p = 0.0012$) and *CD200R1* (**g**) (***$p < 0.001$) mRNA expression. **h**–**j** Studying the in vivo polarization of human macrophages in a human tumor-TAM co-inoculation xenograft mouse model ($n = 4$). **h** Experimental design. **i**, **j** FACS analyses of CD206 (**i**) (**$p = 0.0093$) and CD273 (**j**) (**$p = 0.0013$) expression on TAMs (gated as $hCD45^+hCD11b^+hCD14^+$ cells of TIIs). **k**–**m** Studying the in vitro efficacy of phenelzine in reprogramming human TAMs and enhancing human T-cell antitumor reactivity ($n = 6$). **k** Experimental design. **l**, **m** FACS quantification of live tumor cells (gated as $hCD45^-$ cells) and ESO-T cells (gated as $hCD45^+hCD8^+$ESO-TCR^+ cells). NT no phenelzine treatment. *$p < 0.05$, **$p < 0.01$ and ***$p < 0.001$. **n** QPCR analyses of *MAOA* mRNA expression in human TAMs isolated from ovarian cancer patient tumor samples ($n = 4$). Mo, monocytes isolated from random healthy donor peripheral blood ($n = 10$). ***$p < 0.001$. **o**–**r** Clinical data correlation studies. Kaplan–Meier plots are presented, showing the association between the intratumoral *MAOA* gene expression levels and overall survival (OS) of cancer patients, in an ovarian cancer patient cohort (GSE26712, $n = 182$; **o**), a lymphoma patient cohort (GSE10846, $n = 388$; **p**), a breast cancers patient cohort (GSE9893, $n = 148$; **q**) and a melanoma patient cohort with anti-PD-1 therapy (PRJEB23709, $n = 41$; **r**). Phe phenelzine, NC no cytokine stimulation, NT no phenelzine treatment. Representative of one (**n**), two (**b**–**d**, **h**–**j**) and three (**e**–**g**, **k**–**m**) experiments. Analysed by one-way ANOVA (**l**, **m**), two-way ANOVA (**e**–**g**), Student's *t* test (**i**, **j**, **n**), or by two-sided Wald test in a Cox-PH regression (**o**–**r**). Statistics are all two-sided. Source data are provided as a Source Data file.

therapy with PD-1/PD-L1 blockade therapy may provide synergistic therapeutic benefits through modulating TAM polarization and thereby changing the immunosuppressive TME and improving antitumor immunity (Fig. 6r)[51]. Of note, these whole-tumor lysate transcriptome data analyses could not localise the *MAOA* expression to a specific cell type (e.g., TAMs); future studies of quality transcriptome data generated from single cells or sorted TAMs are needed to obtain such information. Meanwhile, other intratumoral immune cells may also express *MAOA* and can mediate MAO-A-regulated antitumor immunity. For instance, human T cells have been indicated to express *MAOA* (https://www.proteinatlas.org/ENSG00000189221-MAOA/blood); and in our syngeneic mouse tumor model studies using the *Maoa* KO mice, we have detected enhanced antitumor T-cell responses—an effect that may result from a combination of MAO-A's direct regulation of T cells and indirect regulation of T-cell response via modulating TAMs. The study of MAO-A expression in various intratumoral immune cells, as well as MAO-A regulation of the antitumoral immunity of various immune cells, can be interesting directions for future research. Nonetheless, the present clinical data correlation studies identified MAO-A as a possible negative regulator of survival in a broad range of cancer patients, including those receiving existing ICB therapies, suggesting MAO-A blockade as a promising avenue for developing new forms of cancer therapy and combination therapy.

Taken together, these human TAM and clinical correlation studies confirmed MAO-A as a promising drug target in human TAMs and support the translational potential of MAO-A blockade for cancer immunotherapy through targeting TAM reprogramming.

Discussion

Based on our findings, we propose an "intratumoral MAO-A-ROS axis" model to elucidate the role of MAO-A in regulating TAM immunosuppressive polarization (Supplementary Fig. 7). Analogous to the well-characterised MAO-A-ROS axis in the brain, where MAO-A controls ROS levels in neurons and thereby modulates neuron degeneration via regulating neuron oxidative stress, the MAO-A-ROS axis in a solid tumor controls ROS levels in TAMs and thereby modulates TAM immunosuppressive polarization via sensitising the IL-4/IL-13-induced JAK-Stat6 signalling pathway (Supplementary Fig. 7). The resemblance between these mechanisms is intriguing: from an evolutionary point of view, it makes sense that some critical molecular regulatory pathways are preserved between the nervous and immune systems, considering that both systems are evolved to defend a living organism by sensing and reacting to environmental danger and stress. Indeed, neurons and immune cells share a broad collection of surface receptors, secretory molecules, and signal transducers[52]. In particular, many neurotransmitters/neuropeptides and their synthesis/degradation machineries traditionally considered specific for neurons are expressed in immune cells, although their functions in the immune system are to a large extent still unknown[53]. Studying these molecules and their regulatory mechanisms may provide new perspectives in tumor immunology and identifying new drug targets for cancer immunotherapies, as exemplified by our current finding of this "MAO-A-ROS axis" regulation of TAM polarization in the TME.

Considering the importance of TAMs in regulating antitumor immunity, there has been considerable efforts in developing cancer therapeutic strategies targeting TAMs. These strategies can be roughly divided into two categories: (1) those which deplete TAMs, and (2) those which alter TAM immunosuppressive activities[26]. The first category includes strategies targeting TAM recruitment and survival, such as blocking the CCL2-CCR2 axis thereby preventing monocyte mobilisation from the bone marrow and recruitment into inflammatory sites, or blocking the CSF1-CSF1R axis thereby inducing apoptosis of TAMs, or blocking the CXCL12-CXCR4 and angiopoietin 2 (ANG2)-TIE2 axes thereby depleting $TIE2^+$ macrophages that are critical for tumor angiogenesis[26,54]. However, an intrinsic downside of depleting TAMs is the loss of their innate immunostimulatory role as the primary phagocytes and professional antigen-presenting cells (APCs) in solid tumors. Reprogramming or repolarizing immunosuppressive TAMs towards an immunostimulatory phenotype therefore can be an attractive direction; this second category of TAM-repolarizing strategies includes those reprogramming TAMs via CD40 agonists, HDAC inhibitors, PI3Kγ inhibitors, and creatine[26,55–58]. Many of these TAM reprogramming strategies are currently under active clinical evaluation[26]. Notably, CD40 agonists work through activating CD40L-downstream NF-kB pathway[56,59]; HDAC inhibitors work through altering histone modifications[55,60]; PI3Kγ inhibitors work through stimulating NF-κB activation while inhibiting C/EBPβ activation[57,61]; and creatine uptake works through regulating cytokine responses[58]. Our discovery of MAO-A as a critical regulator of TAM polarization through modulating oxidative stress provides a drug target and a mechanism of action (MOA) for expanding TAM-repolarizing strategies.

Compared to many new therapeutic candidates, MAO-A is unique in that it is already an established drug target due to its known functions in the brain[42]. In fact, small-molecule MAOIs

have been developed to block MAO-A enzymatic activity in the brain and are clinically used for treating various neurological disorders[42]. Notably, some MAOIs cross-inhibit the MAO-A isoenzyme MAO-B, that co-expressed with MAO-A in the brain (Supplementary Fig. 7)[31]. However, in human macrophages, especially in M2-like immunosuppressive macrophages, MAO-A is the dominant form (i.e., the expression of *MAOA* was about 40-fold higher than that of *MAOB* in M2-like human macrophages; Supplementary Fig. 8)[46]. Of course, other tissues and cells may express significant levels of MAO-B that is subjected to MAOI inhibition and may mediate part of the MAOI-induced therapeutic effects. In our studies, we tested multiple clinically approved MAOIs (phenelzine, clorgyline, moclobemide, and pirlindole) and demonstrated their efficacy in regulating macrophage ROS levels and immunosuppressive polarization, pointing to the possibility of repurposing these drugs for cancer immunotherapy (Figs. 5 and 6). Developing new cancer drugs is extremely costly and time-consuming; drug repurposing offers an economic and speedy pathway to novel cancer therapies because approved drugs have known safety profiles and modes of actions and thus can enter the clinic quickly[62].

MAOIs had been used extensively over two decades after their introduction in the 1950s, but since then their use has declined because of reported side effects and the introduction of other classes of antidepressant drugs[42]. However, these MAOI side effects may be manageable. For instance, a claimed major side effect of MAOIs is the risk of triggering tyramine-induced hypertensive crisis when patients eat tyramine-rich foods such as aged cheese (hence, "cheese effects"), which has led to cumbersome food restrictions[42]. The development of reversible and increasingly MAO-B-selective MAOI agents administered via a transdermal delivery system (i.e., the EMSAM selegiline transdermal system) has largely avoided the tyramine related "cheese effects" and thereby can relieve food restrictions and improve the overall safety of MAOIs[63]. Interest in MAOIs as a major class of antidepressants is reviving, and repurposing MAOIs for cancer immunotherapy can be an attractive application of these potent drugs[42]. Moreover, many cancer patients suffer from depression and anxiety; these overwhelming emotional changes can negatively interfere with the quality of life and cancer treatment efficacy of cancer patients[64]. Repurposing MAOIs for cancer immunotherapy thus may provide cancer patients with antidepression and antitumor dual benefits, making this therapeutic strategy particularly attractive. Nonetheless, caution about drug: food and drug:drug interactions are still relevant for MAOIs' cancer therapy application, evidenced by the side effects (e.g., hypertension) observed in a recent Phase 2 trial of MAOI phenelzine in biochemical recurrent prostate cancer[65].

Because preclinical evidence largely supports combinatorial approaches being necessary to achieve significant antitumor efficacy, most TAM-targeting strategies currently under clinical evaluation are tested in combination with standard chemotherapy or radiation therapy or in combination with T-cell-directed ICB therapies such as PD-1 or/and PD-L1 blockade therapy[26]. In our study, we found that MAOI treatment synergised with anti-PD-1 treatment in suppressing syngeneic mouse tumor growth (Fig. 5k–o), and that intratumoral *MAOA* gene expression levels dictated poor patient survival in melanoma patients receiving anti-PD-1 therapy (Fig. 6r). These data highlight the promise of MAOI treatment as a valuable component for combination cancer therapies.

Interestingly, MAO-A upregulation has been detected in cancerous tissues compared to normal tissues and MAO-A expression has been associated with cancer metastases and decreased cancer-related patient survival for several cancers, including prostate cancer[66,67], lung cancer[68,69], breast cancer[70], glioma[71] and lymphoma[72]. Together with our finding, these studies suggest the possible multifaceted function of MAO-A in promoting certain cancers, through the direct promotion of tumor development and indirect suppression of antitumor immunity. Consequently, MAO-A blockade therapy may provide dual therapeutic benefits for these cancers, by both suppressing tumor metastasis and enhancing antitumor immunity.

In summary, here we identified MAO-A as a critical molecule regulating TAM immunosuppressive polarization and thereby modulating antitumor immunity, and demonstrated the potential of repurposing established MAOI antidepressants for cancer immunotherapy. Future clinical studies are encouraged to investigate the clinical correlations between MAOI treatment and clinical outcomes in cancer patients and to explore the possibility of repurposing MAOIs for combination cancer therapies. Meanwhile, the immune regulatory function of MAO-A certainly goes beyond regulating TAM polarization. Notably, in another recent study, we have identified MAO-A as an immune checkpoint restraining antitumor T-cell immunity through controlling intratumoral T-cell autocrine serotonin signalling[73]. MAO-A's capacity to regulate various components of antitumor immunity is attractive, suggesting that MAO-A blockade may be multifunctional for cancer immunotherapy. It is also likely that MAO-A regulates immune reactions to other diseases such as infectious diseases and autoimmune diseases. Studying the roles of MAO-A in regulating various immune cells under different health and disease conditions will be interesting topics for future research.

Methods

Mice. C57BL/6J (B6), B6.SJL-*Ptprc*^{a}*Pepc*^{b}/BoyJ (CD45.1, BoyJ), 129S-*Maoa*^{tm1Shih}/J (*Maoa* KO)[33] and NOD.Cg-*Prkdc*^{scid} *Il2rg*^{tm1Wjl}/SzJ (NSG) mice were purchased from the Jackson Laboratory (Bar Harbor). *Maoa* KO mice were backcrossed with C57BL/6J mice for more than nine generations at the University of California, Los Angeles (UCLA). Eight- to twelve-week-old female mice were used for all experiments unless otherwise indicated. Due to ethical reasons, we ended experiments before tumor volume surpassed 1000 mm^3. All mice experiments were repeated at least three times unless specifically mentioned. Replicates of each individual experiment are stated in its figure legends. All animals were maintained at the UCLA animal facilities and all animal experiments have complied with all relevant ethical regulations approved by the Institutional Animal Care and Use Committee of UCLA.

Human tumor samples. All human tumor samples were obtained following institutional guidelines under protocols approved by the institutional review boards (IRBs) at the UCLA Medical Center. Primary human ovarian cancer tumor samples were obtained from the operating room at the UCLA Medical Center from consenting patients and experiments have complied with all relevant ethical regulations using IRB-approved protocols (IRB# 10-000727). Tumors specimens were brought back to the laboratory for further analyses. Detailed samples information is provided in Supplementary Table 1, including diagnosis and staging.

Cell lines and viral vectors. The B16-OVA mouse melanoma cell line and the PG13 retroviral packaging cell line were provided by Dr. Pin Wang (University of Southern California, CA)[74]. The MC38 mouse colon adenocarcinoma cell line was provided by M. Bosenberg (Yale)[44]. The HEK 293T and Phoenix-ECO retroviral packaging cell lines, the A375 human melanoma cell line, and the L929 mouse connective tissue cell line were purchased from the American Type Culture Collection (ATCC). The A375-A2-ESO cell line was previously reported[75]. The Phoenix-ECO-MIG, Phoenix-ECO-MIG-*Maoa*, and PG13-ESO-TCR stable virus-producing cell lines were generated in this study. The MIG (MSCV-IRES-GFP) retroviral vector was reported previously[76–78]. MIG-*Maoa* and Retro/ESO-TCR retroviral vectors were generated in this study.

Syngeneic mouse tumor models. B16-OVA melanoma cells (1×10^6 per animal) or MC38 colon cancer cells (5×10^5 per animal) were subcutaneously (s.c.) injected into experimental mice to form solid tumors. In some experiments, mice received an intraperitoneal (i.p.) injection of phenelzine (30 mg/kg/day) to block MAO-A activity. In some experiments, mice received i.p. injection of clodronate liposomes (200 μl/animal, twice per week) to deplete TAMs; mice received i.p. injection of vehicle liposomes (200 μl/animal, twice per week) were included as controls. In some experiments, mice received i.p. injection of anti-mouse PD-1 antibodies (300 μg/animal, twice per week) to block PD-1; mice received i.p. injection of isotype antibodies was included as controls. During an experiment, tumor growth was

monitored twice per week by measuring tumor size using a Fisherbrand™ Traceable™ digital caliper (Thermo Fisher Scientific); tumor volumes were calculated by formula $1/2 \times L \times W^2$. At the end of an experiment, solid tumors were collected and tumor-infiltrating immune cells were isolated for analysis using QPCR, flow cytometry, and/or scRNASeq.

Bone marrow (BM) transfer mouse tumor model. BM cells were collected from femurs and tibias of *Maoa* WT and *Maoa* KO donor mice, and were separately transferred into BoyJ (CD45.1) wild-type recipient mice that were preconditioned with whole-body irradiation (1200 rads). Recipient mice were maintained on antibiotic water (Amoxil, 0.25 mg/ml) for 4 weeks after BM transplantation. Periodical bleedings were performed to monitor immune cell reconstitution using flow cytometry. Tumor inoculation started at 12 weeks post BM transfer when recipient mice were fully immune reconstituted. B16-OVA mouse melanoma cells were s.c. injected into recipient mice to form solid tumors (1×10^6 cells per animal). Tumor growth was monitored twice per week by measuring tumor size using a Fisherbrand™ Traceable™ digital caliper; tumor volumes were calculated by formula $1/2 \times L \times W^2$. At the end of an experiment, tumor-infiltrating immune cells were isolated for analysis using flow cytometry.

Syngeneic mouse tumor-TAM co-inoculation model. Bone marrow cells were collected from *Maoa* WT and *Maoa* KO mice and were cultured in vitro to generate bone marrow-derived macrophages (BMDMs). B16-OVA tumor cells (1×10^6 cells per mouse) and BMDMs (5×10^6 cells per mouse) were mixed and s.c. injected into BoyJ mice to form solid tumors. Tumor growth was monitored twice per week by measuring tumor size using a Fisherbrand™ Traceable™ digital calliper; tumor volumes were calculated by formula $1/2 \times L \times W^2$. At the end of an experiment, tumors were collected and tumor-infiltrating immune cells were isolated for analysis using flow cytometry.

Xenograft human tumor-TAM co-inoculation model. Human peripheral blood mononuclear cells (PBMCs) of healthy donors were obtained from the CFAR Gene and Cellular Therapy Core Laboratory at UCLA, without identification information under federal and state regulations. Human monocytes were isolated from healthy donor PBMCs via magnetic-activated cell sorting (MACS) using human CD14 microbeads (Miltenyi Biotec, 130-050-201) followed by fluorescence-activated cell sorting (FACS; sorted as $hCD45^+hCD11b^+hCD14^+$ cells) using a FACSAria II flow cytometer (BD Biosciences). Human A375 melanoma cells (10×10^6 cells per animal) and purified human monocytes (5×10^6 cells per animal) were mixed and s.c. injected into NSG mice to form solid tumors. Some experimental animals received i.p. injection of MAOI (phenelzine, 30 mg/kg/day) to block MAO-A activity. At the end of an experiment, tumor-associated immune cells were isolated for analysis using flow cytometry.

Tumor-infiltrating immune cell (TII) isolation and analysis. Solid tumors were collected from experimental mice at the termination of a tumor experiment. Tumors were cut into small pieces and smashed against a 70-μm cell strainer (Corning, 07-201-431) to prepare single cells. Immune cells were enriched through gradient centrifugation with 45% Percoll (Sigma-Aldrich, P4937) at 800×*g* for 30 min at 25 °C without braking, followed by treatment with Tris-buffered ammonium chloride buffer to lyse red blood cells according to a standard protocol (Cold Spring Harbor Protocols). The resulting TII isolates were then used for further analysis.

In some experiments, TII isolates were sorted via FACS using a FACSAria II flow cytometer (BD Biosciences) to purify TAMs (sorted as $DAPI^-CD45.2^+CD11b^+Ly6G^-Ly6C^{-/low}F4/80^+$ cells), which were then subjected to QPCR analysis of *Maoa* mRNA expression in TAMs.

In some experiments, TII isolates were sorted via FACS using a FACSAria II flow cytometer (BD Biosciences) to purify immune cells (sorted as $DAPI^-CD45.2^+$ cells), which were then subjected to scRNASeq analysis of gene expression profiling of TIIs.

In some experiments, TII isolates were directly analysed using MACSQuant Analyzer 10 Flow Cytometer (Miltenyi Biotec) to study the cell surface marker expression of TAMs (pre-gated as $CD45.2^+CD11b^+Ly6G^-Ly6C^{-/low}F4/80^+$ cells) and the intracellular effector molecule production of $CD8^+$ T cells (pre-gated as $CD45.2^+TCR\beta^+CD8^+$ cells).

Mouse monocyte isolation. Peripheral blood samples collected from experimental mice were treated with Tris-buffered ammonium chloride buffer to lyse red blood cells according to a standard protocol (Cold Spring Harbor Protocols). The resulting mononuclear cells were sorted via FACS using a FACSAria II flow cytometer (BD Biosciences) to purify monocytes (sorted as $DAPI^-CD45.2^+CD11b^+Ly6G^-Ly6C^+$ cells), which were then subjected to QPCR analysis of *Maoa* mRNA expression.

Mouse bone marrow-derived macrophages (BMDM) culture and polarization. To generate BMDMs, BM cells were collected from femurs and tibias of *Maoa* WT mice and *Maoa* KO mice, and were cultured in C10 medium containing 20% of L929-conditional medium in a 10-cm dish (2×10^6 cells per ml; 12 ml per dish) for 6 days. At day 6, the resulting BMDMs were collected and reseeded in a six-well plate (1×10^6 cells per ml; 2 ml per well) in C10 medium for 24 h, in the presence or absence of recombinant murine IL-4 (10 ng/ml) (Peprotech, 200-04) and IL-13 (10 ng/ml) (Peprotech, 200-13) to induce BMDM immunosuppressive polarization.

In some experiments, MAOIs were added to the *Maoa* WT BMDM polarization culture 30 min prior to adding recombinant murine IL-4 and IL-13, to block MAO-A activity during BMDM polarization. MAOIs studied were phenelzine (Phe, 20 μM) (Sigma-Aldrich), clorgyline (Clo, 20 μM) (Sigma-Aldrich), moclobemide (Moc, 200 μM) (Sigma-Aldrich), and pirlindole (Pir, 20 μM) (R&D Systems). At 24 h after IL-4/IL-13 stimulation, BMDMs were collected for analysis.

In some experiments, H_2O_2 (100 μM) were added to the *Maoa* WT and *Maoa* KO BMDM polarization culture 30 min prior to adding recombinant murine IL-4 and IL-13. At 30 min after IL-4/IL-13 stimulation, BMDMs were collected for WB analysis; at 24 h after IL-4/IL-13 stimulation, BMDMs were collected for flow cytometry and QPCR analysis.

In some experiments, tyramine (100 μM) (Sigma-Aldrich, T90344) was added to the *Maoa* WT and *Maoa* KO BMDM polarization culture 30 min prior to adding recombinant murine IL-4 and IL-13. At 24 h after IL-4/IL-13 stimulation, BMDMs were collected for flow cytometry and QPCR analysis.

Macrophage suppressive function assay. IL-4/IL-13 polarized *Maoa* WT and *Maoa* KO BMDMs were mixed with splenocytes harvested from B6 wild-type mice at 0:1, 1:2, 1:4 or 1:8 ratio, then cultured in a 24-well plate in C10 medium (1×10^6 splenocytes/ml/well), in the presence of plate-bound anti-mouse CD3ε (5 μg/ml) and soluble anti-mouse CD28 (1 μg/ml) for 2 days. At the end of a culture, cells were collected for flow cytometry analysis.

MIG-*Maoa* retroviral vector construction, production, and macrophage transduction. MIG retroviral vector was reported previously[76–78]. Codon-optimised *Maoa* cDNA (synthesised by IDT) was inserted into a MIG retroviral vector to generate the MIG-*Maoa* retroviral vector. Vsv-g-pseudotyped MIG and MIG-*Maoa* retroviruses were produced using HEK 293T virus packaging cells following a standard calcium precipitation method[77,78], and then were used to transduce Phoenix-ECO cells to generate stable cell lines producing ECO-pseudotyped MIG or MIG-*Maoa* retroviruses (denoted as Phoenix-ECO-MIG and Phoenix-ECO-MIG-*Maoa* cell lines, respectively). For virus production, Phoenix-ECO-MIG and Phoenix-ECO-MIG-*Maoa* cells were seeded at a density of 0.8×10^6 cells per ml in D10 medium, and cultured in a 15-cm dish (30 ml per dish) for 2 days. Virus supernatants were then collected and used for macrophage transduction.

BM cells harvested from *Maoa* WT and *Maoa* KO mice were cultured in a six-well plate in C10 medium containing 20% L929-conditional medium (4×10^6 cells/2 ml/well) for 6 days, to differentiate into BMDMs. From day 1 to day 5, cells were spin-infected daily with virus supernatants supplemented with polybrene (10 μg/ml) at 660×*g* at 30 °C for 90 min. At day 6, recombinant murine IL-4 (10 ng/ml) and IL-13 (10 ng/ml) were added to cell culture to induce BMDM immunosuppressive polarization. At day 7, transduced BMDMs were collected for flow cytometry analysis of transduction efficiency (%GFP^+ cells of total cells); GFP^+ BMDMs were sorted via FACS using a FACSAria II flow cytometer (BD Biosciences) and were then used for QPCR analysis of immunosuppressive gene expression.

Human monocyte-derived macrophage (MDM) culture and polarization. Human peripheral blood mononuclear cells (PBMCs) of healthy donors were obtained from the CFAR Gene and Cellular Therapy Core Laboratory at UCLA, without identification information under federal and state regulations. Human monocytes were isolated from healthy donor PBMCs by adherence. Briefly, PBMCs were suspended in serum-free RPMI 1640 media (Corning Cellgro, 10-040-CV) at 10×10^6 cells/ml. In total, 12.5 ml of the cell suspension were added to each 10-cm dish and incubated for an hour in a humidified 37 °C, 5% CO_2 incubator. Medium that contained non-adherent cells was discarded. Dishes were washed twice and adherent monocytes were cultured in C10 media with human M-CSF (10 ng/ml) (Peprotech, 300-25) for 6 days to generate MDMs. At day 6, the resulting MDMs were collected and reseeded in a 6-well plate in C10 medium (1×10^6 cells/ 2 ml/well) for 48 h, in the presence or absence of recombinant human IL-4 (10 ng/ml) (Peprotech, 214-14) and human IL-13 (10 ng/ml) (Peprotech, 214-13) to induce MDM immunosuppressive polarization. In some experiments, MAOIs (phenelzine, 20 μM) were added to the MDM polarization culture 30 min prior to adding recombinant human IL-4 and human IL-13, to block MAO-A activity during MDM polarization. Polarized MDMs were then collected and used for flow cytometry and QPCR analysis or for setting up the 3D human tumor organoid culture experiments.

Human NY-ESO-1-specific TCR-engineered $CD8^+$ T (ESO-T) cells. The Retro/ESO-TCR vector was constructed by inserting into the parental pMSGV vector a synthetic gene encoding an HLA-A2-restricted, NY-ESO-1 tumor antigen-specific human CD8 TCR (clone 3A1)[75]. Vsv-g-pseudotyped Retro/ESO-TCR retroviruses

were generated by transfecting HEK 293T cells following a standard calcium precipitation protocol and an ultracentrifugation concentration protocol; the viruses were then used to transduce PG13 cells to generate a stable retroviral packaging cell line producing GALV-pseudotyped Retro/ESO-TCR retroviruses (denoted as the PG13-ESO-TCR cell line). For virus production, the PG13-ESO-TCR cells were seeded at a density of 0.8×10^6 cells per ml in D10 medium, and cultured in a 15-cm dish (30 ml per dish) for 2 days; virus supernatants were then harvested and stored at −80 °C for future use.

Healthy donor PBMCs were cultured in a 12-well plate in C10 medium (1×10^6 cells/ml/well) for 2 days, stimulated with Dynabeads™ Human T-Activator CD3/CD28 (10 µl/ml) (GIBCO, 11161D) and recombinant human IL-2 (20 ng/ml) (Peprotech). After 2 days, dynabeads were removed and cells were spin-infected with frozen-thawed Retro/ESO-TCR retroviral supernatants supplemented with polybrene (10 µg/ml) at 660×*g* at 30 °C for 90 min following an established protocol[75]. Transduced human $CD8^+$ T cells (denoted as ESO-T cells) were expanded for another 6–8 days in C10 medium containing recombinant human IL-2 (20 ng/ml) (Peprotech) and then cryopreserved for future use. Mock-transduced human $CD8^+$ T cells (denoted as Mock-T cells) were generated as controls.

3D human tumor/TAM/T-cell organoid culture. A375-A2-ESO human melanoma cell line was generated by engineering the parental A375 cell line to over-express a NY-ESO-1 tumor antigen as well as its matching HLA-A2 molecule[75]. Human MDMs were generated from healthy donor PBMCs and polarized with IL-4/IL-13 in the presence or absence of phenelzine treatment. ESO-T cells were generated by engineering healthy donor PBMC $CD8^+$ T cells to express a NY-ESO-1-specific TCR (clone 3A1). The A375-A2-ESO tumor cells, MDMs, and ESO-T cells were mixed at a 2:1:2 ratio. Mixed cells were centrifuged and resuspended in C10 medium at 1×10^5 cells per µl medium. The cell slurry was adjusted to 5 µl per aggregate and was gently transferred onto a microporous membrane cell insert (Millicell, PICM0RG50) using a 20-µl pipet to form a 3D human tumor/TAM/T-cell organoid. Prior to cell transfer, cell inserts were placed in a six-well plate immersed with 1 ml C10 medium. Two days later, the organoids were dissociated by P1000 pipet tip and disrupted through a 70-µm nylon strainer to generate single-cell suspensions for further analysis.

Reagents. Adherent cell line culture medium (denoted as D10 medium) was made of Dulbecco's modified Eagle's medium (DMEM, Corning Cellgro, 10-013-CV) supplemented with 10% fetal bovine serum (FBS, Sigma-Aldrich, F2442) and 1% penicillin–streptomycin–glutamine (Gibco, 10378016). T-cell and macrophage culture medium (denoted as C10 medium) was made of RPMI 1640 (Corning Cellgro, 10-040-CV) supplemented with 10% FBS (Sigma-Aldrich), 1% penicillin–streptomycin–glutamine (Gibco), 0.2% normocin (Invivogen, ant-nr-2), 1% MEM non-essential amino acids solution (Gibco, 11140050), 1% HEPES (Gibco, 15630056), and 1% sodium pyruvate (Gibco, 11360070).

Macrophage culture reagents, including recombinant murine IL-4, recombinant murine IL-13, recombinant human M-CSF, recombinant human IL-4, and recombinant human IL-13, were purchased from PeproTech. T-cell culture reagents, including purified NA/LE anti-mouse CD3ε (clone 145-2C11), anti-mouse CD28 (clone 37.51), anti-human CD3 (clone OKT3), and anti-human CD28 (clone CD28.2), were purchased from BD Biosciences. Recombinant human IL-2 was purchased from PeproTech. Hydrogen peroxide solution was purchased from Sigma-Aldrich (216763).

In vivo PD-1 blocking antibody (clone RMP1-14) and its isotype control (rat IgG2a) were purchased from BioXCell. In vivo TAM depletion clodronate liposomes and their control vehicle liposomes were purchased from Clodrosome.

Monoamine oxidase inhibitors (MAOIs), including phenelzine, moclobemide and clorgyline, were purchased from Sigma-Aldrich. Pirlindole was purchased from R&D systems.

Flow cytometry. Flow cytometry, also known as FACS (fluorescence-activated cell sorting), was used to analyse surface marker and intracellular effector molecule expression in immune cells. Fluorochrome-conjugated monoclonal antibodies specific for mouse CD45.2 (clone 104), CD11b (Clone M1/70), Ly6G (Clone 1A8), F4/80 (Clone BM8), Ly6C (Clone HK1.4), CD206 (Clone C068C2), CD69 (clone H1.2F3), CD86 (Clone GL-1), I-Ab (Clone AF6-120.1), TCRβ (clone H57-597), CD45.1 (Clone A20), CD4 (Clone GK1.5), CD8 (clone 53-6.7), CD25 (clone PC61), CD44 (clone IM7), CD62L (clone MEL-14) and Granzyme B (Clone QA16A02) were purchased from BioLegend. Mouse Fc Block (anti-mouse CD16/32; clone 2.4G2) was purchased from BD Biosciences. Fluorochrome-conjugated monoclonal antibodies specific for human CD45 (clone H130), CD11b (Clone ICRF44), CD14 (Clone HCD14), CD206 (Clone 15-2), CD273 (Clone 24 F.10C12), TCRαβ (clone I26), CD4 (clone OKT4), CD8 (clone SK1), CD44 (clone IM7), CD62L (clone DREG-56), and human Fc Receptor Blocking Solution (TruStain FcX™, 422302) were purchased from BioLegend. Fixable Viability Dye eFluor 506 was purchased from Thermo Fisher Scientific. DAPI (Thermo Fisher Scientific) was included to exclude dead cells in FACS sorting.

To study cell surface marker expression, cells were stained with Fixable Viability Dye followed by Fc blocking and surface marker staining, following a standard procedure as described previously[78]. To study T-cell intracellular cytotoxicity molecule production, intracellular staining of Granzyme B was performed using the BD Cytofix/CytopermTM Fixation/Permeabilization Kit (BD Biosciences, 55474) following the manufacturer's instructions. These cells were co-stained with surface markers to identify $CD8^+$ T cells (gated as $TCR\beta^+CD8^+$ cells in vitro or $CD45.2^+TCR\beta^+CD8^+$ cells in vivo).

Stained cells were analysed using a MACSQuant Analyzer 10 flow cytometer (Miltenyi Biotec); data were analysed using a FlowJo software (BD Biosciences).

Detailed reagent information is provided in Supplementary Table 2.

Western blot (WB). Total protein was extracted using a RIPA lysis buffer (PIERCE, Roche, Thermo Fisher Scientific) supplemented with protease inhibitor cocktail cOmplete Mini (one tablet/10 ml) (Sigma-Aldrich, 4693159001) and phosphatase inhibitor PhosSTOP (one tablet/10 ml) (Sigma-Aldrich, 4906845001), then transferred to pre-cooled Eppendorf tubes. The lysed solution was kept on ice for 30 min and then centrifuged at 15,000×*g* for 5 min at 4 °C. Supernatants were collected and protein concentrations were quantified using a BCA protein assay (PIERCE, Thermo Fisher Scientific, 23225). Equal amounts of protein were loaded and separated by 8% sodium dodecyl sulfate-polyacrylamide gel electrophoresis (SDS-PAGE), and then transferred to an Immunobilon-P PVDF Membrane (Millipore). The membranes were blocked with a SuperBlock™ T20 (TBS) Blocking Buffer (Thermo Fisher Scientific, 37536). Antibodies were diluted in 5% nonfat milk dissolved in washing buffer TBST (20 mM Tris–HCl, 150 mM NaCl, 0.1% Tween-20).

Primary antibodies against mouse Stat6, p-Stat6 (Tyr641), JAK1, p-JAK1 (Tyr1034/1035), JAK2, p-JAK2 (Tyr1008), JAK3, p-JAK3 (Tyr980/981), HRP-labelled anti-rabbit secondary antibodies, and HRP-labelled anti-mouse secondary antibodies were purchased from Cell Signaling Technology. MAO-A antibody was purchased from Abcam (Clone EPR7101). Primary antibodies against β-actin (Santa Cruz Biotechnology) were used as an internal control for total protein extracts. Signals were visualised using a ChemiDoc Image System (Bio-Rad). Data were analysed using Image J software (Bio-Rad). Signal intensity was normalised using housekeeping protein and compared to a sample labelled in azure in each row.

Detailed reagent information is provided in Supplementary Table 2.

Quantitative real-time PCR (QPCR). The total RNA was extracted from cells using TRIzol reagent (Invitrogen, Thermo Fisher Scientific, 15596018) following the manufacturer's instructions. SuperScript III First-strand (Thermo Fisher Scientific, 18080051) was used for reverse transcription. QPCR was performed using a KAPA SYBR FAST qPCR Master Mix (Kapa Biosystems) and a 7500 Real-time PCR System (Applied Biosystems) according to the manufacturers' instructions. Housekeeping gene *Ube2d2* was used as an internal control for mouse immune cells and *ACTB* was used as an internal control for human immune cells. The relative expression of a target gene was calculated using the $2^{\Delta\Delta CT}$ method. All primers used in this study are listed in Supplementary Table 3.

Reactive oxygen species (ROS) measurement. Cells were stained with surface marker antibodies, washed with PBS, then resuspended in pre-warmed PBS (1×10^6 cells/ml/tube) containing 1 µM CM-H2DCFDA (Thermo Fisher Scientific, C6827). After 15 min of incubation at room temperature, cells were immediately washed with cold PBS followed by flow cytometry analysis. ROS levels were measured by oxidation of the CM-H2DCFDA probes that can be read out as the fluorescence intensity at the FITC/488 channel of a flow cytometer.

Single-cell RNA sequencing (scRNAseq). scRNASeq was used to analyse the gene expression profiles of TIIs. B16-OVA tumors were harvested from *Maoa* WT and *Maoa* KO mice to prepare TII suspensions (ten tumors were combined for each group). TII suspensions were then sorted using a FACSAria II flow cytometer to purify immune cells (gated as $DAPI^-CD45.2^+$ cells). Sorted TIIs were immediately delivered to the Technology Center for Genomics & Bioinformatics (TCGB) facility at UCLA for library construction and sequencing. Cells were stained with trypan blue (Thermo Fisher Scientific, T10282) and counted using a Cell Countess II automated cell counter (Thermo Fisher Scientific). 10,000 TIIs from each experimental group were loaded on the Chromium platform (10X Genomics) and libraries were constructed using a Chromium Single Cell 3' library & Gel Bead Kit V2 (10X Genomics, PN-120237) according to the manufacturer's instructions. Libraries were sequenced on an Illumina Novaseq 6000 System, using a Novaseq 6000 S2 Reagent Kit (100 cycles; 20012862, Illumina). Data analysis was performed using a Cellranger Software Suite (10X Genomics). BCL files were extracted from the sequencer and used as inputs for the cellranger pipeline to generate the digital expression matrix for each sample. Then cellranger aggr command was used to aggregate the two samples into one digital expression matrix. The matrix was analysed using Seurat, an R package designed for single-cell RNA sequencing. Specifically, cells were first filtered to have at least 300 UMIs (unique molecular

identifiers), at least 100 genes, and at most 5% mitochondrial gene expression; only one cell did not pass the filter. The filtered matrix was normalised using the Seurat function NormalizeData. Variable genes were found using the Seurat function FindVariableGenes. The matrix was scaled to regress out the sequencing depth for each cell. Variable genes that had been previously identified were used in principle component analysis (PCA) to reduce the dimensions of the data. Following this, 13 PCs were used in UMAP to further reduce the dimensions to 2. The same 13 PCs were also used to group the cells into different clusters by the Seurat function FindClusters. Next, marker genes were found for each cluster and used to define the cell types. Subsequently, two clusters of TAMs (identified by co-expression of *Mrc1* and *Cd86* signature genes) were extracted and compared between the *Maoa* WT and *Maoa KO* samples. Expression distribution of immunosuppressive and immunostimulatory signature genes in *Maoa* WT and *Maoa* KO TAMs were compared and presented in violin plots. scRNAseq datasets have been uploaded to GEO database with an accession number GSE153615.

Tumor immune dysfunction and exclusion (TIDE) computational method. TIDE analyses were conducted as previously described (http://tide.dfci.harvard.edu)[45]. Two functions of the TIDE computational method were used: (1) the prioritisation function and (2) the survival correlation function.

The prioritisation function of TIDE was used to rank a target gene by its immune dysfunction/risk score, which for TAMs, was calculated as its gene expression log-fold change of M2-like/M1-like MDMs[45]. A transcriptome dataset (GSE35449) was used, which was generated by microarray analysis of the gene expression profiling of in vitro polarized M1-like or M2-like human MDMs[46]. A score higher than 1 indicates the preferential expression of a gene in M2-like compared to M1-like human macrophages. The higher a score is, the more "prioritised" a gene is in relating to TAM immunosuppressive polarization.

The survival correlation function of TIDE was used to study the clinical data correlation between the intratumoral *MAOA* gene expression and patient survival. Four patient cohorts were analysed: ovarian cancer (GSE26712)[48], lymphoma (GSE10846)[49], breast cancer (GSE9893)[50], and melanoma (PRJEB23709)[51]. For each patient cohort, tumor samples were divided into two groups: *MAOA*-high (samples with *MAOA* expression one standard deviation above the average) and *MAOA*-low (remaining samples) groups. The association between the intratumoral *MAOA* gene expression levels and patient overall survival (OS) was computed through the two-sided Wald test in the Cox-PH regression and presented in Kaplan–Meier plots. *p* value indicates the comparison between the *MAOA*-low and *MAOA*-high groups and was calculated by two-sided Wald test in a Cox-PH regression.

Statistical analysis. GraphPad Prism 6 (GraphPad Software) was used for the graphic representation and statistical analysis of the data. All data were presented as the mean ± standard error of the mean (SEM). A two-tailed Student's *t* test was used for comparison between groups. Multiple comparisons were performed using an ordinary one-way ANOVA followed by Tukey's multiple comparisons test or using a two-way ANOVA followed by Sidak's multiple comparisons test. $p < 0.05$ was considered statistically significant. ns not significant; $^{*}p < 0.05$; $^{**}p < 0.01$; $^{***}p < 0.001$. For scRNAseq data analysis, Wilcoxon rank-sum test was utilised to determine the *p* value between the two groups. Benjamini–Hochberg Procedure was used to adjust the *p* value to reduce the false-positive rate. For the Kaplan–Meier plot of the overall patient survival for ovarian cancer, lymphoma, breast cancer, and melanoma with different *MAOA* levels, the *p* value was calculated by two-sided Wald test in a Cox-PH regression.

Reporting summary. Further information on research design is available in the Nature Research Reporting Summary linked to this article.

Data availability

The scRNAseq datasets generated in this study have been deposited in the GEO database under accession code GSE153615. Patient cohorts data analysed, including ovarian cancer (GSE26712)[48], lymphoma (GSE10846)[49], and breast cancer (GSE9893)[50], are publicly available from the GEO database. Patient cohort data of PD-1/PD-L1 blockade therapy in melanoma is publicly available from NCBI BioProject database (PRJEB23709)[51]. The human macrophage transcriptome dataset is publicly available from the GEO database (GSE35449)[46]. TIDE computational method analyses were conducted on TIDE website (http://tide.dfci.harvard.edu)[45]. The remaining data associated with this study are presented in the Article or Supplementary Information. Further information and requests may be directed to and will be fulfilled by the corresponding author, Lili Yang (liliyang@ucla.edu). Source data are provided with this paper.

Received: 25 June 2020; Accepted: 7 April 2021;
Published online: 10 June 2021

References

1. Jenkins, R. W., Thummalapalli, R., Carter, J., Canadas, I. & Barbie, D. A. Molecular and genomic determinants of response to immune checkpoint inhibition in cancer. *Annu. Rev. Med.* **69**, 333–347 (2018).
2. Ribas, A. Releasing the brakes on cancer immunotherapy. *N. Engl. J. Med.* **373**, 1490–1492 (2015).
3. Topalian, S. L. et al. Safety, activity, and immune correlates of anti-PD-1 antibody in cancer. *N. Engl. J. Med.* **366**, 2443–2454 (2012).
4. Dougan, M., Dranoff, G. & Dougan, S. K. Cancer immunotherapy: beyond checkpoint blockade. *Annu. Rev. Cancer Biol.* **3**, 55–75 (2019).
5. Sharpe, A. H. Introduction to checkpoint inhibitors and cancer immunotherapy. *Immunol. Rev.* **276**, 5–8 (2017).
6. Topalian, S. L., Taube, J. M., Anders, R. A. & Pardoll, D. M. Mechanism-driven biomarkers to guide immune checkpoint blockade in cancer therapy. *Nat. Rev. Cancer* **16**, 275–287 (2016).
7. Baumeister, S. H., Freeman, G. J., Dranoff, G. & Sharpe, A. H. Coinhibitory pathways in immunotherapy for cancer. *Annu. Rev. Immunol.* **34**, 539–573 (2016).
8. Sharpe, A. H. & Pauken, K. E. The diverse functions of the PD1 inhibitory pathway. *Nat. Rev. Immunol.* **18**, 153–167 (2018).
9. Peranzoni, E. et al. Macrophages impede CD8 T cells from reaching tumor cells and limit the efficacy of anti-PD-1 treatment. *Proc. Natl Acad. Sci. USA* **115**, E4041–E4050 (2018).
10. Cassetta, L. & Kitamura, T. Targeting tumor-associated macrophages as a potential strategy to enhance the response to immune checkpoint inhibitors. *Front. Cell Dev. Biol.* **6**, 38 (2018).
11. Fujimura, T., Kambayashi, Y., Fujisawa, Y., Hidaka, T. & Aiba, S. Tumor-associated macrophages: therapeutic targets for skin cancer. *Front. Oncol.* **8**, 3 (2018).
12. Awad, R. M., De Vlaeminck, Y., Maebe, J., Goyvaerts, C. & Breckpot, K. Turn back the TIMe: targeting tumor infiltrating myeloid cells to revert cancer progression. *Front. Immunol.* **9**, 1977 (2018).
13. Wynn, T. A., Chawla, A. & Pollard, J. W. Macrophage biology in development, homeostasis and disease. *Nature* **496**, 445–455 (2013).
14. Lavin, Y., Mortha, A., Rahman, A. & Merad, M. Regulation of macrophage development and function in peripheral tissues. *Nat. Rev. Immunol.* **15**, 731–744 (2015).
15. Laviron, M. & Boissonnas, A. Ontogeny of tumor-associated macrophages. *Front. Immunol.* **10**, 1799 (2019).
16. Biswas, S. K. Metabolic reprogramming of immune cells in cancer progression. *Immunity* **43**, 435–449 (2015).
17. Fujimura, T., Kakizaki, A., Furudate, S., Kambayashi, Y. & Aiba, S. Tumor-associated macrophages in skin: how to treat their heterogeneity and plasticity. *J. Dermatol. Sci.* **83**, 167–173 (2016).
18. DeNardo, D. G. et al. CD4(+) T cells regulate pulmonary metastasis of mammary carcinomas by enhancing protumor properties of macrophages. *Cancer Cell* **16**, 91–102 (2009).
19. Noy, R. & Pollard, J. W. Tumor-associated macrophages: from mechanisms to therapy. *Immunity* **41**, 49–61 (2014).
20. Arlauckas, S. P. et al. Arg1 expression defines immunosuppressive subsets of tumor-associated macrophages. *Theranostics* **8**, 5842–5854 (2018).
21. Gabrilovich, D. I. & Nagaraj, S. Myeloid-derived suppressor cells as regulators of the immune system. *Nat. Rev. Immunol.* **9**, 162–174 (2009).
22. Geiger, R. et al. L-arginine modulates T cell metabolism and enhances survival and anti-tumor activity. *Cell* **167**, 829–842 (2016).
23. Schuette, V. et al. Mannose receptor induces T-cell tolerance via inhibition of CD45 and up-regulation of CTLA-4. *Proc. Natl Acad. Sci. USA* **113**, 10649–10654 (2016).
24. Biswas, S. K. & Mantovani, A. Macrophage plasticity and interaction with lymphocyte subsets: cancer as a paradigm. *Nat. Immunol.* **11**, 889–896 (2010).
25. Bercovici, N., Guerin, M. V., Trautmann, A. & Donnadieu, E. The remarkable plasticity of macrophages: a chance to fight cancer. *Front. Immunol.* **10**, 1563 (2019).
26. DeNardo, D. G. & Ruffell, B. Macrophages as regulators of tumour immunity and immunotherapy. *Nat. Rev. Immunol.* **19**, 369–382 (2019).
27. Tiihonen, J. et al. Genetic background of extreme violent behavior. *Mol. Psychiatry* **20**, 786–792 (2015).
28. Gibbons, A. American association of physical anthropologists meeting. Tracking the evolutionary history of a "warrior" gene. *Science* **304**, 818 (2004).
29. Dias, V., Junn, E. & Mouradian, M. M. The role of oxidative stress in Parkinson's disease. *J. Parkinsons Dis.* **3**, 461–491 (2013).
30. Tong, J. et al. Brain monoamine oxidase B and A in human parkinsonian dopamine deficiency disorders. *Brain* **140**, 2460–2474 (2017).
31. Finberg, J. P. & Rabey, J. M. Inhibitors of MAO-A and MAO-B in psychiatry and neurology. *Front. Pharm.* **7**, 340 (2016).
32. Riederer, P. & Laux, G. MAO-inhibitors in Parkinson's Disease. *Exp. Neurobiol.* **20**, 1–17 (2011).

33. Bortolato, M. et al. Social deficits and perseverative behaviors, but not overt aggression, in MAO-A hypomorphic mice. *Neuropsychopharmacology* **36**, 2674–2688 (2011).
34. Zhang, Y. et al. ROS play a critical role in the differentiation of alternatively activated macrophages and the occurrence of tumor-associated macrophages. *Cell Res.* **23**, 898–914 (2013).
35. He, C., Ryan, A. J., Murthy, S. & Carter, A. B. Accelerated development of pulmonary fibrosis via Cu,Zn-superoxide dismutase-induced alternative activation of macrophages. *J. Biol. Chem.* **288**, 20745–20757 (2013).
36. Zhang, L. et al. Oxidative stress and asthma: proteome analysis of chitinase-like proteins and FIZZ1 in lung tissue and bronchoalveolar lavage fluid. *J. Proteome Res.* **8**, 1631–1638 (2009).
37. Fu, C. et al. Activation of the IL-4/STAT6 signaling pathway promotes lung cancer progression by increasing M2 myeloid cells. *Front. Immunol.* **10**, 2638 (2019).
38. Van Dyken, S. J. & Locksley, R. M. Interleukin-4- and interleukin-13-mediated alternatively activated macrophages: roles in homeostasis and disease. *Annu. Rev. Immunol.* **31**, 317–343 (2013).
39. Bhattacharjee, A. et al. IL-4 and IL-13 employ discrete signaling pathways for target gene expression in alternatively activated monocytes/macrophages. *Free Radic. Biol. Med.* **54**, 1–16 (2013).
40. Park, S. J. et al. Astrocytes, but not microglia, rapidly sense H(2)O(2)via STAT6 phosphorylation, resulting in cyclooxygenase-2 expression and prostaglandin release. *J. Immunol.* **188**, 5132–5141 (2012).
41. Duhe, R. J. Redox regulation of Janus kinase: the elephant in the room. *JAKSTAT* **2**, e26141 (2013).
42. Wimbiscus, M., Kostenko, O. & Malone, D. MAO inhibitors: risks, benefits, and lore. *Cleve Clin. J. Med.* **77**, 859–882 (2010).
43. Bortolato, M., Chen, K. & Shih, J. C. Monoamine oxidase inactivation: from pathophysiology to therapeutics. *Adv. Drug Deliv. Rev.* **60**, 1527–1533 (2008).
44. Homet Moreno, B. et al. Response to programmed cell death-1 blockade in a murine melanoma syngeneic model requires costimulation, CD4, and CD8 T cells. *Cancer Immunol. Res.* **4**, 845–857 (2016).
45. Jiang, P. et al. Signatures of T cell dysfunction and exclusion predict cancer immunotherapy response. *Nat. Med.* **24**, 1550–1558 (2018).
46. Beyer, M. et al. High-resolution transcriptome of human macrophages. *PLoS ONE* **7**, e45466 (2012).
47. Thomas, R. et al. NY-ESO-1 based immunotherapy of cancer: current perspectives. *Front. Immunol.* **9**, 947 (2018).
48. Bonome, T. et al. A gene signature predicting for survival in suboptimally debulked patients with ovarian cancer. *Cancer Res.* **68**, 5478–5486 (2008).
49. Lenz, G. et al. Stromal gene signatures in large-B-cell lymphomas. *N. Engl. J. Med.* **359**, 2313–2323 (2008).
50. Chanrion, M. et al. A gene expression signature that can predict the recurrence of tamoxifen-treated primary breast cancer. *Clin. Cancer Res.* **14**, 1744–1752 (2008).
51. Gide, T. N. et al. Distinct immune cell populations define response to anti-PD-1 monotherapy and anti-PD-1/anti-CTLA-4 combined therapy. *Cancer Cell* **35**, 238–255 (2019). e236.
52. Talbot, S., Foster, S. L. & Woolf, C. J. Neuroimmunity: physiology and pathology. *Annu. Rev. Immunol.* **34**, 421–447 (2016).
53. Kerage, D., Sloan, E. K., Mattarollo, S. R. & McCombe, P. A. Interaction of neurotransmitters and neurochemicals with lymphocytes. *J. Neuroimmunol.* **332**, 99–111 (2019).
54. Cannarile, M. A. et al. Colony-stimulating factor 1 receptor (CSF1R) inhibitors in cancer therapy. *J. Immunother. Cancer* **5**, 53 (2017).
55. Guerriero, J. L. et al. Class IIa HDAC inhibition reduces breast tumours and metastases through anti-tumour macrophages. *Nature* **543**, 428–432 (2017).
56. Beatty, G. L. et al. CD40 agonists alter tumor stroma and show efficacy against pancreatic carcinoma in mice and humans. *Science* **331**, 1612–1616 (2011).
57. Kaneda, M. M. et al. PI3Kgamma is a molecular switch that controls immune suppression. *Nature* **539**, 437–442 (2016).
58. Ji, L. et al. Slc6a8-mediated creatine uptake and accumulation reprogram macrophage polarization via regulating cytokine responses. *Immunity* **51**, 272–284 (2019).
59. Zhang, J. Q. et al. Macrophages and CD8(+) T cells mediate the antitumor efficacy of combined CD40 ligation and imatinib therapy in gastrointestinal stromal tumors. *Cancer Immunol. Res.* **6**, 434–447 (2018).
60. Falkenberg, K. J. & Johnstone, R. W. Histone deacetylases and their inhibitors in cancer, neurological diseases and immune disorders. *Nat. Rev. Drug Discov.* **13**, 673–691 (2014).
61. Zheng, W. & Pollard, J. W. Inhibiting macrophage PI3Kgamma to enhance immunotherapy. *Cell Res.* **26**, 1267–1268 (2016).
62. Schein, C. H. Repurposing approved drugs on the pathway to novel therapies. *Med. Res. Rev.* **40**, 586–605 (2019).
63. Jessen, L., Kovalick, L. J. & Azzaro, A. J. The selegiline transdermal system (emsam): a therapeutic option for the treatment of major depressive disorder. *Pharmacy Ther.* **33**, 212–246 (2008).
64. Shoval, G. et al. Adherence to antidepressant medications is associated with reduced premature mortality in patients with cancer: a nationwide cohort study. *Depress Anxiety* **36**, 921–929 (2019).
65. Gross, M. E. et al. Phase 2 trial of monoamine oxidase inhibitor phenelzine in biochemical recurrent prostate cancer. *Prostate Cancer Prostatic Dis.* **24**, 61–68 (2021).
66. Wu, J. B. et al. Monoamine oxidase A mediates prostate tumorigenesis and cancer metastasis. *J. Clin. Investig.* **124**, 2891–2908 (2014).
67. Wu, J. B. et al. MAOA-dependent activation of Shh-IL6-RANKL signaling network promotes prostate cancer metastasis by engaging tumor-stromal cell interactions. *Cancer Cell* **31**, 368–382 (2017).
68. Li, J., Yu, H., Ma, Y. F., Zhao, M. & Tang, J. Identification of genes associated with lung cancer by bioinformatics analysis. *Eur. Rev. Med. Pharm. Sci.* **21**, 2397–2404 (2017).
69. Liu, F. et al. Increased expression of monoamine oxidase A is associated with epithelial to mesenchymal transition and clinicopathological features in non-small cell lung cancer. *Oncol. Lett.* **15**, 3245–3251 (2018).
70. Sun, W. Y., Choi, J., Cha, Y. J. & Koo, J. S. Evaluation of the expression of amine oxidase proteins in breast cancer. *Int. J. Mol. Sci.* **18**, 2775 (2017).
71. Kushal, S. et al. Monoamine oxidase A (MAO A) inhibitors decrease glioma progression. *Oncotarget* **7**, 13842–13853 (2016).
72. Li, P. C. et al. Monoamine oxidase A is highly expressed in classical Hodgkin lymphoma. *J. Pathol.* **243**, 220–229 (2017).
73. Wang, X. et al. Targeting monoamine oxidase A for T cell-based cancer immunotherapy. *Sci. Immunol.* **6**, eabh2383 (2021).
74. Liu, Y. et al. In situ modulation of dendritic cells by injectable thermosensitive hydrogels for cancer vaccines in mice. *Biomacromolecules* **15**, 3836–3845 (2014).
75. Bethune, M. T. et al. Isolation and characterization of NY-ESO-1-specific T cell receptors restricted on various MHC molecules. *Proc. Natl Acad. Sci. USA* **115**, E10702–E10711 (2018).
76. Di Biase, S. et al. Creatine uptake regulates CD8 T cell antitumor immunity. *J. Exp. Med.* **216**, 2869–2882 (2019).
77. Smith, D. J. et al. Genetic engineering of hematopoietic stem cells to generate invariant natural killer T cells. *Proc. Natl Acad. Sci. USA* **112**, 1523–1528 (2015).
78. Li, B. et al. miR-146a modulates autoreactive Th17 cell differentiation and regulates organ-specific autoimmunity. *J. Clin. Investig.* **127**, 3702–3716 (2017).

Acknowledgements

We thank the University of California, Los Angeles (UCLA) animal facility for providing animal support; the UCLA AIDS Institute/CFAR Virology Core/Gene and Cell Therapy Core/Humanized Mouse Core for providing human cells and tissues and humanized mice services; the UCLA BSCRC Flow Cytometry Core Facility and D. Chen (UCLA) for cell-sorting support; the UCLA Technology Center for Genomics & Bioinformatics (TCGB) facility for assisting with scRNAseq; the Laboratories of Marcus Bosenberg (Yale) and Antoni Ribas (UCLA) for providing the MC38 cell line; the Laboratory of Pin Wang (University of Southern California, Los Angeles, California, USA) for providing the B16-OVA and PG13 cell lines and the Life Science Editors and E.L. Siegler for editing the manuscript. This work was supported by a Research Career Development Award from the STOP CANCER Foundation (to L.Y.), a BSCRC-RHF Research Award from the Rose Hills Research Foundation (to L.Y.), a JCCC/BSCRC Ablon Scholars Award from UCLA (to L.Y.), and a Magnolia Council Senior Investigator Grant Award from the Tower Cancer Research Foundation (to L.Y.). J.Y. was a predoctoral fellow supported by the UCLA Broad Stem Cell Research Center (BSCRC) Predoctoral Fellowship. Z.L. was a postdoctoral fellow supported by the UCLA Tumor Immunology Training Grant (USHHS Ruth L. Kirschstein Institutional National Research Service Award # T32 CA 009120). S.Z. was a predoctoral fellow supported by the UCLA Medical Scientist Training Program Grant (T32-GM008042). Y-R.L. was a predoctoral fellow supported by the UCLA Whitcome Predoctoral Fellowship in Molecular Biology.

Author contributions

Y.-C.W. and L.Y. designed the study, analysed the data, and wrote the manuscript. Y.-C. W. performed all experiments, with the assistance from X.W. (Figs. 1b–h, 2m, 5j and Figs. S5b–f, S6c and d), J.Y. (Figs. 3l, m and 6k–m), F.M. and M.P. (Fig. 1k–n and Fig. S1e– k), Z.L. (Fig. S1a, and Figs. 3d, 6d and Fig. S6e–h), Y.Z., S.Z., J.H., A.T. and N.C. (Figs. 1b–h and 2a–f), X.M. (Fig. 4h–j), Y.-R.L. (Fig. 6j–m), A.N. and S.M. (Fig. 6n and Table S1). Y.-C.W. created Figs. 1b, 2a, g, 3a, h, 4a, b, k, 5a, f, k, 6h, k and Supplementary Figs. 3c, 5g, l, o, 6c, e, 7. X.W., S.Z. and X.M. helped with critical reading of the manuscript. L.Y. supervised the entire study.

Competing interests

L.Y., Y-C.W. and X.W. are inventors on patents relating to this study filed by UCLA. The remaining authors declare no competing interests.

Additional information

Supplementary information The online version contains supplementary material available at https://doi.org/10.1038/s41467-021-23164-2.

Correspondence and requests for materials should be addressed to L.Y.

Peer review information *Nature Communications* thanks Mitchell E. Gross and the other, anonymous reviewer(s) for their contribution to the peer review of this work.

Reprints and permission information is available at http://www.nature.com/reprints

Publisher's note Springer Nature remains neutral with regard to jurisdictional claims in published maps and institutional affiliations.

Open Access This article is licensed under a Creative Commons Attribution 4.0 International License, which permits use, sharing, adaptation, distribution and reproduction in any medium or format, as long as you give appropriate credit to the original author(s) and the source, provide a link to the Creative Commons license, and indicate if changes were made. The images or other third party material in this article are included in the article's Creative Commons license, unless indicated otherwise in a credit line to the material. If material is not included in the article's Creative Commons license and your intended use is not permitted by statutory regulation or exceeds the permitted use, you will need to obtain permission directly from the copyright holder. To view a copy of this license, visit http://creativecommons.org/licenses/by/4.0/.

© The Author(s) 2021

Chapter 4: Methods for Studying Mouse and Human Invariant Natural Killer T Cells.

Methods for Studying Mouse and Human Invariant Natural Killer T Cells

Author: Yang Zhou[1, *], Yan-Ruide Li[1, *], Samuel Zeng[1], and Lili Yang[1,2,3,4, §]

Author Affiliation:

[1]Department of Microbiology, Immunology & Molecular Genetics, University of California, Los Angeles, Los Angeles, CA 90095, USA

[2]Eli and Edythe Broad Center of Regenerative Medicine and Stem Cell Research, University of California, Los Angeles, Los Angeles, CA 90095, USA

[3]Jonsson Comprehensive Cancer Center, David Geffen School of Medicine, University of California, Los Angeles, Los Angeles, CA 90095, USA

[4]Molecular Biology Institute, University of California, Los Angeles, CA 90095, USA

*These authors contributed equally to this work.

[§]Corresponding author. Email: liliyang@ucla.edu.

Address Correspondence to:

Lili Yang, Ph.D.

Associate Professor

Department of Microbiology, Immunology & Molecular Genetics

University of California, Los Angeles

Los Angeles, CA 90095, USA.

Email: liliyang@ucla.edu

Abstract

Invariant natural killer T (iNKT) cells are a unique subset of T lymphocytes that recognize lipid antigens presented by nonpolymorphic major histocompatibility complex (MHC) I-like molecule CD1d. iNKT cells play essential roles in regulating immune responses against cancer, viral infection, autoimmune disease, and allergy. However, the study and application of iNKT cells have been hampered by their very small numbers (0.01-1% in mouse and human blood). Here, we describe protocols to 1) generate mouse iNKT cells from mouse mononuclear cells or from mouse hematopoietic stem cells engineered with iNKT T cell receptor (TCR) gene (denoted as mMNC-iNKT cells or mHSC-iNKT cells, respectively), 2) generate human iNKT cells from human peripheral blood mononuclear cells or from human HSC cells engineered with iNKT TCR gene (denoted as hPBMC-iNKT cells or hHSC-iNKT cells, respectively), and 3) characterize mouse and human iNKT cells *in vitro* and *in vivo*.

Key Words

Invariant natural killer T (iNKT) cell, CD1d, T cell receptor (TCR), alpha-galactosylceramide (α-GalCer), glycolipid, gene engineering, hematopoietic stem cell (HSC), cancer immunotherapy

1. Introduction

Invariant natural killer T (iNKT) cells are a unique subpopulation of innate T lymphocytes that express both natural killer (NK) cell markers and a restricted αβ T cell receptor (TCR). The restricted TCR is comprised of a canonical invariant TCRα chain (Vα14-Jα18 in mice; Vα24-Jα18 in human) paired with a semi-variant TCRβ chain (mostly Vβ8.2 in mice; mostly Vβ11 in human) [1, 2]. The early developmental stages of iNKT cells are similar to classical MHC-restricted $CD4^+$ and $CD8^+$ conventional T (Tc) cells [2, 3]. Lymphoid precursor cells arising from hematopoietic stem cells (HSCs) migrate to the thymus,

undergo rearrangement of the TCRβ chain, and develop into CD4 and CD8 double-positive (DP) thymocytes. DP thymocytes then randomly rearrange their TCRα loci to generate intact TCR complexes expressed on the cell surface. However, unlike Tc cells that are selected by peptides presented on MHC-I or MHC-II of thymic epithelial cells, iNKT DP precursors are positively selected by glycolipids presented on CD1d expressed by DP thymocytes themselves [4]. The iNKT TCR-glycolipid-CD1d interaction, along with signals through the signaling lymphocytic activated molecules (SLAM) receptor family, provides co-stimulation for the further development of iNKT cells [3]. Owing to their unique developmental path, iNKT cells exit the thymus expressing a memory T cell phenotype. They further mature in the periphery through upregulating their expression of NK cell markers [5].

Functionally mature iNKT cells are powerful modulators of the immune response [4, 6, 7, 8]. Their most notable function is secreting copious amounts of cytokines upon stimulation, including T helper (Th)1-like (IFN-γ), Th2-like (IL-4, IL-13), Th17-like (IL-17, IL-22), and regulatory (IL-10) cytokines [4]. What cytokines are produced depends on the mechanism of cell activation, the location, and the iNKT cell subsets. iNKT cells also produce cytolytic proteins such as perforin and granzyme B, and surface molecules involved in cytotoxicity such as Fas Ligand (FasL) and tumor necrosis factor α (TNF-α)-related apoptosis-inducing ligand (TRAIL) [9, 10]. Collectively, iNKT cells can profoundly influence many other immune cells, including dendritic cells, macrophages, neutrophils, NK cells, T cells, and B cells, thereby orchestrating the immune responses during infection, autoimmune disease [11], allergy [12], and cancer [9, 13, 14].

However, the extremely low number of iNKT cells, particularly in human peripheral blood (0.01-1% in healthy humans; 0.001-0.1% in cancer patients), is a significant obstacle for studying iNKT cell biology and developing iNKT cell-based therapies [5]. In our lab, we have developed methods to effectively generate large numbers of mouse and human iNKT cells through genetic engineering of

HSCs (denoted as mHSC-iNKT cells and hHSC-iNKT cells, respectively [15, 16, 17]); we also routinely expand mouse iNKT cells from mouse mononuclear cells (denoted as mMNC-iNKT cells), and expand human iNKT cells from human peripheral blood mononuclear cells (denoted as hPBMC-iNKT cells) following established protocols with certain modifications [15, 17]. Here, we share our lab protocols on 1) generating mMNC-iNKT and mHSC-iNKT cells; 2) generating hPBMC-iNKT and hHSC-iNKT cells; 3) characterizing mouse and human iNKT cells with *in vitro* and *in vivo* assays.

2. Materials

Prepare all media in sterile hood (unless otherwise indicated).

2.1 **Generation of mouse iNKT cells**

2.1.1 Isolate and expand mMNC-iNKT cells:

- Mice: C57BL/6J (B6-WT) mouse
- Fetal bovine serum (FBS)
- Phosphate-buffered saline (PBS)
- 33% Percoll: 33% (vol/vol) of 100% Percoll, 67% (vol/vol) of 1x PBS solution
- 40% Percoll: 40% (vol/vol) of 100% Percoll, 60% (vol/vol) of 1x PBS solution
- 60% Percoll: 60% (vol/vol) of 100% Percoll, 40% (vol/vol) of 1x PBS solution
- Anti-mouse CD16/32 Fc block
- Anti-mouse CD19 microbeads
- Anti-mouse CD1d-Tetramer-PE
- Anti-PE microbeads
- 70 μm cell strainer
- Mouse iNKT culture medium: C10 medium supplemented with recombinant mouse IL-2 (final concentration 10 ng/ml) and IL-12 (final concentration 1 ng/ml)
- Equipment: Magnetic beads separator (MACS), MACS Columns (LS column, LD column), water bath, sonicator, irradiator, pH meter

2.1.2 Generate mHSC-iNKT cells:

- Mice: C57BL/6J (B6-WT) mice
- Mouse iNKT TCR sequence [15]

- 5-Fluorouracil (*see* **Note 1**)
- Mouse iNKT retrovirus (*see* **Note 2**)
- Human embryonic kidney cell line HEK293.T
- Polybrene
- Recombinant mouse IL-3
- Recombinant mouse IL-6
- Murine stem cell factor (SCF)
- Antibiotics: sulfmethoxazole and trimethoprim
- Other reagents, material, and equipment were described in Section 2.1

2.2 **Generation of human iNKT cells**

2.2.1 Isolate and expand hPBMC-iNKT cells:

- Human blood from healthy donors
- Ficoll-Paque plus
- Anti-human iNKT MicroBeads
- Recombinant human IL-7
- Recombinant human IL-15
- Tris-Buffered ammonium chloride buffer (TAC buffer or red blood cell lysis buffer): 0.16 M NH_4CL, 0.17 M Tris, ddH_2O
- MACS sorting buffer: phosphate-buffered saline (PBS), 0.5% bovine serum albumin (BSA), and 2 mM EDTA
- C10 medium: RPMI1640 supplemented with 10% (vol/vol) FBS, 1% (vol/vol) penicillin/streptomycin/glutamine, 1% (vol/vol) MEM NEAA, 10 mM HEPES, 1 mM sodium pyruvate and 50 μM β-ME
- Human iNKT culture medium: C10 medium supplemented with recombinant human IL-7 (final 10 ng/ml) and human IL-15 (final concentration 10 ng/ml)
- α-GalCer medium: C10 medium supplemented with α-Galactosylceramide (final concentration 5 μg/ml)

2.2.2 Generate hHSC-iNKT cells:

- Mice: NOD.Cg-Prkdc^{SCID}Il2rg^{tm1Wjl}/SzJ (NOD/SCID/IL-2Rγ$^{-/-}$, NSG) mice
- Human CD34$^+$ hematopoietic stem cells (CD34$^+$ HSCs) (*see* **Note 3**)
- Human fetal thymus tissues
- Human iNKT TCR sequences [17]
- Retronectin

- 2% BSA
- X-VIVO-15 serum-free medium
- Carprofen
- Recombinant human IL-3
- Human Flt3-Ligand (Flt3-L)
- Human stem cell factor (hSCF)
- Human thrombopoietin (TPO)
- 6-well Non-tissue culture treated plates
- Other reagents, materials, and equipment were described in Section 2.1

2.3 **Characterization of mouse or human iNKT cells**

2.3.1 Phenotype analysis of mouse or human iNKT cells:

- Antibodies (*see* **Table 1**)
- Phorbol-12-myristate-13-acetate (PMA): 1 mg PMA dissolved in 400 µl DMSO
- Ionomycin: 1 mg Ionomycin dissolved in 400 µl DMSO
- GolgiStop
- BD Fixation/Permeabilization solution kit
- Recombinant mouse and human IFN-γ (ELISA, standard)
- Recombinant mouse and human IL-4 (ELISA, standard)
- Anti-mouse and human IFN-γ (ELISA, capture)
- Anti-mouse and human IFN-γ (ELISA, detection)
- Anti-mouse and human IL-4 (ELISA, capture)
- Anti-mouse and human IL-4 (ELISA, capture)
- Nunc-Immuno ELISA plate
- ELISA coating buffer: 325 ml of 0.1 M $NaHCO_3$, 50 ml of 0.1 M Na_2CO_3, PH = 9.4, store at room temperature (RT)
- ELISA borate buffered saline (BBS) dilution buffer: 6.07 g H_3BO_3 (0.1 M), 7.32 g NaCl (0.012 M), 20 g 2% BSA, 1 L ddH_2O, PH = 8, store at 4 °C
- ELISA wash buffer (20 X): 1 M Tris (PH = 8.0), 163.5 g NaCl, 10 ml Tween-20
- Tetramethylbenzidine (TMB)
- Streptavidin-HRP conjugate
- TMB reaction stop solution (1 M H_3PO_4): 68.2 ml 85% phosphoric acid, 1 L ddH_2O, store at RT

2.3.2 Function analysis of mouse or human iNKT cells:

- Human CD14 microbeads
- NK isolation kit
- Mouse melanoma cell line B16.F10
- Human multiple myeloma cell line MM.1S
- Human multiple myeloma cell line MM.1S-FG and MM.1S-hCD1d-FG (*see* **Note 4**)
- Human chronic myelogenous leukemia cancer cell line K562
- Human chronic myelogenous leukemia cancer cell line K562-FG (*see* **Note 5**)
- Human melanoma cell line A375
- Human melanoma cell line A375-A2-Eso-FG (*see* **Note 6**)
- D-luciferin
- Isoflurane
- Zeiss Stemi 2000-CS microscope (Carl Zeiss AG)
- IVIS 100 imaging system (Xenogen/PerkinElmer)

3. Methods

3.1 Generation of mMNC-iNKT cells

3.1.1 Prepare MNCs from mouse spleen and liver (Figure 1A)

1. Euthanize mice by CO_2.
2. Clean the skin by spraying with 70% ethanol. Dissect the mouse and collect the spleen, located on the left flank. The liver is preferably flushed of circulating blood prior to collection. To do so, shift the intestines away from the body to uncover the inferior vena cava and use a 5 ml syringe to push approximately 5 ml of PBS through it. The liver should turn yellow/white as a result.
3. Harvested spleen and liver should be collected in separate tubes containing 3-5 ml sterile C10 medium. (*see* **Note 7**)
4. In a sterile hood, disperse the liver and spleen into single cell suspensions by placing each tissue in a 70 µm cell strainer and mashing with a plunger from a 3 ml syringe. Rinse the plunger and cell strainer with C10 medium and transfer the cell suspension into a new 15 ml conical tube.
5. Liver and spleen samples are processed differently. Steps 6-11 refer to processing the liver while steps 12-13 refer to processing the spleen.
6. Add 3 ml of 60% Percoll into a new 15 ml tube.

7. Spin down (600 *g*) the liver cells and resuspend the cell pellet in 3 ml of 40% Percoll in PBS. (*see* **Note 8**)
8. Gently layer the 40% Percoll cell suspension on top of the 60% Percoll. To do this, tilt the conical tube until it is almost horizontal and add the 40% suspension drop by drop. If performed correctly, one should see a sharp demarcation between the 40% and 60%.
9. Spin at 800 *g* for 30 min with no brakes at RT. (*see* **Note 9**)
10. Aspirate the floating debris. There should be a thin layer of cells around the 3 ml line. Collect those cells while avoiding the red blood cells found at the bottom of the tube.
11. Add 5 ml C10 medium to the collection and mix well. Spin down for 5 min at 4 °C. Aspirate the supernatant and resuspend in 5 ml C10 medium.
12. Spin down (600 *g*) the spleen cells and resuspend in 5 ml TAC buffer at room temperature for 10-20 min to lyse the red blood cells.
13. Add an additional 5 ml C10 medium to neutralize the buffer, spin down (600 *g*). Aspirate the supernatant and resuspend the pellet with 5 ml C10 medium. Cells clumps may be observed. Filter through a 70 µm cell strainer to remove dead cell clumps.
14. Count live cell numbers. Cell resuspension can be kept at 4 °C, ready for sorting or FACS staining. (*see* **Note 10**)

3.1.2 Magnetic separation of mMNC-iNKT cells

1. Resuspend MNCs from 3.1.1 in 2% FBS/PBS buffer.
2. Centrifuge the cell mixture, aspirate the supernatant, and resuspend in 100 µl of 2% FBS/PBS.
3. Add 10 µl of anti-mouse CD16/CD32 mAb to block nonspecific binding to Fcγ receptors and incubate for 5 min at 4 °C.
4. Add 20 µl of anti-mouse CD19 microbeads and incubate for 15 min at 4 °C.
5. Meanwhile, prepare a LD column and equilibrate with 2 ml of 2% FBS/PBS buffer.
6. Wash the cells with 2% FBS/PBS buffer and centrifugation at 600 *g* for 5 min at 4 °C.
7. Resuspend cells in 500 µl of buffer and add to the LD column.
8. Collect the $CD19^-$ fraction into a clean 15 ml conical tube. Wash the column twice with 1 ml of 2% FBS/PBS each time and keep collecting the flow through.
9. Spin down the $CD19^-$ fraction and stain with 20 µl of anti-mouse CD1d-Tetramer-PE in 30 µl of 2% FBS/PBS for 20 min on ice.
10. Wash the cells with 2% FBS/PBS buffer and centrifugation at 600 *g* for 5 min at 4 °C.
11. Stain with 20 µl of anti-PE microbeads in 100 µl of 2% FBS/PBS for 15 min on ice.
12. Meanwhile, prepare another LD column and equilibrate with 2 ml of 2% FBS/PBS
13. Wash the cells with 2% FBS/PBS buffer and centrifuge at 600 *g* for 5 min at 4 °C. Resuspend cells in 500 µl of buffer.

14. Load cell suspension into LD column. Mouse iNKT cells will bind to the column by positive selection. Wash the column twice with 1 ml of 2% FBS/PBS each time. The flow through can be discarded but can also be kept for troubleshooting.
15. Remove the LD column from the magnetic field and elute the cells from column.
16. The purity of the iNKT cells by checked by FACS staining and can be further improved via FACS sorting (Figure 1B).

3.1.3 *In vitro* expansion of mMNC-iNKT cells

1. Count the number of mMNC-iNKT cells from 3.1.2.
2. Seed cell at 2 x 10^6 cells per well in the C10 medium, with or without the addition α-GalCer of (final concentration 100 ng/ml) for 5 days. (*see* **Note 11**)
3. On day 3 and day 5, collect cells and run assays for mMNC-iNKT cell expansion using flow cytometry.

3.2 Generation of mouse HSC-iNKT cells (mHSC-iNKTs)

3.2.1 Generate HSC-iNKT mouse (*see* **Note 12**) (Figure 1C)

1. Day 0, treat B6 mice with 5-fluorouracial (250 μg per gram body weight).
2. Day 5, harvest bone marrow (BM) cells from mouse and culture the cells for 4 days in BM cell culture medium containing recombinant mouse IL-3 (20 ng/ml), IL-6 (50 ng/ml), and SCF (50 ng/ml).
3. Day 7 and 8, BM cells were spin-infected with retroviruses (*see* **Note 13**) supplemented with 8 μg/ml of polybrene, at 770 *g*, 30 °C for 90 min.
4. Day 9, BM cells were collected and intravenously injected into B6 recipients that had received 1,200 rads of total body irradiation (~ 1-2 x 10^6 transduced BM cells per recipient). (*see* **Note 14**)
5. The BM recipient mice were maintained on the combined antibiotics sulfamethoxazole and trimethoprim oral suspension in a sterile environment for 6-8 weeks until analysis or use for subsequent experiments.

3.2.2 Isolate and expand mHSC-iNKT cells (refer 3.1)

3.3 Generation of hPBMC-iNKT cells

3.3.1 Isolate PBMCs from human peripheral blood (Figure 2A)

1. Obtain peripheral blood from healthy donors in blood collection tubes with heparin 1,000 U/ml.
2. Centrifuge at 400 *g* for 15 min with no brakes at RT.
3. Aspirate the supernatant and resuspend the cell pellet with PBS (10-12 ml/tube).
4. Transfer the mixture to a 50 ml conical tube. Wash once more using RT PBS (10-12 ml/tube).
5. Aspirate the supernatant and resuspend with 14 ml PBS.
6. Gently layer 14 ml of room temperature Ficoll on top of the mixture, using a 25 ml pipette (*see* **Note 15**)
7. Centrifuge at 970 *g* for 20 min with no brakes at RT.

8. Aspirate the upper PBS layer.
9. Using a 5 ml pipette, carefully collect the PBMCs at the interface.
10. Wash with 10-20 ml PBS and centrifuge at 400 *g* for 7 min at RT.
11. Aspirate the supernatant and resuspend the PBMC pellet in 10 ml TAC buffer for 10-20 min at RT.
12. Centrifuge at 600 *g* for 5 min and remove the supernatant.
13. Wash PBMCs with C10 medium once and resuspend cells in 10 ml of C10 medium.
14. Count live cell numbers.

3.3.2 Magnetic separation of hPBMC-iNKT cells

1. Count the number of cells in PBMC sample. (*see* **Note 16**)
2. Centrifuge cell suspension at 300 *g* for 10 min.
3. Aspirate supernatant completely and resuspend cell pellet in 400 µl of MACS sorting buffer per 1 x 10^8 total cells.
4. Add 100 µl of anti-human iNKT microbeads per 1 x 10^8 total cells. Mix well and incubate for 15 min in the refrigerator (2−8 °C).
5. Wash cells by adding 1−2 mL of buffer per 1 x 10^8 cells and centrifuge at 300 *g* for 10 min. Aspirate supernatant completely and resuspend up to 1 x 10^8 cells in 500 µl of buffer.
6. Place column in the magnetic field of a suitable MACS Separator.
7. Equilibrate column by rinsing with the appropriate amount of buffer. (LS: 3 ml)
8. Apply cell suspension into the column. Collect flow-through containing unlabeled cells. (*see* **Note 17**)
9. Wash column with the appropriate amount of buffer. Collect unlabeled cells that pass through and combine with the effluent. (LS: 3 x 3 mL)
10. Remove column from the separator and place it on a clean 15 ml conical tube.
11. Pipette 3 ml of buffer onto the column. Immediately flush out the magnetically labeled cells by firmly pushing the plunger into the column. (*see* **Note 18**)
12. Check the purity of human iNKT cells with FACS staining.

3.3.3 *In vitro* expansion of hPBMC-iNKT cells

1. Count the number of PBMC-iNKT cells from Magnetic separation. (Usually around 5 x 10^8 PBMC will yield 0.5 - 2 x 10^6 iNKT cells.)
2. Load a portion of the negative fraction (1 - 2 x 10^8 per 5 ml) with α-GalCer (5 µg/ml) (*see* **Note 19**) and irradiate (~70% yield, 6,000 rads); freeze down the remaining negative portion.
3. Seed cells at 1 x 10^6 iNKT: 2 x 10^6 α-GalCer-pulsed PBMC per 3 ml C10 medium per well of a 6-well plate. Add IL-7 and IL-15 at 10 ng/ml to the culture.
4. Monitor cell growth daily. As cells reach saturation, add C10 medium containing human IL-7 and IL-15 at 10 ng/ml and split cultures.

5. Cells can expand 5-10 fold and reach ~80% iNKT cell confluency during the first week. At day 7, cells can be restimulated (repeat steps 2&3). Cells can expand around 10-fold per stimulation.
6. Take a small aliquot of iNKT culture for FACS staining (Figure 2B).
7. The culture reaches > 95% iNKT cell during the second week. iNKT cells can be frozen down and kept in liquid nitrogen for long-term storage. (*see* **Note 20**)

3.4 Generation of human HSC-iNKT cells

3.4.1 Generate HSC-iNKT humanized mouse (Figure 2C) (*see* **Note 21**)

1. Day 1, thaw and pre-stimulate $CD34^+$ PBSCs.
    a) Coat 6-well Non-tissue culture treated plates with retronectin (RN, 20 μg per vial in PBS) at RT for 2 hours.
    b) Aspirate and replace with 1 ml of 2% BSA for 30 min at RT.
    c) Aspirate and replace with 2 ml PBS. (*see* **Note 22**)
    d) Thaw $CD34^+$ PBSC using X-VIVO-15 medium, spin at 300 *g* for 7 min.
    e) Aspirate supernatant and resuspend in 5 ml of X-VIVO-15 medium and count cell number.
    f) Spin down at 300 *g* for 7 min and aspirate supernatant.
    g) Prepare 10 ml of X-VIVO-15 medium supplemented with hSCF (50 ng/ml), hFLT3L (50 ng/ml), hTPO (50 ng/ml), and hIL-3 (10 ng/ml).
    h) Resuspend $CD34^+$ cells in X-VIVO-15/hSCF/hFLT3L/hTPO/hIL-3 medium (1×10^6 cells/ml).
    i) Aspirate PBS in RN-coated well and seed the cells (1×10^6 per well).
    j) Incubate at 37 °C, 5% CO_2.
2. Day 2, transduce $CD34^+$ PBSCs with lentivirus (*see* **Note 23**).
    a) Thaw concentrated virus supernatant on ice.
    b) Pipet thawed supernatant and add directly to well (*see* **Note 24**). Rock plate gently to mix.
    c) Incubate cells at 37 °C, 5% CO_2 for 24 hours.
3. Day 3, prepare thymus pieces and intravenously inject transduced PBSCs to NSG mice.
    a) Prepare fetal thymus fragments and irradiate with 500 rads. (*see* **Note 25**)
    b) Incubate irradiated thymus in C10 medium with antibiotics until surgery. Make sure to wash thymus thoroughly and keep on ice until surgery.
    c) Irradiate NSG mice with 270 rads.
    d) Harvest and count transduced human $CD34^+$ cells 24 hours post transduction, then resuspend in X-VIVO-15 medium. (*see* **Note 26**)
    e) Implant thymus pieces under the kidney capsule of pre-irradiated NSG mouse. Additionally, give retro-orbital injections of transduced PBSCs to each mouse.

f) Suture and staple the incision.

g) Subcutaneously inject 300 μl of 1:100 carprofen diluted in PBS. (*see* **Note 27**)

4. Day 4, 5, daily injection with 300 μl of 1:100 carprofen diluted in PBS.
5. Day 7, remove the staples and monitor the conditions of BLT-iNKT mice.
6. Starting from week 6 post injection, bleed mice monthly and check human cell reconstitution by FACS staining. (*see* **Note 28**)

3.4.2 hHSC-iNKT cells from humanized mouse (Figure 2D)

1. Euthanize mice by CO_2.
2. Place mouse in dorsal recumbency and clean the skin by spraying with 70% ethanol.
3. Cut the skin and expose both the abdomen and chest.
4. Puncture the heart with 26-gauge on 1 ml syringe to collect blood in a heparin-coated collection tube.
5. Collect the lung, liver, spleen and bone marrow from humanized mouse and store the tissues on ice.
6. Disperse tissues into mononuclear cell suspension.
   a) For blood, incubate in 5 ml TAC buffer for 20 min at RT; spin down to remove supernatant and resuspend in 1 ml C10 medium. Store at 4 °C. Sample is ready for staining (refer 3.5.1)
   b) For spleen, lung, and liver, mash tissues in C10 medium through a 70 μm cell strainer using plungers from 5 ml syringes. Collect the single cell suspension in a 15 ml conical tubes, spin down to remove supernatant, and resuspend in 14 ml 33% Percoll in PBS (spleen samples can skip Percoll separation and directly proceed to TAC lysis). Spin at 800 *g* for 30 min with no brakes at RT. Aspirate the supernatant and resuspend the pellet in 5 ml TAC buffer. Incubate for 10 min at RT, then add additional C10 medium and filter through cells strainer. Spin down and resuspend in fresh C10 medium. Store samples at 4 °C. Samples are ready for staining or cryopreservation (refer to 3.5.1)
   c) For bone marrow, use forceps to hold leg bones over a 15 ml conical tube and flush with C10 medium using 25-gauge needle fitted onto a 10 ml syringe. Spin down to remove the supernatant and resuspend in 10 ml TAC buffer. Incubate for 10 min at RT, then filter through a 70 μm cell strainer. Spin down, aspirate the supernatant, and wash with 2 ml C10 medium. Resuspend the sample in C10 medium, store at 4 °C. Sample is ready for staining or cryopreservation (refer 3.5.1)

3.4.3 *In vitro* expansion of hHSC-iNKT cells

1. Healthy donor PBMCs were loaded with α-GalCer (by culturing 1 x 10^8 PBMCs in 5 ml C10 medium containing 5 μg/ml α-GalCer for 1 hour in 6-well TC plate), irradiated at 6,000 rads, and then used to stimulate iNKT cells.
2. To expand iNKT cells, pooled hHSC-iNKT humanized mouse tissue cells were mixed with α-GalCer-pulsed PBMCs (ratio 1:1 or 1:1.5; eg. 1 x 10^6 iNKT tissue cells were mixed with 1.5 x 10^6 irradiated α-GalCer-pulsed PBMCs) and cultured in C10 medium for 7 days. Cells were plated in 6-well plate (2.5 x 10^6/ml, 3

ml/well). Recombinant human IL-7 (10 ng/ml) and IL-15 (10 ng/ml) were added to cell cultures starting from day 2. Cells were split 1:2 once confluent (about every 2-3 days).

3. On day 7, cell cultures were collected and iNKT cells were sorted out using flow cytometry (identified as $hCD45^{+}hTCR\alpha\beta^{+}6B11^{+}$ cells).
4. The sorted iNKT cells (> 99% purify based on flow cytometry analysis) were expanded further with α-GalCer-pulsed PBMCs and human IL-7/IL-15 for another 7 to 14 days. (*see* **Note 29**)
5. Expanded iNKT cells were aliquoted and frozen in LN storage tanks (eg.1 x 10^7 cells per vial for *in vitro* assay and 1 x 10^8 cells per vial for *in vivo* assay).

3.5 Characterization of mouse or human iNKT cells

3.5.1 iNKT cell phenotype analysis

1. Surface and intracellular marker staining (Figures 1D, 1E, and 2E).
    a) Aliquot cells into labeled FACS tubes.
    b) Wash cells with 1 ml C10 media, spin down, aspirate the supernatant.
    c) Wash cells with 1 ml PBS, spin down, aspirate the supernatant.
    d) Resuspend cells in 50 µl PBS with human FcR Block and Fixable Viability Dye e506. (*see* **Note 30**)
    e) Incubate cells at 4 °C for 15 min shielded from light.
    f) Wash cells with 1 ml PBS, spin down, aspirate the supernatant.
    g) Resuspend cells in 50 µl PBS with antibody cocktails.
    h) Incubate cells at 4 °C for 15 min shielded from light.
    i) Wash cells with 1 ml PBS, spin down, aspirate the supernatant.
    j) For surface staining, resuspend the cell pellet in 100-200 µl PBS for flow cytometry.
    k) For intracellular staining, add 250 µl of BD fixation/permeabilization buffer to the cell pellet.
    l) Incubate cells at 4 °C for 20-30 min, shielded from light.
    m) Spin at 600 *g* for 5 min, aspirate the supernatant.
    n) Wash twice with BD washing buffer.
    o) Spin and resuspend the cell pellet in 50 µl intracellular antibodies cocktail.
    p) Incubate cells at 4 °C for 30 min shielded from light.
    q) Wash cells twice with 1ml wash buffer.
    r) Resuspend cells in 100-200 µl PBS for flow cytometry.
2. Stimulate cytokine production (PMA/Ionomycin stimulation)
    a) Resuspend cells at 1 x 10^6/ml in C10 medium containing PMA (final concentration 50 ng/ml) and ionomycin (final concentration 500 ng/ml).
    b) Transfer 1ml of cells into capped FACS tubes.

c) Add GolgiStop to cells (4 μl GolgiStop per 6 ml of C10 medium) and tightly close caps on FACS tubes.

d) Incubate at 37 °C, 5% CO2 for 4-6 hours.

e) Samples are ready for FACS staining (refer 3.5.1.1).

3. ELISA (following standard protocol from BD bioscience) (Figure 1F)

a) Coat Nunc Immunoplates with purified capturing antibody diluted in ELISA coating buffer. Add 50 μl/well and incubate for 2 hours at 37 °C or overnight at 4 °C.

b) Wash plate 4 times with ELISA wash buffer.

c) Block plate with 100 μl/ well of ELISA BBS buffer. Incubate for 30 min at 37 °C or overnight at 4 °C.

d) Wash plate 4 times with ELISA wash buffer.

e) Add samples at 25 μl or 50 μl per well. Incubate for 3 hours at 37 °C or 4 °C overnight.

f) Wash plate 4 times with ELISA wash buffer.

g) Add 50 μl of the biotinylated detection antibody diluted in BBS solution buffer. Incubate for 45 min at RT.

h) Wash plate 4 times with ELISA wash buffer.

i) Add 50 μl/ well of the streptavidin-HRP, diluted 1:1000 in BBS dilution buffer. Incubate for 30 min at RT, shielded from light.

j) Wash plate 8 times with ELISA wash buffer.

k) Mix the TMB developing solution and add 50 μl/ well. Incubate at RT.

l) Monitor the blue color change and stop reaction by adding 50 μl/ well of TMB reaction stop solution.

m) Read absorbance at 450 nm within 30 min.

3.5.2 iNKT cell function analysis

1. mHSC-iNKT cell *in vivo* antitumor efficacy study: mouse B16 melanoma lung metastasis mouse model [15] (Figures 1G-1I)

a) C57BL/6J (B6) mice received intravenous (i.v.) injection of 0.5 - 1 × 10^6 B16.F10 melanoma cells to model lung metastasis over the course of 2 weeks.

b) On day 3 post tumor challenge, the experimental mice received i.v. injection of 1 × 10^6 bone marrow-derived dendritic cells (BMDCs) that were either unloaded or loaded with α-GalCer.

c) On day 14, mice were humanely euthanized, and their lungs were collected and analyzed for melanoma metastasis by counting tumor nodules.

2. hHSC-iNKT cell tumor-attacking mechanism study [17] (Figure 2F)

a) *in vitro* direct tumor cell killing assay. Human multiple myeloma cell line MM.1S was used. MM.1S-FG or MM.1S-hCD1d-FG tumor cells (5-10 x 10^3 cells per well) were co-cultured with hHSC-iNKT cells (ratio 1:1, 1:2, 1:5, and 1:10) in Corning 96-well clear bottom black plates for 24-48 hours, in X-VIVO™ 15 medium with or without the addition of α-GalCer (100 ng/ml). At the end of culture, live tumor cells were quantified by adding 150 mg/ml of D-Luciferin to cell cultures and reading out luciferase activities. In order to verify CD1d-dependent tumor killing mechanism, we blocked CD1d by adding 10 mg/ml LEAF™ purified anti-human CD1d antibody or LEAF™ purified mouse IgG2b κ isotype control antibody to tumor cell cultures at least one hour prior to adding hHSC-iNKT cells. At the end of culture, live tumor cells were quantified by adding D-Luciferin to cell cultures and reading out luciferase activities.

b) *in vitro* NK adjuvant effect assay. Primary human NK cells were isolated from healthy donor PBMCs through an NK Cell Isolation Kit according to the manufacturer's instructions. K562-FG cells (5 x 10^4 cells per well) were co-cultured with NK cells and hHSC-iNKT cells (at ratio of 1: 2: 2) in Corning 96-well clear bottom black plates for 24 hours, in C10 medium with or without α-GalCer-pulsed irradiated PBMCs as antigen presenting cells (APCs). Live tumor cells were quantified by adding D-Luciferin (150 mg/ml) to the cell cultures and reading out luciferase activities.

c) *in vitro* dendritic cells (DC)/cytotoxic T lymphocyte (CTL) adjuvant effect assay. $CD1d^+$/HLA-$A2^+$ human monocyte-derived dendritic cells (MoDCs) were generated by isolating $CD14^+$ monocytes from HLA-$A2^+$ healthy donor PBMCs using anti-human CD14 beads, followed by a 4-days culture in R10 medium supplemented with recombinant human GM-CSF (100 ng/ml) and IL-4 (20 ng/ml). The NY-ESO-1 specific $CD8^+$ human CTLs were co-cultured with $CD1d^+$/HLA-$A2^+$ MoDCs in C10 medium for 3 days, with or without hHSC-iNKT cells (cell ratio 1:1:1) and α-GalCer (100 ng/ml). Tumor-killing potential of ESO-T cells was measured by adding A375-A2-ESO-FG tumor cells (1:1 ratio to input ESO-T cells) to the ESO-T/MoDC co-culture 24 hours post co-culture setup, and quantifying live tumor cells by luciferase activity reading in another 24 hours. (*see* **Note 31**)

d) *in vitro* macrophage inhibition assay. $CD14^+$ monocytes were isolated from healthy donor PBMCs, followed by co-culturing with hHSC-iNKT cells (ratio 1:1) for 24-48 hours in C10 medium with or without the addition of α-GalCer (100 ng/ml). At the end of culture, cells were collected for flow cytometry analysis.

3. hHSC-iNKT cell *in vivo* antitumor efficacy study: MM.1S human multiple myeloma xenograft NSG mouse model [17] (Figures 2G-2I)

a) NSG mice were pre-conditioned with 175 rads of total body irradiation and inoculated with 0.5 - 1 x 10^6 MM.1S-hCD1d-FG or MM.1S-FG cells intravenously (day 0) to develop multiple myeloma over the course of about 3 weeks.

b) Three days post-tumor inoculation (day 3), mice received i.v. injection of vehicle (PBS) or 1 x 10^7 hHSC-iNKT cells. Recombinant human IL-15 was intraperitoneally injected to experimental animals to support the peripheral maintenance of hHSC-iNKT cells twice per week starting from day 3 (500 ng per animal per injection).

c) The tumor burden was monitored twice per week by bioluminescence (BLI) measurement.

d) At around week 3, mice were humanely euthanized (refer to 3.4.2) and tissues (peripheral blood, spleen, liver, and bone marrow) were collected for flow cytometry analysis.

4. Notes

1. 5-Fluorouracil (5-FU) is a chemotherapy drug used to treat cancer. 5-FU can inhibit thymidylate synthetase function during pyrimidine synthesis. The carcinogenicity and acute toxicity of 5-FU require proper handling from lab personnel.
2. The generation of mouse iNKT TCR gene delivery retroviral vector was described in our previous publication [15].
3. Human $CD34^+$ HSCs are commercially available from HemaCare Corporation (Northridge, California, USA).
4. Human multiple myeloma (MM) cell line MM.1S, human chronic myelogenous leukemia cancer cell line K562, and human melanoma cell line A375 were all purchased from the American Type Culture Collection (ATCC) (Manassas, Virginia, USA) and cultured in ATCC recommended media. The stable MM.1S-FG and MM.1S-hCD1d-FG tumor cell lines were engineered by transducing the parental MM.1S cell line with the lentiviral vectors encoding the intended gene(s) to overexpress human CD1d, and/or firefly luciferase and enhanced green fluorescence protein (GFP) dual-reporters (FG). $CD1d^+$ and/or GFP^+ cells were sorted by flow cytometry 72 hours post viral transduction to generate stable cell lines.
5. The stable K562-FG tumor cell line was engineered by transducing the parental K562 cell line with lentiviral vectors encoding FG. GFP^+ cells were sorted by flow cytometry post 72 hours of virus transduction to generate stable cell line.
6. The stable A375-A2-Eso-FG tumor cell line was engineered by transducing the parental A375 cell line with lentiviral vectors encoding human HLA-A2.1, human NY-ESO-1, and FG.
7. Keeping tissues on ice during processing improves the viability of cells.
8. 33%, 40% and 60% Percoll can be prepared beforehand and stored long term at 4 °C. However, Percoll must be warmed back to RT before usage.

9. Centrifuge must be equilibrated to RT before starting and the centrifuge brakes must be turned off. Excessive deceleration can remix the separating layers.
10. Cells from spleen and liver can be combined for *in vitro* expansion if needed. Cells from multiple mice can be combined if needed.
11. mMNC-iNKT cells may be expanded and cultured *in vitro* for up to 3 weeks using repetitive stimulations with anti-CD3ε and anti-CD28 every 7-8 days [18]. α-GalCer stimulation leads to apoptosis and is not suitable for long-term expansion of mouse iNKT cells [18].
12. We have established a B6-miNKT mouse model through genetic engineering of hematopoietic stem cells [15] to produce large numbers of iNKT cells. Compared to B6-WT mice, B6-miNKT mice provide a significantly higher yield of iNKT cells.
13. Spin infections on two sequential days increase retrovirus transduction rate. Preferably, the second infection should be performed within 12-15 hours after the first one to infect cells at different stages of the cell cycle.
14. For a secondary BM transfer, fresh whole BM cells harvested from the primary BM recipients are intravenously injected into secondary B6 recipient mice that had received 1,200 rads of total body irradiation (~1 x 10^7 total BM cells per recipient). Details were described in previous publications [15, 16].
15. Tilt the tube and bring the pipette close to surface of the blood/PBS mixture. Slowly pipette out 1-2 ml. Then detach the pipette to allow gravity to dispense the reminder of the Ficoll. When the flow stops, reattach the pipette to push out any remaining Ficoll before removing the pipette from the conical tube. Be extremely careful at this step to make sure that the interface is not disturbed.
16. Choose the right column to use based on the sample cell number. For example, if there are ~2 x 10^8 total PBMCs, use one LS column.
17. Do not let the column dry out and avoid adding bubbles into the column. Bubbles inside the column can interfere with the sample and decrease selection efficacy.
18. To increase the purity, the eluted fraction can be enriched over a second column. Repeat the magnetic separation procedure as described if needed.
19. α-GalCer glycolipid and DMSO are immiscible at RT. To prepare the stock α-GalCer (1 μg/μl), add the proper volume of DMSO into the α-GalCer powder and heat it at 80 °C in a water bath for 10 minutes, followed by 10 minutes of sonication at 50 °C. Then, vortex the vial for a full 2 minutes until the solution turns clear. Aliquot it into glass vials and store them in a -20 °C freezer. To prepare

the α-GalCer working solution (5 μg/ml), heat the aliquot at 80 °C for 5 min followed by 5 min of sonicating at 50 °C. Then vortex the aliquot for a full 60 seconds and add 200 μl of pre-warmed C10 medium. Sonicate for another 5 min and vortex for 60 seconds. Add the rest of the pre-warmed C10 medium to make the final concentration 5 μg/ml. α-GalCer aliquots from -20 °C are single-used. Do not refreeze after diluting with media.

20. Cell expansion fold is donor-dependent. iNKT cells from different donors can be *in vitro* expanded for up to three weeks.
21. Standard BLT (human bone marrow-liver-thymus engrafted NOD/SCID/$\gamma c^{-/-}$) humanized mouse is established by co-implanting human fetal liver and thymus pieces under the renal capsule of NSG mouse together with intravenously injection of human $CD34^+$ HSCs. In our modified approach, only thymus pieces are placed under the renal capsule together with intravenous injection of engineered $CD34^+$ HSC.
22. RN-coated plate with PBS can be left for several hours in the hood.
23. Pre-stimulate $CD34^+$ cells for 12-18 hours before transduction. One option is to coat the plate in the late afternoon and seed cells at around 6pm. The next morning, add the virus for transduction.
24. The generation of human iNKT lentivirus is described in our prior publication [15]. Do not vortex, just very gently mix the concentrated virus. If necessary, adding Poloxamer and PEG-2 can improve virus transduction rate [19].
25. Both fresh and frozen fetal thymus can be used for implantation. Fetal thymus should be pre-cut into $1mm^3$ cube size. Each mouse can be implanted with 1-2 pieces of thymus fragments.
26. Keep small portions of un-transduced and transduced $CD34^+$ cells in X-VIVO-15 media supplemented with cytokines post virus transduction for a 72-hours culture. Collect cells and perform intracellular staining of Vβ11 to detect the virus transduction efficacy.
27. Carprofen works as painkiller to relieve the pain from surgery. It can be substitute with other analgesics based on institution recommendation.
28. The viral transduction rate, the quality of human fetal thymus and the quality of surgery will all contribute to the quality of HSC reconstitutions. BLT-iNKT mice can live around 6 months to 1 year.
29. Sorted iNKT cells are expected to expand 10-fold in the first week and another 10-fold in the second week.
30. Optimize antibody dilution beforehand.

31. NY-ESO-1 specific $CD8^+$ human cytotoxic T lymphocytes (CTLs, or ESO-T cells) were generated through engineering human $CD34^+$ HSCs with a TCR gene encoding a 1G4 TCR (HLA-A2-restricted, NY-ESO-1 tumor antigen-specific) and differentiating the TCR gene-engineered HSCs into CD8+ CTLs in an Artificial Thymic Organoid (ATO) culture [17].

Figures

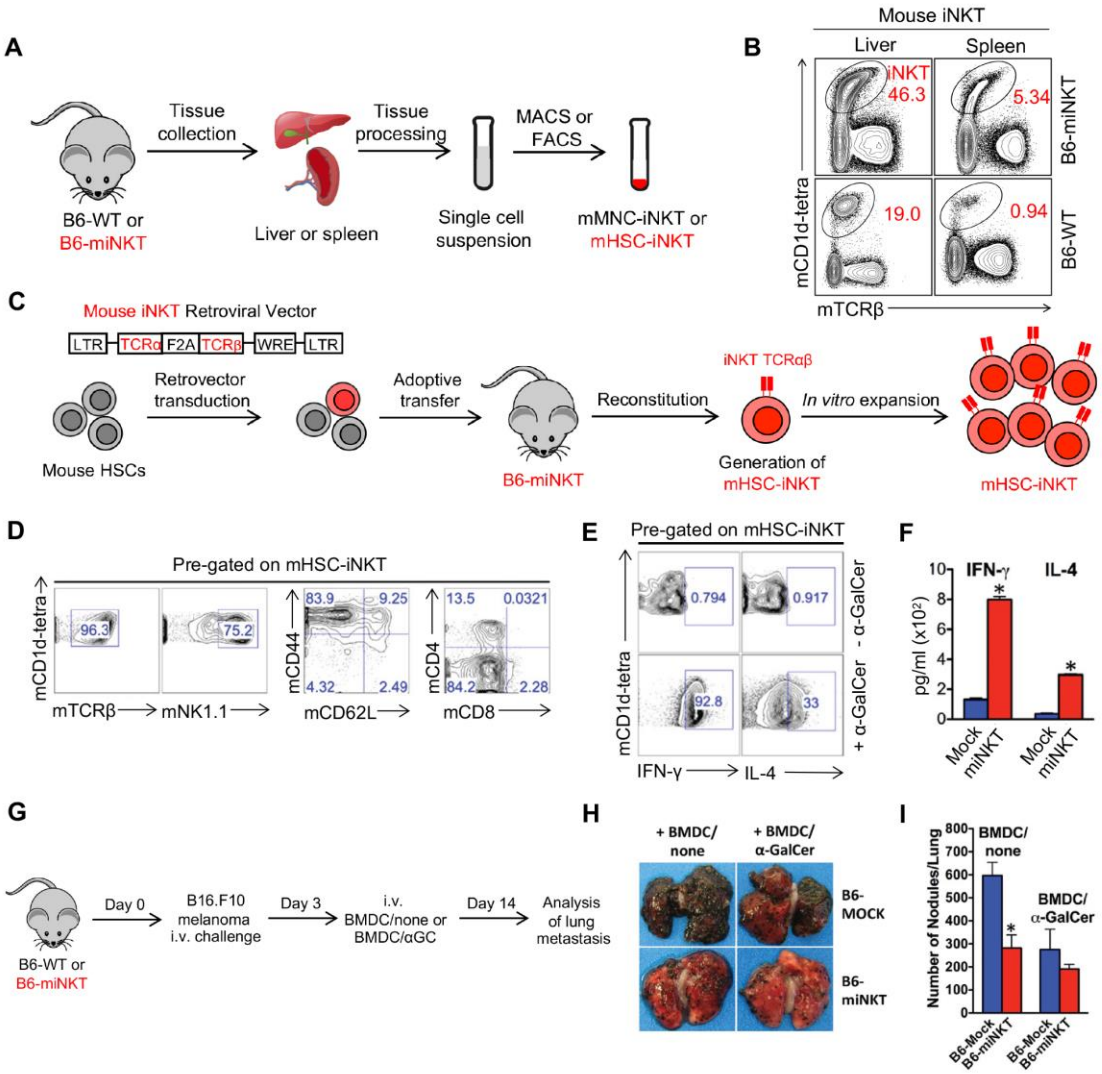

Figure 1: Generation and characterization of mouse iNKT cells.

(A) Diagram depicting the isolation of mMNC-iNKT cells and mHSC-iNKT cells.

(B) FACS detection of mouse iNKT cells in liver and spleen of B6-miNKT mice or B6-WT mice.

(C) Experimental design for generating mHSC-iNKT cells in a B6-miNKT mouse model.

(D) FACS detection of the surface markers of mHSC-iNKT cells. These iNKT cells were detected in the liver of B6-miNKT mice for up to 6 months after HSCs adoptive transfer.

(E-F) Functionality of mHSC-iNKT cells tested *in vitro*. Spleen cells collected from B6-miNKT mice were cultured *in vitro* in the presence of α-GalCer (100 ng/ml) (E) FACS detection of intracellular cytokine production in mHSC-iNKT cells 3 days post α-GalCer stimulation. (F) ELISA analysis of cytokine production of mHSC-iNKT cells in the cell culture medium 3 days post α-GalCer stimulation.

(G-I) Study *in vivo* antitumor efficacy of mHSC-iNKT cells using an B16.F10 melanoma lung metastasis mouse model. (G) Experimental design. (H) Photos of lung tumor nodules. Representative of 2 experiments. (I) Enumeration of lung tumor nodules.

Data were presented as the mean ± SEM. *$P < 0.01$, by Student's *t* test.

(Note that D-I were reproduced from ref. 15 with permission from NAS, copyright (2015) National Academy of Sciences)

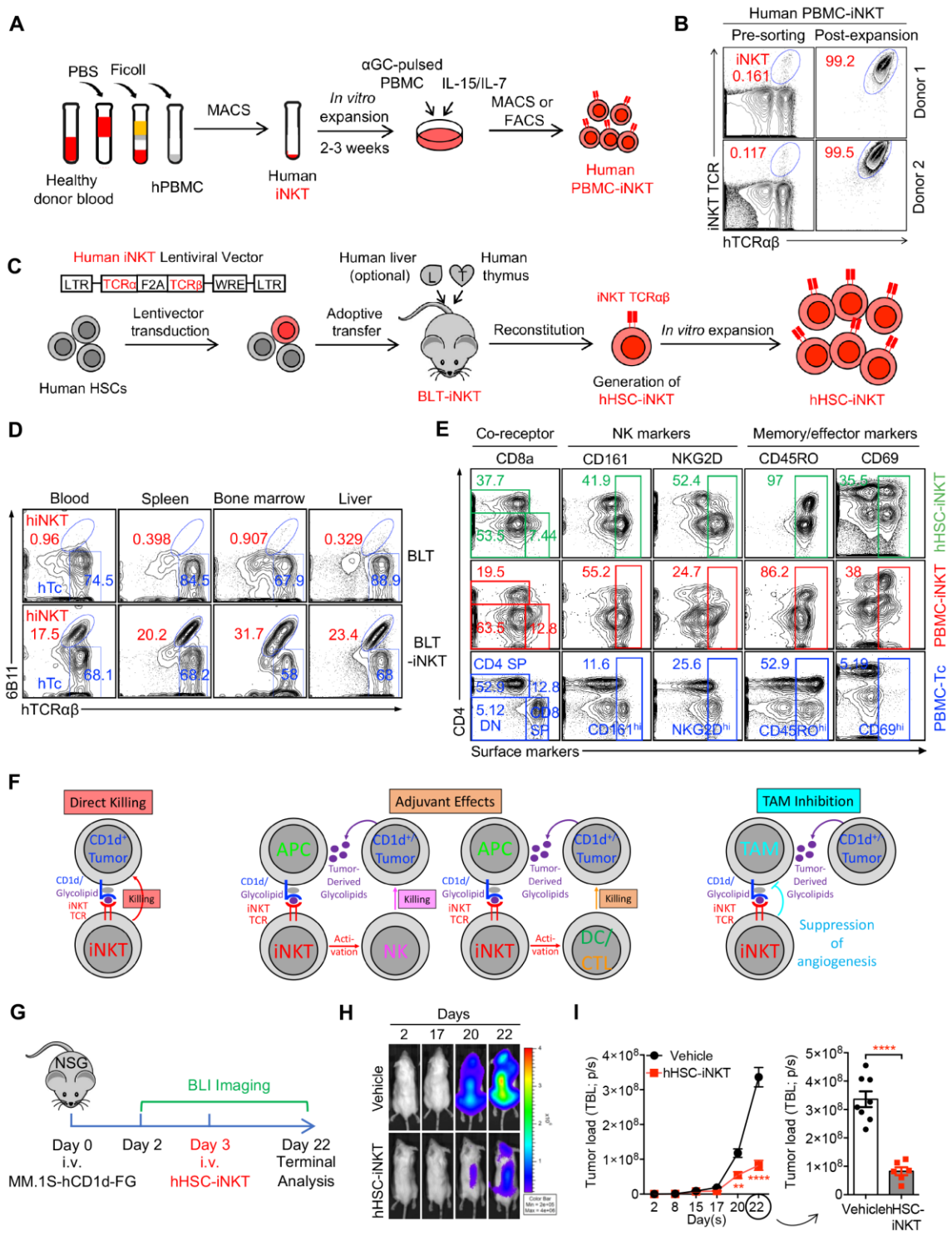

Figure 2: Generation and characterization of human iNKT cells.

(A) Diagram depicting the isolation and *in vitro* expansion of hPBMC-iNKT cells. (αGC: α-GalCer.)

(B) FACS detection of hPBMC-iNKT cells before or after MACS sorting using anti-human iNKT microbeads.

(C) Experimental design to generate hHSC-iNKT cells in a bone marrow-liver-thymus (BLT) humanized mouse model.

(D) FACS detection of hHSC-iNKT cells in control BLT and BLT-iNKT mice tissues, at week 20-post-HSC transfer. Control BLT mice were generated by adoptively transferring mock-transduced human HSCs into NSG mice engrafted with human thymus.

(E) FACS detection of the surface markers of hHSC-iNKT cells isolated from the spleen of BLT-iNKT mice. Human PBMC-iNKT cells and human PBMC-derived conventional αβ T (PBMC-Tc) cells were included as controls.

(F) Diagram showing the possible mechanisms used by human iNKT cells to attack tumor cells. APC, antigen presenting cell; NK, natural killer cell; DC, dendritic cell; CTL, cytotoxic T lymphocyte; TAM, tumor-associated macrophage.

(G-I) Study *in vivo* antitumor efficacy of hHSC-iNKT cells using an MM.1S-hCD1d-FG human MM xenograft NSG mouse model. (G) Experimental design. (H) BLI images showing tumor burden in experimental mice over time. Representative of 3 experiments. (I) Quantification of (H) (n = 6 - 8).

Data were presented as the mean ± SEM. ****P < 0.0001, by Student's *t* test.

(Note that D-I were reproduced from ref. 17 with permission from Elsevier, copyright (2019) Elsevier)

Table 1: List of antibodies.

Antibodies		
Anti-human CD45 (Clone H130)	Biolegend	CAT#304026, RFID: AB_893337
Anti-human TCRαβ (Clone I26)	Biolegend	CAT#306716, RRID: AB_1953257
Anti-human CD4 (Clone OKT4)	Biolegend	CAT#317414, RRID: AB_571959
Anti-human CD8 (Clone SK1)	Biolegend	CAT#344714, RRID: AB_2044006
Anti-human CD45RO (Clone UCHL1)	Biolegend	CAT#304216, RRID: AB_493659
Anti-human CD161 (Clone HP-3G10)	Biolegend	CAT#339928, RRID: AB_2563967
Anti-human CD69 (Clone FN50)	Biolegend	CAT#310914, RRID: AB_314849
Anti-human CD56 (Clone HCD56)	Biolegend	CAT#318304, RRID: AB_604100
Anti-human CD62L (Clone DREG-56)	Biolegend	CAT#304822, RRID: AB_830801
Anti-human CD14 (Clone HCD14)	Biolegend	CAT#325608, RRID: AB_830681
Anti-human CD1d (Clone 51.1)	Biolegend	CAT#350308, RRID: AB_10642829
Anti-mouse TCRβ (Clone 1B3.3)	Biolegend	CAT#156305, RRID: AB_2800701
Anti-mouse NK1.1 (Clone PK136)	Biolegend	CAT#108710, RRID: AB_313397
Anti-mouse CD62L (Clone MEL-14)	Biolegend	CAT#104411, RRID: AB_30566881
Anti-mouse CD44 (Clone IM7)	Biolegend	CAT#103012, RRID: AB_312963
Anti-mouse CD4 (Clone GK1.5)	Biolegend	CAT#100412, RRID: AB_312697
Anti-mouse CD8 (Clone 53-6.7)	Biolegend	CAT#100712, RRID: AB_312751
Anti-mouse CD3 (Clone 17A2)	Biolegend	CAT#100236, RRID: AB_2561456
Anti-mouse IFN-γ (Clone XMG1.2)	Biolegend	CAT#505809, RRID: AB_315403
Anti-mouse IL-4 (Clone 11B11)	Biolegend	CAT#504103, RRID: AB_315317
Anti-mouse CD1d (Clone K253)	Biolegend	CAT#140805, RRID: AB_10643277
Anti-human CD34 (Clone 581)	BD Biosciences	CAT#555822, RRID: AB_396151
Anti-human TCR Vα24-Jβ18 (Clone 6B11)	BD Biosciences	CAT#552825, RRID: AB_394478
Anti-human Vβ11	Beckman-Coulter	CAT#A66905
Human Fc Receptor Blocking Solution (TrueStain FcX)	Biolegend	CAT#422302

Mouse Fc Block (anti-mouse CD16/32)	BD Biosciences	CAT#553142, RRID: AB_394657
LEAF purified anti-human CD1d antibody (Clone 51.1)	Biolegend	CAT#350304
LEAF purified Mouse IgG2b, k isotype ctrl (Clone MG2b-57)	Biolegend	CAT#401212
Mouse Fluorochrome-conjugated mCD1d/PSC-57 tetramer	NIH Tetramer Core Facility	

References

1. Bendelac A, Savage PB, Teyton L. The biology of NKT cells. *Annual review of immunology* **25**, 297-336 (2007).

2. Bennstein SB. Unraveling Natural Killer T-Cells Development. *Front Immunol* **8**, 1950 (2017).

3. Mori L, Lepore M, De Libero G. The Immunology of CD1- and MR1-Restricted T Cells. *Annu Rev Immunol* **34**, 479-510 (2016).

4. Godfrey DI, Stankovic S, Baxter AG. Raising the NKT cell family. *Nat Immunol* **11**, 197-206 (2010).

5. Godfrey DI, Berzins SP. Control points in NKT-cell development. *Nat Rev Immunol* **7**, 505-518 (2007).

6. Fujii SI, Shimizu K. Immune Networks and Therapeutic Targeting of iNKT Cells in Cancer. *Trends Immunol* **40**, 984-997 (2019).

7. Nagato K, *et al.* Accumulation of activated invariant natural killer T cells in the tumor microenvironment after alpha-galactosylceramide-pulsed antigen presenting cells. *J Clin Immunol* **32**, 1071-1081 (2012).

8. Exley MA, *et al.* Adoptive Transfer of Invariant NKT Cells as Immunotherapy for Advanced Melanoma: A Phase I Clinical Trial. *Clin Cancer Res* **23**, 3510-3519 (2017).

9. Takami M, Ihara F, Motohashi S. Clinical Application of iNKT Cell-mediated Anti-tumor Activity Against Lung Cancer and Head and Neck Cancer. *Front Immunol* **9**, 2021 (2018).

10. Bedard M, Salio M, Cerundolo V. Harnessing the Power of Invariant Natural Killer T Cells in Cancer Immunotherapy. *Front Immunol* **8**, 1829 (2017).

11. Torina A, Guggino G, La Manna MP, Sireci G. The Janus Face of NKT Cell Function in Autoimmunity and Infectious Diseases. *Int J Mol Sci* **19**, (2018).

12. Lundblad LKA, *et al.* The role of iNKT cells on the phenotypes of allergic airways in a mouse model. *Pulm Pharmacol Ther* **45**, 80-89 (2017).

13. Nair S, Dhodapkar MV. Natural Killer T Cells in Cancer Immunotherapy. *Front Immunol* **8**, 1178 (2017).

14. de Lalla C, *et al.* Invariant NKT cell reconstitution in pediatric leukemia patients given HLA-haploidentical stem cell transplantation defines distinct CD4+ and CD4- subset dynamics and correlates with remission state. *J Immunol* **186**, 4490-4499 (2011).

15. Smith DJ, *et al.* Genetic engineering of hematopoietic stem cells to generate invariant natural killer T cells. *Proceedings of the National Academy of Sciences of the United States of America* **112**, 1523-1528 (2015).

16. Smith DJ, *et al.* Propagating Humanized BLT Mice for the Study of Human Immunology and Immunotherapy. *Stem Cells Dev* **25**, 1863-1873 (2016).

17. Zhu Y, *et al.* Development of Hematopoietic Stem Cell-Engineered Invariant Natural Killer T Cell Therapy for Cancer. *Cell stem cell* **25**, 542-557 e549 (2019).

18. Watarai H, Nakagawa R, Omori-Miyake M, Dashtsoodol N, Taniguchi M. Methods for detection, isolation and culture of mouse and human invariant NKT cells. *Nat Protoc* **3**, 70-78 (2008).

19. Masiuk KE, Zhang R, Osborne K, Hollis RP, Campo-Fernandez B, Kohn DB. PGE2 and Poloxamer Synperonic F108 Enhance Transduction of Human HSPCs with a beta-Globin Lentiviral Vector. *Mol Ther Methods Clin Dev* **13**, 390-398 (2019).

Acknowledgements

We thank the University of California, Los Angeles (UCLA) animal facility for providing animal support and the UCLA Virology Core for providing human blood from healthy donors. This work was supported by a Director's New Innovator Award from the NIH (DP2 CA196335, to L.Y.), a Partnering Opportunity for Translational Research Projects Award from the California Institute for Regenerative Medicine (CIRM TRAN1-08533, to L.Y.), a Stem Cell Research Award from the Concern Foundation (to L.Y.), a Research Career Development Award from the STOP CANCER Foundation (to L.Y.), and a BSCRC-RHF Research Award from the Rose Hills Research Foundation (to L.Y.). Y.-R.L. is a predoctoral fellow supported by the UCLA Whitcome Predoctoral Fellowship in Molecular Biology. We acknowledge Tasha Tsao and Emily Peng for proofreading the content.

Chapter 5: Development of off-the-shelf HSC-engineered iNKT cells for alleviating GvHD while preserving GvL in the treatment of blood cancers

Development of off-the-shelf HSC-engineered iNKT cells for alleviating GvHD while preserving GvL in the treatment of blood cancers

Samuel Zeng[1,*], Yan-Ruide Li[1,*], Yang Zhou[1], Zhe Li[1], Jiaji Yu[1], Yu-Chen Wang[1], Josh Ku[1], Noah Cook[1], Adam Kramer[1], Jie Huang[1], Lili Yang[1,2,3,4,§]

[1]Department of Microbiology, Immunology & Molecular Genetics, University of California, Los Angeles, Los Angeles, CA 90095, USA

[2]Eli and Edythe Broad Center of Regenerative Medicine and Stem Cell Research, University of California, Los Angeles, Los Angeles, CA 90095, USA

[3]Jonsson Comprehensive Cancer Center, David Geffen School of Medicine, University of California, Los Angeles, Los Angeles, CA 90095, USA

[4]Molecular Biology Institute, University of California, Los Angeles, CA 90095, USA

*These authors contributed equally to this work.

[§]Corresponding author:

Lili Yang, Ph.D.

Assistant Professor

Department of Microbiology, Immunology & Molecular Genetics

University of California, Los Angeles

Los Angeles, CA 90095, USA

Phone: 310-825-8609

E-mail: liliyang@ucla.edu

Website: http://www.liliyanglab.com

Keywords: Invariant natural killer T cells; Hematopoietic stem cell engineering; Ex vivo T cell differentiation; Graft versus host disease; Graft versus leukemia/lymphoma effect

Abstract

Allogeneic hematopoietic cell transplantation (allo-HCT) is a curative therapy for hematologic malignancies (i.e. leukemia/lymphoma), owing to graft versus leukemia (GvL) effect mediated by alloreactive T cells; however, the same T cells also mediate graft versus host disease (GvHD), a severe side effect limiting the wide-spread application of allo-HCT in clinic. Invariant natural killer T (iNKT) cells can ameliorate GvHD while preserving GvL effect, but the clinical application is limited by their scarcity. Here, we show that large amounts of iNKT cells from a single donor can be generated by combining hematopoietic stem cell (HSC) gene engineering and an HSC *in vitro* differentiation system. The engineered iNKT cells are predominantly $CD4^{-}CD8^{-}$ and $CD4^{-}CD8^{+}$ and have similar cytokine profile and cytolytic function to the same endogenous iNKT subsets. Engineered iNKT cells from third-party donors eliminate $CD14^{+}$ macrophages in mixed lymphocyte culture and reduce Th1-differentiation in a CD1d-dependent manner. Third-party iNKT cells also ameliorate GvHD while preserving GvL effect in Xeno-GvHD models through depletion of donor-type $CD14^{+}$ macrophages. These results indicate that engineered third-party iNKT cells can serve as "off-the-shelf" iNKT cell source for clinical application to ameliorate of GvHD while preserving GvL effect. (191)

Introduction

Allogeneic hematopoietic cell transplantation (allo-HCT) is a curative therapy for hematologic malignancies such as leukemia/lymphoma owing to the graft-versus leukemia/lymphoma (GvL) effect elicited by alloreactive donor T cells[1, 2, 3]. In 2018 alone, more than 47,000 bone marrow transplantations were performed worldwide, 19,000 (41%) of which were allogeneic and nearly all for the treatment of leukemia/lymphoma[4]. However, the development of graft-versus-host disease (GvHD) mediated by alloreactive donor T cells responding to minor or major histocompatibility antigen disparities between donor and recipient remains a major cause of patient morbidity and mortality for patients receiving T-cell replete allo-HCT[5, 6]. T cell depletion of the graft can reduce the incidence and severity of GvHD in patients but is associated with an increased risk of graft rejection, infections, and leukemia relapse[7]. Therefore, extensive research has been focused on identifying other cellular components of the graft that could modulate donor T cells and reduce the risk and severity of GvHD without diminishing normal immunological functions, including NK[8], B[9], and $CD4^+CD25^{hi}FoxP3^+$ T regulatory (Treg) cells[10, 11].

Invariant nature killer T (iNKT) cells have also been studied extensively for their roles in modulating GvHD and GvL. iNKT cells are a small subset of αβ T cells that express both a semi-invariant T cell receptor (Vα24-Jα18 in humans and Vα14-Jα18 in mice paired with a limited selection of Vβ chains) and natural killer cell markers (e.g., CD161 in humans and NK1.1 in mice)[12, 13, 14, 15, 16, 17, 18]. Unlike conventional αβ TCRs that recognize peptide antigens presented on classical polymorphic MHC Class I and II molecules, the iNKT TCR recognizes glycolipid antigens presented on non-polymorphic MHC Class I-like molecule CD1d[19]. iNKT cells in mouse include $CD4^+$ and $CD4^-CD8^-$ (double negative, DN) subsets[17], and iNKT cells in human include $CD4^+$, $CD8^+$ and DN subsets[17]. iNKT cells express high levels of cytokine mRNA and produce large amounts of cytokines upon primary

stimulation[17]. iNKT cell subset have differential cytokine patterns and cytolytic functions: $CD4^+$ iNKT cell subset produce much higher levels of IL-4 as compared to $CD8^+$ and DN subsets; the latter subsets express much higher levels of granzyme B and perforin and have much stronger cytolytic function as compared to the former[17].

The beneficial roles of iNKT cells in reducing GvHD while retaining GvL in murine allo-HCT has been well reported[20, 21, 22, 23]. Previous studies demonstrated that total lymphoid irradiation (TLI) conditioning prior to allo-HCT prevented GvHD and preserved GvL effect due to the selectively depletion of host conventional T cells and relative expansion of NKT cells[20, 21]. The host-type iNKT cells interact with donor-type myeloid cells to augment donor-type Treg expansion[22]. Addition of recipient-type, donor-type, or third party iNKT into the allograft was also shown to significantly reduce the risk of GvHD in allo-HCT without diminishing GvL by polarizing donor T cells to a Th_2 phenotype[23, 24].

The protective roles of human iNKT cells against GvHD have also been highlighted by multiple clinical studies. Non-myeloablative conditioning with TLI/ATG prior to allo-HCT coincided with a higher iNKT/T cell ratio, decreased incidences of GvHD, and retained GvL effect[25, 26]. Patients with GvHD early after transplantation were found to have reduced numbers of total circulating iNKT cells[27] whereas enhanced iNKT cell reconstitution following allo-HCT positively correlated with a reduction in GvHD without loss of GVL effect[28]. In particular, low $CD4^-$ but not $CD4^+$ iNKT cell numbers in donor allograft was associated with clinically significant reduction in GvHD in patients receiving HLA-identical allo-HCT[29]. Thus, increasing the iNKT cell numbers in the allograft may provide an attractive strategy for suppressing GvHD while preserving GvL effect.

However, the research and clinical applications of iNKT cells are greatly hindered by their low numbers and high variability in humans (~0.001-1% in blood)[30]. To overcome this critical limitation, we

have previously established a method to generate large amounts of human iNKT cells through TCR gene engineering of hematopoietic stem cells (HSCs) followed by *in vivo* reconstitution; using this method, we have successfully generated both mouse and human HSC-engineered iNKT (HSC-iNKT) cells[31, 32]. While such an *in vivo* approach to providing iNKT cells maybe suitable for autologous transplantation, applying this for allogeneic transplantation faces significant hurdles[31, 32]. Here, we intended to build on the HSC-iNKT engineering approach and develop an *ex vivo* culture method to produce large amounts of third party human iNKT cells; these cells can potentially be used as a "universal" and "off-shelf" reagent for improving allo-HCT outcomes by ameliorating GvHD while preserving GvL effect.

Results

Ex vivo generation and characterization of human HSC-engineered iNKT cells

Human $CD34^+$ hematopoietic stem and progenitor cells (HSCs) were collected from cord blood (CB-HSCs) or granulocyte-colony stimulating factor (G-CSF)-mobilized human periphery blood (PB-HSCs). These HSCs were then transfected with a Lenti/iNKT-sr39TK lentiviral vector, followed by culturing *in vitro* in a 2-stage artificial thymic organoid (ATO)/α-galactosylceramide (αGC) culture system (Fig. 1a). The gene-engineered HSCs efficiently differentiated into iNKT cells in the ATO culture system (Stage 1) over 8 weeks (Fig. 1a,b). The percentage of cells that expressed transgenic iNKT TCR increased from < 1% before culture to ~ 70% after culture (Fig. 1b) with over 100-fold expansion (Fig. 1a,d). These engineered HSC-iNKT cells were further expanded with αGC-loaded irradiated PBMCs (Stage 2) for another 2-3 weeks (Fig. 1a,c), resulting in > 97% iNKT cells among total cultured cells and another 100-1000-fold expansion (Fig. 1a,d). This manufacturing process was robust and of high yield and high purity for all 12 donors tested (4 CB-HSCs and 8 PB-HSCs) (Fig. 1c,d). Based on the results, it was estimated that from one CB donor (comprising ~5 x 10^6 CB-HSCs), ~5 x 10^{11} HSC-iNKT cells could be

generated; from one PB-HSC donor (comprising ~5 x 10^8 PB-HSCs), ~3 x 10^{12} HSC-iNKT cells could be generated (Fig. 1d).

To ensure the safety profile of HSC-iNKT cell product, we included a sr39TK PET imaging/suicide gene in the lentiviral vector, which allows for the *in vivo* monitoring of these cells using PET imaging and the elimination of these cells through ganciclovir (GCV)-induced depletion in case of a serious adverse event (Fig. 1a). In cell culture, GCV induced effective killing of HSC-iNKT cells (Supplementary Fig. 1a,b). In an NSG mouse xenograft model, GCV induced efficient depletion of HSC-iNKT cells from all tissues examined (e.g., blood, liver, spleen, and lung) (Supplementary Fig. 1c-e). Therefore, the engineered HSC-iNKT cell product is equipped with a powerful "kill switch", significantly enhancing its safety profile.

We next compared the phenotype and functionality of engineered HSC-iNKT cells to PBMC-iNKT cells and conventional αβ T (PBMC-Tcon) sorted from healthy donor periphery blood. Engineered iNKT cells were predominantly $CD8^+$ and DN whereas greater than 50% of PBMC-iNKT cells were $CD4^+$ (Fig. 1e). HSC-iNKT cells displayed a phenotype closely resembling PBMC-iNKT cells and distinct from PBMC-Tcon cells: they expressed high levels of memory T cell markers (i.e., CD45RO) and NK cell markers (i.e., CD161, NKG2D, and DNAM-1) and expressed exceedingly high levels of Th1 cytokines (i.e., IFN-γ, TNF-α, and IL-2) as well as high levels of cytotoxic molecules (i.e., Perforin and Granzyme B); comparatively, fresh PBMC-Tcon cells expressed low levels of Th1 cytokines and medium levels of perforin and granzyme B (Fig. 1e). HSC-iNKT produced lower Th2 cytokine IL-4 compared to PBMC-iNKT cells, indicating engineered iNKT cells are similar to endogenous $CD8^+$ and DN iNKT subsets.

Third party HSC-iNKT (^{3rd}HSC-iNKT) cells ameliorate Xeno-GvHD in NSG mice engrafted with human PBMC

Different from Foxp3^{+}CD4^{+} T cells that recognize polymorphic MHCII-peptide complex, iNKT cells recognize non-polymorphic CD1d-lipid complex[19]. In addition, the engineered iNKT cells were predominantly CD4^{-} subsets, and CD4^{-} but not CD4^{+} iNKT cells were reported to be associated with reduced GvHD in patients[29]. Thus, we tested whether ^{3rd}HSC-iNKT cells can suppress GvHD induced by donor alloreactive T cells, using a xeno-GvHD model of NSG mice engrafted with human PBMC[33]. Non-lethal total body irradiation (TBI, 100 cGy)-conditioned NSG mice were injected intravenously (i.v.) with healthy donor PBMCs (2 x 10^7) with or without the addition of ^{3rd}HSC-iNKT cells (2 x 10^7). The recipients were monitored daily for clinical signs of GvHD (Fig. 2a). The addition of ^{3rd}HSC-iNKT cells significantly delayed GvHD onset, reduced bodyweight-loss and prolong the survival. (Fig. 2b-d). The delayed onset and reduced GvHD severity were associated with delay of donor-type Tcon cell expansion in the peripheral blood (Fig. 2e).

To further characterize the changes in GvHD severity, the acute and chronic GvHD overlapping target organs (i.e., lung, liver, and skin) and chronic GvHD prototypical target organs (i.e., salivary glands)[34] were collected for pathological analysis on day 40 after engrafting donor PBMC (PBMC) only or both donor PBMC and ^{3rd}HSC-iNKT cells. As compared with control NSG mice, the recipients engrafted with PBMC alone showed severe infiltration and damage in the liver and lung; although the skin tissue did not have severe infiltration, there was an enlarged epidermis, a sign of excessive collagen deposition[34]; the salivary gland also showed infiltration and damage of gland follicles (Fig. 2g-j). These suggest that by 40 days after PBMC engraftment, the recipients had overlapping acute and chronic GvHD. The recipients given additional of ^{3rd}HSC-iNKT cells showed marked reduction in the T cell infiltration in the liver, lung, and salivary gland as well as tissue damage scores (Fig. 2g-j). Addition of

^{3rd}HSC-iNKT cells markedly reduced hair loss and enlargement of epidermis although T cell infiltration in the skin tissues was mild and no significant difference was observed between recipients with or without addition of ^{3rd}HSC-iNKT cells (Fig. 2g-j).

Flow cytometry analysis also indicated significantly less donor T cell population in the blood and spleen, and less infiltration in GvHD target organs lung, liver, bone marrow (Fig. S2a, b). Furthermore, intracellular cytokine staining showed that by day 40 after PBMC injection, a large portion of $CD4^+$ T cells had differentiated into Th1-polarized IFN-γ^+ T cells, with subsets that were IFN-γ^+ GM-CSF^+ and IFN-γ^+ IL-4^+ T cells (Fig. S2c). Addition of ^{3rd}HSC-iNKT reduced the total percentage of IFN-γ^+ $CD4^+$ T cells in the spleen, liver, and lung tissues, IFN-γ^+ GM-CSF^+ subset in spleen and liver, but not IFN- γ^+ IL-4^+ subsets all three tissues (Fig. S2c). These results indicated that ^{3rd}HSC-iNKT cells suppress Th1 expansion of donor-type pathogenic T cells in the GvHD target tissues of NSG recipients with overlapping acute and chronic GVHD.

^{3rd}HSC-iNKT cells eliminate donor $CD14^+$ myeloid cells in part through CD1d recognition

Donor-type myeloid cell-derived antigen presenting cells have been reported to exacerbate acute and chronic GvHD induced by donor T cells[5, 35, 36]. Donor T cell production of GM-CSF has also been reported to recruit donor myeloid cells, which in turn amplifies the activation of allogeneic T cells and exacerbating GvHD severity[37, 38]. Consistently, we observed that removal of $CD14^+$ myeloid cells in the PBMC reduced xeno-GvHD in NSG recipients (Fig. S3). We also observed that infusion of ^{3rd}HSC-iNKT to recipients given $CD14^-$-PBMC did not ameliorate GvHD (Fig. 3a-e). In contrast, amelioration of whole PBMC-induced Xeno-GvHD by infusion of ^{3rd}HSC-iNKT was associated with dramatic reduction of donor $CD14^+$ myeloid cells in the blood, spleen, lymph node, and GvHD target tissues liver and lung within three days of injections (Fig. 3h). Furthermore, comparison of the residual $CD14^+$

myeloid cells in the peripheral blood of ^{3rd}HSC-iNKT recipients to that of PBMC recipients found a significant reduction in CD1d expression (Fig. 3i). In contrast, donor T and B cell, which expressed significantly less CD1d compared to CD14$^+$ myeloid cells (Fig. S4a,b), had no observable changes in % at 3 days after the addition of ^{3rd}HSC-iNKT cells (Fig. S4d,e). Additionally, donor T cells have yet to become activated at this time, indicated by the absence of IFN-γ and GM-CSF production (Fig. S4f).

To validate the *in vivo* indications that ^{3rd}HSC-iNKT cells eliminate donor-type CD1d$^+$CD14$^+$ myeloid cells, we used *in vitro* MLR with anti-CD1d blockade (Fig. 4a). We observed that CD14$^+$ myeloid cells expressed the highest levels of CD1d among T, B and CD14$^+$ cells in the PBMC before culture (Fig. 4b). MLR culture with ^{3rd}HSC-iNKT cells for one day was sufficient to markedly reduce the percentage and number of CD14$^+$ myeloid cells (Fig. 4c,d). Additionally, residual CD14$^+$ myeloid cells in cultures that contained ^{3rd}HSC-iNKT expressed significantly less CD1d (Fig. 4e). Loss of CD14$^+$ myeloid population was partially restored by addition of blocking anti-CD1d together with ^{3rd}HSC-iNKT cells (Fig. 4c,d). However, at one day after addition of ^{3rd}HSC-iNKT cells, no immediate impact on B and T cell numbers in the MLR culture was observed (Fig. 4c,d). On the other hand, at four days after addition of ^{3rd}HSC-iNKT cells, significant reduction of IFN-γ concentration in the culture supernatant was observed, although little impact on IL-4 concentration was observed (Fig. 4f). Taken together, ^{3rd}HSC-iNKT cells eliminate donor-type CD1d$^+$ myeloid cells in a CD1d-dependent manner and inhibit expansion of IFN-γ-producing Th/Tc1 cells.

^{3rd}HSC-iNKT cells preserved GvL activity while ameliorating GvHD

We next tested whether the ^{3rd}HSC-iNKT cells could preserve GvL effect while ameliorating GvHD using human B cell lymphoma cell line, Raji, and a human acute myeloid leukemia (AML), HL60. We engineered these cells to overexpress the firefly luciferase and EGFP (FG) dual-reporters to enable the

convenient measurement of tumor killing using *in vitro* luminescence reading or *in vivo* bioluminescence imaging (BLI). When co-cultured *in vitro*, ^{3rd}HSC-iNKT cells effectively killed the Raji-FG and HL60-FG cells in a natural killer cell (NK) activating receptor (i.e., NKG2D and DNAM-1)-mediated tumor targeting manner (Supplementary Fig. 3a-f), suggesting a potent antitumor capacity of ^{3rd}HSC-iNKT cells through intrinsic NK function.

NSG mice were inoculated intravenously (i.v.) with Raji-FG cells, followed by adoptive transfer of healthy donor whole PBMCs without or with the addition of ^{3rd}HSC-iNKT cells (denoted as PBMC and PBMC+^{3rd}HSC-iNKT, respectively) (Fig. 5a). Control NSG mice that received Raji-FG cells only (denoted as Vehicle) died as a result of high tumor burden by 27 days after innoculation, while both PBMC and PBMC+^{3rd}HSC-iNKT recipients showed rapid clearance of the Raji-FG cells (Fig. 5b,c). However, PBMC recipients all died by 58 days with severe clinical GvHD, rapid weight loss, and rapid expansion of human T cells (Fig. 5d-g). Recipients given PBMC+^{3rd}HSC-iNKT survived significantly longer, for up to 106 days with a much slower progression of clinical GvHD and decline in weight (Fig. 5d-g).

Similarly, NSG mice bearing HL60-FG AML cells were injected PBMC or PBMC plus iNKT cells. The mice that received HL60-FG cells died as a result of heavy tumor burden (Fig. 6b,c). Both PBMC and PBMC+^{3rd}HSC-iNKT recipients showed rapid clearance of the HL60-FG cells (Fig. 6b,c). However, PBMC recipients failed to survival longer than the NSG control (Fig. 6f) owing to severe clinical signs of GvHD (Fig. 6d), rapid weight loss (Fig. 6e), and rapid expansion of human donor T cells (Fig. 6g). In contrast, PBMC+^{3rd}HSC-iNKT recipients showed ameliorated GvHD and all survived significantly longer (Fig. 6f). These results strongly support the capability of ^{3rd}HSC-iNKT cells to ameliorate GvHD without diminishing GvL activity.

Discussion

iNKT cells were proposed to prevent GvHD while preserving GvL effect a decade ago[25, 26], but its clinical application was hindered by the scarcity of iNKT cells in the peripheral blood[30] and the limited ex vivo expansion. In this report, we show that large amounts of iNKT cells can be generated from engineered HSC of a single healthy human donor via a 2-Step HSC-iNKT *ex vivo* differentiation culture system; and the third-party iNKT cells can ameliorate GvHD while preserving GvL effect in Xeno-GvHD models. Thus, the third-party iNKT cells can serve an off-shelf source and provide a solution to the critical shortage of iNKT cells for prevention GvHD in clinic.

First, the engineered iNKT cells are predominantly $CD8^+$ and $CD4^-CD8^-$ subsets and are functionally similar to the endogenous iNKT cells. The engineered $CD8^+$ and DN iNKT cells produce large amounts of IFN-γ and TNF-α with minimal amounts of IL-4 as well as expressing high levels of perforin and granzyme B. These features are similar to endogenous $CD8^+$ and DN iNKT cells. Interestingly, increase of $CD4^-$ but not $CD4^+$ iNKT cells in human transplant were reported to be associated with reduction of GvHD[29]. We expect that the addition of engineered iNKT cells derived from donor- or third-party HSC will prevent GvHD in patients.

Second, GvHD prevention mechanism by the engineered $CD8^+$ and DN iNKT cells are different from $CD4^+$ iNKT cells. Although human iNKT cells include $CD4^+$, $CD8^+$ and DN subset, the immune regulatory functions of iNKT cells are mostly based on studies with murine [22, 23] and human $CD4^+$ iNKT cells[38, 39]. $CD4^+$ iNKT cells produce large amounts of both IFN-γ and IL-4, and they prevent GvHD via augmenting conventional T differentiation from Th1 shift to Th2[20, 21,22, 23] as well as augmenting expansion of donor myeloid suppressor cells ($CD11b^-Gr\text{-}1^{int}$ MDSC) that subsequently expand donor T_{reg} cells[23]. In contrast, engineered $CD8^+$ and DN HSC-iNKT cells have strong cytolytic function while producing large amount of IFN-γ with minimal IL-4, and they prevent GVHD via eliminating

$CD1d^{hi}CD14^{+}$ donor-type macrophages instead of induction of Th1 to Th2 type shift and reducing infiltrating Th1 cells.

Third, engineered HSC-iNKT cells have strong GvL effect while ameliorating GvHD. GvHD is mediated by alloreactive T cells that recognize polymorphic host MHC-antigen complex[5, 6]. In contrast, iNKT cells recognize non-polymorphic CD1d-glycolipid complex[19]. Thus, the cytolytic $CD8^{+}$ and DN iNKT cells do not attack MHC-mismatched host tissues but kill the $CD1d^{h}iCD14^{+}$ donor-type macrophages, leading to reduction of donor-type APCs that expand the infiltrating T cells in the GvHD target tissues, while preserving donor-type T cells killing of the host-type tumor cells. In addition, the iNKT cells can also directly kill the CD1d expression hematological tumor cells. It is likely that they can also kill some of host-type APCs that initiate GvHD[36]. Thus, the engineered iNKT cells can be an ideal cell product for augmenting GvL activity while ameliorating GvHD.

Fourth, the rapid killing effect of $CD8^{+}$ and DN iNKT cells allows third-party engineered iNKT cells to prevent GvHD. The convenient cell source for cellular therapy will be an off-shelf third-party cell source. Third party mouse iNKT cells were previously reported to be effective in preventing GvHD despite being rejected rapidly following transplantation[23]. We observed that engineered HSC-iNKT cells eliminated $CD14^{+}$ donor-type macrophage by the third day after infusion of HSC-iNKT cells and the GvHD amelioration effect last for more than 35 days. The rapid killing takes place before alloreactive T cell activation that will likely eliminate the third-party HSC-iNKT cells. Thus, the unique mechanisms of GvHD prevention by engineered $CD8^{+}$ and DN HSC-iNKT cells laid a solid foundation for using the off-shelf third-party source.

Finally, the combination of HSC-engineering and *ex vivo* differentiation technology can generate huge numbers of iNKT cells from single donors. Starting with mobilized peripheral blood, this method can generate a 2500-fold expansion in HSC-iNKT cells; using the less accessible cord blood, this

method can provide a 100,000-fold expansion. Both numbers dwarf what could be reasonably harvested from peripheral blood[30].

Despite their promises however, the current ^{3rd}HSC-iNKT cell products can still be improved upon: the manufacture could benefit from replacing with a feeder-free culture system which will considerably disentangle the clinical and commercial development; the sr39TK/GCV suicide switch could be switched to other suicide switch systems (e.g., inducible Cas9 or truncated EGFR) with less immunogenicity[39]. Further exploration of ^{3rd}HSC-iNKT cells as off-the-shelf cell carriers for developing iNKT-coupled allo-HCT for treating blood cancers will certainly be interesting directions for future study.

Materials and Methods

Mice

NOD.Cg-Prkdc^{SCID}Il2rg^{tm1Wjl}/SzJ (NOD/SCID/IL-2Rγ$^{-/-}$, NSG) mice were maintained in the animal facilities at the University of California, Los Angeles (UCLA). Six- to ten-week-old mice were used for all experiments unless otherwise indicated. All animal experiments were approved by the Institutional Animal Care and Use Committee of UCLA.

Cell lines and viral vector

The murine bone marrow derived stromal cell line MS5-DLL4 was obtained from Dr. Gay Crooks' lab (UCLA). Human Raji B cell lymphoma cell line, HL60 acute myeloid leukemia cell line, and HEK 293T cell line were purchased from the American Type Culture Collection (ATCC). 293T were cultured in D10 medium. Raji and HL60 cells were cultured in R10 medium.

Lentiviral vectors used in this study were all constructed from a parental lentivector pMNDW as previously described[31]. The Lenti/iNKT-sr39TK vector was constructed by inserting into pMNDW vector a synthetic tricistronic gene encoding human iNKT TCRα-F2A-TCRβ-P2A-sr39TK; the Lenti/FG vector was constructed by inserting into pMNDW a synthetic bicistronic gene encoding Fluc-P2A-EGFP. The synthetic gene fragments were obtained from GenScript and IDT. Lentiviruses were produced using HEK 293T cells, following a standard calcium precipitation protocol and an

ultracentrifigation concentration protocol as previously described[31, 32]. Lentivector titers were measured by transducing HT29 cells with serial dilutions and performing digital qPCR, following established protocols[31, 32].

To make stable tumor cell lines overexpressing firefly luciferase and enhanced green fluorescence protein (FG) dual-reporters, parental tumor cell lines were transduced with lentiviral vectors encoding the intended gene(s). 72h following lentiviral transduction, cells were subjected to flow cytometry sorting to isolate gene-engineered cells for making stable cell lines. Two stable tumor cell lines were generated for this study, including Raji-FG and HL60-FG.

Human periphery blood mononuclear cells (PBMCs)

Healthy donor human PBMCs were obtained from the UCLA/CFAR Virology Core Laboratory, with identification information removed under federal and state regulations. Cells were cryopreserved in Cryostor CS10 (BioLife Solution) using CoolCell (BioCision), and were stored in liquid nitrogen for all experiments and long-term storage.

Media and reagents

α-Galactosylceramide (αGC, KRN7000) was purchased from Avanti Polar Lipids. Recombinant human IL-2, IL-3, IL-4, IL-7, IL-15, Flt3-Ligand, Stem Cell Factor (SCF), Thrombopoietin (TPO), and Granulocyte-Macrophage Colony-Stimulating Factor (GM-CSF) were purchased from Peprotech. Ganciclovir (GCV) was purchased from Sigma.

X-VIVO 15 Serum-free Hematopoietic Cell Medium was purchased from Lonza. RPMI 1640 and DMEM cell culture medium were purchased from Corning Cellgro. Fetal bovine serum (FBS) was purchased from Sigma. Medium supplements, including Penicillin-Streptomycine-Glutamine (P/S/G), MEM non-essential amino acids (NEAA), HEPES Buffer Solution, and Sodium Pyruvate, were purchased from GIBCO. Beta-Mercaptoethanol (β-ME) was purchased from Sigma. Normocin was purchased from InvivoGen. Complete lymphocyte culture medium (denoted as C10 medium) was made of RPMI 1640 supplemented with FBS (10% vol/vol), P/S/G (1% vol/vol), MEM NEAA (1% vol/vol), HEPES (10 mM), Sodium Pyruvate (1 mM), β-ME (50 mM), and Normocin (100 mg/ml). Medium for culturing human Raji and HL60 tumor cell lines (denoted as R10 medium) was made of RPMI 1640 supplemented with FBS (10% vol/vol) and P/S/G (1% vol/vol). Medium for culturing HEK 293T cell line (denoted as D10 medium) was made of DMEM supplemented with FBS (10% vol/vol) and P/S/G (1% vol/vol).

Antibodies and flow cytometry

All flow cytometry stains were performed in PBS for 15 min at 4 °C. The samples were stained with Fixable Viability Dye eFluor506 (e506) mixed with Mouse Fc Block (anti-mouse CD16/32) or Human Fc Receptor Blocking Solution (TrueStain FcX) prior to antibody staining. Antibody staining was performed at a dilution according to the manufacturer's instructions. Fluorochrome-conjugated antibodies specific for human CD45 (Clone H130), TCRαβ (Clone I26), CD4 (Clone OKT4), CD8 (Clone SK1), CD45RO (Clone UCHL1), CD161 (Clone HP-3G10), CD69 (Clone FN50), CD56 (Clone HCD56), CD62L (Clone DREG-56), CD14 (Clone HCD14), CD1d (Clone 51.1), NKG2D (Clone 1D11), DNAM-1 (Clone 11A8), IFN-γ (Clone B27), granzyme B (Clone QA16A02), Perforin (Clone dG9), TNF-α (Clone Mab11), IL-2 (Clone MQ1-17H12), HLA-A2 (Clone BB7.2) were purchased from BioLegend; Fluorochrome-conjugated antibodies specific for human CD34 (Clone 581) and TCR Vα24-Jβ18 (Clone 6B11) were purchased from BD Biosciences. Human Fc Receptor Blocking Solution (TrueStain FcX) was purchased from Biolegend, and Mouse Fc Block (anti-mouse CD16/32) was purchased from BD Biosciences. Fixable Viability Dye e506 were purchased from Affymetrix eBioscience. Intracellular cytokines were stained using a Cell Fixation/Permeabilization Kit (BD Biosciences). Stained cells were analyzed using a MACSQuant Analyzer 10 flow cytometer (Miltenyi Biotech). FlowJo software was utilized to analyze the data.

Enzyme-linked immunosorbent cytokine assays (ELISA)

The ELISAs for detecting human cytokines were performed following a standard protocol from BD Biosciences. Supernatants from co-culture assays were collected and assayed to quantify IFN-γ. Capture and biotinylated pairs for detecting cytokines were purchased from BD Biosciences. The streptavidin-HRP conjugate was purchased from Invitrogen. Human cytokine standards were purchased from eBioscience. Tetramethylbenzidine (TMB) substrate was purchased from KPL. The samples were analyzed for absorbance at 450 nm using an Infinite M1000 microplate reader (Tecan).

***In vitro* generation of HSC-engineered iNKT (HSC-iNKT) cells**

Frozen-thawed human $CD34^+$ HSCs were revived in HSC-culture medium comprised of X-VIVO 15 Serum-free Hematopoietic Cell Medium supplemented with SCF (50 ng/ml), FLT3-L (50 ng/ml), TPO (50 ng/ml), and IL-3 (10 ng/ml) for 24 hours. Cells were then transduced with Lenti/iNKT-sr39TK viruses for another 24 hours following an established protocol[31]. The transduced HSCs were then collected and put into a 2-Stage *in vitro* HSC-iNKT culture.

During Stage 1, gene-engineered HSCs were differentiated into iNKT cells in an artificial thymic organoid (ATO) culture over 8 weeks. ATOs was generated following a modification of a previously established protocol[40]. Briefly, MS5-

DLL4 cells were harvested by trypsinization and resuspended in fresh serum free ATO culture medium (‘‘RB27’’) comprised of RPMI 1640 (Corning), 4% B27 supplement (ThermoFisher Scientific), 30 mM L-ascorbic acid 2-phosphate sesquimagnesium salt hydrate (Sigma-Aldrich) reconstituted in PBS, 1% penicillin/streptomycin (Gemini Bio-Products), 1% Glutamax (ThermoFisher Scientific), 5 ng/ml rhFLT3L and 5 ng/ml rhIL-7 (Peprotech). 1.5-6 x 10^5 MS5-DLL4 cells were combined with 0.3-10 x 10^4 transduced HSCs per ATO in 1.5 mL Eppendorf tubes (up to 12 ATOs per tube) and centrifuged at 300 g for 5 min at 4 °C in a swinging bucket centrifuge. After removing supernatants, the cell pellet was resuspended in 6 ml RB27 per ATO and briefly vortexed. ATOs were then plated on a 0.4 mm Millicell transwell insert (EMD Millipore; Cat. PICM0RG50) placed in a 6-well plate containing 1 mL RB27 per well. Every 3-4 days, medium was changed completely by aspiration from around the cell insert followed by replacement with 1 ml fresh RB27/cytokines. To harvest ATOs, FACS buffer (PBS/0.5% bovine serum album/2mM EDTA) was added to each well and ATO were disaggregated by brief pipetting with a 1 ml ‘‘P1000’’ pipet, followed by passage through a 50 mm nylon strainer.

During Stage 2, HSC-iNKT cells isolated from ATOs were expanded with αGC-loaded PBMCs (αGC-PBMCs). To prepare αGC-PBMCs, 1-10 x 10^7 PBMCs were incubated in 5 ml C10 medium containing 5 μg/ml αGC for 1 hour, followed by irradiation at 6,000 rads. ATO cells were mixed with irradiated αGC-PBMCs at ratio 1:1, followed by culturing for 2 weeks in C10 medium supplemented with human IL-7 (10 ng/ml) and IL-15 (10 ng/ml); cell cultures were split, and fresh media/cytokines were added if needed. The Stage 2 expansion culture could be extended to 3 weeks by adding additional αGC-PBMCs at ratio 1:1 at the end of week 2. At the end of Stage 2 culture, the resulting HSC-iNKT cell products were collected and cryopreserved for future use.

Generation of PBMC-derived conventional T (PBMC-Tc) and iNKT (PBMC-iNKT) cells

Healthy donor PBMCs were obtained from the UCLA/CFAR Virology Core Laboratory and were used to generate the PBMC-Tc and PBMC-iNKT cells.

To generate PBMC-Tc cells, PBMCs were stimulated with CD3/CD28 T-activator beads (ThermoFisher Scientific) and cultured in C10 medium supplemented with human IL-2 (20 ng/mL) for 2-3 weeks, following the manufacturer’s instructions.

To generate PBMC-iNKT cells, PBMCs were enrich for iNKT cells using anti-iNKT microbeads (Miltenyi Biotech) and MACS-sorting, followed by stimulation with donor-matched irradiated αGC-PBMCs at the ratio of 1:1 and cultured in C10 medium supplemented with human IL-7 (10 ng/ml) and IL-15 (10 ng/ml) for 2-3 weeks. If necessary, the resulting

PBMC-iNKT cells could be further purified using Fluorescence-Activated Cell Sorting (FACS) via human iNKT TCR antibody (Clone 6B11; BD Biosciences) staining.

HSC-iNKT cell phenotype and functional study

HSC-iNKT cells were analyzed in comparison with PBMC-Tc and PBMC-iNKT cells. Phenotype of these cells was studied using flow cytometry, by analyzing cell surface markers including co-receptors (i.e., CD4 and CD8), NK cell receptors (i.e., CD161, NKG2D, and DNAM-1), and memory T cell markers (i.e., CD45RO). The capacity of these cells to produce cytokines (i.e., IFN-γ, TNF-α, IL-2, and IL-4) and cytotoxic molecules (i.e., perforin and granzyme B) were studied using flow cytometry via intracellular staining.

Ganciclovir (GCV) *in vitro* and *in vivo* killing assay

For GCV *in vitro* killing assay, HSC-iNKT cells were cultured in C10 medium in the presence of titrated amount of GCV (0-50 μM) for 4 days; live HSC-iNKT cells were then counted using a hematocytometer (VWR) via Trypan Blue staining (Fisher Scientific).

GCV *in vivo* killing assay was performed using an NSG xenograft mouse model. NSG mice received i.v. injection of 1 x 10^7 HSC-iNKT cells on day 0, followed by i.p. injection of GCV for 5 consecutive days (50 mg/kg per injection per day). On day 5, mice were terminated. Multiple tissues (i.e., blood, spleen, liver, and lung) were collected and processed for flow cytometry analysis to detect tissue-infiltrating HSC-iNKT cells (identified as iNKT TCR^+CD45^+), following established protocols [31].

***In vitro* tumor cell killing assay**

Tumor cells (1 x 10^4 cells per well) were co-cultured with HSC-iNKT cells (at ratios indicated in figure legends) in Corning 96-well clear bottom black plates for 24 hours, in C10 medium. At the end of culture, live tumor cells were quantified by adding D-luciferin (150 μg/ml; Caliper Life Science) to cell cultures and reading out luciferase activities using an Infinite M1000 microplate reader (Tecan).

In some experiments, 10 μg/ml of LEAF™ purified anti-human NKG2D (Clone 1D11, Biolegend), anti-human DNAM-1 antibody (Clone 11A8, Biolegend), or LEAF™ purified mouse lgG2bk isotype control antibody (Clone MG2B-57, Biolegend) was added to co-cultures, to study NK activating receptor-mediated tumor cell killing mechanism.

***In vitro* mixed lymphocyte reaction (MLR) Assay: Studying ^{3rd}HSC-iNKT cell inhibition of allogeneic T cell response**

PBMCs of multiple healthy donors were irradiated at 2,500 rads and used as stimulators, and allogeneic PBMCs were used as responders. In order to separate the different donor PBMCs when performing flow cytometry, HLA-A2$^+$ responders and HLA-A2$^-$ stimulators were used in this study. Irradiated stimulators (2.5 x 10^5 cells/well) and responders (1 x 10^4 cells/well) were co-cultured with or without the addition of ^{3rd}HSC-iNKT cells (1 x 10^4 cells/well) in 96-well round bottom plates in C10 medium for up to 4 days. For detection of composition and phenotype using flow cytometry, cells were collected on day 1. For IFN-γ production using ELISA, cell culture supernatants were collected on day 4. To study CD1d-dependent killing mechanism of ^{3rd}HSC-iNKT cells, 10 μg/ml of LEAF™ purified anti-human CD1d (Clone 51.1, Biolegend) or LEAF™ purified mouse lgG2bk isotype control antibody (Clone MG2B-57, Biolegend) was added to co-cultures.

Bioluminescence live animal imaging (BLI)

BLI was performed using an IVIS 100 imaging system (Xenogen/PerkinElmer) or a Spectral Advanced Molecular Imaging (AMI) HTX imaging system (Spectral instrument Imaging). Live animal imaging was acquired 5 minutes after intraperitoneal (i.p.) injection of D-Luciferin (1 mg per mouse). Imaging results were analyzed using a Living Imaging 2.50 software (Xenogen/ PerkinElmer) or an AURA imaging software (Spectral Instrument Imaging).

Human PBMC xenograft NSG mouse model: studying ^{3rd}HSC-iNKT cell *in vivo* amelioration of GvHD

NSG mice were pre-conditioned with 100 rads of total body irradiation (day -1), followed by intravenous injection of 2 x 10^7 healthy donor PBMCs with or without the addition of 2 x 10^7 ^{3rd}HSC-iNKT cells. Mice were weighed daily, bled weekly, and scored 0-2 per other clinical signs of GvHD (i.e., body weight, activity, posture, skin thickening, diarrhea, and dishevelment). Mice were sacrificed when moribund. Various mouse tissues (i.e., blood, spleen, liver, lung, bone marrow, skin, and salivary ligand) were harvested and processed for either flow cytometry or histologic analysis.

Human PBMC xenograft NSG mouse model: studying CD14$^+$ myeloid cell *in vivo* amelioration of GvHD

NSG mice were pre-conditioned with 100 rads of total body irradiation (day -1), followed by intravenous injection of 2 x 10^7 healthy donor PBMCs or 9 x 10^6 CD14-depleted donor PBMCs. The amount of PBMCs given was normalized to contain the

same number of T cells. Mice were weighed daily, bled weekly, and scored 0-2 per other clinical signs of GvHD (i.e., body weight, activity, posture, skin thickening, diarrhea, and dishevelment).

Human CD14$^-$ PBMC xenograft NSG mouse model: studying ^{3rd}HSC-iNKT cell *in vivo* amelioration of GvHD

NSG mice were pre-conditioned with 100 rads of total body irradiation (day -1), followed by intravenous injection of 9 x 10^6 CD14-depleted donor PBMCs with or without the addition of 2 x 10^7 ^{3rd}HSC-iNKT cells. Mice were weighed daily, bled weekly, and scored 0-2 per other clinical signs of GvHD (i.e., body weight, activity, posture, skin thickening, diarrhea, and dishevelment).

Raji-FG human B cell lymphoma xenograft NSG mouse model: studying ^{3rd}HSC-iNKT cell *in vivo* retention of GvL

NSG mice were pre-conditioned with 100 rads of total body irradiation (day -1), followed by subcutaneous inoculation with 1 x 10^5 Raji-FG cells (day 0). On day 3, the tumor-bearing experimental mice received intravenous (i.v.) injection of 2 x 10^7 healthy donor PBMCs with or without the addition of 2 x 10^7 ^{3rd}HSC-iNKT cells. Tumor load were monitored over time using BLI. Mice were also weighed daily, bled weekly, and scored 0-2 per other clinical signs of GvHD (i.e., body weight, activity, posture, skin thickening, diarrhea, and dishevelment). Mice were sacrificed when moribund.

HL60-FG human acute myeloid leukemia xenograft NSG mouse model: studying ^{3rd}HSC-iNKT cell *in vivo* retention of GvL

NSG mice were pre-conditioned with 175 rads of total body irradiation (day -1), followed by intravenous inoculation with 2 x 10^5 HL60-FG (day 0). On day 3, the tumor-bearing experimental mice received intravenous (i.v.) injection of 2 x 10^7 healthy donor PBMCs with or without the addition of 2 x 10^7 ^{3rd}HSC-iNKT cells. Tumor load were monitored over time using BLI. Mice were also weighed daily, bled weekly, and scored 0-2 per other clinical signs of GvHD (i.e., body weight, activity, posture, skin thickening, diarrhea, and dishevelment). Mice were sacrificed when moribund.

Histological analysis

Tissues (i.e., liver, lung, salivary glands, and skin) were collected from the experimental mice, fixed in 10% Neutral Buffered Formalin for up to 36 hours, then embedded in paraffin for sectioning (5 μm thickness). Tissue sections were prepared and stained with Hematoxylin and Eosin (H&E) or anti-CD3 by the UCLA Translational Pathology Core Laboratory, following

the Core's standard protocols. For H&E, stained sections were imaged on a Zeiss Observer II upright microscope. All images were captured at either 100x or 200x and processed using Zen Blue software. GVHD pathological score was calculated as follows: skin: epidermal changes(0-3), dermal changes (0-3), adipose changes (0-3); salivary: infiltration (0-4), follicular destruction (0-4); liver: duct infiltration (0-3), number of ducts involved (0-3), liver cell apoptosis (0-3); lung: infiltrates (0-3); pneumonitis (0-3), overall appearance (0-3). For CD3 surface area measurements, anti-CD3 stained sections were scanned in their entirety using Hamamatsu Nanozoomer 2.0 HT. The %CD3+ area was determined by $CD3^+$ area divided by total tissue area, using Image-Pro Premier software.

Statistical analysis

GraphPad Prism 6 (Graphpad Software) was used for statistical data analysis. Student's two-tailed *t* test was used for pairwise comparisons. Ordinary 1-way ANOVA followed by Tukey's multiple comparisons test was used for multiple comparisons. Log rank (Mantel-Cox) test adjusted for multiple comparisons was used for Meier survival curves analysis. Data are presented as the mean ± SEM, unless otherwise indicated. In all figures and figure legends, "n" represents the number of samples or animals utilized in the indicated experiments. A P value of less than 0.05 was considered significant. ns, not significant; *P < 0.05; **P < 0.01; ***P < 0.001; ****P < 0.0001.

Reporting summary

Further information on research design is available in the Nature Research Reporting Summary linked to this article.

Data availability

All data associated with this study are present in the paper or Supplemental information.

Figures

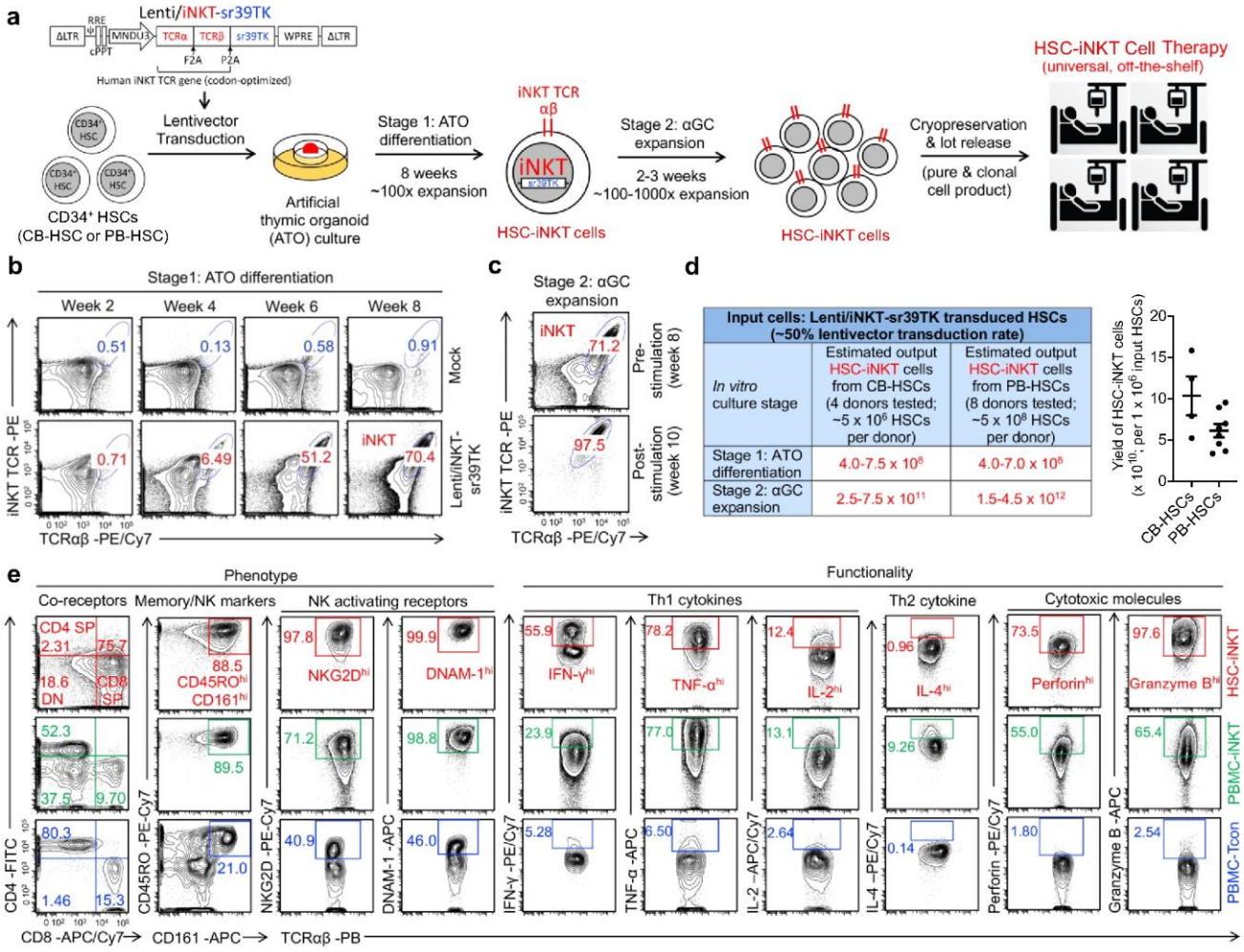

Figure 1: *Ex vivo* generation and characterization of HSC-engineered iNKT cells

a. Experimental design. HSC, hematopoietic stem cell; CB, cord blood; PBSC, periphery blood stem cell; αGC, α-galactosylceramide; Lenti/iNKT-sr39TK, lentiviral vector encoding an iNKT TCR gene and an sr39TK suicide/PET imaging gene; F2A, foot-and-mouth disease virus 2A self-cleavage sequence; P2A, porcine teschovirus-1 2A self-cleavage sequence.

b-c. FACS monitoring of HSC-iNKT cell development during a 2-Stage *in vitro* culture. iNKT cells are identified as iNKT TCR$^+$TCRαβ$^+$ cells. **b.** Generation of iNKT cells during Stage 1 ATO differentiation culture. **c**. Expansion of iNKT cells during Stage 2 αGC expansion culture.

d. Summary of the *ex vivo* HSC-iNKT cells generation.

e. FACS detection of surface markers, intracellular cytokines, and cytotoxic molecules of HSC-iNKT cells. Healthy donor periphery blood mononuclear cell (PBMC)-derived conventional αβ T (PBMC-Tcon) and iNKT (PBMC-iNKT) cells were included for comparison.

Representative figures from over 10 replicates (**a-e**).

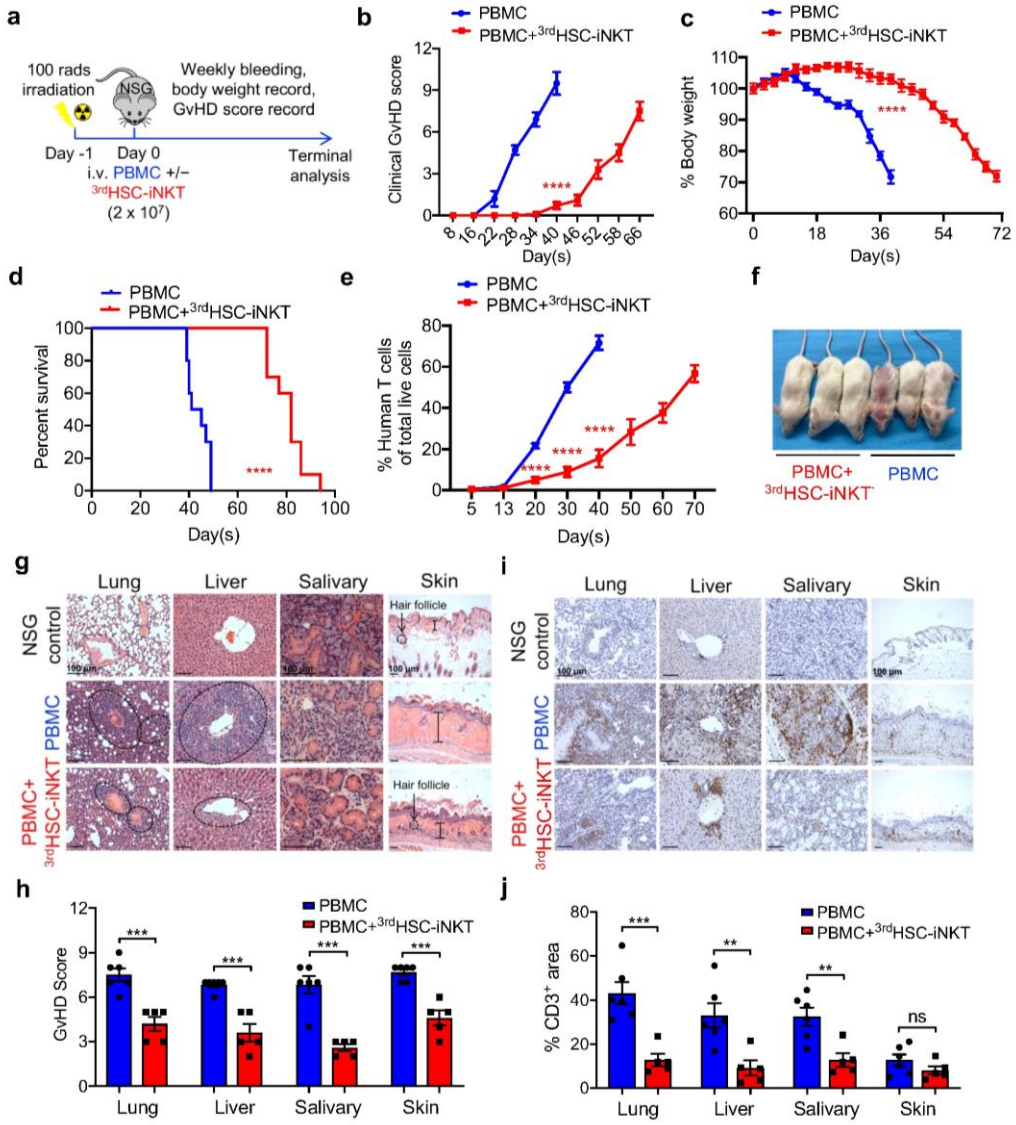

Figure 2: Third-party HSC-iNKT (^{3rd}HSC-iNKT) cells ameliorate GvHD in NSG mice engrafted with human PBMC

a-f. Sublethally irradiated NSG mice received intravenous injection of 2 x 10^7 healthy donor PBMCs with or without the addition of 2 x 10^7 ^{3rd}HSC-iNKT cells and were then observed for GvHD development. **a.** Experimental design. **b.** Clinical signs of GvHD (0-2 per category: body weight, activity, posture, skin thickening, diarrhea, and dishevelment; data on day 40, ****$p < 0.0001$). **c.** Percent of starting body weight (data on day 40, ****$p < 0.0001$). **d.** Kaplan-Meier survival curves (****$p < 0.0001$). **e.** FACS detection of human T cells in peripheral blood (data on day 20, 30, and 40, ****$p < 0.0001$). **f.** Representative photograph of experimental mice on day 40. N = 10 per group.

g-j, Histological analyses of GvHD target organs (i.e., lung, liver, salivary glands, and skin) of **e**xperimental mice sacrificed 40 days following PBMC inoculation. **g.** H&E-stained tissue sections. Scale bar: 100 μm. **h.** Quantification of **g** (***$p < 0.001$). N = 5-6. **i.** Human CD3 antibody-stained tissue sections. Scale bar: 100 μm. **j.** Quantification of **i** (lung, ***$p < 0.001$; liver, **$p = 0.0068$; salivary, **$p = 0.0051$). N = 5-6

Representative of 3 experiments. All data are presented as the mean ± SEM. *$p < 0.05$, **$p < 0.01$, ***$p < 0.001$, and ****$p < 0.0001$ by Student's *t* test (**c-e, h, and j**) or by log rank (Mantel-Cox) test adjusted for multiple comparisons (**d**). Statistics are all two-sided.

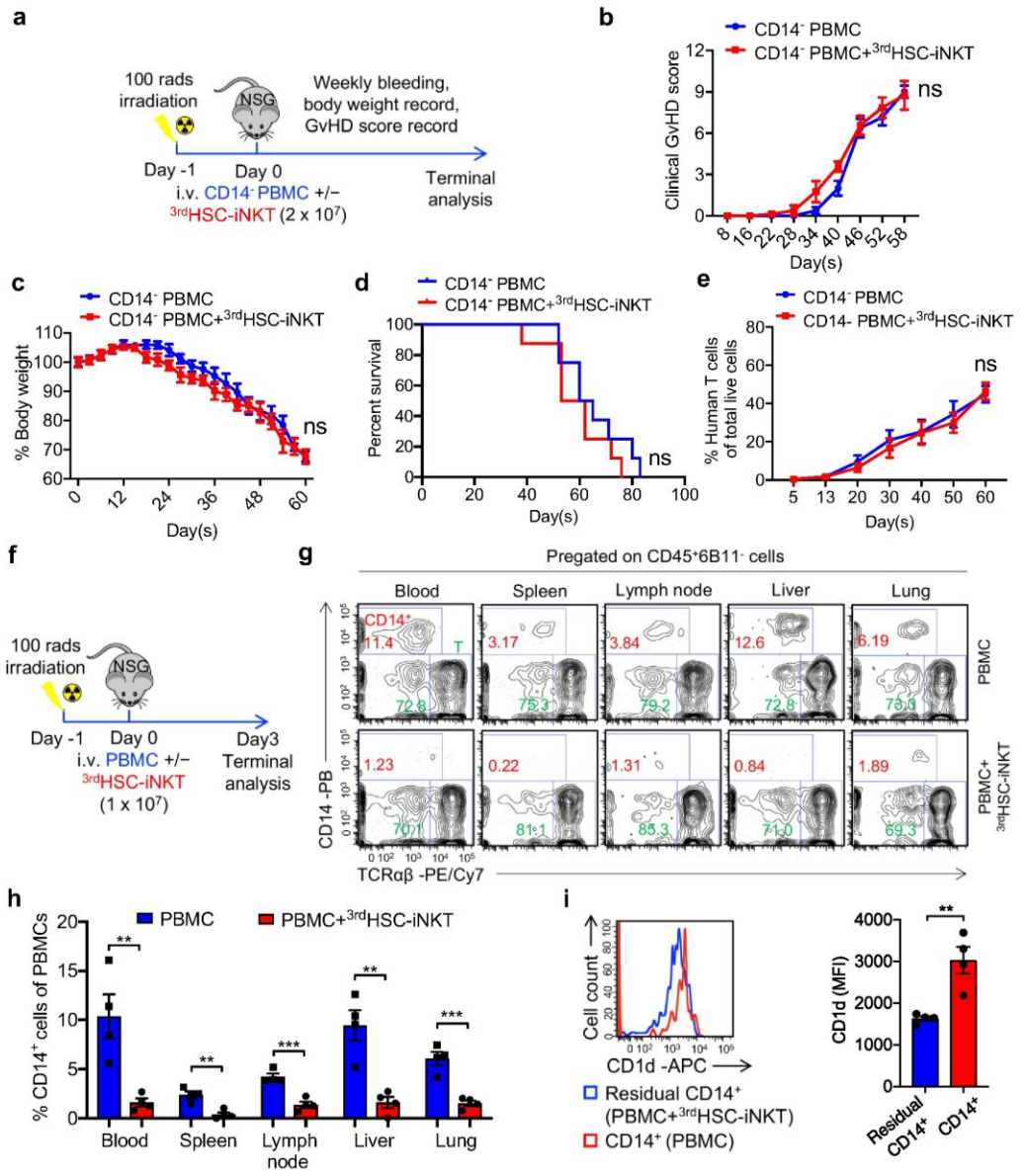

Figure 3: 3rdHSC-iNKT cells ameliorate GvHD through rapid depletion of donor CD14$^+$ myeloid cells that exacerbate GvHD

a-e. Sublethally irradiated NSG mice received intravenous injection of 9 x 10^6 CD14-depleted donor PBMCs with or without the addition of 2 x 10^7 3rdHSC-iNKT cells and were then observed for GvHD development. **a.** Experimental design. **b.** Clinical signs of GvHD. **c.** Percent of starting body weight. **d.** Kaplan-Meier survival curves. **e.** human T cell percentage in peripheral blood. N = 8.

f-h.. Sublethally irradiated NSG mice received intravenous injection of 2 x 10^7 healthy donor PBMCs with or without the addition of 2 x 10^7 3rdHSC-iNKT cells and were sacrificed on 3 days after injections. **f.** Experimental design. **g.** Representative FACs depicting the proportion of donor CD14$^+$ myeloid cells in the lymphohematopoietic system (e.g. blood, spleen, lymph nodes) and GvHD target organs (liver, lung). **h.** quantification of g. **i.** Representative FACS and quantification of CD1d expression of CD14$^+$ myeloid cells from peripheral blood.

Representative of 2 experiments. All data are presented as the mean ± SEM. *$p < 0.05$, **$p < 0.01$, ***$p < 0.001$, and ****$p < 0.0001$ by Student's *t* test (**b, c, e, g, h)** or by log rank (Mantel-Cox) test adjusted for multiple comparisons (**d**). Statistics are all two-sided.

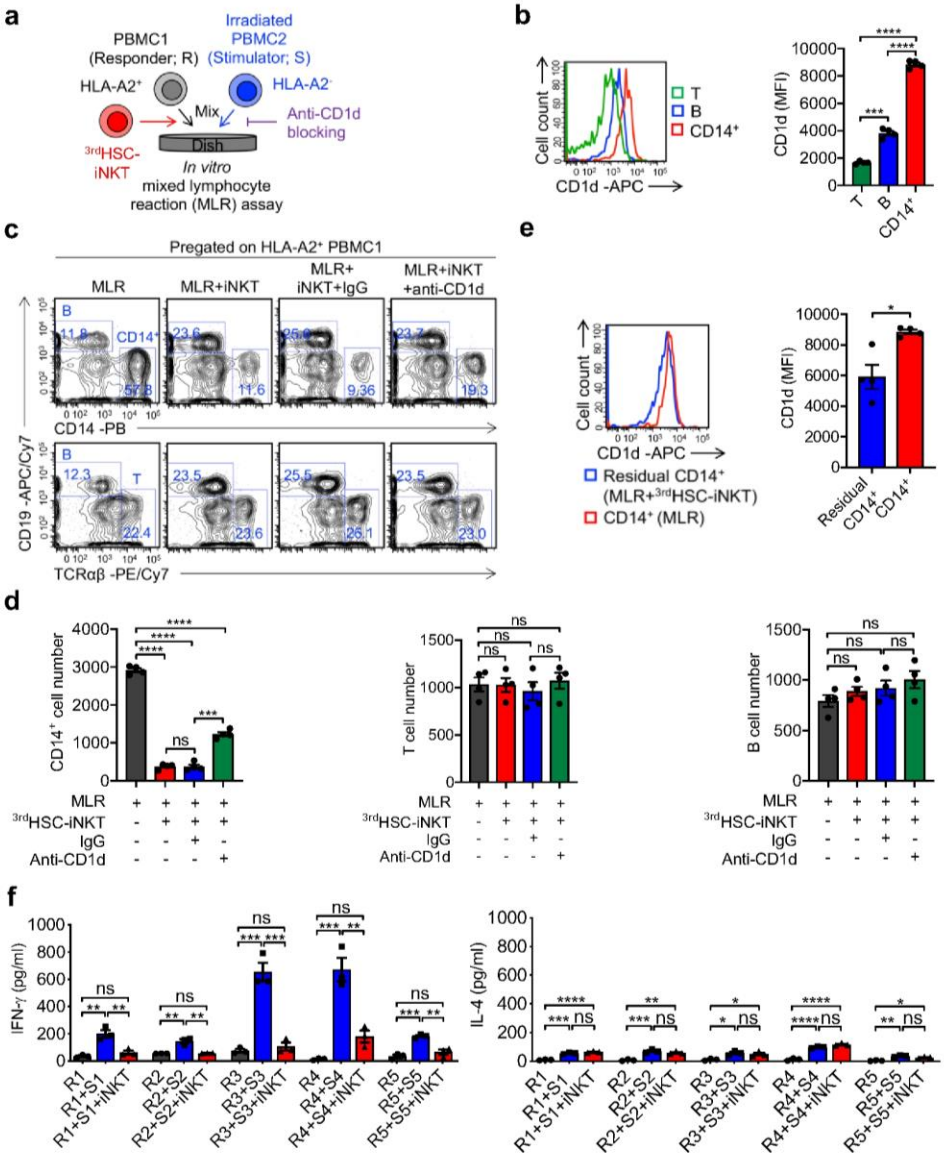

Figure 4: ^{3rd}HSC-iNKT cells ameliorate GvHD through eliminating donor CD14$^+$ myeloid cells in part through CD1d recognition

In vitro mixed lymphocyte reaction (MLR) assay was performed using healthy donor PBMCs (responders) co-cultured with irradiated, allogeneic PBMCs (stimulators) with or without the addition of ^{3rd}HSC-iNKT cells. Where applicable, purified anti-human CD1d or IgG isotype control were also added. In order to identify responders and stimulators by flow cytometry, HLA-A2$^+$ responders and HLA-A2$^-$ stimulators were used in the study. **a.** Experimental scheme. **b**. FACS analyses of CD1d expression on the indicated cells and the quantification prior to culture (***$p < 0.001$, ****$p < 0.0001$). **c.** FACS detection of T, B, and CD14$^+$ cells of responders in multiple MLR assays one day after MLR co-culture. **d**. Quantification of **c** (***$p <$ 0.001, and ****$p < 0.0001$). N = 4. **e**. Representative FACS and quantification of CD1d expression of CD14$^+$ myeloid cells one day after MLR co-culture with and without the addition of ^{3rd}HSC-iNKT cells. N = 4. **f.** ELISA analyses of IFN-γ and IL-4 production in the supernatant from multiple stimulator/responder pairs at day 4 (**$p < 0.01$, ***$p < 0.001$). N = 3. **c-e.** FACS analyses of PBMC collected one day after MLR co-culture.

Representative of 3 experiments. All data are presented as the mean ± SEM. **$p < 0.01$, ***$p < 0.001$, and ****$p <$ 0.0001 by one-way ANOVA. Statistics are all two-sided.

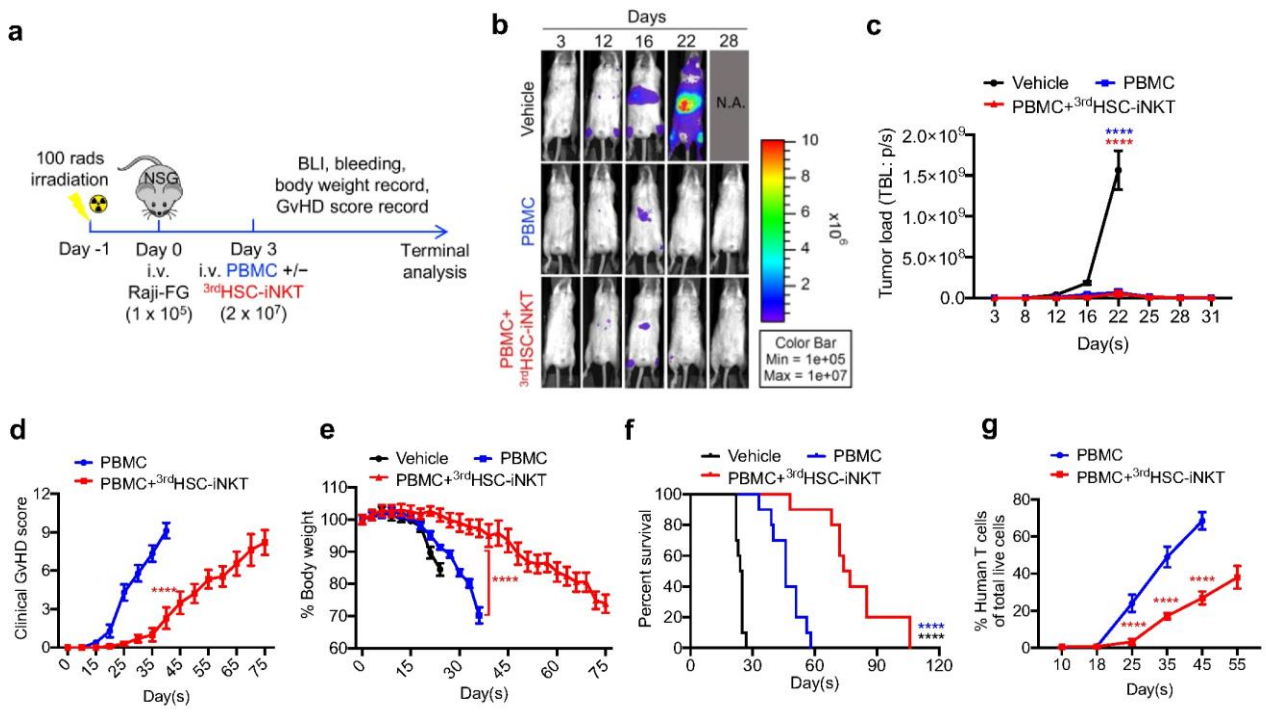

Figure 5: ^{3rd}HSC-iNKT cells preserve GvL while ameliorating GvHD in a human B cell lymphoma xenograft NSG mouse model

Sublethally irradiated NSG mice were inoculated 1 x 10^5 Raji-FG on day 0, followed by intravenous injection of 2 x 10^7 healthy donor PBMCs with or without the addition of 2 x 10^7 ^{3rd}HSC-iNKT cells. Mice were monitored for tumor burden and GvHD development. BLI, bioluminescence imaging. **a.** Experimental design. **b.** BLI images showing tumor loads in experimental mice over time. **c.** Quantification of **b** (****$p < 0.0001$). N = 10. **d.** clinical GvHD signs (data on day 40, ****$p < 0.0001$). **e.** Percent of starting body weight (data on day 36, ****$p < 0.0001$). **f.** Kaplan-Meier survival curves (****$p < 0.0001$). **g.** human T cell percentage in peripheral blood (data on day 25, 35, and 45, ****$p < 0.0001$) of experimental mice over time. N = 10.

Representative of 2 experiments. All data are presented as the mean ± SEM. ****$p < 0.0001$ by Student's *t* test (**d, e, g**), one-way ANOVA (**c**), or by log rank (Mantel-Cox) test adjusted for multiple comparisons (**f**). Statistics are all two-sided.

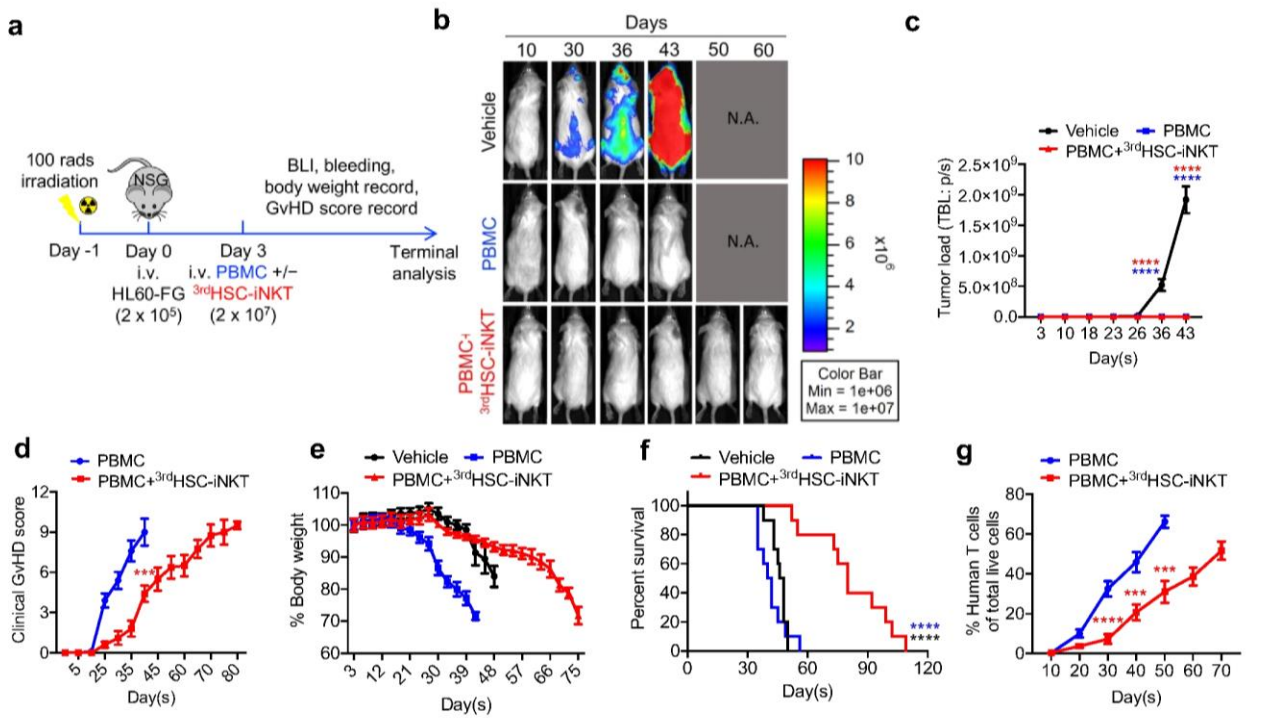

Figure 6: ^{3rd}HSC-iNKT cells preserve GvL while ameliorating GvHD in a human acute myeloid leukemia (AML) xenograft NSG mouse model

Sublethally irradiated NSG mice were inoculated 2 x 10^5 HL60-FG on day 0, followed by intravenous injection of 2 x 10^7 healthy donor PBMCs with or without the addition of 2 x 10^7 ^{3rd}HSC-iNKT cells. Mice were monitored for tumor burden and GvHD development. **a.** Experimental design. **b.** BLI images showing tumor loads in experimental mice over time. **c.** Quantification of **b** (****$p < 0.0001$). **d.** clinical GvHD signs (data on day 40, ***$p < 0.001$). **e.** Percent of starting body weight. **f.** Kaplan-Meier survival curves (****$p < 0.0001$). **g.** human T cell percentage in peripheral blood (data on day 30, 40, and 50, ***$p < 0.001$ and ****$p < 0.0001$). N = 10.

Representative of 2 experiments. All data are presented as the mean ± SEM. ***$p < 0.001$, ****$p < 0.0001$ by Student's *t* test (**d, e, g**), one-way ANOVA (**c**), or by log rank (Mantel-Cox) test adjusted for multiple comparisons (**f**). Statistics are all two-sided.

Supplemental Information

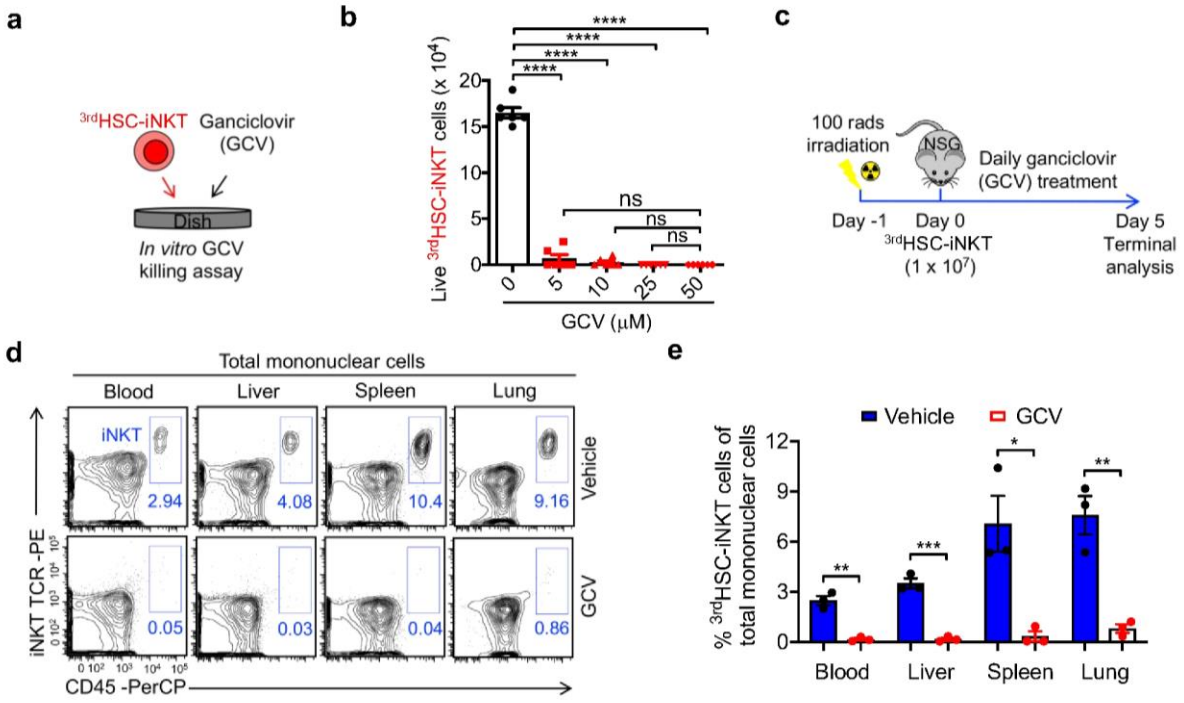

Figure S1: Controlled depletion of HSC-iNKT cells

a-b, *In vitro* controlled depletion of HSC-iNKT cells via GCV treatment. GCV, ganciclovir. **a.** Experimental design. **b**. Quantification of live cells via cell counting (****$p < 0.0001$). N = 6. **c-e**. *In vivo* controlled depletion of HSC-iNKT cells via GCV treatment. **c.** Experimental design. **d.** FACS detection of HSC-iNKT cells in the peripheral blood, liver, spleen, and lung of NSG mice at day 5. **e.** Quantification of **d** (blood, **$p = 0.0012$; liver, ***$p < 0.001$; spleen, *$p = 0.0165$; lung, **$p = 0.0044$). N = 3.

Representative of 2 (**c-e**) and 3 (**a-b**) experiments. All data are presented as the mean ± SEM. *$p < 0.05$, **$p < 0.01$, ***$p < 0.001$, and ****$p < 0.0001$ by Student's *t* test (**e**) or by one-way ANOVA (**b**). Statistics are all two-sided.

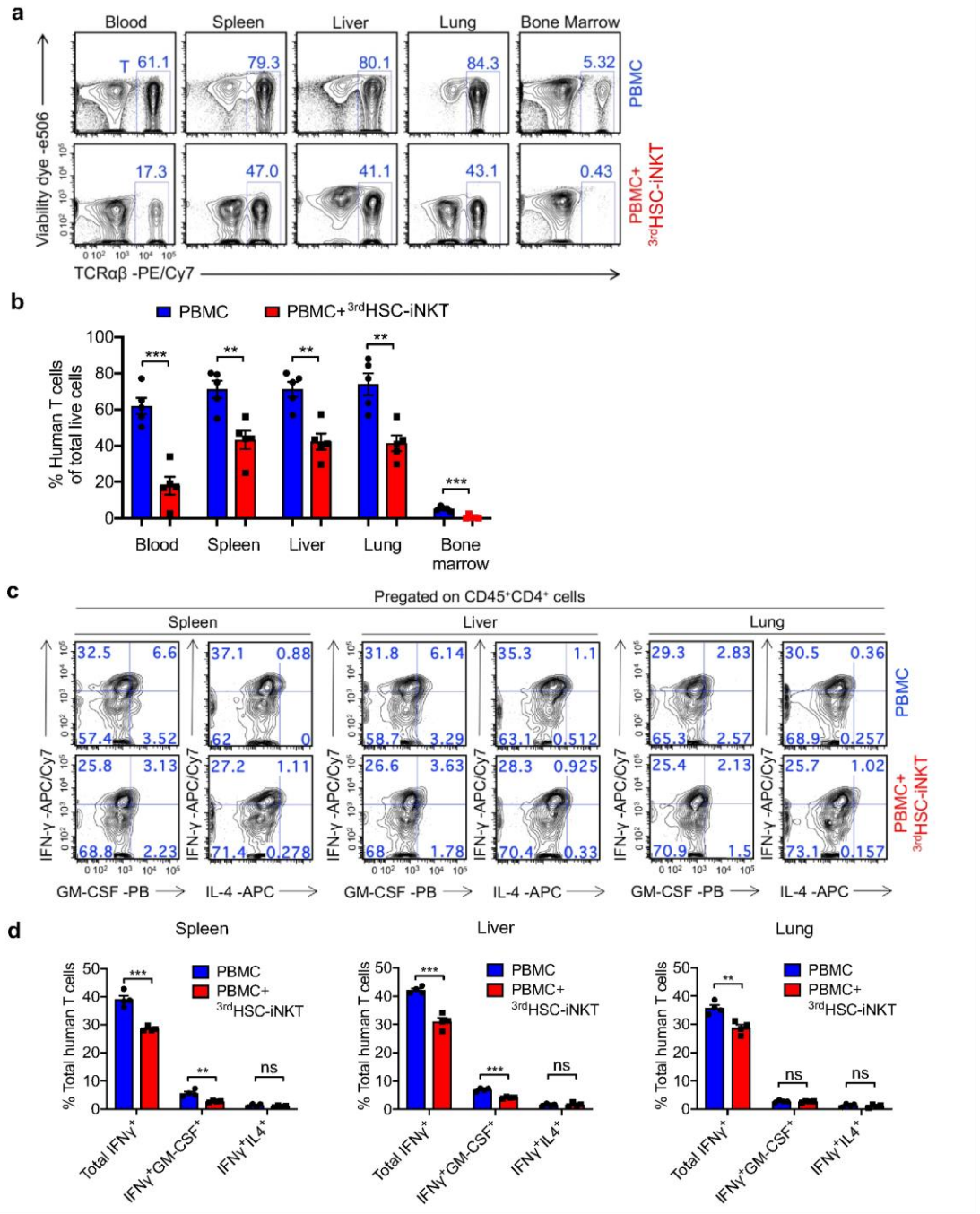

Figure S2: ^{3rd}HSC-iNKT reduces donor T cell expansion and diminishes Th1 response

a. FACS detection of human T cells in the lymphohematopoietic system (e.g. blood, spleen, bone marrow), GvHD target organs (liver, lung) on day 40 after PBMC inoculation. **b**. Quantification of **a** (blood, ***$p < 0.001$; spleen, **$p = 0.0038$; liver, **$p = 0.0015$; lung, **$p = 0.0023$; bone marrow, ***$p < 0.001$). N = 5**. c.** Representative FACS of human $CD4^+$ T cell IFN-γ, GM-CSF, and IL-4 cytokine production in the spleen, liver, and lung on day 40 after PBMC inoculation. **d.** Quantification of c.

Representative of 3 replicate experiments. All data are presented as the mean ± SEM. **$p < 0.01$ and ***$p < 0.001$ by Student's *t* test. Statistics are all two-sided.

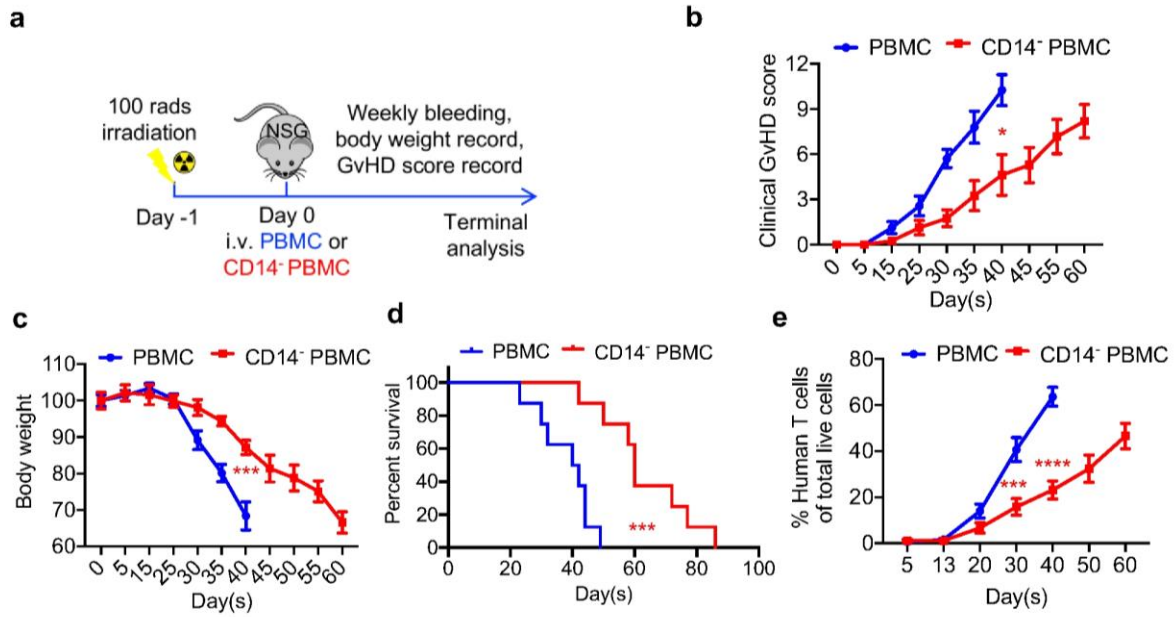

Figure S3: Donor CD14^{+} myeloid cells exacerbate GvHD in NSG mice engrafted with human PBMC

Sublethally irradiated NSG mice received intravenous injection of 2 x 10^{7} healthy donor PBMCs or 9 x 10^{6} CD14-depleted donor PBMCs (amount of PBMC given was normalized to contain the same number of T cells) and were then observed for GvHD development. **a**. Experimental design. **b.** clinical signs of GvHD signs (*p = 0.0218). **c.** Percent of starting body weight (data on day 40, ***$p < 0.001$). **d.** Kaplan-Meier survival curves (***$p < 0.001$). **e**. human T cell percentage in peripheral blood (***$p < 0.001$, ****$p < 0.0001$) of experimental mice over time. N = 8.

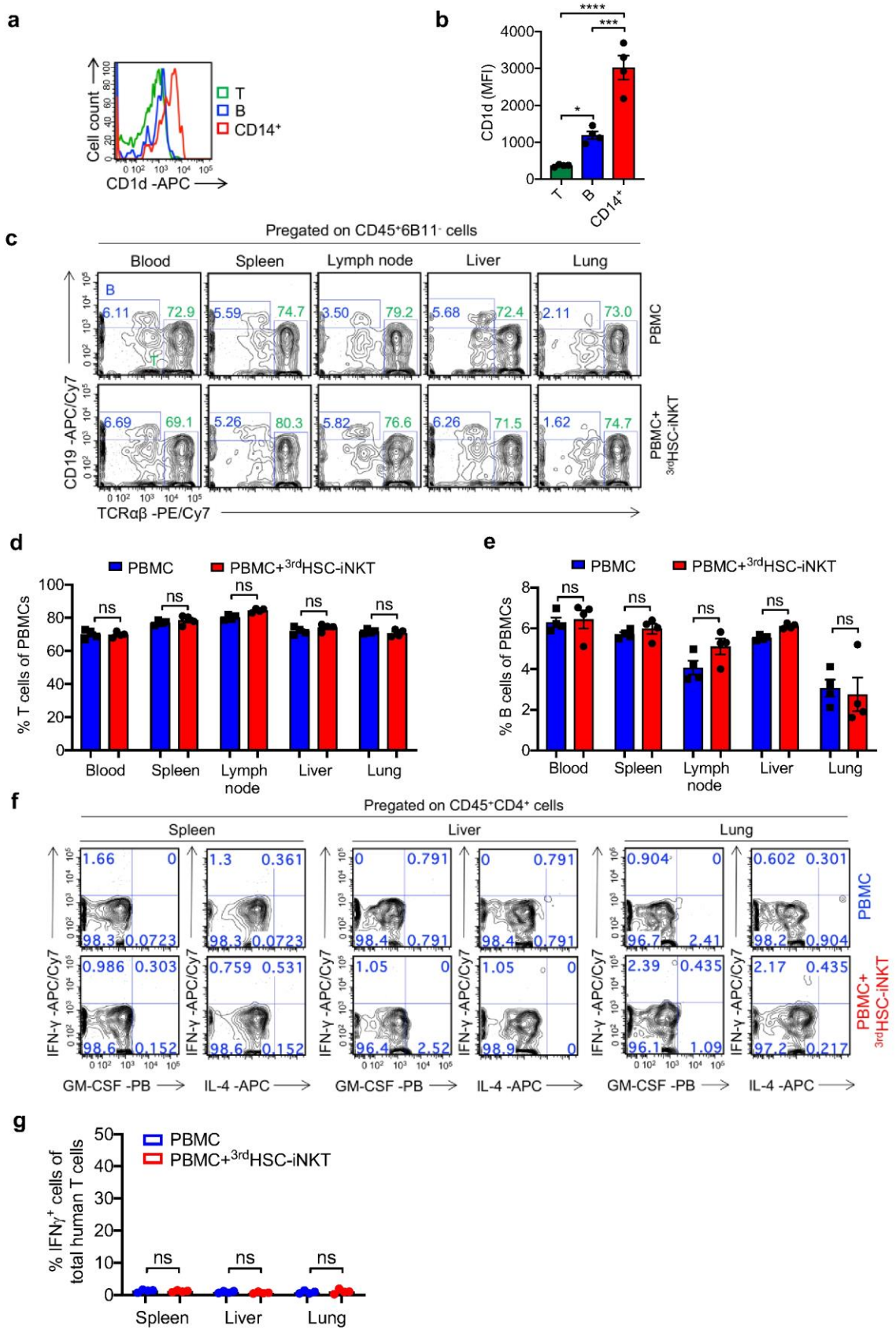
a
Cell count
CD1d -APC
T
B
CD14+
b
CD1d (MFI)
T
B
CD14+
c
Pregated on CD45+6B11- cells
Blood
Spleen
Lymph node
Liver
Lung
PBMC
PBMC+ 3rdHSC-iNKT
CD19 -APC/Cy7
TCRαβ -PE/Cy7
d
PBMC
PBMC+3rdHSC-iNKT
% T cells of PBMCs
ns
Blood
Spleen
Lymph node
Liver
Lung
e
PBMC
PBMC+3rdHSC-iNKT
% B cells of PBMCs
ns
Blood
Spleen
Lymph node
Liver
Lung
f
Pregated on CD45+CD4+ cells
Spleen
Liver
Lung
PBMC
PBMC+ 3rdHSC-iNKT
IFN-γ -APC/Cy7
GM-CSF -PB
IL-4 -APC
g
PBMC
PBMC+3rdHSC-iNKT
% IFNγ+ cells of total human T cells
ns
Spleen
Liver
Lung

Figure S4: No observable changes in T and B % 3 days after the addition of ^{3rd}HSC-iNKT cells

Sublethally irradiated NSG mice received intravenous injection of 2 x 10^7 healthy donor PBMCs with or without the addition of 2 x 10^7 ^{3rd}HSC-iNKT cells and were sacrificed on 3 days after injections. **a.** Comparison of CD1d expression of human $CD14^+$ myeloid, B, and T cells in peripheral blood of PBMCs recipients. **b.** Quantification of a. **c.** Representative FACs depicting the proportion of donor T and B cells in the blood, spleen, lymph node, liver and lung of PBMC and PBMC + ^{3rd}HSC-iNKT recipients. Quantification of **d.** T cells and **e.** B cells. **f.** Representative FACS of human T cell IFN-γ and GM-CSF production in the spleen, liver, and lung 3 days after injections and quantifications.

Representative of 2 replicate experiments. All data are presented as the mean ± SEM. $^{**}p < 0.01$ and $^{***}p < 0.001$ by Student's *t* test. Statistics are all two-sided.

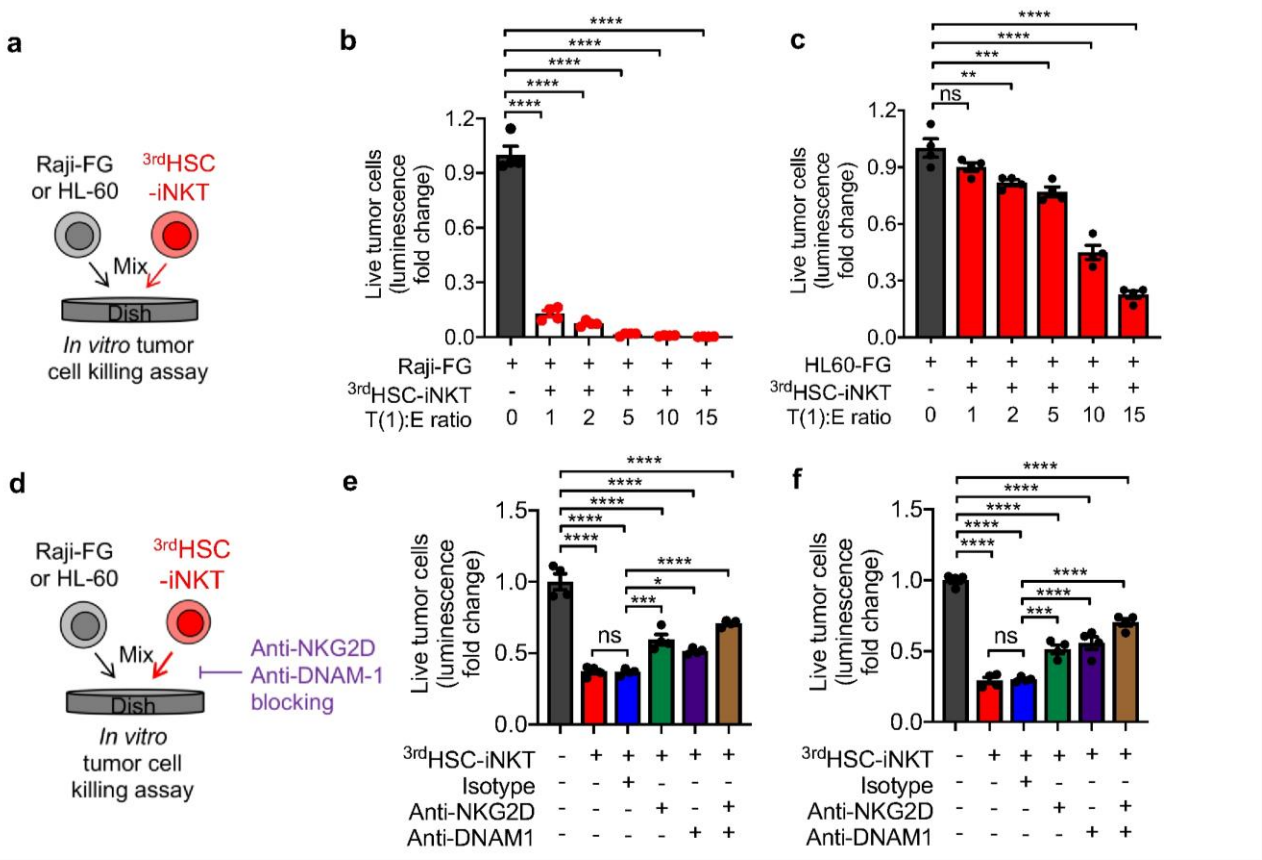

Figure S5: HSC-iNKT cells target tumors through intrinsic NK function

a-c, In vitro direct killing of human tumor cells by HSC-iNKT cells. Two human tumor cell lines were studied: Raji (lymphoma) and HL60 (acute myeloid leukemia, AML). **(a)** Experimental design. **(b and c)** Tumor killing data of Raji-FG human lymphoma cells **(b)** and HL60-FG human AML cells **(c)** at 24-hours (**p < 0.01, ***p < 0.001, and ****p < 0.0001). N = 4.

d-f, Tumor killing mechanisms of HSC-iNKT cells. NKG2D and DNAM-1 mediated pathways were studied. **(d)** Experimental design. **(e)** Tumor killing data of Raji-FG human lymphoma cells at 24-hours (tumor:iNKT ratio 3:1; *p < 0.05, ***p < 0.001, and ****p < 0.0001). N = 4. **(f)** Tumor killing data of HL60-FG human AML cells at 24-hours (tumor:iNKT ratio 1:15; ***p < 0.001 and ****p < 0.0001). N = 4.

References

1. Gribben JG, O'Brien S. Update on therapy of chronic lymphocytic leukemia. *Journal of clinical oncology : official journal of the American Society of Clinical Oncology* **29**, 544-550 (2011).

2. Appelbaum FR. Haematopoietic cell transplantation as immunotherapy. *Nature* **411**, 385-389 (2001).

3. Shlomchik WD. Graft-versus-host disease. *Nature reviews Immunology* **7**, 340-352 (2007).

4. Passweg JR, *et al.* The EBMT activity survey on hematopoietic-cell transplantation and cellular therapy 2018: CAR-T's come into focus. *Bone Marrow Transplantation* **55**, 1604-1613 (2020).

5. Chakraverty R, Sykes M. The role of antigen-presenting cells in triggering graft-versus-host disease and graft-versus-leukemia. *Blood* **110**, 9-17 (2007).

6. Ferrara JL, Levine JE, Reddy P, Holler E. Graft-versus-host disease. *Lancet* **373**, 1550-1561 (2009).

7. Apperley JF, *et al.* Bone marrow transplantation for patients with chronic myeloid leukaemia: T-cell depletion with Campath-1 reduces the incidence of graft-versus-host disease but may increase the risk of leukaemic relapse. *Bone Marrow Transplant* **1**, 53-66 (1986).

8. Yamasaki S, *et al.* Influence of transplanted dose of CD56+ cells on development of graft-versus-host disease in patients receiving G-CSF-mobilized peripheral blood progenitor cells from HLA-identical sibling donors. *Bone Marrow Transplant* **32**, 505-510 (2003).

9. Shimabukuro-Vornhagen A, Hallek MJ, Storb RF, von Bergwelt-Baildon MS. The role of B cells in the pathogenesis of graft-versus-host disease. *Blood* **114**, 4919-4927 (2009).

10. Pabst C, Schirutschke H, Ehninger G, Bornhauser M, Platzbecker U. The graft content of donor T cells expressing gamma delta TCR+ and CD4+foxp3+ predicts the risk of acute graft versus host disease after transplantation of allogeneic peripheral blood stem cells from unrelated donors. *Clinical cancer research : an official journal of the American Association for Cancer Research* **13**, 2916-2922 (2007).

11. Wolf D, *et al.* Regulatory T-cells in the graft and the risk of acute graft-versus-host disease after allogeneic stem cell transplantation. *Transplantation* **83**, 1107-1113 (2007).

12. Lantz O, Bendelac A. An invariant T cell receptor alpha chain is used by a unique subset of major histocompatibility complex class I-specific CD4+ and CD4-8- T cells in mice and humans. *The Journal of experimental medicine* **180**, 1097-1106 (1994).

13. Bendelac A, Savage PB, Teyton L. The biology of NKT cells. *Annual review of immunology* **25**, 297-336 (2007).

14. Brennan PJ, Brigl M, Brenner MB. Invariant natural killer T cells: an innate activation scheme linked to diverse effector functions. *Nature reviews Immunology* **13**, 101-117 (2013).

15. Taniguchi M, Harada M, Kojo S, Nakayama T, Wakao H. The regulatory role of Valpha14 NKT cells in innate and acquired immune response. *Annual review of immunology* **21**, 483-513 (2003).

16. Kronenberg M. Toward an understanding of NKT cell biology: progress and paradoxes. *Annual review of immunology* **23**, 877-900 (2005).

17. Brigl M, Brenner MB. CD1: antigen presentation and T cell function. *Annual review of immunology* **22**, 817-890 (2004).

18. Kumar A, Suryadevara N, Hill TM, Bezbradica JS, Van Kaer L, Joyce S. Natural Killer T Cells: An Ecological Evolutionary Developmental Biology Perspective. *Frontiers in immunology* **8**, 1858 (2017).

19. Cohen NR, Garg S, Brenner MB. Antigen Presentation by CD1 Lipids, T Cells, and NKT Cells in Microbial Immunity. *Adv Immunol* **102**, 1-94 (2009).

20. Zeng D, *et al.* Bone marrow NK1.1(-) and NK1.1(+) T cells reciprocally regulate acute graft versus host disease. *The Journal of experimental medicine* **189**, 1073-1081 (1999).

21. Lan F, Zeng D, Higuchi M, Higgins JP, Strober S. Host conditioning with total lymphoid irradiation and antithymocyte globulin prevents graft-versus-host disease: the role of CD1-reactive natural killer T cells. *Biology of blood and marrow transplantation : journal of the American Society for Blood and Marrow Transplantation* **9**, 355-363 (2003).

22. Pillai AB, George TI, Dutt S, Strober S. Host natural killer T cells induce an interleukin-4-dependent expansion of donor CD4+CD25+Foxp3+ T regulatory cells that protects against graft-versus-host disease. *Blood* **113**, 4458-4467 (2009).

23. Schneidawind D, *et al.* CD4+ invariant natural killer T cells protect from murine GVHD lethality through expansion of donor CD4+CD25+FoxP3+ regulatory T cells. *Blood* **124**, 3320-3328 (2014).

24. Schneidawind D, *et al.* Third-party CD4+ invariant natural killer T cells protect from murine GVHD lethality. *Blood* **125**, 3491-3500 (2015).

25. Lowsky R, *et al.* Protective conditioning for acute graft-versus-host disease. *The New England journal of medicine* **353**, 1321-1331 (2005).

26. Kohrt HE, *et al.* TLI and ATG conditioning with low risk of graft-versus-host disease retains antitumor reactions after allogeneic hematopoietic cell transplantation from related and unrelated donors. *Blood* **114**, 1099-1109 (2009).

27. Haraguchi K, *et al.* Recovery of V α 24+ NKT cells after hematopoietic stem cell transplantation. *Bone marrow transplantation* **34**, 595-602 (2004).

28. Rubio M-T, *et al.* Early posttransplantation donor-derived invariant natural killer T-cell recovery predicts the occurrence of acute graft-versus-host disease and overall survival. *Blood* **120**, 2144-2154 (2012).

29. Chaidos A, *et al.* Graft invariant natural killer T-cell dose predicts risk of acute graft-versus-host disease in allogeneic hematopoietic stem cell transplantation. *Blood* **119**, 5030-5036 (2012).

30. Krijgsman D, Hokland M, Kuppen PJK. The Role of Natural Killer T Cells in Cancer-A Phenotypical and Functional Approach. *Frontiers in immunology* **9**, 367 (2018).

31. Smith DJ, *et al.* Genetic engineering of hematopoietic stem cells to generate invariant natural killer T cells. *Proceedings of the National Academy of Sciences of the United States of America* **112**, 1523-1528 (2015).

32. Zhu Y, *et al.* Development of Hematopoietic Stem Cell-Engineered Invariant Natural Killer T Cell Therapy for Cancer. *Cell stem cell* **25**, 542-557 e549 (2019).

33. Shultz LD, Ishikawa F, Greiner DL. Humanized mice in translational biomedical research. *Nature reviews Immunology* **7**, 118-130 (2007).

34. Wu T, *et al.* Thymic damage, impaired negative selection, and development of chronic graft-versus-host disease caused by donor CD4+ and CD8+ T cells. *Journal of immunology* **191**, 488-499 (2013).

35. Jardine L, *et al.* Donor monocyte-derived macrophages promote human acute graft-versus-host disease. *The Journal of clinical investigation* **130**, 4574-4586 (2020).

36. Anderson BE, McNiff JM, Jain D, Blazar BR, Shlomchik WD, Shlomchik MJ. Distinct roles for donor- and host-derived antigen-presenting cells and costimulatory molecules in murine chronic graft-versus-host disease: requirements depend on target organ. *Blood* **105**, 2227-2234 (2005).

37. Tugues S, *et al.* Graft-versus-host disease, but not graft-versus-leukemia immunity, is mediated by GM-CSF-licensed myeloid cells. *Sci Transl Med* **10**, (2018).

38. Piper C, *et al.* Pathogenic Bhlhe40+ GM-CSF+ CD4+ T cells promote indirect alloantigen presentation in the GI tract during GVHD. *Blood* **135**, 568-581 (2020).

39. Thomis DC, *et al.* A Fas-based suicide switch in human T cells for the treatment of graft-versus-host disease. *Blood* **97**, 1249-1257 (2001).

40. Seet CS, *et al.* Generation of mature T cells from human hematopoietic stem and progenitor cells in artificial thymic organoids. *Nature methods* **14**, 521-530 (2017).

Acknowledgments

We thank the University of California, Los Angeles (UCLA) animal facility for providing animal support; the UCLA Translational Pathology Core Laboratory (TPCL) for providing histology support; the UCLA CFAR Virology Core for providing human cells; and the UCLA BSCRC Flow Cytometry Core Facility for cell sorting support. This work was supported by a Director's New Innovator Award from the NIH (DP2 CA196335, to L.Y.), a Partnering Opportunity for Translational Research Projects Award and a Partnering Opportunity for Discovery Stage Award from the California Institute for Regenerative Medicine (CIRM TRAN1-08533 and DISC2-11157, to L.Y.), a Stem Cell Research Award from the Concern Foundation (to L.Y.), a Research Career Development Award from the STOP CANCER Foundation (to L.Y.), and a BSCRC-RHF Research Award from the Rose Hills Research Foundation (to L.Y.), and an Ablon Scholars Award (to L.Y.).

S.Z is a predoctoral fellow supported by the UCLA Medical Scientist Training Program Grant (T32-GM008042). Y.-R.L. is a predoctoral fellow supported by the UCLA Whitcome Predoctoral Fellowship in Molecular Biology. Z.L. is a postdoctoral fellow supported by the UCLA Tumour Immunology Training Grant (USHHS Ruth L. Kirschstein Institutional National Research Service Award, T32-CA009120). J.Y. is a predoctoral fellow supported by the UCLA Broad Stem Cell Research Center (BSCRC) Predoctoral Fellowship.

Author information

Affiliations

Department of Microbiology, Immunology and Molecular Genetics. University of California, Los Angeles, CA 90095, United States

Samuel Zeng, Yan-Ruide Li, Yang Zhou, Zhe Li, Jiaji Yu, Yu-Chen Wang, Josh Ku, Noah Cook, Adam Kramer, Jie Huang & Lili Yang

Contributions

S.Z., Y.-R.L., and L.Y. designed the experiments, analyzed the data, and wrote the manuscript. L.Y. conceived and oversaw the study, with assistance from S.Z., Y.-R.L. S.Z. and Y.-R.L. performed all experiments, with assistance from Y.Z., Z.L., J.Y., Y-C.W., J.K., N.C., A.K. and J.H.

Corresponding authors

Correspondence to Lili Yang.

Ethics declarations

Competing interests

The authors declare no other competing financial interests.

Chapter 6: Conclusions

T cells of the mammalian adaptive immune system provide crucial protection against spontaneously emerging cancerous cells. When operating as intended, host T cells recognize and eliminate these errant cells before they become detrimental to health. Cancer cells in turn, in an effort to escape the so called "immune surveillance," co-opt many of the pathways normally used by the body to prevent excessive activation and proliferation of T cells and create highly immunosuppressive tumor microenvironments (TMI)[1]. Research over the past several decades have identified many of these checkpoints, and several immune checkpoint blockade (ICB) therapies have been developed over the past decade that can release this suppression and harness the antitumor potential of CD8 T cells[2, 3]. Blockade of the cytotoxic T lymphocyte–associated protein 4 (CTLA-4) and programmed cell death protein 1 (PD-1)/programmed cell death 1 ligand 1 (PD-L1) inhibitory pathways have achieved remarkable clinical responses and revolutionized the treatment of many cancers; so far, the U.S. Food and Drug Administration (FDA) has approved these two ICB therapies for treating more than 10 different malignancies [2, 3]. Nevertheless, only a fraction of patients with cancer respond to CTLA-4 and PD-1/PD-L1 blockade therapies, and relapse risk increase the longer blockade therapies are utilized[4]. These limitations of existing ICB therapies are thought to be largely caused by the presence of multiple immune checkpoint pathways, as well as the different roles of individual immune checkpoint pathways in regulating specific cancer types and disease stages [4]. Thus, the identification of new immune checkpoints and the development of new combination treatments are a major focus of current cancer immunotherapy studies.

Novel role of MAO-A in regulating CD8 T cell anti-tumor immunity

Monoamine oxidase A (MAO-A) is an enzyme located on the outer membrane of mitochondria that catalyzes the degradation of biogenic and dietary monoamines[5, 6]. MAO-A is best known for its function in the brain, whereby it influences human mood and behavior through regulating the homeostasis of key

monoamine neuronal transmitters including serotonin, dopamine, epinephrine, and norepinephrine[5, 6]. The role of MAO-A outside of the brain, and in particular its involvement in anti-tumor immunity, is still relatively unknown. In Chapter 2, I show a novel role of MAO-A in modulating $CD8^+$ anti-tumor response and propose an "intratumoral MAO-A–serotonin axis" model. In this model, MAO-A controls the availability of serotonin in a tumor cell–T cell immune synapse to regulate antitumor T cell reactivity, not unlike MAO-A modulating serotonin availability in the neuron-neuron synapse in the brain to modulate signal strength. Given that both the nervous system and the immune system are evolved to defend a living organism by sensing and reacting to environmental danger, externally and internally, it is unsurprisingly that some critical molecular regulatory pathways are shared cells[7]. Indeed, neurons and immune cells share a broad collection of signal transducers, surface receptors, and secretory molecules[7, 9]. Further study of the neurotransmitters and neuropeptides thought to be exclusive to neuronal function may provide exciting new opportunities to generating knowledge and identifying new drug targets for developing next-generation cancer immunotherapies

Novel role of MAO-A in promoting the immunosuppressive phenotype in tumor associated macrophages

Intriguingly, the role of MAO-A in anti-tumor immunity is not limited to just polarizing TAM towards an immunosuppressive phenotype. In Chapter 3, I find that MAO-A plays another previously unidentified role of promoting the immunosuppressive phenotype of tumor associated macrophages (TAM). Analogous to the MAO-A-ROS axis in the brain, in which MAO-A controls ROS levels in neurons and utilizes oxidative stress to modulates neuron degeneration, the "intratumoural" MAO-A-ROS axis proposes MAO-A regulates TAM ROS levels and promotes immunosuppressive polarization through sensitizing the IL-4/IL-13-induced JAK-Stat6 signaling pathway. As previously mentioned, there is a broad collection of surface receptors, secretory molecules, signal transducers shared by

neurons and immune cells[7]. Even many of the synthesis/degradation machineries traditionally considered specific for neurons are expressed in immune cells; however, their functions in the immune system remain largely unknown[8]. Studying these molecules and their regulatory mechanisms may provide new perspectives in tumor immunology and identifying new drug targets for cancer immunotherapies.

Repurposing of SSRI for Cancer Immunotherapy

In Chapter 2, I find that antigen-TCR stimulation in CD8 T cells induces MAO-A expression, which in turn restrains T cell activation. This negative-feedback loop qualifies MAO-A as an immune checkpoint and adds it to the expanding immune checkpoint family comprising PD-1/PD-L1, CTLA-4, Tim-3, LAG-3, T cell immunoreceptor with Ig and ITIM domains (TIGIT), V-domain Ig suppressor of T cell activation (VISTA), and others[1]. MAO-A, however, is unique because it is already a well-established drug target. A multitude of small-molecule monoamine oxidase inhibitors (MAOI) are already clinically approved that regulate serotonin signaling in the brain and used to treat depression[10]. Indeed, the preclinical animal studies in Chapter 2 and 3 that explored the benefits of targeting MAO-A for immunotherapy were performed using multiple clinically approved MAOIs (phenelzine, moclobemide, and clorgyline). The observed benefits to antitumor immunity observed in these preclinical animal models points to the exciting possibility of repurposing these drugs for cancer immunotherapy.

Unlike developing new cancer drugs, which is extremely costly and time consuming, repurposing drugs offers an economic and speedy pathway to additional cancer therapies because approved drugs have known safety profiles and modes of actions and thus can enter the clinic quickly[11]. MAOIs were introduced in the 1950s and were used extensively over the subsequent two decades. Since then, their

use has dwindled because of reported side effects and the introduction of other classes of antidepressant agents[10]. However, these MAOI side effects were vastly overstated and should be revisited[10]. For instance, a claimed major side effect of MAOIs is their risk of triggering tyramine-induced hypertensive crisis when patients eat tyramine-rich foods such as aged cheese (hence, "the cheese effects"); this concern led to cumbersome food restrictions that are now considered largely unnecessary[10]. A transdermal delivery system for selegiline (Emsam) has also been developed that can largely avoid potential food restrictions[10]. Therefore, interest in MAOIs as a major class of antidepressants is reviving[10], and repurposing MAOIs for cancer immunotherapy can be an attractive new application of these potent drugs.

Depression and anxiety are common in patients with cancer: Prevalent rates of major depression among patients with cancer are four times higher than the general population, and up to a quarter of patients with cancer have clinically significant depression and anxiety symptoms[12]. Repurposing MAOIs for cancer immunotherapy thus may provide patients with cancer with dual antidepressant and antitumor benefits. A large majority of antidepressants, including MAOIs, selective serotonin reuptake inhibitors (SSRIs), serotonin modulators and stimulators (SMSs), serotonin antagonists and reuptake inhibitors (SARIs), and serotonin-norepinephrine reuptake inhibitors (SNRIs), all work through regulating serotonin signaling in the brain via inhibiting the various key molecules that control serotonin degradation, reuptake, and detection[13]. Chapter 3 revealed the existence of a MAO-A–serotonin axis in tumors that regulates CD8 T cell antitumor immunity. It is plausible to postulate that the other key serotonin regulatory molecules that function in the brain may also function in the tumor regulating T cell antitumor immunity[13]. A recent nationwide cohort study in Israel reported that adherence to antidepressant medications is associated with reduced premature mortality in patients with cancer[12].

Another clinical study reported lymphocyte subset changes associated with antidepressant treatments in patients with a major depression disorder[14]. Studying patients with cancer for possible correlations between antidepressant treatments, antitumor immune responses, and clinical outcomes therefore might yield valuable knowledge informing the immune regulatory function of antidepressants and instructing the potential repurposing of select antidepressant drugs for cancer immunotherapy.

Engineered invariant natural killer T cell additives for overcoming GvHD risk in allogeneic hematopoietic stem cell transplantation

Whereby targeting of MAO-A for immunotherapy emphasizes unleashing the host immune system to target cancer, allogeneic hematopoietic stem cell transplantation focuses on utilizing donor T cell that recognize minor histocompatibility antigens to target residual malignancies. Nearly twenty thousand allogeneic hematopoietic stem cell transplantation (allo-HCT) are performed each year, the vast majority for the treatment of leukemia/lymphoma[15]. Although relapse remains low following allo-HCT, graft-versus-host disease (GvHD) mediated by alloreactive donor T cells remains the major cause of patient morbidity and mortality following T-cell replete allo-HCT[16, 17]. iNKT cells were proposed to prevent GvHD while preserving graft versus leukemia/lymphoma (GvL) effect over a decade ago[18, 19]. However, clinical application of iNKT cells is hindered by their scarcity of iNKT cells in the peripheral blood[20]. In Chapter 4, two protocols are presented for generating large quantities of mouse and human iNKT cells *in vivo* through TCR engineering of hematopoietic stem cells (HSC-engineered iNKT) followed by a murine intermediate. The resultant engineered murine and human iNKT cells are in large quantities and mediate significant antitumor activity, reducing the metastases of B16 melanoma and multiple myeloma, respectively. However, the reliance on a living intermediate for iNKT cell generation places significant obstacles to the clinical translation of these two methods.

With this consideration in mind, the human HSC-engineered iNKT cells presented in Chapter 5 are instead generated through a two-step *in vitro* culture system. The resultant HSC-engineered iNKT cells are of high yield and purity. Admittedly, the current human HSC-engineered iNKT cells can still be further improved upon, notably from replacing with a feeder-free culture system which will considerably disentangle the clinical and commercial development. Such an endeavor is currently underway.

It is interesting to note that HSC-engineered iNKT are predominantly $CD8^+$ and $CD4^-CD8^-$ (DN) subsets and appear Th1-polarized, producing large amounts of IFN-γ and TNF-α and minimal IL-4 and expressing high levels of perforin and granzyme B upon stimulation. These features are remarkably similar to endogenous $CD8^+$ and DN iNKT cells and distinct from $CD4^+$ iNKT cells[17]. Although $CD4^-$, and not $CD4^+$, iNKT cell numbers in donor allograft was previously reported to be associated with clinically significant reduction in GvHD in patients receiving HLA-identical allo-HCT[21], research into the role of iNKT cells for reducing GvHD has largely focused on endogenous $CD4^+$ iNKT populations, in part due to endogenous $CD8^+$ and DN iNKT cells being comparatively less abundant[18, 19, 22, 23, 24, 25]. Among these publications, the accepted mechanism through which endogenous $CD4^+$ iNKT cells prevent GvHD without diminishing GvL is through polarizing donor T cells towards a Th_2 phenotype, upregulating IL-4 expression, and expanding Treg populations[24, 25, 26]. My data in Chapter 5 indicate that the engineered $CD4^-$ HSC-engineered iNKT cells prevent GvHD through a different mechanism, namely through the rapid elimination of $CD1d^+$ donor $CD14^+$ myeloid cells that exacerbate GvHD. This is consistent with *in vitro* studies demonstrating that $CD4^-$ iNKT cells display direct cytotoxicity against CD1d-expressing mature myeloid DCs[21]. Due to the limitations of the NSG humanized mouse model, whether $CD4^-$ HSC-engineered iNKT can also target host $CD1d^+$ antigen presenting cells is unknown. However, given that iNKT cells recognize non-polymorphic CD1d-glycolipid complex[27], which is the same between donor and host, they likely will also eliminate host APCs in the context of allo-HCT.

Overall, data in Chapter 5 suggests $CD4^+$ and $CD4^-$ iNKT cells likely mediate distinct effects that collectively results in a beneficial effector response for transplant recipients.

HSC-engineered iNKT cells rapidly eliminate $CD1d^+$ myeloid cells, but they themselves become scarce within a week of injection. Although no tracing experiment was performed to determine the eventual fate of the HSC-engineered iNKT cells, third party mouse iNKT cells were previously reported to be effective in preventing GvHD despite being rejected rapidly following transplantation[23], suggesting third party HSC-engineered iNKT cells may likewise be eliminated by donor T cells eventually, but only after having first eliminated the $CD1d^+$ myeloid cells. Such a situation is actually favorable, allowing HSC-engineered iNKT cells to be used as a temporary additive for ameliorating acute GvHD risks immediately following allo-HCT. Development of acute GvHD is associated with elevated risk of chronic GvHD[28]. Although the HSC-engineered iNKT cells carry a sr39TK/GCV suicide switch allowing for *in vivo* depletion via ganciclovir administration, not needing to utilize this method can be considered a benefit. Being a self-limiting therapy, HSC-engineered iNKT cells are thus highly suitable to function as an off-shelf, third-party additive to the allograft. Further exploration of HSC-engineered iNKT as off-the-shelf cell carriers for chimeric antigen receptors (CAR) for CAR-iNKT-coupled allo-HCT for treating blood cancers will likewise be interesting directions for future studies.

References

1. Baumeister SH, Freeman GJ, Dranoff G, Sharpe AH. Coinhibitory Pathways in Immunotherapy for Cancer. *Annual review of immunology* **34**, 539-573 (2016).

2. Page DB, Postow MA, Callahan MK, Allison JP, Wolchok JD. Immune modulation in cancer with antibodies. *Annual review of medicine* **65**, 185-202 (2014).

3. Ribas A. Releasing the Brakes on Cancer Immunotherapy. *The New England journal of medicine* **373**, 1490-1492 (2015).

4. Dougan M, Dranoff G, Dougan SK. Cancer Immunotherapy: Beyond Checkpoint Blockade. *Annual Review of Cancer Biology* **3**, 55-75 (2019).

5. Shih JC, Chen K, Ridd MJ. Monoamine oxidase: from genes to behavior. *Annual review of neuroscience* **22**, 197-217 (1999).

6. Pintar JE, Breakefield XO. Monoamine oxidase (MAO) activity as a determinant in human neurophysiology. *Behavior genetics* **12**, 53-68 (1982).

7. Talbot S, Foster SL, Woolf CJ. Neuroimmunity: Physiology and Pathology. *Annual review of immunology* **34**, 421-447 (2016).

8. Kerage D, Sloan EK, Mattarollo SR, McCombe PA. Interaction of neurotransmitters and neurochemicals with lymphocytes. *Journal of neuroimmunology* **332**, 99-111 (2019).

9. Levite M. Nerve-Driven Immunity : Neurotransmitters and Neuropeptides in the Immune System.). Springer Vienna (2012).

10. Wimbiscus M, Kostenko O, Malone D. MAO inhibitors: Risks, benefits, and lore. *Cleveland Clinic Journal of Medicine* **77**, 859-882 (2010).

11. Schein CH. Repurposing approved drugs on the pathway to novel therapies. *Medicinal Research Reviews* **40**, 586-605 (2020).

12. Shoval G, *et al.* Adherence to antidepressant medications is associated with reduced premature mortality in patients with cancer: A nationwide cohort study. *Depression and Anxiety* **36**, 921-929 (2019).

13. Pilowsky PM. Serotonin : The Mediator that Spans Evolution.). Elsevier Science (2018).

14. Hernandez ME, Martinez-Fong D, Perez-Tapia M, Estrada-Garcia I, Estrada-Parra S, Pavon L. Evaluation of the effect of selective serotonin-reuptake inhibitors on lymphocyte subsets in patients with a major depressive disorder. *European neuropsychopharmacology : the journal of the European College of Neuropsychopharmacology* **20**, 88-95 (2010).

15. Passweg JR, *et al.* The EBMT activity survey on hematopoietic-cell transplantation and cellular therapy 2018: CAR-T's come into focus. *Bone Marrow Transplantation* **55**, 1604-1613 (2020).

16. Chakraverty R, Sykes M. The role of antigen-presenting cells in triggering graft-versus-host disease and graft-versus-leukemia. *Blood* **110**, 9-17 (2007).

17. Ferrara JL, Levine JE, Reddy P, Holler E. Graft-versus-host disease. *Lancet* **373**, 1550-1561 (2009).

18. Lowsky R, *et al.* Protective conditioning for acute graft-versus-host disease. *The New England journal of medicine* **353**, 1321-1331 (2005).

19. Kohrt HE, *et al.* TLI and ATG conditioning with low risk of graft-versus-host disease retains antitumor reactions after allogeneic hematopoietic cell transplantation from related and unrelated donors. *Blood* **114**, 1099-1109 (2009).

20. Krijgsman D, Hokland M, Kuppen PJK. The Role of Natural Killer T Cells in Cancer-A Phenotypical and Functional Approach. *Frontiers in immunology* **9**, 367 (2018).

21. Chaidos A, *et al.* Graft invariant natural killer T-cell dose predicts risk of acute graft-versus-host disease in allogeneic hematopoietic stem cell transplantation. *Blood* **119**, 5030-5036 (2012).

22. Lan F, Zeng D, Higuchi M, Higgins JP, Strober S. Host conditioning with total lymphoid irradiation and antithymocyte globulin prevents graft-versus-host disease: the role of CD1-reactive natural killer T cells. *Biology of blood and marrow transplantation : journal of the American Society for Blood and Marrow Transplantation* **9**, 355-363 (2003).

23. Zeng D, *et al.* Bone marrow NK1.1(-) and NK1.1(+) T cells reciprocally regulate acute graft versus host disease. *The Journal of experimental medicine* **189**, 1073-1081 (1999).

24. Schneidawind D, *et al.* Third-party CD4+ invariant natural killer T cells protect from murine GVHD lethality. *Blood* **125**, 3491-3500 (2015).

25. Schneidawind D, *et al.* CD4+ invariant natural killer T cells protect from murine GVHD lethality through expansion of donor CD4+CD25+FoxP3+ regulatory T cells. *Blood* **124**, 3320-3328 (2014).

26. Pillai AB, George TI, Dutt S, Strober S. Host natural killer T cells induce an interleukin-4-dependent expansion of donor CD4+CD25+Foxp3+ T regulatory cells that protects against graft-versus-host disease. *Blood* **113**, 4458-4467 (2009).

27. Cohen NR, Garg S, Brenner MB. Antigen Presentation by CD1 Lipids, T Cells, and NKT Cells in Microbial Immunity. *Adv Immunol* **102**, 1-94 (2009).

28. Kok LMC, *et al.* Risk factors associated with the development of moderate to severe chronic graft-versus-host disease after non-myeloablative conditioning allogeneic stem cell transplantation in patients with AML or MDS. *Human Cell* **33**, 243-251 (2020).